Multi-qubit circuit quantum electrodynamics

Oliver Viehmann

München 2013

Multi-qubit circuit quantum electrodynamics

Oliver Viehmann

Dissertation
an der Fakultät für Physik
der Ludwig–Maximilians–Universität
München

vorgelegt von
Oliver Viehmann
aus Roth

München, den 17. Juli 2013

Erstgutachter: Prof. Dr. Florian Marquardt
Zweitgutachter: Prof. Dr. Jan von Delft
Tag der mündlichen Prüfung: 3. September 2013

Contents

Abstract

Circuit QED systems are macroscopic, man-made quantum systems in which superconducting artificial atoms, also called Josephson qubits, interact with a quantized electromagnetic field. These systems have been devised to mimic the physics of elementary quantum optical systems with real atoms in a scalable and more flexible framework. This opens up a variety of possible applications of circuit QED systems. For instance, they provide a promising platform for processing quantum information. Recent years have seen rapid experimental progress on these systems, and experiments with multi-component circuit QED architectures are currently starting to come within reach.

In this thesis, circuit QED systems with multiple Josephson qubits are studied theoretically. We focus on simple and experimentally realistic extensions of the currently operated circuit QED setups and pursue investigations in two main directions.

First, we consider the equilibrium behavior of circuit QED systems containing a large number of mutually noninteracting Josephson charge qubits. The currently accepted standard description of circuit QED predicts the possibility of superradiant phase transitions in such systems. However, a full microscopic treatment shows that a no-go theorem for superradiant phase transitions known from atomic physics applies to circuit QED systems as well. This reveals previously unknown limitations of the applicability of the standard theory of circuit QED to multi-qubit systems.

Second, we explore the potential of circuit QED for quantum simulations of interacting quantum many-body systems. We propose and analyze a circuit QED architecture that implements the quantum Ising chain in a time-dependent transverse magnetic field. Our setup can be used to study quench dynamics, the propagation of localized excitations, and other non-equilibrium features in this paradigmatic model in the theory of non-equilibrium thermodynamics and quantum-critical phenomena. The setup is based on a design that could easily be extended to break the integrability of the Ising chain. We substantiate our proposal by suggesting concrete experimental protocols and calculating the physics to be expected. In addition to this, we provide a systematic study of the influence of disorder on the (non-equilibrium) behavior of our quantum simulator. Finally, we report on first results towards the experimental realization of our proposal and compare them with theory.

The thesis also contains a brief historical overview of and an extended introduction to the field of circuit QED. A detailed summary of the new research presented in this thesis is given at the end of this introduction, in Section 2.4.1.

Deutschsprachige Zusammenfassung

Der Gegenstand dieser Dissertation sind Circuit-QED-Systeme mit vielen künstlichen Atomen. Diese artifiziellen makroskopischen Quantensysteme beruhen auf der Nichtlinearität von Josephson-Kontakten und der makroskopischen Quantenkohärenz und geringen Dissipation in supraleitenden Bauelementen. Sie wurden als skalierbares Äquivalent zu elementaren quantenoptischen Systemen mit natürlichen Atomen konzipiert. Die künstlichen Atome wechselwirken dementsprechend mit einem quantisierten elektromagnetischen Feld. Die Bezeichnung "Circuit-QED" (Schaltkreis-Quantenelektrodynamik) geht darauf zurück.

Die möglichen Anwendungen dieser Systeme sind vielfältig. Beispielsweise können schon heute einfache Protokolle zur Verarbeitung von Quanteninformation mit Circuit-QED-Systemen implementiert werden. Damit stellen diese Systeme gegenwärtig einen der vielversprechendsten Ansätze für skalierbares Quantencomputing dar. Quantenbits, die kleinsten Einheiten an Quanteninformation, werden dabei in den Eigenzuständen der künstlichen Atome kodiert. Aus diesem Grund bezeichnet man häufig die künstlichen Atome selbst als "Josephson-Qubits" (Josephson-Quantenbits). Angesichts des rasanten experimentellen Fortschrittes in diesem Bereich der Physik darf man annehmen, dass komplexere Circuit-QED-Systeme, die eine größere Zahl an unterschiedlichen Bauelementen einbegreifen, in naher Zukunft experimentell zugänglich sein werden.

In dieser Arbeit werden die Eigenschaften und möglichen Anwendungen von Circuit-QED-Systemen mit vielen Josephson-Qubits theoretisch untersucht. Wir konzentrieren uns dabei auf einfach realisierbare Erweiterungen der aktuellen Circuit-QED-Architekturen und verfolgen zwei verschiedene Stoßrichtungen.

Erstens betrachten wir das Gleichgewichtsverhalten eines Circuit-QED-Systems mit einer großen Zahl supraleitender Josephson-Qubits, die über ihren Ladungsfreiheitsgrad an Felder koppeln können, aber nicht direkt miteinander wechselwirken. Die gegenwärtig allgemein akzeptierte Standardbeschreibung von Circuit-QED sagt die Möglichkeit eines superradianten Phasenübergangs in solch einem System voraus. Eine fundamentale, mikroskopische Untersuchung zeigt jedoch, dass ein Unmöglichkeitsbeweis für superradiante Phasenübergänge aus der Atomphysik auch für Circuit-QED-Systeme greift. Dieses Ergebnis offenbart bislang unbekannte Einschränkungen der Gültigkeit der Standardbeschreibung für Circuit-QED-Systeme mit vielen Josephson-Qubits.

Zweitens erforschen wir das Potential von Circuit-QED-Systemen für Quantensimulationen von wechselwirkenden Vielteilchenquantensystemen. Wir entwerfen und analysieren eine Circuit-QED-Architektur, die eine Quanten-Ising-Kette in einem zeitabhängigen transversalen

Magnetfeld simuliert. Unser System kann benutzt werden, um die Dynamik der Ising-Kette nach einer nichtadiabatischen Änderung eines Systemparameters, die Propagation lokalisierter Anregungen und andere Nichtgleichgewichtsphänomene zu studieren. Es ist zu erwähnen, dass die Quanten-Ising-Kette häufig als Beispielsystem in theoretischen Untersuchungen zur Nichtgleichgewichtsthermodynamik und zu quantenkritischem Verhalten dient. Das von uns vorgeschlagene Circuit-QED-System sollte leicht erweitert werden können, um die Integrabilität der Ising-Kette zu brechen. Wir untermauern die vorausgesagten Eigenschaften des Systems mit detaillierten Rechnungen. Weiterhin stellen wir eine systematische Untersuchung des Einflusses von Unordnung auf das Nichtgleichgewichtsverhalten unseres Quantensimulators an. Schliesslich wird über die ersten experimentellen Ergebnisse zu seiner Realisierung Bericht erstattet und diese werden mit unseren theoretischen Analysen verglichen.

Diese Dissertation umfasst auch einen knappen Abriss der Entwicklungen in der Physik, die unmittelbar relevant für das Forschungsfeld Circuit-QED waren oder sind, sowie eine ausführliche Einführung in das Feld. Unsere Forschungsergebnisse in diesem Zusammenhang, die bereits in Fachzeitschriften veröffentlicht wurden, sind als Nachdrucke der entsprechenden Artikel enthalten (in den Kapiteln 3.4, 4.5 und 4.6).

List of publications

This thesis is based on the following journal articles:

1. *Superradiant Phase Transitions and the Standard Description of Circuit QED*,
   Oliver Viehmann, J. von Delft, and F. Marquardt,
   pulished in Physical Review Letters **107**, 113602 (2011),
   see Section 3.4.

2. *Observing the Nonequilibrium Dynamics of the Quantum Transverse-Field Ising Chain in Circuit QED*,
   Oliver Viehmann, J. von Delft, and F. Marquardt,
   pulished in Physical Review Letters **110**, 030601 (2013),
   see Section 4.5.

3. *The quantum transverse-field Ising chain in circuit quantum electrodynamics: effects of disorder on the nonequilibrium dynamics*,
   Oliver Viehmann, J. von Delft, and F. Marquardt,
   pulished in New Journal of Physics **15**, 035013 (2013),
   see Section 4.6.

Further publications by the author of this thesis:

4. *Polynomial invariants for discrimination and classification of four-qubit entanglement*,
   Oliver Viehmann, C. Eltschka, and J. Siewert,
   published in Physical Review A **83**, 052330 (2011).

5. *Reply to Comment on "Superradiant Phase Transitions and the Standard Description of Circuit QED"*,
   Oliver Viehmann, J. von Delft, and F. Marquardt,
   E-print, arXiv:1202.2916 (2012).

6. *Rescaling multipartite entanglement measures for mixed states*,
   Oliver Viehmann, C. Eltschka, and J. Siewert,
   published in Applied Physics B **106**, 533 (2012).

Chapter 1

What set the stage for circuit QED

Circuit quantum electrodynamics (QED) systems are engineered, macroscopic quantum systems in which superconducting artificial atoms interact with quanta of the electromagnetic field. Conceived less than 10 years ago by Blais *et al.* (2004) and Wallraff *et al.* (2004), circuit QED has already proved to be a versatile testbed for fundamental quantum physics and a promising platform for processing quantum information. The tremendous progress of the experimental technology has lead to circuit QED architectures with multiple components and steadily increasing coherence times, and new types of larger-scale circuit QED systems are now on the verge of becoming experimentally realizable. In this thesis, the prospects of exploring novel, many-body quantum phenomena in such circuit QED systems are studied theoretically. We pursue two main lines of research. We investigate whether the strong collective light-matter coupling in circuit QED systems with a large number of artificial atoms can drive an equilibrium superradiant phase transition (Chapter 3). And we contribute to the idea of quantum simulations with circuit QED systems by proposing and analyzing a circuit QED quantum simulator of non-equilibrium spin-chain dynamics (Chapter 4).

To prepare and to motivate this endeavour, we start out by putting the field of circuit QED into a larger context and briefly review the most important achievements that circuit QED is based on or driven by (in the present chapter). This will help us to explain the theoretical foundations of circuit QED and to appreciate the work done in this field so far (Chapter 2). Against this background, the goals of the research presented in this thesis (Chapters 3 and 4) can then be easily further clarified, and the results obtained be outlined (Section 2.4.1).

Even though quantum mechanics had been tested in experiments with ensembles of quantum systems (such as spectroscopy of atomic gases) over decades, it was not before the 1970s that isolation and measurements of individual quantum systems started to become possible. Landmarks in this development are the trapping of a single electron by Wineland *et al.* (1973), the demonstration of Doppler laser cooling of trapped ions by Wineland *et al.* (1978) and Neuhauser *et al.* (1978), or the fluorescence imaging of a single laser-cooled ion by Neuhauser *et al.* (1980). These achievements enabled fundamental tests of quantum mechanics at the level of a single quantum object, for example, the observation of quantum jumps (Nagourney *et al.*, 1986; Bergquist *et al.*, 1986; Sauter *et al.*, 1986) or high-precision g-factor measurements (Van Dyck *et al.*, 1987). What is more, they also laid the foundations for the seminal demonstrations of quantum-state manipu-

lations on trapped ions in the 1990s. To name just two of them, Meekhof *et al.* (1996) prepared a trapped ion in a non-classical motional state, and Monroe *et al.* (1996) entangled the internal state of an ion with its spatial position. This ability to control and to manipulate individual quantum systems is at the heart of all quantum technologies such as circuit QED.

At about the same time, researchers started to explore effects that rely explicitly on the interaction of atoms with a *quantized* electromagnetic field. To produce the necessary ratio of atom-photon coupling and loss rates, the atoms were excited to Rydberg states, which have large electric dipole elements with other Rydberg states and long spontaneous decay times, and were sent through a high-finesse microwave cavity. These ideas had a massive influence on the field of circuit QED, as we will see later. They facilitated the observation of the enhancement (Goy *et al.*, 1983) and suppression (Hulet *et al.*, 1985) of the atomic decay due to the presence of the (off-)resonant cavity (termed Purcell effect, (Purcell, 1946)), the demonstration of a one-atom maser (Meschede *et al.*, 1985), or the measurement of collapse and revival of the Rabi nutation of the atoms (Rempe *et al.*, 1987), the latter already strongly indicating the quantization of the electromagnetic field inside the cavity. Further development of the experimental technology lead to a series of breakthrough 'cavity QED' experiments in the 1990s, including the observation of quantum Rabi oscillations in the time-domain (Brune *et al.*, 1996b), the preparation of Schrödinger cat states and the time-resolved measurement of their decoherence (Brune *et al.*, 1996a), or the demonstration of cavity-mediated entanglement between atoms (Hagley *et al.*, 1997). Many of these experiments have been repeated or have inspired similar experiments in the circuit QED setting.

In the mid-1990s, much research on trapped ions, in cavity QED, and in other fields became stirred by the results of quantum information theory, which had been hitherto considered purely academic. This discipline has its origins in the pioneering work of Wootters and Zurek (1982) on the no-cloning theorem, of Wiesner (1983) on quantum money, of Bennett and Brassard (1984) on quantum cryptography, of Bennett and Wiesner (1992) on superdense coding, or of Bennett *et al.* (1993) on quantum teleportation: All information is encoded in a physical system and, thus, ultimately governed by the laws of quantum mechanics. These papers showed that taking into account quantum mechanics can profoundly affect our possibilities of processing the information and even allows one to perform certain tasks in some sense 'better' than on the basis of classical physics. Further theoretical research on quantum information processing finally lead to the invention of quantum algorithms that solve certain problems genuinely faster than (known to be) classically possible (Deutsch and Jozsa, 1992; Grover, 1996), culminating in Shor's algorithm for integer factorization (Shor, 1994).

A vital attempt to bridge the gap between the theory of such quantum computations and their experimental implementations was made by Cirac and Zoller (1995). They showed how a universal set of quantum gates (Barenco *et al.*, 1995), *i.e.*, a set of operations on quantum bits sufficient for all quantum computations, can be implemented with trapped ions. A minimal version of this proposal was experimentally realized by Monroe *et al.* (1995). This first step towards building a quantum computer did not only fuel the experimental progress with trapped ions. It also opened the quest for other physical systems which come closer to fulfilling DiVincenzo's criteria for a workable quantum computer (DiVincenzo, 2000) than systems of trapped ions (Loss and DiVincenzo, 1998; Kane, 1998; Knill *et al.*, 2001). Circuit QED systems have a high po-

tential in this regard, as will be discussed at length later. As an aside, we mention a few key results in the context of quantum information processing which have been accomplished with quantum technologies not touched upon in this thesis: the factorization of the number 15 using Shor's algorithm and liquid-state nuclear magnetic resonance (Vandersypen *et al.*, 2001), the demonstration of quantum teleportation using entangled photons (Bouwmeester *et al.*, 1997), the coherent manipulation and spin-echo protection of a two-electron spin qubit in a double quantum dot (Petta *et al.*, 2005), the nonlinear strong coupling of a single self-assembled quantum dot and a photonic crystal cavity (Yoshie *et al.*, 2004; Hennessy *et al.*, 2007), and the coherent control of nuclear and electronic spin qubits formed by a nitrogen-vacancy centre in diamond (Dutt *et al.*, 2007) or a phosphorus impurity in silicon (Pla *et al.*, 2013).

A final important development preceding circuit QED was the interest in 'macroscopic quantum physics', which arose in the 1980s. The question was whether a collective state variable of a macroscopic system, such as the position of a mechanical resonator, can exhibit quantum behavior (Leggett, 1980). The variable studied then was the phase difference of the superconducting order parameter across a Josephson junction. This phase difference is proportional to the time integral of the voltage across the junction and therefore usually a well-defined classical variable of a macroscopic system. So-called macroscopic quantum tunneling of the phase difference through classically forbidden regions was first investigated experimentally by Voss and Webb (1981) and convincingly demonstrated by Devoret *et al.* (1985). The quantization of the anharmonic excitations of the corresponding phase particle was measured by Martinis *et al.* (1985). The (squared) modulus of the superconducting order parameter, describing the density of superconducting electrons, is usually also a nonfluctuating, classical quantity. Observing its quantum behavior requires low-capacitance junctions and was first achieved by Nakamura *et al.* (1997) and Bouchiat *et al.* (1998).

Besides being interesting for its own sake, these macroscopic quantum phenomena were soon realized to be beneficial for quantum computing applications. They allow one to build solid-state based superconducting quantum devices for this purpose, with adjustable properties and not suffering as severely from scalability problems as other quantum technologies. The essential elements in these devices are superconducting Josephson qubits[1] (also called artificial atoms), which exist in a variety of flavors, but which all make use of the quantization of the collective superconducting degrees of freedom one way or the other. As integral part of circuit QED systems, the most important types of superconducting qubits will be reviewed in the next chapter. We remark that Josephson-junction devices have been the first systems to explore macroscopic quantum phenomena since they have very little internal dissipation and large enough energy scales so that thermal fluctuations can be easily frozen out. Today, due to the enormous progress in fabrication and cooling techniques, also collective motional degrees of freedom (center of mass) of nanomechanical devices are about to be placed into the quantum regime (O'Connell *et al.*, 2010; Teufel *et al.*, 2011; Chan *et al.*, 2011).

Circuit QED merges together the concepts of macroscopic quantum systems and cavity QED, borrows ideas from trapped-ion physics, and is driven to a large degree by the innovations of

1. We follow here the common overloading of the notion 'qubit' and refer to the carriers of bits of quantum information as qubits themselves.

quantum information theory. Having gathered the most important developments preceding and influencing the field of circuit QED, we now move on and discuss explicitly the physics of circuit QED systems (Sections 2.1 and 2.2) and their state of the art (Section 2.3). This will show us that it is timely and of high interest to investigate circuit QED systems with multiple qubits, both for quantum information processing applications and the study of atom-field interactions. Here, the new work presented in this thesis ties in, as outlined in Section 2.4.1.

Chapter 2

Introduction to circuit QED

2.1 Superconducting qubits

Superconducting qubits are nonlinear quantum circuits made out of superconducting material and the key elements of circuit QED systems. The necessary nonlinearity to act as artificial atoms in cavity QED type experiments or for quantum information purposes is inherited from one or a few Josephson junctions embedded in these circuits. Electrical circuits, in general, offer a great design flexibility and can be integrated on a chip, for which elaborate microfabrication techniques are available. They do not need to be trapped or laser-cooled, and, with regard to fabrication, moving to large-scale circuit systems is easy. This makes electrical circuits appealing for building qubits. The challenge, however, is to isolate them well enough from the environment so that they exhibit quantum coherence over the time-scale of an experiment. It is the unique properties of superconductivity and Josephson junctions that make it possible to obtain the desired nonlinear quantum behavior. We will briefly review these concepts before we discuss the different types of superconducting qubits and how they can be coupled to form circuit QED systems. More details on superconducting qubits can be found in the review articles by Makhlin *et al.* (2001), Devoret *et al.* (2004), Schoelkopf and Girvin (2008), Clarke and Wilhelm (2008), and Devoret and Schoelkopf (2013).

Superconductivity

If the temperature falls below a critical value, some materials suddenly lose all electrical resistivity (Kamerlingh Onnes, 1911) and expel magnetic fields from (parts of) their interior (Meissner and Ochsenfeld, 1933). This phenomenon is known as the superconducting phase transition, and the new properties mentioned are referred to as superconductivity. A century of intense research on superconductivity has produced an extensive textbook literature on the subject (*e.g.*, Schrieffer (1983); Tinkham (1996); Ketterson and Song (1999)), but has still left open many fundamental questions about this fascinating physics.

The Bardeen-Cooper-Schrieffer (BCS) theory (Bardeen *et al.*, 1957) provides a microscopic explanation for the superconductivity found in many metals, metallic alloys, and heavily doped

nonmetallic materials (so-called conventional superconductors). It tells us that an attractive interaction between the conduction electrons causes them to form boson-like pairs, termed Cooper pairs. In the ground state of the system, these are condensed in momentum space. The elementary excitations are (fermionic) Bogoliubov quasiparticles and are separated from the ground state at least by a nonzero energy gap Δ. In conventional superconductors, the electron-pairing relies on an indirect electron-electron interaction mediated by phonons. BCS theory comprises former phenomenological theories of superconductivity. Gor'kov (1959) constructed from BCS theory a macroscopic wave function $\Psi(\mathbf{r})$ (extended over the whole superconductor and depending, like a single-particle wave function, just on one spatial coordinate $\mathbf{r}$) which describes the condensate of Cooper pairs. He showed that Ψ is equal to the order parameter (or the wave function) of the Ginzburg-Landau theory of superconductivity (Ginzburg and Landau, 1950) under conditions where the latter is expected to be valid. BCS theory can therefore also be used to derive the London equations (London, 1950).

The properties of superconductors we have discussed so far are promising for building quantum coherent circuits. Superconductors are practically free of dissipation (which would destroy quantum coherence), and quasiparticle excitations can be frozen out using modern cryogenics. However, the condition $k_\mathrm{B}T \ll \Delta$ only guarantees that a superconductor is fully described by a single, macroscopic wave function. To observe coherent quantum behavior of this collective degree of freedom, the superconducting circuit must be engineered in a way that there are excitations $\hbar\Omega_j$ of the collective degree of freedom that fulfil $\hbar\Omega_j \ll \Delta$. Moreover, these excitations have to be sufficiently isolated from thermal (and other) noise, which requires $k_\mathrm{B}T \ll \hbar\Omega_j$ (Devoret *et al.*, 2004). For building superconducting qubits, one engineers circuits with $\Omega_j/2\pi \sim 10\mathrm{GHz}$, corresponding to $\sim 0.5\mathrm{K}$. The base temperature of a dilution refrigerator is $\sim 20\mathrm{mK}$. At this temperature, the energy gap, *e.g.*, of the frequently used BCS-superconductor aluminum corresponds to $\sim 4\mathrm{K}$, so that the energy scales are well separated. The residual AC-resistivity of standard BCS-superconductors is negligible for these temperatures and frequencies Ω_j, as can be estimated by means of the Mattis-Bardeen formula (Mattis and Bardeen, 1958).

Josephson junctions I – lossless nonlinear inductors

Interesting quantum physics arises if the superconducting quantum circuit contains a nonlinearity. This allows one to single out a certain, non-degenerate transition frequency of the circuit and to use the corresponding states as artificial two-level system, *e.g.*, for encoding a qubit. Josephson junctions are the only known nonlinear non-dissipative circuit elements. A Josephson junction consists of two pieces of superconductor separated by a so-called weak link. The weak link can be a narrow constriction of the superconducting material, a layer of normal metal, or, most commonly in circuit QED, a thin insulating layer. We will assume this last case unless stated otherwise. Josephson showed that Cooper pairs can tunnel coherently through such a weak link, carrying a lossless *supercurrent* (Josephson, 1962)

$$I = I_\mathrm{c} \sin\phi. \tag{2.1}$$

The critical current I_c is the maximum supercurrent the Josephson junction can sustain before Cooper pairs break up. It can be related to geometric and material properties of the Josephson

junction by means of the formula of Ambegaokar and Baratoff (1963), which is important for designing Josephson junctions in practice. In particular, I_c is proportional to the area of the junction. Furthermore, $\phi = \phi_2 - \phi_1$, where the ϕ_j are the phases of the superconducting wave functions in the neighbourhood of the Josephson junction[1]. The time evolution of ϕ is governed by (Josephson, 1962)

$$\dot{\phi} = 2eV/\hbar. \tag{2.2}$$

This equation relates the phase difference and the voltage V across the Josephson junction (e is the elementary charge, and $\hbar$ is Planck's constant h divided by 2π). The Josephson equations (2.1) and (2.2) are essential for the dynamics of Josephson junctions (but not exhaustive, see below) and give rise to the famous DC and AC Josephson effects, which were first observed by Anderson and Rowell (1963) and by Shapiro (1963) and Giaever (1965), respectively. Note that the dynamical variables appearing in the Josephson equations are taken to be classical. However, as was indicated in Chapter 1, they can display quantum behavior under certain circumstances. We will see that superconducting qubits rely on exactly that.

It is instructive to combine the Josephson equations into a single one by introducing the *branch flux* (Devoret, 1997)

$$\Phi(t) = \int_{-\infty}^{t} V(t')dt' \tag{2.3}$$

across the Josephson junction. One obtains

$$I = I_c \sin(2\pi\Phi/\Phi_0). \tag{2.4}$$

Here, $\Phi_0 = h/2e$ is the magnetic flux quantum. Equation (2.4) relates the current and the flux through the Josephson junction, similar to the constitutive equation $I = \Phi/L$ of a linear inductor with inductance L. Thus, the Josephson junction can be viewed as a nonlinear inductor, with Equation (2.4) its constitutive equation. We remark that branch fluxes can be defined for all two-port circuit elements, for instance, for a capacitor, where V is then the voltage across its plates. For linear inductors as above, the branch flux is simply the magnetic flux threading the inductor. Branch fluxes will be essential for deriving a quantum theory of circuits. For later purposes, we calculate the energy stored in a Josephson inductor as a function of Φ,

$$E(t) = \int_{-\infty}^{t} I(t')V(t')dt' = -E_J \cos(2\pi\Phi(t)/\Phi_0), \tag{2.5}$$

where we have introduced the Josephson (tunneling) energy $E_J = \Phi_0 I_c/2\pi$.

Josephson junctions II – the RCSJ model

Physical implementations of Josephson junctions are not fully described by the Josephson equations. To begin with, the superconductors on both sides of the Josephson junction form an intrinsic capacitor. This capacitive part of the Josephson junction can be accurately modeled by

1. Rigorously, $\phi = \phi_2 - \phi_1 + (2e/\hbar)\int_1^2 \mathbf{A}d\mathbf{x}$, where the vector potential $\mathbf{A}$ is integrated along a line across the junction. However, the line integral can be gauged away in the absence of a magnetic field (Tinkham, 1996).

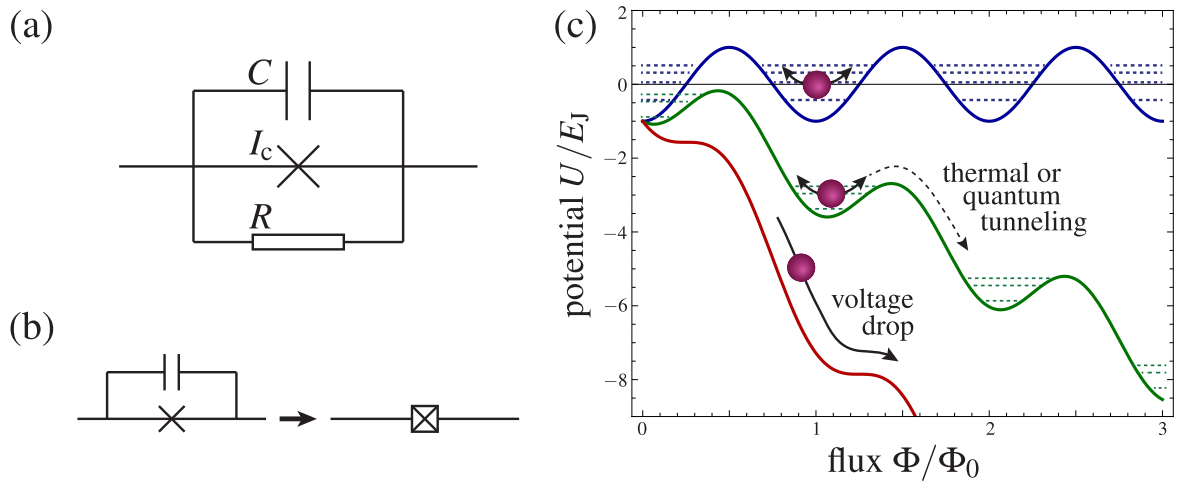

Figure 2.1: RCSJ model of a Josephson junction. (a) Circuit diagram of the RCSJ model. The Josephson element, denoted by a cross and characterized by its critical current I_c, is shunted by a capacitance C and a resistance R. (b) Frequently used electronic symbol of a capacitively shunted Josephson element. (c) Tilted washboard potential of the RCSJ model for $I/I_c = 0, 0.4, 1$ (blue, green, red). The (metastable) bound quantum states of the phase particle are indicated as dashed lines. They are not uniformly spaced due to the anharmonicity of the potential wells.

a capacitance C in parallel with the *Josephson element*, the purely inductive part of the Josephson junction (Figure 2.1(a)). Moreover, in addition to the supercurrent, there can be dissipative quasiparticle tunneling through a Josephson junction. Such dissipative currents cause a nonzero voltage drop across the junction. This effect can be incorporated by a shunt resistance R in the circuit model of a Josephson junction since this circuit element dissipates energy only in the presence of a voltage and leaves the lossless zero-voltage state unaffected (Figure 2.1(a)). We remark that the shunt resistance can be highly temperature and voltage dependent. For instance, the quasiparticle current in the subgap regime $eV < 2\Delta$ is very small for a Josephson junction with insulating interlayer at low enough temperatures and mainly due to junction defects. At $eV > 2\Delta$, Cooper pairs can be broken, resulting in a sudden increase of the dissipative current. Nevertheless, for simplicity R is frequently taken to be a linear resistance (Tinkham, 1996).

We can review here only the most essential features of this intensely studied model of a resistively and capacitively shunted Josephson junction (RCSJ) (Stewart, 1968; McCumber, 1968) However, our discussion will illustrate parts of our previous considerations and prepare some of the following because the RCSJ model is also the theoretical backbone of macroscopic quantum tunneling and of one specific type of superconducting qubits (phase qubits). For a fuller treatment of the RCSJ model, see, *e.g.*, Tinkham (1996).

Let us consider the equation of motion of the RCSJ circuit shown in Figure 2.1(a). By invoking Kirchoff's laws,

$$I = I_c \sin(2\pi\Phi/\Phi_0) + C\ddot{\Phi} + \dot{\Phi}/R, \tag{2.6}$$

where the Josephson junction may be biased by a current I. After rearranging terms,

$$C\ddot{\Phi} + \dot{\Phi}/R = -\frac{\partial}{\partial\Phi}\big[-I\Phi - E_\mathrm{J}\cos(2\pi\Phi/\Phi_0)\big], \tag{2.7}$$

one finds that the equation of motion of the RCSJ model is that of a damped classical particle with mass C and coordinate Φ in a *tilted washboard potential* $U = -I\Phi - E_\mathrm{J}\cos(2\pi\Phi/\Phi_0)$ (Figure 2.1(c)). Equations (2.6) and (2.7) allow static solutions ($\dot{\Phi} = 0$) for the motion of the *phase particle*[2] if $I/I_\mathrm{c} \leq 1$. This is equivalent with the existence of local minima in the tilted washboard potential. The phase particle being at rest in a local minimum corresponds to the situation where the Josephson junction is operated in its dissipation-free, zero-voltage state. If the bias current exceeds the critical current of the junction, $I/I_\mathrm{c} > 1$, static solutions of the equation of motion are not possible, and there has to be a nonzero voltage across the junction. Thus, upon increase of the bias current, a Josephson junction initially in the zero-voltage state will at some point jump to a nonzero voltage state, yielding its well-known gapped $I-V$ characteristic. Depending on the mass C and the damping parameter R, this can happen already for $I/I_\mathrm{c} < 1$ due to thermal agitation. On the other hand, unbound solutions of the equation of motion ($\langle\dot{\Phi}\rangle > 0$) for $I > I_\mathrm{c}$ can remain unbound when I is reduced below I_c. This is the reason for hysteresis effects in the $I-V$ characteristics of weakly damped Josephson junctions.

So far the dynamics of the Josephson junction (the phase particle) have been described classically. Before approaching the quantum theory of Josephson junctions and other circuits formally in the next paragraph, let us discuss qualitatively the effects of quantum mechanics on the RCSJ model.

Quantum mechanics predicts the bound states of the phase particle in the tilted washboard potential to be quantized in energy. Crucially, the allowed energy levels in the anharmonic potential wells have nonuniform level spacing, as indicated in Figure 2.1(c). We emphasize again that this is a consequence only of the Josephson nonlinear inductance and a precondition for addressing a specific pair of states as two-level system. Unlike its classical counterpart, a quantum phase particle shows zero point fluctuations in the ground state of a potential well. And, even at zero temperature, it has a nonzero rate of escape from a well due to quantum tunneling. Thus, quantum mechanics renders the zero-voltage state of a current biased Josephson junction metastable. Since the phase particle represents the state of a macroscopic system, its quantum tunnelling has been named macroscopic quantum tunneling. Finally, dissipation shifts and broadens the energy levels in the potential wells and strongly suppresses the probability of quantum tunneling (exponentially for $T = 0$ (Caldeira and Leggett, 1981, 1983)).

2. At this point, a few remarks on the terminology might be appropriate. The branch flux Φ across a Josephson junction and the phase difference ϕ, often simply called *phase*, are interchangeable via $\phi = 2\pi\Phi/\Phi_0$, and both are used as dynamical variables in the literature. Branch fluxes can be defined also for circuit elements other than Josephson junctions, and they are the starting point for a general theory of (quantum) circuits, which will be discussed in the next section. For this reason, we will usually use a branch flux Φ also for describing a Josephson junction. However, sometimes it is more convenient to use the phase ϕ in this context, either to save notation or to differentiate the dynamical variable of the Josephson junction, *e.g.*, from the magnetic flux threading a linear inductor. This has influenced device names such as 'phase qubit' and 'flux qubit', and also explains why the pseudo particle in the RCSJ model is usually dubbed 'phase particle'.

Nevertheless, these deliberations have been confirmed by numerous experiments, out of which we have already mentioned the demonstration of macroscopic quantum tunneling by Devoret *et al.* (1985), following early experiments by Voss and Webb (1981) on the same subject. Here, we highlight the measurement of the energy level quantization in the wells of the tilted washboard potential by Martinis *et al.* (1985), which constitutes the first experimental demonstration of quantized energy levels of a macroscopic system at all. Martinis and colleagues irradiated a current-biased Josephson junction in the zero voltage state with microwaves and measured the escape rates of the junction into the nonzero voltage state. Only when the microwave frequency matched with one of the discrete level spacings, they could detect an increase of the escape rate, indicating that the junction was able to absorb energy[3].

Quantum circuit theory

The experiments on macroscopic quantum physics with Josephson junctions prove that collective state variables of superconducting circuits can display quantum behavior. For the mathematical description of these effects, one needs a quantum theory of circuits in which the state variables of a circuit are represented by appropriate operators and their dynamics are governed by a quantum Hamiltonian.

The standard way of systematically deriving and quantizing the Hamiltonian of an arbitrary circuit network of capacitors, inductors, and Josephson junctions was formulated by Devoret (1997), building on the pioneering work of Yurke and Denker (1984). In the following, we summarize the key elements of this procedure. It is based on the branch fluxes Φ_j (Equation (2.3)) across the circuit elements j.[4] Working with branch fluxes has the advantage that Kirchhoff's laws yield usual second-order equations of motion also for circuits with Josephson junctions. This allows one to find a generating Lagrangian, which is then transformed into a Hamiltonian and quantized. To find a Lagrangian for the circuit network, one first has to express the set of all branch fluxes, which may depend on each other due to the constraints imposed by Kirchhoff's laws, by a number of independent ones. For the elementary circuits we will encounter in the following, this is not difficult. A prescription how it can be done for arbitrarily complex networks in terms of *node fluxes* is detailed in Devoret (1997). The Lagrangian of the system is then the energy of the capacitive circuit elements minus the energy of the inductive circuit elements, expressed by the independent fluxes and their time derivatives. For instance, in the case of a simple LC oscillator (Figure2.2(a)), $\Phi_\mathrm{L} = -\Phi_\mathrm{C} \equiv \Phi$ and the Lagrangian $\mathcal{L}$ reads

$$\mathcal{L}_\mathrm{LC} = \frac{1}{2}C\dot{\Phi}^2 - \frac{1}{2L}\Phi^2. \tag{2.8}$$

Note that this is the Lagrangian of a mechanical harmonic oscillator with coordinate Φ, mass C, and spring constant $1/L$. Thus, the capacitive energies in a circuit can be viewed as the kinetic energy of one or several phase particles, and the inductive energies as their potential energies.

3. To be precise, the microwave frequency was kept fixed and the level spacing was tuned via the bias current in this experiment. The measured escape rates were then compared with those without microwave irradiation.
4. The circuit elements sit on the 'branches' of the 'circuit tree', thus the name *branch* flux.

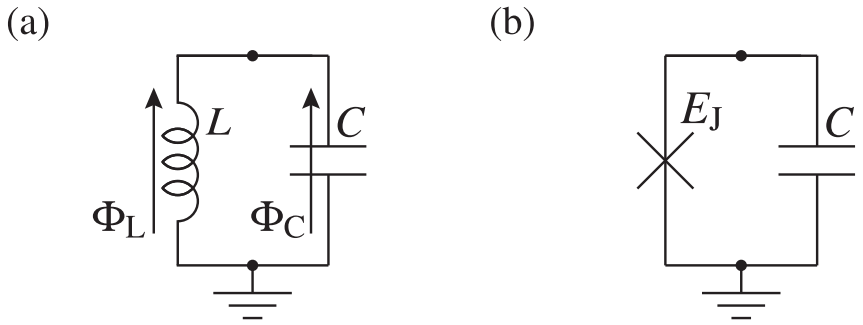

Figure 2.2: (a) LC circuit. The branch flux Φ_L (Φ_C) through the inductor (capacitor) is indicated by an arrow. (b) The same circuit as in (a) but with the linear inductor replaced by a Josephson element (a nonlinear inductor). This circuit can be seen as a minimal model for a Josephson junction.

Another example for this correspondence is the equation of motion of the RCSJ model (Equation (2.7)), where C is the inertia of the phase particle, and the potential is determined by the inductive energy of the Josephson element (Equation (2.5)) and the bias current, which can be thought of as stemming from a large, flux-loaded inductor (see Devoret (1997) for the treatment of voltage and current sources within the present formalism). The canonically conjugated momenta $Q_j = \partial\mathcal{L}/\partial\dot{\Phi}_j$ are charges and can be shown to exist in any meaningful circuit (the Φ_j are now assumed to be independent). The Hamiltonian $\mathcal{H}(Q_j,\Phi_j)$ of the system results from a Legendre transformation. In case of the LC oscillator,

$$\mathcal{H}_{\mathrm{LC}} = \frac{Q^2}{2C} + \frac{\Phi^2}{2L}. \tag{2.9}$$

We remark that the effects of linear dissipative elements can be modeled within the Hamiltonian formalism (Caldeira and Leggett, 1981, 1983; Esteve *et al.*, 1986). Such elements build in dissipation phenomenologically. Depending on the problem at hand, it can be more appropriate to do this not on the level of circuit theory, but on the basis of effective models derived from it, using, *e.g.*, Lindblad master equations.

We are now in the position to quantize the circuit theory by promoting the canonical coordinates to operators that obey the canonical commutation relation

$$[\hat{\Phi}_j, \hat{Q}_j] = i\hbar. \tag{2.10}$$

From here on, one applies the rules and tools of quantum mechanics to calculate any quantity of interest. For instance, we can diagonalize the quantum Hamiltonian of the LC circuit by introducing the usual bosonic annihilation and creation operators a and $a^\dagger$ so that

$$\hat{\Phi} = \Phi_{\mathrm{ZPF}}(a^\dagger + a), \tag{2.11}$$

$$\hat{Q} = iQ_{\mathrm{ZPF}}(a^\dagger - a), \tag{2.12}$$

$$\hat{\mathcal{H}}_{\mathrm{LC}} = \hbar\Omega(a^\dagger a + 1/2). \tag{2.13}$$

Here, $\Omega = 1/\sqrt{LC}$ is the classical resonance frequency of the circuit. The zero-point fluctuations of the flux and the charge are given by $\Phi_{\mathrm{ZPF}} = \sqrt{\hbar Z/2}$ and $Q_{\mathrm{ZPF}} = \sqrt{\hbar/2Z}$, where $Z = \sqrt{L/C}$ is the impedance magnitude of both the capacitor and the inductor on resonance. Notice that if Φ_{ZPF} is of the order of the flux quantum Φ_0, Q_{ZPF} is of the order of the electron charge e (and Z is of the order of the resistance quantum h/e^2 (Girvin, 2013)).

We conclude this section by adding a few remarks on the quantum LC circuit, the macroscopic quantum mechanics of a Josephson junction, and the microscopic justification of our quantum circuit theory. The quantum LC circuit is an elementary toy system which helps to gain insight into some important concepts of circuit QED systems and superconducting qubits. Note, for instance, that the zero-point fluctuations of $\hat{\Phi}$ and $\hat{Q}$ imposed by Heisenberg's uncertainty relation are determined by the ratio of L and C, but not by fundamental natural constants such as the electron mass. Thus, one can engineer circuits so that one or the other variable shows less quantum fluctuations by increasing either the contribution of the capacitive or of the inductive energy to the total energy. This is essential in the design of superconducting qubits. Note further that with current microfabrication techniques, one can easily produce structures with $C \sim 1$ pF and $L \sim 0.1$ nH, yielding $\Omega/2\pi \sim 16$ GHz (Makhlin *et al.*, 2001; Devoret *et al.*, 2004). Thus, by considering the LC circuit, we estimate that the condition $k_{\mathrm{B}}T \ll \hbar\Omega \ll \Delta$ should be satisfiable by superconducting qubits.

Let us now derive the quantum Hamiltonian $\hat{\mathcal{H}}_{\mathrm{J}}$ of a minimal model for an isolated Josephson junction. It consists of a Josephson element in parallel with a capacitance C (Figure 2.2(b)). Following the procedure described above and using Equation (2.5), one gets

$$\hat{\mathcal{H}}_{\mathrm{J}} = \frac{\hat{Q}^2}{2C} - E_{\mathrm{J}}\cos(2\pi\hat{\Phi}/\Phi_0). \tag{2.14}$$

So far we have treated the Josephson element phenomenologically as a nonlinear inductor with constitutive equation (2.4), without having cared about the microscopic origin of this inductance. We have argued that there is experimental evidence that the flux through the inductor behaves quantum mechanically and thus have introduced a quantum theory of circuits based on this macroscopic flux. Now we point out that this theory is consistent with a microscopic description of a Josephson junction (Devoret, 1997). We assume that charge tunnels through the junction in units of the Cooper pair charge $-2e$. Excess Cooper pairs on one side of the junction charge the capacitor and are counted by a *number operator* $\hat{n} = \sum_{n=-\infty}^{\infty} n|n\rangle\langle n|$. Thus, the microscopic Hamiltonian of the circuit of Figure 2.2(b) reads

$$\hat{\mathcal{H}}_{\mathrm{J,mic}} = 4E_{\mathrm{C}}\hat{n}^2 - \frac{E_{\mathrm{J}}}{2}\sum_{n=-\infty}^{\infty}\left[|n\rangle\langle n+1| + |n+1\rangle\langle n|\right]. \tag{2.15}$$

Here, $E_{\mathrm{C}} = e^2/2C$ is the single-electron charging energy of the capacitor. The second term describes the tunneling of Cooper pairs with a tunneling energy E_{J}, which we take here for simplicity as a phenomenological parameter. It can now be shown that this Hamiltonian can be reformulated as

$$\hat{\mathcal{H}}_{\mathrm{J,mic}} = 4E_{\mathrm{C}}\hat{n}^2 - E_{\mathrm{J}}\cos\hat{\phi}, \tag{2.16}$$

with a microscopically defined (using number states $|n\rangle$) operator $\hat{\phi}$ which obeys $[\hat{n},\hat{\phi}] = i$ (some care has to be taken here, see Devoret (1997)). Equation (2.16) allows one to derive the Josephson equations (2.1) and (2.2) as operator equations.[5] Thus, we can identify $\hat{\phi}$ as the *phase-difference operator*, and we can give a microscopic meaning to the macroscopic quantum variables via $\hat{Q} = -2e\hat{n}$ and $\hat{\Phi} = \Phi_0/2\pi \times \hat{\phi}$. Notice that the granularity of the charge, which is obvious in Equations (2.15) and (2.16), is also present in Equation (2.14). The Hamiltonian $\hat{\mathcal{H}}_\mathrm{J}$ and the physical state of the system are invariant under $\Phi \to \Phi + \Phi_0$. Thus, we demand the same symmetry for the wave functions in the Φ basis. It follows that the eigenvalues of $\hat{Q} = -i\hbar\partial/\partial\Phi$ are $-2en$ for $n \in \mathbb{Z}_0$. However, if the junction was shunted by a linear inductor with energy $\hat{\Phi}^2/2L$, the system would not have this invariance. Hence, $\hat{Q}$ would have continuous eigenvalues. This is because charge could move continuously onto the capacitor via the shunting inductor (Koch *et al.*, 2007).

Finally, we remark that realizing low-capacitance junctions with $E_\mathrm{C} \gg E_\mathrm{J}$, so that the capacitive character of the junction dominates the Josephson behavior, requires advanced techniques. For comparison, the first single-electron transistor was demonstrated only in 1987 (Fulton and Dolan, 1987). In the early experiments with larger Josephson junctions, the phase / branch flux was essentially well defined (also in the experiments on macroscopic quantum tunneling), which is why these experiments usually revealed the classical Josephson dynamics of Equations (2.1) and (2.2).

Qubit types – an overview

Even though macroscopic quantum tunneling and the energy quantization in the wells of the RCSJ potential unequivocally demonstrated macroscopic quantum physics in Josephson devices, the age of superconducting qubits had not dawned before it became possible to create coherent superpositions of macroscopic quantum states. In devices with well-defined phase, this was hindered for a long time by the difficulty to precisely control the required bias circuitry (see below) and its detrimental effects on the system's coherence. The first experiments that demonstrated such coherent superposition were performed by Nakamura *et al.* (1997) and Bouchiat *et al.* (1998), making use of low-capacitance junctions ($E_\mathrm{C} \gg E_\mathrm{J}$) and superposing different number states $|n\rangle$. This triggered a huge development in the research on superconducting qubits, motivated mainly by the goal to find a scalable architecture for quantum computing. Today, there is a whole zoo of superconducting qubits. It includes the

- Cooper-pair box (Nakamura *et al.*, 1997)
- flux qubit (Friedman *et al.*, 2000)
- quantronium (Vion *et al.*, 2002)
- phase qubit (Martinis *et al.*, 2002)
- transmon (Schuster *et al.*, 2007)
- fluxonium (Manucharyan *et al.*, 2009)
- hybrid qubit (Steffen *et al.*, 2010)
- Xmon (Barends *et al.*, 2013),

where we have listed the qubits in the order of historical appearance without paying attention to

5. These are simply the equations of motion of $\hat{n}$ and $\hat{\phi}$ with current and voltage operators defined by $\hat{I} = -2e \times d\hat{n}/dt$ and $\hat{V} = -2e\hat{n}/C$, respectively.

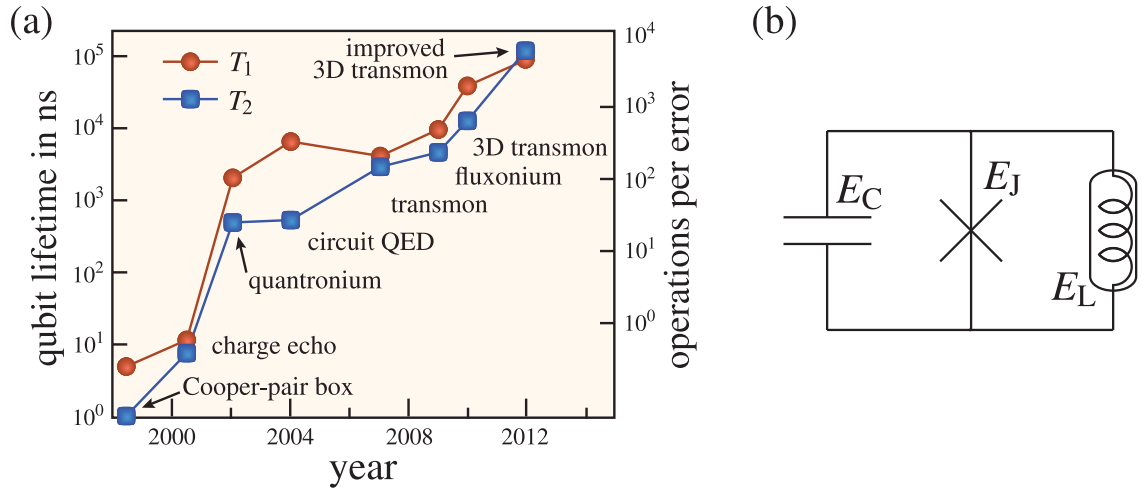

Figure 2.3: (a) Moore's law type exponential increase of the lifetime of superconducting charge qubits, measured by the energy relaxation time T_1 and the dephasing time T_2 (panel adapted from Devoret and Schoelkopf (2013)). Other types of qubits have improved in a similar fashion. The time required for a qubit operation (right vertical axis) was assumed to be 50 ns. This is realistic for multi-qubit entangling gates (Reed *et al.*, 2012). Single-qubit operations can be considerably faster. The time for a specific operation is limited by the qubit's anharmonicity and various coupling parameters and thus has not significantly decreased during the last years. Plotted are the qubit lifetimes obtained with the first generation of each lifetime-improving new qubit design. Devices and techniques not mentioned before are: charge echo (Nakamura *et al.*, 2002), the 3D transmon (Paik *et al.*, 2011), and the improved 3D transmon (Sears *et al.*, 2012; Rigetti *et al.*, 2012). (b) Schematic circuit diagram of a superconducting qubit. Its characteristic energies are the single electron charging energy E_C, the Josephson energy E_J, and the energy of the shunt inductor at one flux quantum, E_L. Possible bias circuitry is not shown. The box around the shunt inductor is meant to indicate that its inductance can be nonlinear. The ratio of the characteristic energies and the bias of the circuit essentially define the different qubit types.

possible super-categories (see below). All these qubit types are based on the Josephson nonlinearity. All different designs seek to reduce in different ways the qubit decoherence due to the manifold ubiquitous noise sources, while retaining enough nonlinearity and optimizing desired features such as manipulability or accessibility to measurement. Up to now, the performance of the superconducting qubits continues to increase rapidly – if measured by the crucial qubit energy relaxation and dephasing times T_1 and T_2, even exponentially (Figure 2.3(a)). Other figures of merit, like the bits of information that can be measured from a qubit during its lifetime (this number combines signal-to-noise ratio and measurement speed), have shown a similar evolution (Devoret and Schoelkopf, 2013).

Superconducting qubits are formed by simple circuits that can be described schematically by the circuit diagram in Figure 2.3(b) (Girvin, 2013; Devoret and Schoelkopf, 2013). The central element is a Josephson nonlinear inductor with Josephson energy E_J. It is shunted by a

capacitor with single-electron charging energy E_C and by a (possibly nonlinear) inductor, which is characterized by E_L, the energy needed to thread it with one flux quantum. The different qubit types differ by the ratio of these characteristic energies, by the way the elements are implemented, and by the way the circuit is biased (not shown): Phase qubits have one large Josephson junction and no additional shunt capacitor ($E_J \gg E_C$), and are current-biased via a linear inductor. Also flux qubits do not have an additional shunt capacitor, but they are flux-biased and the shunt inductor usually consists of two Josephson junctions. Most *charge qubits*, namely Cooper-pair boxes, quantroniums, transmons, and transmon variants such as Xmons, do not have a shunt inductor ($E_L = 0$), but possibly a shunt capacitor in addition to the capacitance of the junction. We remark that names such as 'charge qubits' refer to the quantum variable to which one couples in order to manipulate or read out the qubit state (*i.e.*, this variable is off-diagonal in the qubit eigenbasis). Fluxoniums and hybrid qubits can also be controlled via their charge degree of freedom, but have a drastically different, flux-qubit-like topology. For instance, the fluxonium has a shunt inductance formed by ~ 50 Josephson junctions.

Not all qubit types can be discussed here in detail. We will briefly sketch the basic principles of phase qubits and flux qubits. Many important experiments have been done with them, and they will reappear when we review these experiments in later sections. Our focus in the survey of superconducting qubits will be on Cooper-pair boxes and transmons, since the former have been conceptionally very important and the latter are currently probably the most successful qubits. Moreover, parts of the new research presented in this thesis are explicitly referring to Cooper-pair boxes and transmons. For a comprehensive discussion of the different types of superconducting qubits, we refer to the review articles mentioned at the beginning of this section.

Phase qubits

The prototype of a phase qubit (Martinis *et al.*, 2002) consists of but a single, large ($\sim 10\,\mu\text{m}^2$), current-biased Josephson tunnel junction, just as the devices used to study macroscopic quantum tunneling (Figure 2.1(a)). Fabrication of such junctions is relatively easy and can be done with conventional optical lithography, whereas all other Josephson qubits necessitate electron beam lithography. Since the charging energy is low (typically $E_J/E_C \sim 10^4$) and $\hat{Q}$ fluctuates strongly, the junction is not susceptible to the omnipresent charge noise, which is a major issue for all superconducting qubits. However, much effort must be put into sufficiently protecting the junction against noise from and dissipation into the leads, which requires the use of impedance transformers to feed in bias and control currents.

For operating this phase qubit, the junction is biased by a current I close to its critical current I_c, but is still in the zero-voltage state. The potential of the junction as a function of the phase forms a tilted washboard, similar to the green curve in Figure 2.1(c). The bias current is typically chosen such that there are $3-4$ metastable bound states in a well of the tilted washboard potential, which is approximately cubic in this regime. The two lowest-lying energy levels in such a well, separated by an energy $\hbar\Omega$, are used as qubit levels. Restricted to this subspace, the

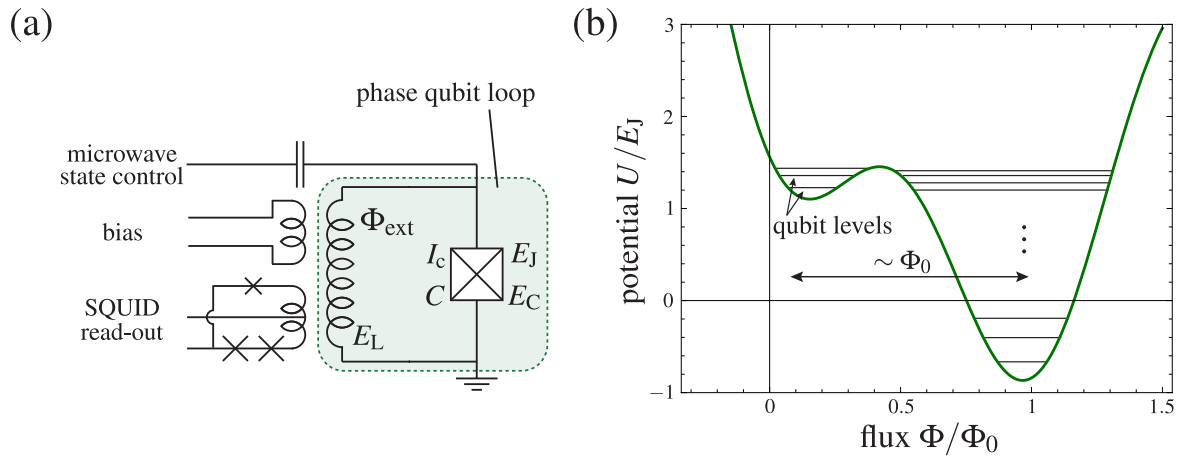

Figure 2.4: Phase qubit. (a) Circuit diagram of the phase qubit and its surrounding circuitry. The qubit consists of a Josephson junction embedded in a superconducting loop with parameters as defined in Figures 2.1(a) and 2.3(b). Operation of the qubit requires a flux bias $\Phi_{\rm ext}$, which is inductively coupled into the loop. The qubit state can be manipulated by applying microwave pulses and is read out using a SQUID magnetometer. (b) Flux potential and qubit levels of the phase qubit. The parameters in this plot are $E_{\rm L}/E_{\rm J} = 4$ and $\Phi_{\rm ext}/\Phi_0 = 0.8$.

Hamiltonian of the junction reads

$$\hat{\mathcal{H}} = \frac{\hbar\Omega}{2}\sigma_z + \sqrt{\frac{\hbar}{2\Omega C}}\delta I(\sigma_x + \chi\sigma_z), \tag{2.17}$$

where $\sigma_{x/z}$ is a Pauli matrix, $\delta I = I_{\rm c} - I$, and χ is of magnitude $\sim 1/4$ (Devoret *et al.*, 2004). Thus, one can drive qubit rotations by appropriately choosing $\delta I(t)$ (which couples to the phase difference across the junction, represented here by σ_x – thus the name 'phase qubit'). The transition frequency Ω of the qubit can be tuned to some extend by varying the DC component of the bias current I. One advantage of phase qubits compared to others used to be the availability of fast high-fidelity single-shot read-out. For this purpose, the potential population in the excited qubit state is swapped to the second or third excited state in the well by applying a suitable drive. This drive will not affect the population of the ground state due to the level anharmonicity. The higher excited states have a drastically increased probability of tunneling out of the well into the continuum. If the qubit was initially excited, this tunneling will cause a finite voltage drop across the junction after the read-out pulse. However, today there are equally efficient (even non-destructive) read-out techniques for other qubit types.

In currently operated designs of the phase qubit, the junction is embedded in a superconducting loop. The loop is coupled capacitively to a microwave source for state manipulations and, via mutual inductances, to an external flux bias $\Phi_{\rm ext}$ and a DC SQUID magnetometer (Simmonds *et al.* (2004); see Figure 2.4(a)). The flux potential of the loop is of the form

$$U = E_{\rm L}[(\Phi - \Phi_{\rm ext})/\Phi_0]^2 - E_{\rm J}\cos(2\pi\Phi/\Phi_0), \tag{2.18}$$

where $E_L = \Phi_0^2/2L$ and L is the linear inductance of the loop (Figure 2.4(b)). Let us assume $E_L < 2\pi^2 E_J$, which is readily achieved using a large Josephson junction. Then, by increasing Φ_{ext}, metastable levels can be created in the vicinity of the global minimum of the potential. Using such levels as qubit states has the advantage that the junction remains in a zero-voltage state after the read-out, which avoids the generation of quasiparticles and self-heating. Upon tunneling of the phase particle, the flux through the loop changes by $\sim \Phi_0$, which can be measured by means of the SQUID magnetometer (Clarke and Braginski, 2006). More recent read-out schemes than the one described above usually simply lower the potential barrier adiabatically so that the excited qubit tunnels out of the well directly.

Phase qubits have been coupled capacitively to other qubits and microwave resonators, as will be discussed later. They can be easily integrated into larger circuits and are therefore one of the most promising qubits for quantum information processing. Their coherence times suffer from junction imperfections, whose number increases with the junction area, and are not as high as for some other qubits (several 100 ns).

Flux qubits

Flux qubits, also known as persistent current qubits, share some similarities with the loop version of the phase qubit. Both qubits have the same circuit topology, both are biased by an external flux. Flux qubits exist in a broad range of designs. However, their underlying physics is essentially the same. It will be explained on the example of the archetype flux qubit, the radio frequency (RF) SQUID. Based on this, we sketch a frequently used design variant, the flux qubit with three junctions.

The RF SQUID consists of a relatively large Josephson junction ($\sim 0.1-1\,\mu m^2$, $E_J/E_C \sim 50$), shunted by an inductive loop with inductance L (Figure 2.5(a)). The loop is biased by an external flux Φ_{ext}. Thus, the flux potential U has the same form as for the phase qubit (Equation (2.18)). However, unlike phase qubits, flux qubits are biased in the vicinity of $\Phi_{ext} = (n+1/2)\Phi_0$, $n \in \mathbb{Z}_0$. For these values of Φ_{ext}, the flux potential has a degenerate global minimum as long as $E_L = \Phi_0^2/2L < 2\pi^2 E_J$ (see Figure 2.5(b)). Moreover, flux qubits use the ground and the first excited state of the system as qubit levels, and not metastable states (this is not strictly true for all flux qubits, see later). Under the stated conditions, the two global minima of the flux potential form a double well and are separated by one local maximum at $\Phi = \Phi_{ext}$. In this situation, it is energetically favorable for the system to increase or to decrease the total flux through the loop relative to the flux bias in order to minimize the potential energy. This requires the flow of a clockwise or a counterclockwise persistent supercurrent in the loop.

One can now obtain a strong anharmonicity of the low-lying quantum states of the system by chosing the potential barrier low enough so that there is a tunnel coupling $\Omega/2$ between the wells (Friedman *et al.*, 2000). Let us denote the states with lowest energy and well-defined current direction by $|\circlearrowright\rangle$ and $|\circlearrowleft\rangle$, and the magnitude of this current by I_q. If the minima of the potential wells are exactly degenerate, the ground and the first excited state of the system are given approximately by the symmetric and the antisymmetric superpositions of $|\circlearrowright\rangle$ and $|\circlearrowleft\rangle$. These states are separated by an energy $\hbar\Omega$, and we refer to them by $|\downarrow\rangle$ and $|\uparrow\rangle$. If the flux bias slightly differs from the *sweet spots* $\Phi_{ext} = (n+1/2)\Phi_0$, there is an energy difference of

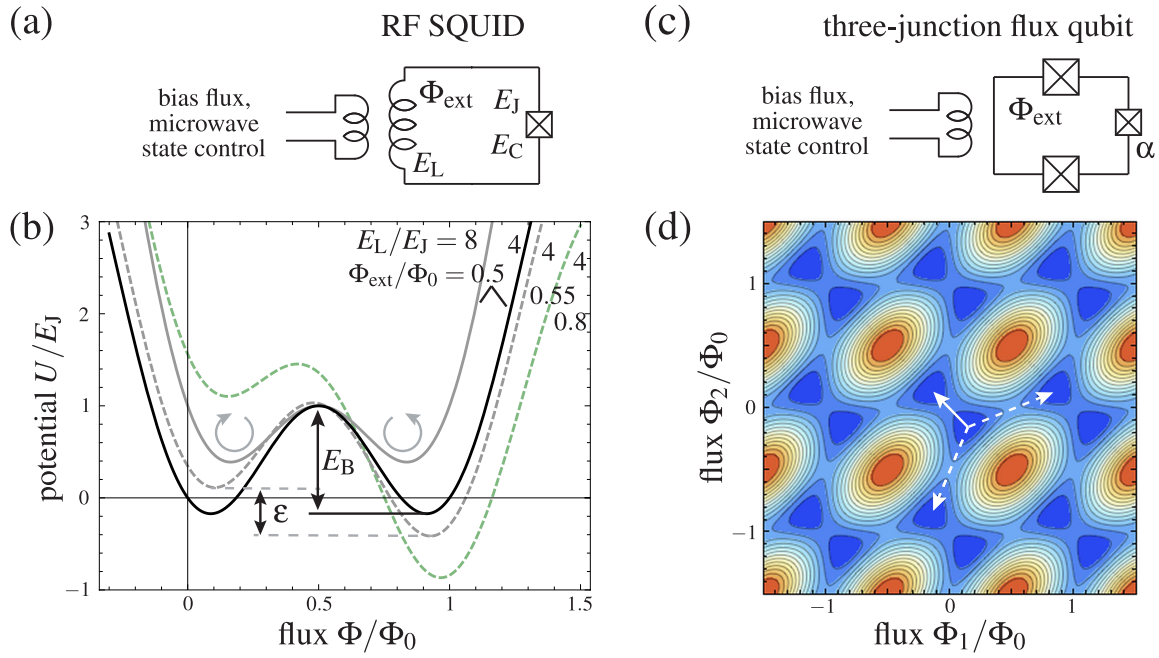

Figure 2.5: Flux qubits. (a) Circuit diagram of the RF SQUID. (b) Flux potential U of the RF SQUID vs. flux Φ. The solid lines show U with the bias flux $\Phi_{\rm ext}$ chosen at the sweet spot $\Phi_{\rm ext} = \Phi_0/2$ for different values $E_{\rm L}/E_{\rm J} = 8,4$ (black, gray). The barrier height $E_{\rm B}$ decreases as this ratio increases. If the flux is trapped in one of the wells, this corresponds to a (counter-)clockwise circulating current in the ring. The dashed lines are for the flux bias $\Phi_{\rm ext}/\Phi_0 = 0.55, 0.8$ (gray, green) being away from the sweet spot (and $E_{\rm L}/E_{\rm J} = 4$). This detuning causes an energy difference ε between the local minima. The relation of flux and phase qubits is illustrated by the green curve, which is identical to the potential of the phase qubit in Figure 2.4(b). (c) Circuit diagram of a common variant of the flux qubit, consisting of a superconducting loop interrupted by three Josephson junctions, one of which is smaller by a factor α than the other two. (d) Flux potential U of the circuit in (c) with $\alpha = 0.85$ and $\Phi_{\rm ext} = \Phi_0/2$ as a function of the independent branch fluxes Φ_1 and Φ_2 (see text). The color scale ranges from blue (low) to red (high). Each well has one neighbouring well into which the system can tunnel easily if initially trapped in this well (indicated by a solid arrow), and two further neighbouring wells that are separated from it by higher barriers. Tunneling into one of these wells (indicated by dashed arrows) is therefore suppressed.

magnitude $|\varepsilon| = 2I_{\rm q}|\Phi_0/2 - \Phi_{\rm ext}|$ between the states $|\circlearrowleft\rangle$ and $|\circlearrowright\rangle$ (assuming $n = 0$ (Clarke and Wilhelm, 2008)), which modifies their weights in the eigenstates of the system. The best qubit is formed by ground and first excited state if the system is biased to a sweet spot. There the level spacing $\sqrt{(\hbar\Omega)^2 + \varepsilon^2}$ is first-order insensitive to fluctuations of $\Phi_{\rm ext}$, which cause decoherence.

In the eigenbasis of these states ($|\downarrow\rangle$ and $|\uparrow\rangle$),

$$\hat{\mathcal{H}} = \frac{\hbar\Omega}{2}\sigma_z + \frac{\varepsilon}{2}\sigma_x. \tag{2.19}$$

Thus, by driving the flux bias Φ_{ext}, one can generate qubit rotations. The qubit splitting Ω decreases exponentially with $\sqrt{E_B/E_C}$, where we have introduced the barrier height $E_B = 3E_J/2 \times [E_L/(2\pi^2 E_J) - 1]^2$. This relation, the dielectric losses in the junction (which increase with junction area), and the effects of charge noise (which decrease with junction area) impose upper and lower bounds on the ratio E_J/E_C. To tune the qubit frequency Ω, the Josephson junction is often split into two smaller junctions with Josephson energies $E_J/2$, and the resulting loop is individually biased with a second flux Φ_q. The two junctions then behave as one with effective Josephson energy $E_J(\Phi_q) = E_J \cos(\pi\Phi_q/\Phi_0)$ (Makhlin *et al.* (2001); see also Figure 2.6(b)). This construction is commonly called a *split junction*.

The state of the qubit is read out by a DC SQUID, which is often directly integrated in the circuit of the flux qubit. Notice that the SQUID measures the magnetic flux produced by the circulating current and therefore σ_x. However, σ_z can be measured, *e.g.*, by adiabatically transferring the population in the states $|\downarrow\rangle$ and $|\uparrow\rangle$ to the states $|\circlearrowleft\rangle$ and $|\circlearrowright\rangle$, respectively.

The RF SQUID needs to be operated in a regime where the degenerate potential wells are separated by a small barrier. This corresponds to the condition $E_L \lesssim 2\pi^2 E_J$. It turns out that for otherwise suitable values of E_J, the self-inductance L and, hence, the area of the loop have to be quite large in order to yield the smallness of E_L required by the above condition. This makes the RF SQUID susceptible for flux noise. The problem can be circumvented by replacing the linear inductance of the loop by two further Josephson junctions, larger by a factor $1/\alpha$ than the first junction, see Figure 2.5(c) (Mooij *et al.*, 1999; van der Wal *et al.*, 2000). There are now three branch fluxes Φ_j describing the circuit. One of them can be eliminated by virtue of Kirchhoff's laws, say, Φ_3, the branch flux of the small junction. In terms of the other two branch fluxes, the flux potential reads

$$U = -E_J\big[\cos(2\pi\Phi_1/\Phi_0) + \cos(2\pi\Phi_2/\Phi_0) + \alpha\cos(2\pi(\Phi_{\text{ext}} + \Phi_2 - \Phi_1)/\Phi_0)\big], \tag{2.20}$$

where $\Phi_{\text{ext}} \approx (n + 1/2)\Phi_0$ is a flux bias as before. This potential is plotted in Figure 2.5(d). It froms a periodic hexagonal pattern of potential wells. At the sweet spot $\Phi_{\text{ext}} = \Phi_0/2$, the depths of all potential wells agrees. However, there is an asymmetry of the potential barriers between neighboring wells: each wells has one neighboring well separated from it by a low barrier and two further neighbors separated from it by higher barriers. This is a consequence of the different junction sizes. Typical values for the junction-asymmetry are $\alpha \sim 0.8$. The states in the wells correspond to circulating currents in the loop. Just as for the RF SQUID, a qubit is formed due to tunneling between 'low-barrier' neighboring wells. Tunneling to other wells is strongly suppressed due to the higher saddle in between. The relative depths of neighboring wells can be modified by slightly varying Φ_{ext}, which is a further analogy to the RF SQUID, and the system can be driven this way. Also the readout is identical that of the RF SQUID.

Flux qubits can be coupled to magnetic fields, *e.g.*, of microwave resonators, or to the magnetic moments produced by the circulating currents of other flux qubits. They have excellent

coherence times $\gtrsim 1\ \mu$s, but these become impaired by increasing complexity of the devices. With respect to implementing quantum gates, other technologies are therefore currently more advanced. We also remark that flux qubits are presently the only commercially available superconducting quantum bits, used for approaches to adiabatic quantum computing (Johnson *et al.*, 2011).

Charge qubits I – the Cooper-pair box

Conventional charge qubits are topologically different from phase and flux qubits. They do not possess an additional DC conducting connection between the leads of the Josephson junction besides the junction itself. That is, the Josephson junction separates *islands* of superconducting material, and charge transport between them can take place only in discrete portions of size $-2e$, the Cooper-pair charge. In the simplified picture of Figure 2.3(b), this corresponds to the case of an infinite shunt inductance ($E_\mathrm{L} = 0$). In this section, we discuss the most elementary charge qubit, the Cooper-pair box.

It has been already mentioned that quantum superpositions of the states of macroscopic systems were first demonstrated by Nakamura *et al.* (1997) and Bouchiat *et al.* (1998), using low-capacitance Josephson devices. These devices had been considered by Büttiker (1987) before, although not as potential solid-state qubits, and are now known as Cooper-pair boxes. The quantum time evolution of a Cooper-pair box was observed the first time in a highly influential experiment by Nakamura *et al.* (1999), which demonstrated spectacularly the potential of Josephson devices for quantum information processing.

The circuit diagram of a Cooper-pair box is shown in Figure 2.6(a). It consists of a small Josephson junction ($\sim 0.01\ \mu\mathrm{m}^2$), separating a small piece of superconductor (the island or the 'box') from a bias circuit which allows one to apply a bias voltage V_g to the island via a *gate capacitance* C_g. The intrinsic capacitance of the Josephson junction is usually denoted by C_J in this context. The characteristic energies E_J and $E_\mathrm{C} = e^2/2C_\Sigma$ are designed to satisfy $E_\mathrm{J} \lesssim E_\mathrm{C}$ (and $k_\mathrm{B}T \ll E_\mathrm{J}, E_\mathrm{C} \ll \Delta$ as usual), where $C_\Sigma = C_\mathrm{J} + C_\mathrm{g}$ is the total capacitance of the island. This requires the junction and the island to be small. The Hamiltonian of the circuit is usually written in the form (see, *e.g.*, Devoret *et al.* (2004))

$$\hat{\mathcal{H}} = 4E_\mathrm{C}(\hat{n} - n_\mathrm{g})^2 - E_\mathrm{J}\cos\hat{\phi}, \tag{2.21}$$

where $\hat{n}$ and $\hat{\phi}$ are the number and the phase operator (cf. Equations (2.14) – (2.16)). Using $\hat{n}$ and $\hat{\phi}$ instead of $\hat{Q}$ and $\hat{\Phi}$ is convenient here since, as discussed earlier, the physical invariance of the system under $\hat{\phi} \to \hat{\phi} + 2\pi$ implies that $\hat{n}$ has integer eigenvalues. The *gate charge* $n_\mathrm{g} = Q_\mathrm{r}/2e + C_\mathrm{g}V_\mathrm{g}/2e$ is continuous and models the effect of the bias voltage V_g and of static noise fields represented by a (scalar) *residual offset charge* Q_r. These noise fields are caused, for instance, by defects in the substrate and can substantially contribute to the charging energy of low-capacitance circuits. Decoherence arises if Q_r has a time-dependent component. In reality, this charge noise is typically found to have a $1/f$ power spectral density (Devoret *et al.*, 2004) and is one of the main sources of decoherence in low-capacitance circuits.

We emphasize that the usual derivation of Equation (2.21) (Büttiker, 1987) on the basis of the circuit network of Figure 2.6(a) presumes $C_\mathrm{g}/C_\mathrm{J} \ll 1$ (and $Q_\mathrm{r} = 0$; the residual offset charge

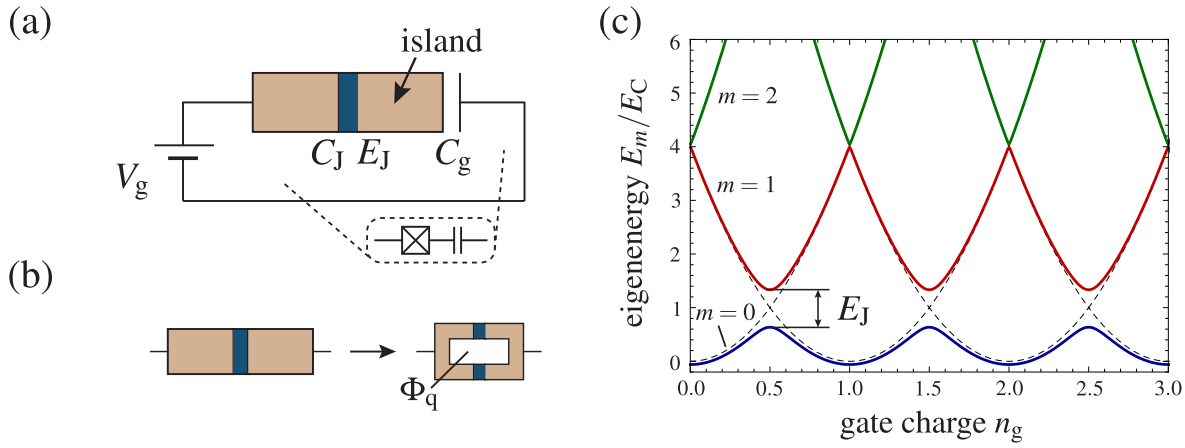

Figure 2.6: The Cooper-pair box. (a) Schematics of the Cooper-pair box and its sourrounding circuitry. The actual circuit diagram of the island is shown in the inset. (b) Circuit design modification to obtain a tunable effective Josephson inductance. Two Josephson junctions with Josephson energies $E_J/2$ intersecting a superconducting loop behave as one with effective Josephson energy $E_J(\Phi_q) = E_J \cos(\pi\Phi_q/\Phi_0)$, tunable by a bias flux Φ_q. (c) Eigenenergies E_m of the Cooper-pair box Hamiltonian vs. gate charge n_g for $E_J/E_C = 0$ (dashed) and $E_J/E_C = 0.7$ (solid). The colors blue, red, green of the solid curves represent the cases $m = 0, 1, 2$, respectively.

is just phenomenologically added and has no direct representation in the circuit network). This is often forgotten, even in such prominent applications of Equation (2.21) as the standard theory of circuit QED (Blais *et al.*, 2004). Nevertheless, Equation (2.21) and theories based on it often provide at least a qualitatively correct description of (systems with) Cooper-pair boxes and related qubits. However, it is one of main conclusions of this theses that this is not always the case. As we show on the explicit example of the possibility of *superradiant phase transitions* in circuit QED, even the well-established standard theory of circuit QED can lead to qualitatively incorrect predictions. This might be a consequence of the simplifications made by using Equation (2.21) as qubit Hamiltonian.

Let us continue discussing the Cooper-pair box on the basis of Equation (2.21). Under the condition $E_J \lesssim E_C$, the number of Cooper-pairs on the island essentially is a good quantum number because the Cooper-pair charging energy $4E_C$ is much larger that E_J. Typical values are $E_J/4E_C \sim 0.1$. This implies that the branch flux across the junction fluctuates wildly. Or, in the picture we have employed before, that the phase particle is highly delocalized over the cosine-shaped flux potential. The well-defined charge makes the system susceptible for the omnipresent charge noise. However, similar to what we have discussed for the flux qubit, there is a sweet spot of the bias voltage where the system becomes first-order insensitive to charge noise. Operated at this point, the Cooper-pair box can form a decent qubit. To understand the origin of this sweet spot, we plot the eigenenergies E_m of the Hamiltonian (2.21) as a function of the gate charge n_g in Figure 2.6(c). The function $E_m(n_g)$, also known as the charge dispersion of E_m, is given in terms of Mathieu's functions (Cottet, 2002) and can be calculated numerically for arbitrary parameters

E_C and E_J with arbitrary precision. Alternatively, since we are interested only in the low-energy sector of $\hat{\mathcal{H}}$, we can expand Equation (2.21) like in Equation (2.15) and drop all number states except the two with n closest to n_g ($n = \lfloor n_g \rfloor$ and $n = \lceil n_g \rceil$) from the Hamiltonian. This is a good approximation for $E_J/4E_C \ll 1$ because all others number states are far off in energy. The analytical formulas provided below have been calculated in this way.

One observes that for $E_J/E_C = 0$ the eigenenergies form parabolas around all integers n (dashed lines). These correspond to the charging energy when there are n excess Cooper-pairs on the island. Note that the parabolas cross at half-integer values of n_g. Switching on a small coupling $E_J/E_C > 0$ (solid lines) introduces avoided crossings of width $\approx E_J$ at these points. In the vicinity of the avoided crossings, the level splitting becomes independent of the gate charge. Thus, by biasing the Cooper-pair box to one of these avoided crossings, one can create a qubit from its ground and first excited state with a strong anharmonicity and greatly reduced dephasing due to charge noise. Using the approximation described above, one finds that the ground and the excited qubit states are the symmetric and the antisymmetric superpositions of $|n\rangle$ and $|n+1\rangle$ if $n_g = n + 1/2$. In the basis formed by these eigenstates, the Hamiltonian of the system near the sweet spot $n_g = n + 1/2$ is, as for the flux qubit, approximately given by

$$\hat{\mathcal{H}} = \frac{\hbar\Omega}{2}\sigma_z + \frac{\varepsilon}{2}\sigma_x, \tag{2.22}$$

where $\hbar\Omega = E_J$ and $\varepsilon = 4E_C(1-2n_g)$. Hence, near the sweet spot, one can induce qubit rotations via the gate charge n_g, and the level splitting $E_1 - E_0 = \sqrt{(\hbar\Omega)^2 + \varepsilon^2}$ is indeed independent of terms linear in this parameter.

We add some remarks on the measurement and experimental issues with the Cooper-pair box. The charge state of the Cooper-pair box can be read out, for instance, by coupling the island capacitively to an appropriately biased single-electron transistor. In this way, the charge state can be mapped on the properties of charge transport through the transistor. In order to distinguish the qubit states at the sweet spot, one has to transfer adiabatically the population of these states to charge eigenstates, analogously to the measurement of the flux qubit. However, with the advent of circuit QED, more powerful techniques to measure charge qubits became available, which will be discussed later. Again in analogy to the flux qubit, using a split junction enables *in situ* flux tuning of the resulting effective Josephson energy $E_J(\Phi_q) = E_J \cos(\pi\Phi_q/\Phi_0)$, which in turn allows one to vary the qubit level splitting $\hbar\Omega$ at the sweet spot (Figure 2.6(b)). Biased to this point, the dephasing time T_2 of the Cooper-pair box can reach $T_2 \sim 0.5\,\mu$s. Moreover, Cooper-pair box energy relaxation times $T_1 \sim 7\,\mu$s can be achieved if the circuit is engineered in a way that reduces the density of the electromagetic modes at the qubit transition frequency[6] (Wallraff *et al.*, 2005). However, even if operated at the sweet spot, low-frequency noise from electrons moving between defects can lead to sudden jumps of the gate charge n_g and force a readjustment of the bias voltage (Clarke and Wilhelm, 2008). This makes working with Cooper-pair boxes tedious and was the main reason why experimentalists started to search for alternative charge qubits. We will see in the next section how this problem can be cured by a slight change of the qubit design.

6. This *Purcell protection*, which we already encountered in Chapter 1 in the context of cavity QED, is one of the feats of circuit QED.

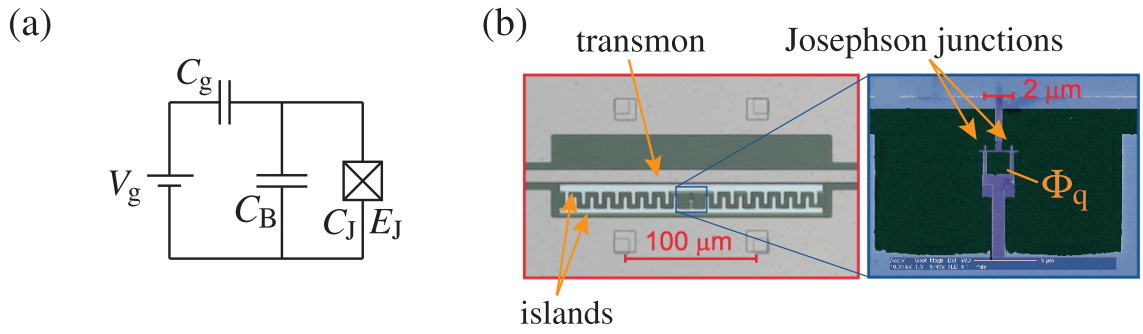

Figure 2.7: (a) Circuit diagram of a transmon. The Josephson junction is shunted by a capacitance C_B, otherwise the circuit is identical to that of a Cooper-pair box (Figure 2.6). (b) Micrograph of a transmon embedded in a circuit QED system (left) and zoom-in on the split Josephson junction of the transmon (right). The effective Josephson energy E_J of the split junction can be tuned by applying a bias flux Φ_q. The pictures in this panel are copied from Schuster *et al.* (2007) by courtesy of R. Schoelkopf.

Charge qubits II – the transmon

Transmon qubits have essentially the same circuit topology as Cooper-pair boxes and can be described by the very same Hamiltonian $\hat{\mathcal{H}} = 4E_C(\hat{n} - n_g)^2 - E_J \cos\hat{\phi}$ (Equation (2.21)). However, unlike Cooper-pair boxes, transmons are characterized by $E_J/E_C \gg 1$. To achieve this parameter ratio, the Josephson junction is shunted by a large capacitor C_B (Figure 2.7(a)). This reduces the charging energy E_C of the island drastically, but does not affect the circuit Hamiltonian otherwise (Koch *et al.*, 2007). In order to minimize dielectric losses, the junction size and therefore E_J are not significantly increased compared to the Cooper-pair box. The transmon makes use of the fact that the charge dispersion of the eigenvalues $E_m(n_g)$ of the Hamiltonian (2.21) vanishes exponentially with the ratio E_J/E_C, whereas the anharmonicity of the eigenenergies vanishes only with a slow power law of E_J/E_C. As we will see below, one can find a broad optimal parameter range in which the charge dispersion has virtually disappeared, but in which the anharmonicity of the qubit is still large enough for the fastest qubit manipulations achievable with standard techniques ($\sim 1 - 10$ ns). In this regime, the detrimental effects of charge noise are completely suppressed without the need of applying a gate voltage at all. Typical ratios realized in experiments are $E_J/E_C \sim 50$, which also optimize other features of the transmon such as its transition frequency or the strength it couples to other systems. Figure 2.7(b) shows an electron micrograph of a transmon qubit with flux-tunable split junction. The split junction connects two superconducting islands which form the shunt capacitance of the transmon. The interdigitated fingers of the island serve to increase the shunt capacitance. There is no DC conducting electrical connection of the transmon to any other electrode. Other parts of the experimental (circuit QED) setup visible in the figure will become clear in the next chapter. The transmon was thoroughly theoretically studied by Koch *et al.* (2007). Much of our discussion in this section can be found in greater detail in their article.

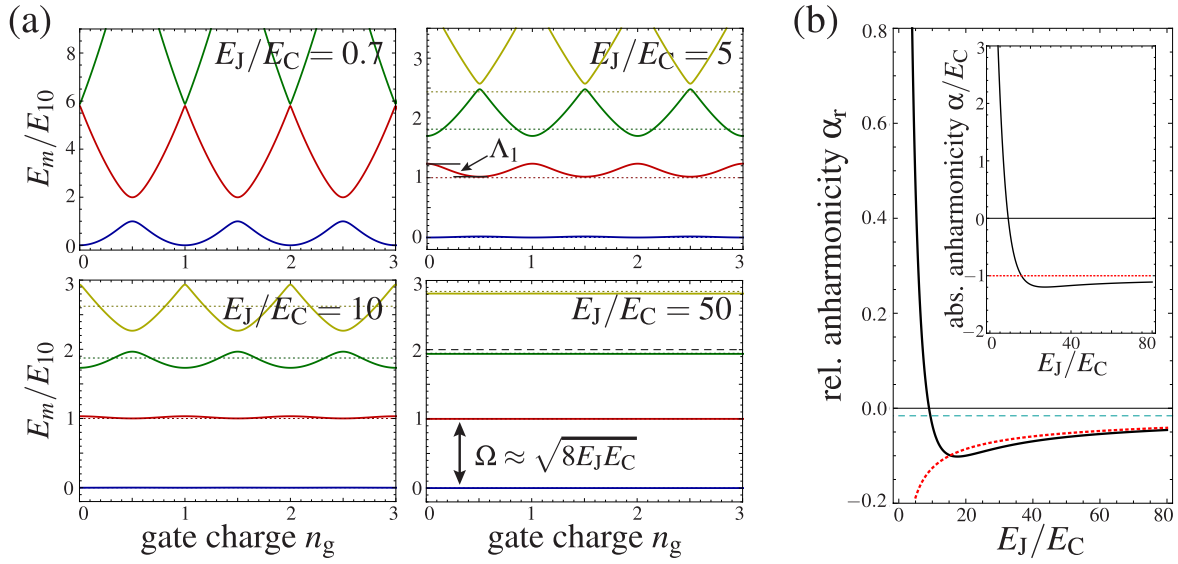

Figure 2.8: (a) Charge dispersion of the eigenvalues E_m of the Cooper-pair box/transmon Hamiltonian for different ratios of E_J/E_C (solid lines). The curves for $m = 0,1,2,3$ are colored blue, red, green, yellow, respectively. The minimum of $E_0(n_g)$ is set to zero, and the energy is measured in units of the level spacing $E_{10} = E_1 - E_0$ at the sweet spot $n_g = 1/2$. The amplitude Λ_m of the charge dispersion, indicated in one of the plots, decreases exponentially with E_J/E_C (see main text). The dotted lines represent the perturbative results for E_m (only shown for plots in the perturbative regime $E_J/E_C \gg 1$). To illustrate the remaining anharmonicity for a typical transmon ($E_J/E_C \sim 50$), the energy of twice the qubit transition $2E_{10}$ is shown in the corresponding plot (dashed black line). (b) Relative and absolute (inset) anharmonicity of the Cooper-pair box/transmon qubit levels vs. E_J/E_C. The solid curves follow from exact calculations, the red dashed curves represent the perturbative result. The minimum relative anharmonicity for ns qubit operations, $|\alpha_r| > 1/20\pi$, is indicated by a dashed cyan line.

A measure for the charge dispersion of the eigenenergies E_m of $\hat{\mathcal{H}}$ is the difference Λ_m between the extrema of $E_m(n_g)$, $\Lambda_m = E_m(n_g = 1/2) - E_m(n_g = 0)$. This quantity can be calculated in the limit $E_J/E_C \gg 1$ by semiclassical means from the exact Mathieu solutions for the eigenvalues of $\hat{\mathcal{H}}$. One obtains (Koch *et al.*, 2007)

$$\Lambda_m \approx (-1)^m E_C \frac{2^{4m+5}}{m!}\sqrt{\frac{2}{\pi}}\left(\frac{E_J}{2E_C}\right)^{\frac{m}{2}+\frac{3}{4}} e^{-8\sqrt{E_J/E_C}}, \tag{2.23}$$

which decreases exponentially with $\sqrt{E_J/E_C}$. An approximate expression for the eigenenergies E_m can be gained by noticing that for $E_J/E_C \gg 1$ the phase ϕ undergoes only small quantum fluctuations around $\phi = 0$. Upon expanding the cosine term to fourth order in ϕ, the transmon Hamiltonian becomes a harmonic oscillator with Duffing-type perturbation, which is smaller

than the harmonic terms by factor $\sqrt{E_C/E_J}$. To first order in this parameter,

$$E_m \approx \sqrt{8E_C E_J}\left(m+\frac{1}{2}\right) - \frac{E_C}{12}(6m^2+6m+3) - E_J. \tag{2.24}$$

It is interesting to note that the effects of the gate charge n_g are completely suppressed in such an approach. This is because the ϕ-periodicity of the Hamiltonian is lost and, consequently, the cyclic boundary condition on the wave functions has to be dropped. However, as soon as there are no boundary conditions on the wave functions, the canonical variable transformation $\{\hat{n},\hat{\phi}\} \to \{\hat{\tilde{n}} = \hat{n} + n_g, \hat{\phi}\}$ does not have any effect at all. Figure 2.8(a) illustrates the exponential decrease of the charge dispersion with E_J/E_C and the simultaneously increasing accuracy of the above approximation (2.24) for the eigenvalues E_m. The plots interpolate between a typical Cooper-pair box parameter ratio $E_J/E_C = 0.7$ (as in Figure 2.6(c)) and a typical transmon ratio $E_J/E_C = 50$. One can see that the charge dispersion is suppressed more strongly for lower-lying states. Already for $E_J/E_C = 10$, the dispersion of the qubit states E_0 and E_1 is rather weak. For $E_J/E_C = 20$ (not plotted), the energy dispersion $\Lambda_1/(E_1(n_g) - E_0(n_g)) \sim 10^{-3}$ becomes negligible compared to the qubit transition frequency. For the usual parameter ratio $E_J/E_C \sim 50$, there is essentially no charge dispersion also in higher-excited levels (which can be relevant for certain protocols), and the system is very well approximated by describing it as Duffing oscillator.

In order to benefit from the reduced sensitivity of the qubit to charge noise, we must ensure that the system is still anharmonic enough to be considered as qubit. Figure 2.8(b) shows the *absolute anharmonicity* $\alpha = E_{21} - E_{10}$ (inset) and the *relative anharmonicity* $\alpha_r = \alpha/E_{10}$ of the qubit as function of E_J/E_C. We have used the abbreviation $E_{ij} = E_i - E_j$, and evaluated the eigenenergies at the sweet spot $n_g = 1/2$. The absolute anharmonicity first decreases, cuts the axis at $E_J/E_C \approx 9$, and then converges to the n_g-independent, perturbative result $\alpha \to -E_C$. To judge this result, we have to compare it to the (desired) experimental time scale. For instance, in order to carry out qubit operations within a time $\tau \sim 1$ ns, we estimate that the absolute anharmonicity has to satisfy $|\alpha| > \hbar/\tau$. Using $\alpha = \alpha_r E_{10}$ and assuming further $E_{10}/h = \Omega/2\pi \sim 10$ GHz, we estimate $|\alpha_r| > (20\pi)^{-1}$. This restricts the optimal parameter range of sufficient anharmonicity and negligible charge dispersion to values $20 \lesssim E_J/E_C \lesssim 500$, which is not difficult to engineer. Note that we have picked $\tau \ll T_1 \sim 1\,\mu$s. This implies that in the optimal regime of E_J/E_C also the qubit line width is much smaller than its anharmonicity (the fundamental condition for qubit operation). Concretely, the line width is ~ 1 MHz, and the anharmonicity can be estimated as $E_C/h \sim 500$ MHz by virtue of Equation (2.24) and $E_J/E_C \sim 50$. We remark that the trade-off between anharmonicity and robustness with respect to noise seems to be general and is not only found for charge qubits (Devoret *et al.*, 2004).

Transmon-type qubits have currently the best coherence times among all superconducting qubits ($T_1, T_2 \sim 100\,\mu$s). Due to their sheer size (compared to Cooper-pair boxes), transmons possess large transition dipole moments and couple strongly to the electromagnetic field. Since the charge is not a good quantum number in the transmon regime, the state of a transmon cannot be read out by measuring the charge on its islands. However, there are powerful, non-destructive measurement schemes if the transmon is coupled to an harmonic oscillator such as an on-chip superconducting microwave cavity. For these reasons, superconducting qubits of the transmon type are at the heart of many present-day circuit QED experiments.

2.2 Basics of circuit cavity QED

The field of circuit QED was born with the idea to combine superconducting qubits with some of the seminal concepts of cavity QED (Marquardt and Bruder, 2001; You and Nori, 2003; Yang *et al.*, 2003; Blais *et al.*, 2004). As we have explained in Chapter 1, the main objective of the early cavity QED experiments was to achieve *strong coupling* of individual atoms and photons. Strong coupling means that the coupling effects are not rendered indiscernible by energy relaxation. One successful approach to this goal is to send long-lived Rydberg atoms through a high-finesse microwave cavity. This setup combines low loss rates with large coupling, the latter resulting from the large transition dipole moment of the Rydberg atoms.[7]

In the early days of superconducting qubits, the prospects for observing their strong coupling with individual photons must have seemed not very encouraging since their lifetimes used to be, and still are, many orders of magnitude shorter than those of Rydberg atoms (~ 30 ms). Blais *et al.* (2004) realized that this problem can be circumvented by fabricating a Cooper-pair box inside a quasi *one-dimensional* (1D) transmission line resonator functioning as cavity. The trick in this approach is that the light-matter-coupling scales not only in proportion to the transition dipole of the matter, but also inversely proportional to the mode volume of the electromagnetic field. Using 1D resonators reduces this mode volume to a degree that, in combination with the relatively large dipole moment of the Cooper-pair box, pushes the *circuit cavity QED* system into the regime of strong coupling. The experimental demonstration of this proposal by Wallraff *et al.* (2004) arguably initiated large parts of the intense research on circuit QED of recent years.

However, besides the interesting possibility of doing cavity QED experiments with superconducting qubits, the circuit cavity QED architecture brings about several new features that lift systems with superconducting qubits to a new level as quantum information processing tools. Most importantly, the cavity provides a clean electromagnetic environment for the superconducting qubit. It suppresses vacuum fluctuations of the electromagnetic field at frequencies different from its resonance ω_c (for simplicity, we assume only one such resonance unless noted otherwise). Thus, if the qubit transition frequency Ω is sufficiently detuned from ω_c, the radiative decay of the qubit can be strongly suppressed (even though not fully since the qubit wave function always acquires a small photonic part, see below). Nevertheless, manipulations of the qubit are possible in this off-resonant, so-called *dispersive* regime, by appropriately driving the resonator. The cavity can be fabricated on-chip, in the same process as the superconducting qubits. Made out of superconducting material, it can reach high finesse. Moreover, the cavity can act as *quantum bus*, that is, it can facilitate entangling interactions between distant qubits or even between superconducting qubits and other carriers of quantum information (such as quantum dots or nitrogen-vacancy centers). Finally, as already indicated, one can use the cavity for nondestructive simultaneous read-out of the qubits coupled to it. These features provide good reasons to envision circuit cavity QED systems as scalable architecture for quantum information processing.

In this chapter, we collect the most important aspects of the theoretical background of circuit

7. We remark that strong coupling of atoms and photons was also demonstrated in the optical domain, that is, using non-Rydberg atoms and visible light (Thompson *et al.*, 1992), which has not been mentioned in Chapter 1.

cavity QED. Our discussion will be based mostly on the celebrated Jaynes-Cummings model for two-level atoms interacting with a single bosonic mode. This model suffices to explain the different regimes of (circuit) cavity QED, state manipulations, measurements, and most experiments performed with these systems so far. For circuit QED systems with very weak anharmonicity and/or multiple cavity modes, in particular for the novel high-coherence 3D circuit cavity QED systems, the Jaynes-Cummings model has to be slightly extended. These extensions will also be discussed briefly. Finally, we remark that we use the term 'circuit cavity QED' to refer to systems of superconducting qubits interacting with one or more discrete, (nearly) harmonic modes. Today, there are also systems in which superconducting qubits interact with a continuum of propagating electromagnetic waves. These are also embraced by the slightly more general notion 'circuit QED'.

The circuit cavity QED setup

The layout of an archetype circuit cavity QED system as proposed by Blais *et al.* (2004) is shown schematically in Figure 2.9(a). It is comprised of a full-wavelength section of a superconducting coplanar waveguide transmission line and of a Cooper-pair box fabricated between the center trace and a ground plane of the coplanar waveguide. One may think of the coplanar waveguide as a flat version of a usual coaxial cable. The capacitive gaps in the center trace act as mirrors for the electromagnetic field, and the length of the coplanar waveguide in between (~ 1 cm) sets the resonance frequency of the so-formed cavity. The capacitance of the gaps determines the coupling strength of the cavity to the external wiring (usual 50 Ω transmission lines), which are also used for driving and read-out of the system. If the qubit is made with a split junction, it can be brought into and out of resonance with the cavity *in situ*. Charge qubits such as Cooper-pair boxes couple capacitively to the center trace. Thus, the qubit should be placed at an antinode of the voltage standing wave for maximizing the coupling strength. The qubit can be voltage-biased by applying a DC voltage between the center trace of the transmission line outside the cavity and the ground plane. A part of this voltage will then drop across the qubit.

Figure 2.9(b) shows an electron micrograph of one of the first circuit cavity QED systems implemented (Wallraff *et al.*, 2004)[8]. The device is patterned as a thin layer of superconducting material (niobium in this case, beige) on an oxidized silicon chip (green). The size of the components is indicated in the plots. A false-color micrograph of the Cooper-pair box (blue) is shown in the blue-framed inset. The thin blue line parallel to the center trace is the low-capacitance island of the Cooper-pair box. It is connected via two Josephson junctions, located at the intersections of the island with the perpendicular fingers, to a big reservoir with negligible charging energy. The reservoir overlaps the ground plane in this sample. More recent versions of this 1D circuit QED architecture usually contain (several) transmons instead of the Cooper-pair box, and may be equipped with additional lines in the ground planes for individually flux-biasing or driving the qubits.

8. Together with these authors, Chiorescu *et al.* (2004) reported on an experiment where a flux qubit was coupled to a lumped-element cavity (that is, a LC circuit).

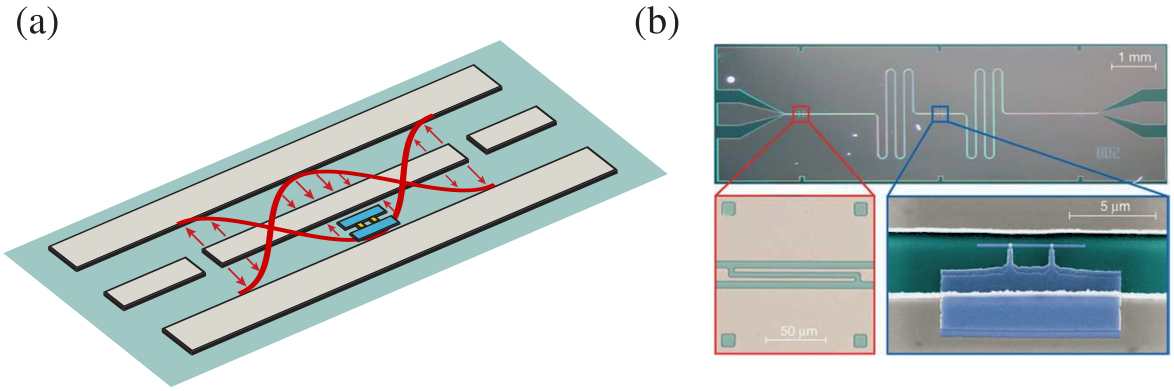

Figure 2.9: The circuit cavity QED setup. (a) Schematic layout. The voltage standing wave is indicated in red. Superconducting charge qubits are placed at its antinodes. (b) Micrograph of an early circuit cavity QED setup (reproduced from Wallraff *et al.* (2004) by courtesy of A. Wallraff). The device is described in the main text.

The Jaynes-Cummings Hamiltonian and beyond

The Jaynes-Cummings Hamiltonian (Jaynes and Cummings, 1963) is a minimal model for an anharmonic (artificial) atom interacting with a bosonic mode of frequency ω_c. Despite its simplicity, the Jaynes-Cummings Hamiltonian captures the essential physics, for instance, of optical and microwave cavity QED systems with real atoms (Raimond *et al.*, 2001), of trapped ions (Meekhof *et al.*, 1996), of quantum dots in photonic crystal cavities (Faraon *et al.*, 2008), and of (most) circuit cavity QED systems (Blais *et al.*, 2004). It is assumed that the bosonic mode is near-resonant with only one specific internal transition of the atom[9] with frequency Ω and that the atom is prepared in the corresponding subspace. Spatial degrees of freedom are neglected. The model reads

$$\hat{\mathcal{H}}_{\mathrm{JC}} = \hbar\omega_c a^\dagger a + \frac{\hbar\Omega}{2}\sigma_z + \hbar g(a\sigma_+ + a^\dagger\sigma_-), \tag{2.25}$$

where a is a bosonic operator and $\sigma_{z/+/-}$ a spin-$1/2$ matrix as before. The Hamiltonian $\hat{\mathcal{H}}_{\mathrm{JC}}$ provides a good description of the kept degrees of freedom if ω_c and Ω have a comparable magnitude and if the coupling energy $\hbar g$ satisfies $\hbar g \ll \hbar\omega_c, \hbar\Omega$. If this is not the case, *counter-rotating* terms $\hbar g(a^\dagger\sigma_+ + a\sigma_-)$ have to be included, which prohibits a simple analytical diagonalization of the Hamiltonian (Braak, 2011). The generalization of $\hat{\mathcal{H}}_{\mathrm{JC}}$ to many atoms is known as Tavis-Cummings model (Tavis and Cummings, 1968). Important quantities needed to describe cavity QED systems in addition to the Jaynes-Cummings Hamiltonian are the atomic decay rate γ and the cavity decay rate κ. These rates capture possible interactions of atom and cavity mode with degrees of freedom not represented in $\hat{\mathcal{H}}_{\mathrm{JC}}$, which are assumed to be irreversible. Atomic decay

9. Even when not talking about cavity QED with real atoms, we often simply use the term 'atom' to refer to the anharmonic part of the system.

can be caused, for instance, by transitions out of the considered subspace for Rydberg atoms or by dielectric losses for superconducting qubits. Cavity decay happens when photons leak out of the cavity. A further important irreversible process, which we do not take into account until Section 4.7, is the pure dephasing of the atom due to random fluctuations in the atomic level spacing Ω. We mention, however, that the atomic decay and pure dephasing rates γ and γ_φ are related to the energy relaxation and dephasing times via $T_1^{-1} = \gamma$ and $T_2^{-1} = \gamma/2 + \gamma_\varphi$.

Before discussing the features of the Jaynes-Cummings model, we make some remarks on its derivation both for the paradigmatic cavity QED system – the one with real atoms – and for a circuit cavity QED system. A detailed analysis of these derivations is part of the new results presented in Chapter 3 of this thesis. After that, at the end of this section, a brief introduction will be given to the theories used for describing circuit QED systems for which the Jaynes-Cummings Hamiltonian is oversimplified.

To describe an atom traversing a cavity, it suffices to consider the low-energy limit of the full relativistic theory of QED (Walls and Milburn, 1994). It is obtained by quantizing the vector potential $\mathbf{A}$ in the minimal coupling Hamiltonian of atom and field,

$$\mathcal{H} = \sum_{j=1}^{n} \frac{[\mathbf{p}_j - q_j \mathbf{A}(\mathbf{r}_j, t)]^2}{2m_j} + V_{\text{int}}(\mathbf{r}_1, \ldots, \mathbf{r}_n) + \mathcal{H}_{\text{rad}}, \tag{2.26}$$

where V_{int} is the potential energy of the n charged particles constituting the atom, $\mathbf{r}_j$ and $\mathbf{p}_j$ their position and momentum operators, q_j their charge, and m_j their mass. Here and (mostly) in the following, hats to distinguish operators from numbers are omitted. In the Coulomb gauge, the classical vector potential $\mathbf{A}$ satisfies the wave equation $(c^{-2} \times \partial^2/\partial t^2 - \nabla^2)\mathbf{A} = 0$, where c is the speed of light. Assuming a rectangular volume V,

$$\mathbf{A}(\mathbf{r}, t) = \sum_{n,\lambda} \sqrt{\frac{\hbar}{2\varepsilon_0 \omega_n V}} \mathbf{e}_{n,\lambda} \left(a_{n,\lambda} e^{i(\mathbf{k}_n \mathbf{r} - \omega_n t)} + a_{n,\lambda}^\dagger e^{-i(\mathbf{k}_n \mathbf{r} - \omega_n t)} \right), \tag{2.27}$$

with the vacuum permittivity ε_0 and the two orthonormal polarization vectors $\mathbf{e}_{n,\lambda}$ ($\lambda = 1, 2$), which satisfy $\mathbf{k}_n \cdot \mathbf{e}_{n,\lambda} = 0$. The dispersion relation is $\omega_n = c|\mathbf{k}_n|$, where the $\mathbf{k}_n$ depend on the boundary conditions. The field is quantized by elevating the $a_{n,\lambda}$ to bosonic operators. The Hamiltonian of the free field then reads $\mathcal{H}_{\text{rad}} = \sum_{n,\lambda} \hbar \omega_{n,\lambda} a_{n,\lambda}^\dagger a_{n,\lambda}$. Starting from Equations (2.26) and (2.27), one arrives at the Jaynes-Cummings Hamiltonian by (i) neglecting the center-of-mass motion of the atom, (ii) making the *dipole approximation* $e^{ikr} \approx 1$ (since the atom is assumed to be much smaller than the wavelength of the radiaton), (iii) dropping all but one field mode and all but two atomic eigenstates, and (iv) dropping the $\mathbf{A}^2$ terms. Then, in a convenient choice of basis, the Hamiltonian takes on the form of Equation (2.25), however including the counter-rotating terms. Since these only mix states distant in energy, they can be safely neglected for small g. For cavity QED experiments with Rydberg atoms, representative parameter values are $\omega_c/2\pi, \Omega/2\pi \sim 50$ GHz, and $g/2\pi \sim 50$ kHz.

In the standard description of circuit QED (Blais *et al.*, 2004), the coplanar waveguide cavity is modeled as a series of inductors in which each node is capacitively coupled to ground. After

taking the continuum limit, the classical Lagrangian of the system reads

$$\mathcal{L} = \int_{-L_c/2}^{L_c/2} dx \left(\frac{l}{2} j^2 - \frac{1}{2c} q^2 \right) \tag{2.28}$$

$$= \int_{-L_c/2}^{L_c/2} dx \left(\frac{l}{2} \dot{\theta}^2 - \frac{1}{2c} (\nabla \theta)^2 \right), \tag{2.29}$$

where it was assumed that the cavity has a length L_c. Further, c and l are its capacitance and inductance per unit length, respectively, and $\theta(x,t) = \int_{-L_c/2}^{x} dx' q(x,t)$. Thus, the equation of motion for θ is a wave equation. Due to charge neutrality, it has to be solved under the boundary condition $\theta(-L_c/2,t) = \theta(L_c/2,t) = 0$. It follows that $\theta(x,t)$ is a superposition of standing waves with wave vectors $k = m\pi/L_c$ ($m \in \mathbb{N}_+$) and frequencies $\omega_k = k/\sqrt{lc}$. In terms of the time-dependent expansion coefficients $\varphi_k(t)$ of θ,

$$\mathcal{L} = \sum_k \frac{l}{2} \dot{\varphi}_k^2 - \frac{1}{2c} \left(\frac{k\pi}{L_c} \right)^2 \varphi_k^2. \tag{2.30}$$

Upon quantizing the φ_k and expressing them as usual by means of bosonic a_k, one arrives at both a quantum description of the cavity, $\mathcal{H}_{\rm rad} = \sum_k \hbar\omega_k (a_k^\dagger a_k + 1/2)$, and at a quantum expression for θ in terms of the a_k. With that, we also obtain a quantum expression for the voltage in the resonator, $V(x,t) = 1/c \times \partial\theta/\partial x$. Note that $V(x,t)$ has contributions from all k modes. In the usual theory of circuit QED, this quantum voltage, evaluated at the position of the qubit, is added to the classical gate voltage V_g. That is, the gate charge n_g in Equation (2.21) acquires contributions $\propto (a_k^\dagger + a_k)$. This establishes a coupling of the qubit with a quantized field. As in the case of atomic cavity QED, a number of simplifications lead to the Jaynes-Cummings Hamiltonian: Among the modes in $V(x,t)$ with antinodes at the position at the qubit, only the one energetically closest to the qubit transition is kept (typically engineered to be the $k = 2$ mode, which has two nodes and three antinodes, like in Figure 2.9(a)). Then, like in the case of atomic cavity QED, upon making the two-level approximation for the superconducting qubit and dropping a term $\propto (a^\dagger + a)^2$ and the counter-rotating terms, one eventually arrives at the Jaynes-Cummings Hamiltonian (2.25). This procedure of deriving a circuit QED theory essentially holds for Cooper-pair boxes (Blais *et al.*, 2004) and transmons (Koch *et al.*, 2007) alike. However, it should be remarked that, for Cooper-pair boxes, one obtains additional terms if the classical gate charge n_g is not biased to a sweet spot. Typical parameter values in circuit cavity QED are $\omega_c/2\pi, \Omega/2\pi \sim 10$ GHz, and $g/2\pi \sim 10(100)$ MHz for Cooper-pair boxes (transmons).

The two-level approximation is not always justified in circuit QED. Transmons are only weakly anharmonic so that higher excited levels should be generally taken into account. A generalization of the Jaynes-Cummings Hamiltonian appropriate for 1D circuit cavity QED systems with transmons, but valid also for Cooper-pair boxes, reads (Koch *et al.*, 2007)

$$\mathcal{H} = \hbar\omega_c a^\dagger a + \sum_m E_m |m\rangle\langle m| + \hbar \sum_{m,m'} g_{m,m'} |m\rangle\langle m'| (a^\dagger + a). \tag{2.31}$$

Here, E_m and $|m\rangle$ are the eigenenergies and eigenstates of the Cooper-pair box/transmon Hamiltonian (Equation (2.21)), and $g_{m,m'} \propto V_{\mathrm{ZPF}}\langle m|\hat{n}|m'\rangle$, where $\hat{n}$ is the number operator and $V_{\mathrm{ZPF}} = \sqrt{\hbar\omega_{\mathrm{c}}/L_{\mathrm{c}}c}$ are the zero-point fluctuations of the quantum voltage. The multi-level transmon QED model of Equation (2.31) and its generalization to multiple qubits capture some interesting features of systems with transmons the Jaynes-Cummings Hamiltonian cannot account for. For instance, two-qubit quantum gates with transmons often explicitly make use of higher excited levels (see later). Moreover, since a transmon is almost a harmonic oscillator, there is a selection rule for these qubits, $g_{m,m'} \approx \delta_{m',m\pm1} g_{m,m'}$. After all, however, the physics of the model (2.31) is not fundamentally different from the usual Jaynes-Cummings model. Operations like state manipulations or read-out are implemented identically for Cooper-pair boxes and transmons and can be understood on the basis of the simpler model.

For describing the novel 3D circuit QED systems invented by Paik *et al.* (2011), also the generalized Jaynes-Cummings Hamiltonian of Equation (2.31) is generally not suited. These circuit QED systems consist of a large, *3D transmon* qubit embedded in a 3D cavity and are currently subject to much research because of their improved coherence times. We will later discuss some experiments done with these systems. Here we make a few remarks on their theoretical description. Due to the very weak anharmonicity, the strong coupling, and the large size of the 3D transmons, it is not adequate to assume that the cavity mode is not distorted by the presence of the qubit, and, thus, to independently quantize qubit and field and then to treat their *coupling* perturbatively. A more appropriate approach, developed by Nigg *et al.* (2012) and known as *black-box quantization*, is to divide the classical circuit into a purely linear part (including the linear part of the Josephson inductance), and a purely nonlinear element with energy $-(E_{\mathrm{J}}/4!)\phi^4$, corresponding to the transmon's Duffing term. Higher terms $O(\phi^6)$ from the expansion of $-E_{\mathrm{J}}\cos\phi$ are usually neglected. The (strongly) coupled eigenmodes of the linear circuit, $\phi_j(t)$, oscillate with frequencies ω'_j and are mixtures of the linearized transmon and the cavity modes. The ϕ_j form an excellent basis to quantize the system and to treat the *nonlinear Josephson term* as a small perturbation. The quantum Hamiltonian of the linear part of the system reads $\mathcal{H}_{\mathrm{l}} = \hbar\sum_j \omega'_j a_j^\dagger a_j$. Due to Kirchhoff's law, the dimensionless flux $\hat{\phi}$ across the nonlinear part of the Josephson inductance can be expressed as $\hat{\phi} = \sum_j \hat{\phi}_j = \sum_j \phi_{\mathrm{ZPF},j}(a_j^\dagger + a_j)$. In practice, the ω'_j and $\phi_{\mathrm{ZPF},j}$ are calculated using commercial finite-element solvers. Putting things together, and neglecting counter-rotating terms, one eventually arrives at the Hamiltonian for a 3D circuit QED system

$$\mathcal{H}_{\mathrm{3D}} = \hbar\sum_j \omega_j a_j^\dagger a_j + \frac{\hbar}{2}\sum_{j,k}\chi_{j,k} a_j^\dagger a_j a_k^\dagger a_k, \tag{2.32}$$

where $\omega'_j \to \omega_j$ indicates that the eigenmodes are slightly renormalized by the nonlinearity, and the $\chi_{j,k}$ are functions of E_{J} and the $\phi_{\mathrm{ZPF},j}$. Note that every mode inherits an anharmonicity from the Josephson junction (self-Kerr effect). Moreover, the presence of an excitation in the mode j will also shift the frequency of the mode $k \neq j$ (cross-Kerr effect). Since the qubit and the cavity modes are treated on an equal footing, there is no distinction between qubit and cavity modes in Equation (2.32). Usually, one simply calls the most anharmonic mode the qubit. Now, on the basis of Equation (2.32), one can introduce approximations such as the two-level

approximation for the qubit, if appropriate. The accurateness of the Hamiltonian (2.32) was recently impressively demonstrated by Kirchmair *et al.* (2013), whose experiment we will briefly describe in Section 2.3.

Resonant regime – Vacuum Rabi splitting

Let us return to the simplest model of atom-field interactions, the Jaynes-Cummings Hamiltonian

$$\hat{\mathcal{H}}_{\mathrm{JC}} = \hbar\omega_{\mathrm{c}} a^{\dagger}a + \frac{\hbar\Omega}{2}\sigma_z + \hbar g(a\sigma_+ + a^{\dagger}\sigma_-). \tag{2.25}$$

The Hamiltonian couples only states with an equal number n of excitations, that is $|\downarrow, n\rangle$ and $|\uparrow, n-1\rangle$, and is readily diagonalized in this subspace. One finds

$$E_{n,\pm} = \hbar\omega_{\mathrm{c}} n \pm \frac{\hbar}{2}\sqrt{4g^2 n + \Delta^2} \tag{2.33}$$

in the manifold with $n \geq 1$ excitations. The energy of the ground state $|\downarrow, 0\rangle$ is

$$E_0 = \frac{\hbar\Delta}{2}. \tag{2.34}$$

We have used the common abbreviation $\Delta = \omega_{\mathrm{c}} - \Omega$ for the detuning of the qubit from cavity, and we have added the zero point fluctuations of the field, $\hbar\omega_{\mathrm{c}}/2$.

In this section, we discuss the resonant regime, where $\Delta \ll g$. In the resonant regime, the effects of the coupling g are strongest and, therefore, the demonstration of coherent light-matter coupling is easiest. Thus, experimental implementations of the Jaynes-Cummings Hamiltonian are usually first explored on resonance.

Assuming $\Delta = 0$, one reads off from Equation (2.33) that the manifold with n excitations forms a doublet with energy splitting $2\hbar g\sqrt{n}$ (see Figure 2.10(a)). In this situation, the eigenstates $|n, \pm\rangle$ belonging to $E_{n,\pm}$ are given by the coherent superpositions

$$|n, \pm\rangle = \frac{1}{\sqrt{2}}(|\downarrow, n\rangle \pm |\uparrow, n-1\rangle). \tag{2.35}$$

The simplest way to demonstrate this coherent coupling is to probe the cavity with a weak spectroscopy tone of frequency ω and to measure the transmitted intensity (orange boxes in Figure 2.10). Note that from the ground state only transitions into the $n = 1$ manifold are dipole-allowed. In this manifold, since the excitation is carried half by the cavity and half by the atom, the line width of the resonances is $\hbar(\gamma + \kappa)/2$. If $g \gg \gamma, \kappa$, the splitting of the resonances, which is also known as *vacuum Rabi splitting*, can be resolved, and the coupling is said to be *strong*. Vacuum Rabi splitting was first observed in atomic cavity QED by Thompson *et al.* (1992) and in circuit cavity QED by Wallraff *et al.* (2004) (see Figure 2.10(b)). A few remarks: (i) If there are $N > 1$ atoms, the splitting of the $n = 1$ manifold is given by $2g\sqrt{N}$. This makes it easier to reach the regime of strong coupling. Moreover, as we discuss in Chapter 3, this can even lead to a superradiant phase transition when the splitting becomes comparable to ω_{c}. (ii) 'Weak' or

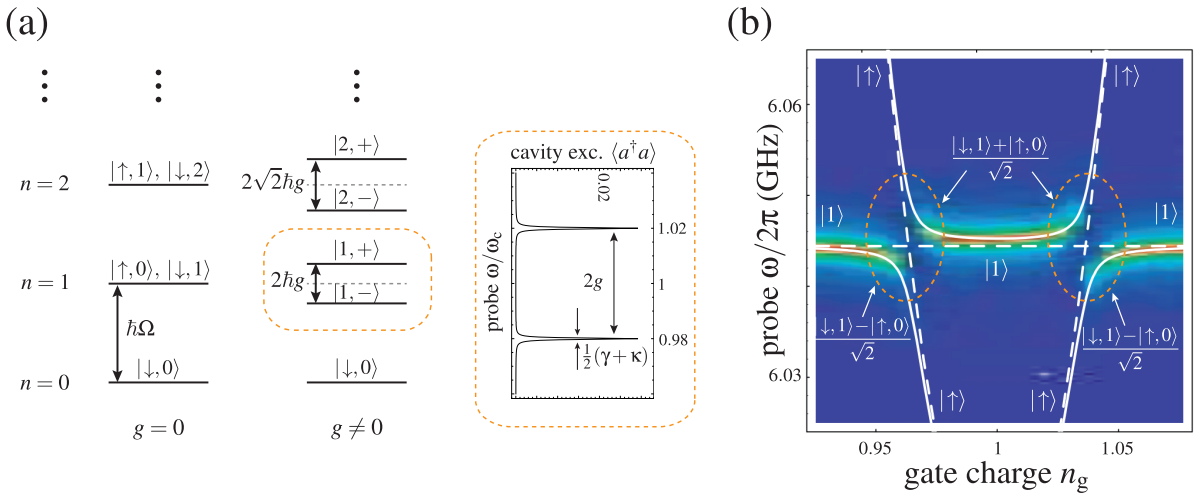

Figure 2.10: The resonant Jaynes-Cummings model. (a) Energy spectrum of the uncoupled ($g=0$) and the coupled ($g\neq 0$) resonant Jaynes-Cummings model. The $n=1$ doublet is accessible, *e.g.*, by weakly probing the cavity transmission. This is illustrated by the plot in the big orange box. It shows the steady state of the cavity excitation $\langle a^\dagger a\rangle$, which is a measure for the transmission in a spectroscopy experiment, as a function of the probe frequency ω, calculated for the typical parameters of an early 1D transmon circuit QED system (by numerically solving a Lindblad master equation). The resonances are separated by many line widths, and the system is clearly in the regime of strong coupling. The parameters are, in units of ω_c, $g=0.02$, $\kappa=10^{-4}$, $\gamma=10^{-3}$, and the amplitude of the spectroscopy drive $F/\hbar=10^{-4}$. (b) First experimental realization of strong (resonant) atom-field coupling in circuit QED (as published in Wallraff *et al.* (2004), courtesy of A. Wallraff). The transmission of the cavity is probed while the gate charge biasing a Cooper-pair box is varied (the device used is shown in Figure 2.9(b)). In the regions of the orange ovals, the Cooper-pair box comes into resonance with the cavity. Where the distance between the resonances is minimal, the system is described by the theory of panel (a).

'linear' spectroscopy means that the number of photons in the cavity remains $\ll 1$. If the spectroscopy tone starts to significantly populate the cavity, the line width of resonances will increase beyond $\hbar(\gamma+\kappa)/2$ (so-called *power broadening*). Depending on the coupling strength g, additional resonances due to multiphoton transitions into manifolds with $n>1$ can also show up. (iii) The observation of the vacuum Rabi splitting does not suffice to demonstrate the nonlinear coupling of a two-level atom and a bosonic mode. The same splitting separates the eigenmodes of two coupled (possibly classical) harmonic oscillators on resonance. Thus, to substantiate the 'quantumness' of the system, one either has to find a way to measure the splittings of the doublets with $n>1$. This was first achieved by Fink *et al.* (2008) in circuit QED, using pump-probe techniques, and by Bishop *et al.* (2009), who carefully analyzed the aforementioned multiphoton resonances. Or, one can demonstrate so-called *quantum Rabi oscillations*, which we discuss next.

Quantum Rabi oscillations are a hallmark of the resonant Jaynes-Cummings coupling. If the system is prepared in a product state, say, $|\downarrow, n\rangle$, it will undergo a nontrivial time evolution in the subspace of n excitations, spanned by the eigenstates $|n, \pm\rangle$ (for $n \geq 1$). One can easily show that the qubit excitation probability $P_\uparrow(t)$ after such an initialization follows

$$P_\uparrow(t) = \frac{1}{2}(1 - \cos(2g\sqrt{n}t)). \tag{2.36}$$

The dependence of the oscillation frequency on $\sqrt{n}$ is a consequence of the nonlinear atom-field coupling. The more excitations are present, the stronger the coupling, and the faster the exchange of the excitation between atom and field. The first observation of these quantum Rabi oscillations was made by Brune *et al.* (1996b), using Rydberg atoms. The special case of $n = 1$, that is, the coherent energy exchange between a single atom and the cavity with only a single quantum of energy present, is known as *vacuum Rabi oscillation*. These were also observed by Brune *et al.* (1996b) and, for the first time in circuit cavity QED, by Johansson *et al.* (2006).

Off-resonant regime – Measurement and state manipulations

The off-resonant or *dispersive* regime of the Jaynes-Cummings Hamiltonian is characterized by $g/|\Delta| \ll 1$, where $\Delta = \omega_c - \Omega$ is the detuning of the qubit from the cavity. In this regime, quantum fluctuations and external noise of the electromagnetic field at the qubit frequency are suppressed by the cavity, and the qubit can enjoy protection against spontaneous and stimulated decay. Nevertheless, it can be measured, manipulated, and, if there is more than one qubit in the cavity, coupled to other qubits. For quantum information applications, (circuit) cavity QED systems are therefore mostly operated in the dispersive regime. In this section, we discuss the theory behind the most important features of the dispersive regime. The pioneering works in this context, in which much of the following can be found in greater detail, have been authored by Blais *et al.* (2004) and Blais *et al.* (2007).

In the dispersive regime, the states $|\downarrow, n\rangle$ and $|\uparrow, n-1\rangle$ are not degenerate and will not be strongly mixed (assuming small n). To first order in $g\sqrt{n}/\Delta$,

$$|n, +\rangle \approx |\downarrow, n\rangle + \frac{g\sqrt{n}}{\Delta}|\uparrow, n-1\rangle, \tag{2.37}$$

$$|n, -\rangle \approx -\frac{g\sqrt{n}}{\Delta}|\downarrow, n\rangle + |\uparrow, n-1\rangle, \tag{2.38}$$

for $\Delta > 0$. For $\Delta < 0$, the right-hand sides of Equations (2.37) and (2.38) have to be interchanged. Focussing on $n = 1$, we can estimate that there is a probability $(g/\Delta)^2$ that an excitation of the atom (represented by $|1, -\rangle$ for $\Delta > 0$) populates the cavity, and vice versa. This implies that the decay rates $\Gamma_{1,\pm}$ of the eigenstates are given by

$$\Gamma_{1,+} \approx \kappa + (g/\Delta)^2\gamma \tag{2.39}$$

$$\Gamma_{1,-} \approx \gamma + (g/\Delta)^2\kappa. \tag{2.40}$$

Again, for $\Delta < 0$ the RHSs have to be interchanged. Hence, the qubit inherits a channel for radiative decay from the cavity, which however can be eliminated by choosing Δ large enough. This dependence of the atomic decay rate on the detuning from the cavity is known as the Purcell effect (Purcell, 1946; Houck *et al.*, 2008). As long as the qubit's decay rate changes appreciably with Δ, the qubit is said to be *Purcell limited*, and otherwise to be *Purcell protected*.

For further discussing the dispersive regime, it is instructive to derive an approximation to the Jaynes-Cummings Hamiltonian valid for $g\sqrt{n}/|\Delta| \ll 1$. One way to do this, which can be conveniently generalized to multiple qubits and atoms with more than two levels, is to apply the unitary transformation (Blais *et al.*, 2004)

$$U = \exp\left(\frac{g}{\Delta}(a^\dagger \sigma_- - a\sigma_+)\right) \tag{2.41}$$

to the Jaynes-Cummings Hamiltonian (2.25) divided by Δ, and to keep terms up to second order in g/Δ. This yields (up to a constant)

$$U\mathcal{H}_{\mathrm{JC}}U^\dagger \approx \hbar\left(\omega_c - \frac{g^2}{\Delta}\sigma_z\right)a^\dagger a + \frac{\hbar}{2}\left(\Omega - \frac{g^2}{\Delta}\right)\sigma_z. \tag{2.42}$$

The transformation U can be understood as a rotation in Hilbert space. It maps the low-energy eigenstates of $\mathcal{H}_{\mathrm{JC}}$ for $g/|\Delta| \ll 1$, which are approximately given in Equations (2.37) and (2.38), onto $|\uparrow\downarrow, n\rangle$, and makes it easy to read off their energies via Equation (2.42). This reveals a remarkable feature of the dispersive regime of the Jaynes-Cummings Hamiltonian: Its low-energy spectrum possesses two harmonic ladders, one of them, belonging to the manifold $|\uparrow, .\rangle$, with level spacing $\omega_c - g^2/\Delta$, the other one, belonging to the manifold $|\downarrow, .\rangle$, with level spacing $\omega_c + g^2/\Delta$ (see Figure 2.11(a); Figure 2.11(b) shows both the resonant and the dispersive regime). Since the eigenstates $|\uparrow\downarrow, n\rangle$ of $U\mathcal{H}_{\mathrm{JC}}U^\dagger$ differ only slightly from those of $\mathcal{H}_{\mathrm{JC}}$ (see Equations (2.37) and (2.38)), we can say that the cavity experiences just a small frequency shift due to the presence of the off-resonant qubit, which however depends on the state of the qubit. This means that one can learn about the state of the off-resonant qubit by measuring the direction of the cavity's frequency shift. Importantly, such a *dispersive read-out* would even constitute a *quantum nondemolition measurement*, which has, in principle, only the effect of projecting the qubit to $|\uparrow\rangle$ or $|\downarrow\rangle$. What is more, if there are several qubits in the cavity and their detunings Δ_j are appropriately chosen, it should be possible to jointly read out their state since the dispersive shifts of the resonator frequency caused by each qubit can be shown to simply add up (Blais *et al.*, 2004).

Indeed, dispersive read-out is the standard measurement technique in circuit cavity QED (a second important method uses the qubit-state dependent response of the cavity population to a drive of very high power at the bare cavity frequency ω_c (Reed *et al.*, 2010)). The frequency shift of the cavity can be determined experimentally either by weakly driving the cavity at, say, $\omega_c + g^2/\Delta$ and measuring if there is a significant transmission of the signal or not. Or, one can probe the cavity weakly at its bare frequency ω_c, in which case the phase of the reflected signal contains information on whether the resonance of the cavity is above or below ω_c. This last method is particularly useful if the dispersive shift is weaker than the resonator's line width, $g^2/\Delta < \kappa$ (the so-called *weak dispersive regime*, in distinction to the *strong dispersive regime* with $g^2/\Delta > \kappa, \gamma$; see below for the relevance of γ). Dispersive qubit read-out in circuit cavity QED was

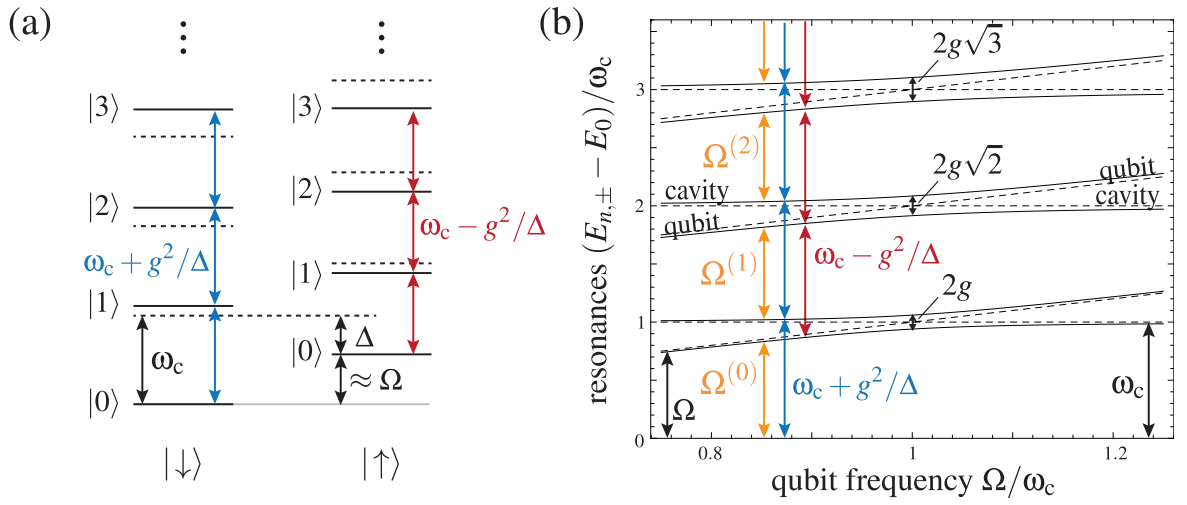

Figure 2.11: (a) Dispersive regime of the Jaynes-Cummings Hamiltonian for $\Delta = \omega_c - \Omega > 0$. The spectrum consists approximately of two harmonic ladders. Their level spacings $\omega_c \pm g^2/\Delta$ depend on the state of the qubit. The energy offset between the ladders is not exactly Ω (but $\Omega - g^2/\Delta$) because of the qubit's Lamb shift. (b) Transition energies $E_{n,\pm} - E_0$ of the Jaynes-Cummings model vs. qubit frequency Ω for couplings $g/\omega_c = 0.06$ (solid) and $g = 0$ (dashed). On resonance, the avoided crossings increase $\sim \sqrt{n}$. Off resonance, the system becomes approximately linear. The qubit-state-dependent cavity frequencies from panel (a) are indicated. Moreover, the Stark- and Lamb-shifted qubit frequencies are indicated (orange). The label $\Omega^{(j)}$ was used to point at the qubit freuqency if j photons are present. To simplify the labeling, it was set $\hbar = 1$ in both panels.

first demonstrated by Schuster *et al.* (2005). Mainly because of the difficulty of detecting low-intensity microwave signals, measurement in circuit cavity QED required long averaging of the noisy measurement signals and used to be one of the weaknesses of this approach to quantum optics and quantum information processing. However, with the advent of low-noise Josephson bifurcation and parametric amplifiers, it is now possible to measure the state of a superconducting qubit in a circuit cavity QED system within a few ns with high fidelity. This facilitated, for example, the observation of quantum jumps of the state of a transmon (Vijay *et al.*, 2011). The measurement in circuit QED has even evolved so far that fundamental questions concerning the measurement process can be experimentally addressed. For instance, Vijay *et al.* (2012) were able to feed back the information about the qubit state obtained by a weak measurement into the system and to stabilize in that way Rabi oscillations (see below) of the qubit indefinitely.

Another insightful perspective on the low-energy sector of the dispersive Jaynes-Cummings Hamiltonian is obtained by a rearranging the terms on the RHS of Equation (2.42),

$$U\mathcal{H}_{\mathrm{JC}}U^\dagger \approx \hbar\omega_c a^\dagger a + \frac{\hbar}{2}\left(\Omega - \frac{2g^2}{\Delta}\left(a^\dagger a + \frac{1}{2}\right)\right)\sigma_z. \tag{2.43}$$

Expressed in this form, the dispersive effect of the state of the field on the qubit frequency is

emphasized. The terms in the large parentheses can be interpreted as the qubit transition frequency, modified by the dispersive interaction (see Figure 2.11(b)). Obviously, this frequency depends on the number of photons in the cavity. This is a manifestation of the AC Stark effect. In the strong dispersive regime, in particular if $g^2/\Delta > \gamma$, measuring the qubit transition frequency facilitates a nondestructive interrogation of the photon number in the cavity, as demonstrated and utilized by Johnson *et al.* (2010) and Kirchmair *et al.* (2013). An earlier experiment based on the AC Stark effect involved spectroscopic measurement of the photon-resolved qubit frequencies. The intensities of the lines then enabled an estimate of the probability distribution of having n photons in the cavity (Schuster *et al.*, 2007). We remark that a fluctuating photon number in the cavity causes fluctuations of the qubit frequency via the AC Stark effect and, thus, causes dephasing. In measurements of the qubit state, the dephasing due to the photon shot noise constitutes the measurement back-action on the conjugated variable. Moreover, stray cavity photons are believed to be one of the main sources of dephasing in current cirucit QED devices and require careful shielding of the cavity against electromagnetic noise (Sears *et al.*, 2012). Remarkably, also the zero-point fluctuations of the electromagnetic field alter the qubit transition frequency by an amount $2g^2/\Delta \times 1/2$. This single-mode Lamb shift was observed in circuit cavity QED by Fragner *et al.* (2008).

We now investigate the possibilities of controlled qubit state manipulations. Such manipulations are usually achieved in the dispersive regime by externally driving the cavity at a frequency ω close to the qubit frequency. In this approach, the cavity will be only virtually populated and the external drive acts essentially classical. Moreover, the reflected signal of a drive far detuned from the cavity cannot contain relevant phase information and will therefore not measure the qubit.

A drive with potentially time-dependent amplitude $F(t)$ can be modeled by adding the term $F(a^\dagger e^{-i\omega t} + a e^{i\omega t})$ to the Jaynes-Cummings Hamiltonian (2.25) (we assume that F is real). It is convenient to simplify the time-dependence by applying the unitary transformation

$$U' = \exp\left(i\hbar t(\omega a^\dagger a + \frac{\omega}{2}\sigma_z)\right) \tag{2.44}$$

to $\mathcal{H}_{\rm JC}$ according to $\mathcal{H}'_{\rm JC} = U'\mathcal{H}_{\rm JC}(U')^\dagger + i(\partial U'/\partial t)(U')^\dagger$. Note that this transformation, which is usually referred to as 'going to a frame rotating at the drive frequency ω', just adds a phase to $|{\uparrow\downarrow}, n\rangle$. One obtains

$$\mathcal{H}'_{\rm JC} = \hbar\delta_{\rm c} a^\dagger a + \frac{\hbar\delta_{\rm q}}{2}\sigma_z + \hbar g(a\sigma_+ + a^\dagger\sigma_-) + F(a^\dagger + a), \tag{2.45}$$

where $\delta_{\rm c} = \omega_{\rm c} - \omega$ and $\delta_{\rm q} = \Omega - \omega$. Now we displace the cavity field via $D(\alpha) = \exp(\alpha a^\dagger - \alpha^* a)$ by an amount $\alpha = F/\hbar\delta_{\rm c}$. This yields

$$\mathcal{H}''_{\rm JC} = \hbar\delta_{\rm c} a^\dagger a + \frac{\hbar\delta_{\rm q}}{2}\sigma_z + \hbar g(a\sigma_+ + a^\dagger\sigma_-) - \frac{\hbar\Omega_{\rm R}}{2}\sigma_x, \tag{2.46}$$

where the *Rabi frequency* $\Omega_{\rm R} = 2gF/\hbar\delta_{\rm c}$ was introduced. Since the qubit is operated in the dipersive regime ($\delta_{\rm c} - \delta_{\rm q} = \Delta \gg g$), we can use again the transformation (2.41) to obtain

$$\mathcal{H}^{\rm R}_{\rm JC} = \hbar\delta_{\rm c} a^\dagger a + \frac{\hbar}{2}\left(\delta_{\rm q} - \frac{2g^2}{\Delta}\left(a^\dagger a + \frac{1}{2}\right)\right)\sigma_z - \frac{\hbar\Omega_{\rm R}}{2}\sigma_x, \tag{2.47}$$

where we have kept terms to second order in g/Δ and have dropped a term $\propto \Omega_R(g/\Delta)\sigma_z(a^\dagger + a)$ (Blais *et al.*, 2007). Note that $\delta_q = \Omega - \omega$ depends on the drive frequency ω. Thus, the second term of $\mathcal{H}_{JC}^R$ can be made small by appropriately choosing ω. Concretely, since $\langle a^\dagger a\rangle \approx 0$ in the dispersive regime, one has to arrange $\delta_q \approx g^2/\Delta$ for this purpose. The resulting Hamiltonian generates coherent rotations with angular frequency Ω_R about the x axis in the rotating frame. In the lab frame, this corresponds to a spiral movement of the qubit state up and down the Bloch sphere whereby the qubit excitation probability oscillates with angular frequency Ω_R. For instance, in the rotating frame, the pure qubit state $|\downarrow\rangle$ would evolve into $|\uparrow\rangle$ and back. Since these states are not affected by the transformation (2.44), this happens also in the lab frame. Thus, by driving a qubit in the dispersive regime near its resonance frequency, one can create a coherent and cyclic evolution of the qubit excitation probability, known as Rabi oscillations. A so-called π pulse of duration $t = \pi/\Omega_R$ inverts the qubit excitation, and a $\pi/2$ pulse rotates the Bloch vector of the qubit from a pole of the Bloch sphere to the $x-y$ plane and vice versa. Such pulses can be realized in circuit cavity QED with a fidelity $\geq 99\%$ on a time scale of a few ns. Note that the Rabi frequency depends on the drive amplitude, $\Omega_R \propto F$. Note also the similarity of Ω_R and the frequency of the quantum Rabi oscillations of Equation (2.36), which depends on the amplitude of the quantized field $\propto \sqrt{n}$ in the resonant cavity.

With tools similar to the ones used above, one can work out a variety of gates for single and multiple qubits operated in the dispersive regime. For instance, if the system is strongly driven with a tone off-resonant with the cavity and close to, but still off-resonant with the qubit, the qubit transition frequency Ω will be AC Stark shifted due to virtual qubit transitions. This will neither measure nor strongly dephase the qubit since the photon population of the cavity remains small. One can use this effect for rapid changes of the qubit frequency Ω if the qubit does not have a split junction or no individual fast flux line (Majer *et al.*, 2007). Note that a temporary change of Ω also generates an additional phase, that is, an additional rotation about the z axis in the qubit evolution (termed *phase gate*). Multi-qubit gates usually do not rely on external driving. Rather, the excited states (often also higher excited states) of qubits coupled dispersively to the same cavity are brought into resonance. By means of the transformation (2.41), one can show, for instance, that if the excited states of two qubits which are coupled to the same cavity with equal strength g are resonant, the Hamiltonian of the system reads (Blais *et al.*, 2004)

$$\mathcal{H} \approx \hbar\left(\omega_c - \frac{g^2}{\Delta}(\sigma_z^1 + \sigma_z^2)\right)a^\dagger a + \frac{\hbar}{2}\left(\Omega - \frac{g^2}{\Delta}\right)(\sigma_z^1 + \sigma_z^2) - \frac{\hbar g^2}{\Delta}(\sigma_+^1\sigma_-^2 + \sigma_-^1\sigma_+^2), \qquad (2.48)$$

where the operators with index $1(2)$ act on the first (second) qubit. The last term is an entangling interaction between the qubits, mediated via virtual photons. It is suppressed if the qubits are off-resonant with each other. Majer *et al.* (2007) were the first to entangle two qubits in the circuit cavity QED architecture, making use of most of the above techniques: the authors prepared a state $|\uparrow,\downarrow\rangle$ of two mutually off-resonant qubits in the dispersive regime by applying a π pulse to one of them. Then, they shifted the qubits into resonance by a Stark pulse. At a certain pulse duration, the time evolution generated by the Hamiltonian (2.48) amounted exactly to the so-called $\sqrt{\text{iSWAP}}$ gate, which yielded the entangled state $1/\sqrt{2}(|\uparrow,\downarrow\rangle + |\downarrow,\uparrow\rangle)$. After switching off the Stark pulse, the state of both qubits was measured simultaneously, utilizing the four different dispersive shifts of the cavity frequency caused by the four different qubit product states $|\uparrow\downarrow,\uparrow\downarrow\rangle$.

2.3 State of the art in circuit QED

In the preceding sections, we have outlined the basic principles behind circuit QED and mentioned the key experiments which have utilized or demonstrated these principles first. Some aspects of this discussion have already indicated that circuit QED is proceeding at an unabated rapid pace. In addition to the main applications of circuit QED anticipated by the pioneers of the field, namely as a testbed for fundamental non-linear quantum optics and as a toolbox for processing quantum information, new topics such as the physics of the measurement process or quantum simulations are currently becoming increasingly important. In this section, we review some recent achievements in each of the different areas of circuit QED (which cannot always be clearly separated). Most of the theory relevant to this section is detailed, *e.g.*, in the textbooks on quantum optics by Scully and Zubairy (1997) and Walls and Milburn (1994), and in the textbook on quantum information science by Nielsen and Chuang (2000).

Quantum optics with superconducting circuits

With the advances of the experimental technology in circuit QED, it became possible to transfer many of the iconic quantum optical experiments with real atoms to this platform (and to the microwave domain), and, in quite a few cases, even to outperform previous approaches.

For instance, Astafiev *et al.* (2007) demonstrated lasing with a single artificial atom in a microwave cavity. The population of a Cooper-pair box was inverted by two sequential single-electron tunneling events, which changed the number of Cooper pairs on the island (the good quantum number) by one. The lasing action was confirmed by measuring the spectral narrowing of the emitted microwaves below κ and the amplification of an external microwave signal.

Fink *et al.* (2009) investigated the Tavis-Cummings model and were able to show the theoretically predicted $\sqrt{N}$ dependence of the resonant atom-field coupling. Compared to other implementations of the model, *e.g.*, with dilute atomic beams traversing a cavity, such experiments can be performed in circuit QED without fluctuations in the atom number. Since the $N = 3$ superconducting artificial atoms had been equipped with individual flux bias, they could be brought into resonance with the cavity one by one. If there are N atoms on resonance with the cavity, only one collective atomic excitation hybridizes with the cavity. The corresponding states are split by $2g\sqrt{N}$ and the excitation is carried with probabilities $1/2$ by the cavity and $1/2N$ by one specific atom. The other $N-1$ atomic states with one excitation do not couple to the cavity and remain dark in the spectroscopy experiment. All of these features of the resonant Tavis-Cummings model were observed in the experiment.

A further well-known quantum optical phenomenon re-observed in circuit QED is the splitting of a strongly and resonantly driven atomic transition, which becomes manifest in the *Mollow triplet* and the *Autler-Townes doublet*. The drive and the atomic transition form a resonant Jaynes-Cummings system (we remark that this does not require a cavity). If the photon number n in the drive is high, the Jaynes-Cummings doublets have an almost uniform splitting since $2g\sqrt{n} \approx 2g\sqrt{n+1}$. With increasing drive power, this splitting can eventually become larger than

the line width of the atomic transition. If at the same time (i) the fluorescence from the driven atom is measured or its spectrum is probed with a weak spectroscopy tone, one can observe the described splitting as three lines at Ω and $\Omega \pm 2g\sqrt{n}$ – the Mollow triplet. Note that $2g\sqrt{n}$ is the frequency of the Rabi oscillations, see Equation (2.36). If at the same time (ii) the energy difference between the driven atomic transition and a third atomic level is probed, one will find two lines split by $2g\sqrt{n}$ – the Autler-Townes doublet. Baur *et al.* (2009) observed these phenomena in the dispersive regime of circuit cavity QED, using the cavity only for a sophisticated spectroscopy scheme.

Forn-Díaz *et al.* (2010) observed the *Bloch-Siegert* shift of a flux qubit strongly coupled to a microwave resonator. The Bloch-Siegert shift is the shift of the transition frequency of a two-level atom coupled to an electromagnetic field exclusively due to the usually neglected counter-rotating terms. This shift can be made visible by strongly driving the atomic transition (also the counter-rotating coupling increases in proportion to the drive amplitude $\sim \sqrt{n}$), or by approaching the regime of so-called *ultrastrong coupling* $g/\omega_c \gtrsim 0.1$, as was done by Forn-Díaz *et al.* (2010). We remark that ultrastrong coupling in circuit QED had been seen first by Niemczyk *et al.* (2010).

Other typical quantum optical experiments transferred to circuit QED include the following: The elastic scattering of light from a single flux qubit in an open transmission line was investigated by Astafiev *et al.* (2010). They found an almost perfect extinction of the transmitted power (94%) due to destructive interference of the forward-scattered and the incident wave (and a Mollow triplet in the inelastically scattered fraction of the power for stronger drive). Abdumalikov *et al.* (2010) demonstrated *electromagnetically induced transparency* in a similar setup. This phenomenon requires a three-level atom (usually many atoms instead of one) with two dipole-allowed and one dipole-forbidden transition between the three levels. If one of the allowed transitions is driven with an appropriate control tone, the second transition can become non-absorptive for a weak probe tone. Loosely speaking, this is because the excitation pathways of the atom in response to the two tones interfere destructively (Fleischhauer *et al.*, 2005). Thereby, the atom resides in a *dark state*. This state does not necessarily have to be the ground state of the atom, but can also be formed by a superposition of the two states that are not dipole-coupled (depending on the amplitude ratio of control and probe tone). The latter phenomenon is known as *coherent population trapping* and was observed in a phase qubit by Kelly *et al.* (2010). By carefully choosing drives and initial conditions, one can modify the dark state and so swap population between the two uncoupled states in a process called *stimulated Raman adiabatic passage*, which was predicted to be realizable with quantronium qubits by Siewert *et al.* (2009).

A slightly different line of research on quantum optics with superconducting circuits puts a stronger emphasis on the quantum nature of the electromagnetic field in these systems. An important experiment in this regard was the preparation of single microwave photons on demand by Houck *et al.* (2007). The authors used a circuit QED system with a transmon qubit sufficiently detuned from the cavity that the qubit was in a well-defined state $\alpha|\downarrow\rangle + \beta|\uparrow\rangle$ that could be prepared with the means introduced in the last section. However, the qubit was close enough to the cavity so that its dominant decay process was radiative decay via the cavity (see the RHS of Equation (2.40)). The authors used an asymmetric cavity with only one port, the output port, strongly coupled to the external circuitry. The strong coupling was chosen such that κ was

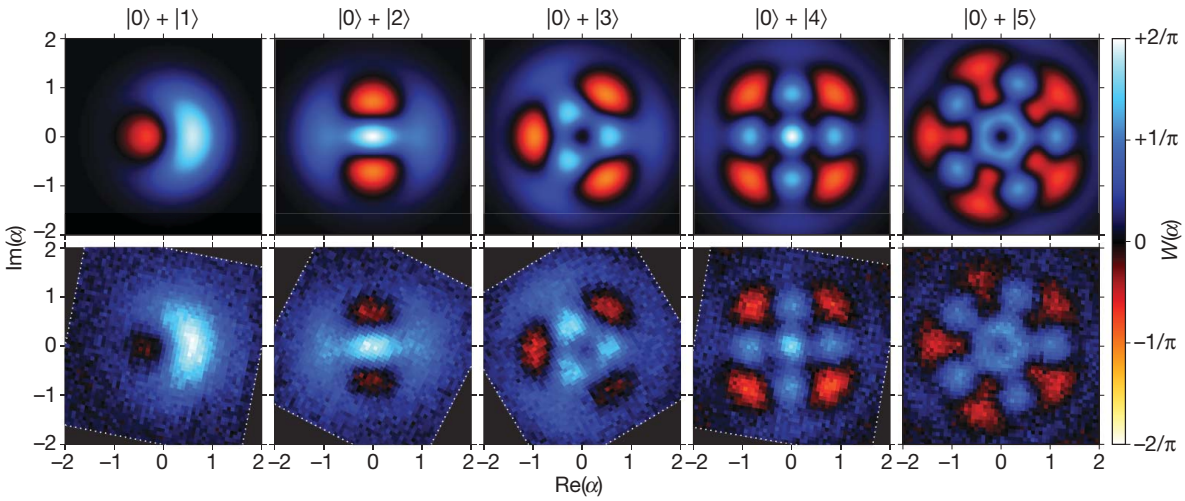

Figure 2.12: Results on the synthesis of arbitrary cavity states in circuit QED obtained by Hofheinz *et al.* (2009) (courtesy of A. Cleland). Upper row, calculated Wigner densities $W(\alpha)$ for the cavity states $|0\rangle + |j\rangle$ for $j = 1, \ldots 5$ as a function of the complex resonator amplitude α. Lower row, measured Wigner densities after a state-preparation protocol for $|0\rangle + |j\rangle$ has been performed. The protocol is based on the interaction of the cavity with a superconducting phase qubit.

sufficiently high for the qubit to decay radiatively, but that this radiative decay was still slower than the time required to prepare the qubit state. The asymmetry of the cavity ports ensured that the photons were emitted only at the output port from the cavity. Due to the lack of single-photon detectors, the authors had to work hard, but succeeded, to demonstrate that their setup was indeed able to map deterministically qubit states $\alpha|\downarrow\rangle + \beta|\uparrow\rangle$ onto photonic states $\alpha|0\rangle + \beta|1\rangle$ which are then emitted from the cavity. This experiment forms the basis for some impressive experiments on the preparation of non-classical states of the cavity field and the current experiments with itinerant microwave photons, which we summarize in the following.

Pushing further the ideas of Houck *et al.* (2007), Hofheinz *et al.* (2008) created Fock states with up to $n = 6$ photons in a microwave resonator coupled to a phase qubit. To that end, they applied a π pulse to the off-resonant qubit. Then the qubit was tuned into resonance with the cavity for the duration of half a Rabi cycle, that is, until the qubit's excitation was swapped into the cavity. Bringing the qubit out of resonance afterwards, the procedure was repeated to increase the photon number in cavity further. Due to the increasing frequency of the quantum Rabi oscillations in proportion to $\sqrt{n}$ (see Equation (2.36)), the interaction time of the qubit and the cavity had to be reduced with increasing n. The measurement of the photonic Fock states was achieved essentially by the reverse protocol, similar in spirit to the seminal Rydberg-experiment by Brune *et al.* (1996b). The authors brought the qubit again into resonance with the resonator for a variable time t and measured the time-dependent excitation probability $P_\uparrow(t)$ of the qubit. This excitation probability allows one to analyze the photon-number distribution p_n in the cavity since one can easily show that each $|n\rangle$ contributes an independent quantum Rabi oscillation to $P_\uparrow(t)$,

$P_\uparrow = \sum_{n\geq 1}(p_n/2)(1-\cos(2g\sqrt{n}t))$, and $p_0 = 1-\sum_{n\geq 1} p_n$. In a subsequent work, Hofheinz *et al.* (2009) deterministically created arbitrary states of the form $|\psi\rangle = |\downarrow\rangle \otimes \sum_n c_n|n\rangle$ (with a limited number of photons). They followed a protocol proposed by Law and Eberly (1996), which requires only the abilities to rotate the qubit about the x axis by a variable angle and to bring the qubit into resonance with the cavity for a variable amount of time. Moreover, Hofheinz *et al.* (2009) were also able to measure the Wigner density (Walls and Milburn, 1994) of the cavity, using a protocol based on the displacement of the cavity field and the subsequent measurement of the photon number distribution like in their previous experiment. They found an astonishing agreement between measured and expected Wigner densities, as illustrated in Figure 2.12.

Quite some research is currently directed to the study of itinerant microwave photons that have been generated by a single-microwave sources. There has been remarkable process in surmounting the difficulties of measuring the weak signals stemming from propagating microwaves due to advances in digital signal processing (Bozyigit *et al.*, 2011) and the increasingly adept usage of low-noise Josephson parametric amplifiers (Castellanos-Beltran *et al.*, 2008). For instance, Bozyigit *et al.* (2011) were able to characterize the output of a single microwave photon source via the measurement of Glauber's first and second order correlation functions of the emitted electromagnetic field, $G^{(1)}$ and $G^{(2)}$ (actually another standard quantum optical experiment transferred to the microwave domain; see Walls and Milburn (1994) for a treatment of the field correlation functions). The lack of the (nonlinear) photon number detectors used for such measurements in the optical domain was overcome by feeding the output of the photon source into a beam splitter and simultaneously recording the field quadrature amplitudes at the outputs of the beam splitter with the usual linear detectors used in the microwave domain, which in principle also allows one to extract all statistical moments of the photon source (da Silva *et al.*, 2010). Using this technique, Bozyigit *et al.* (2011) were able to show single photon coherence in $G^{(1)}$ measurements and photon antibunching in $G^{(2)}$ measurements, the latter being a smoking gun for the quantum nature of their microwave source. In subsequent works, state tomography of non-classical itinerant fields was performed (Eichler *et al.*, 2011; Mallet *et al.*, 2011). Eichler *et al.* (2012) brought an excited qubit into resonance with a cavity for a quarter of a Rabi cycle. Using a Josephson parametric amplifier, the itinerant photonic state emitted from the strongly coupled output port of the cavity could be shown to be entangled with the qubit. Entanglement between itinerant microwave fields in different transmission lines was prepared by Flurin *et al.* (2012) and Menzel *et al.* (2012). The Hong-Ou-Mandel effect, the interference of two identical photons simultaneously entering the input ports of a beam splitter, has been demonstrated with two independent single-microwave sources by Lang *et al.* (2013).

The last experiment discussed in this section is one of the first major applications of the novel high-coherence 3D circuit QED design invented by Paik *et al.* (2011). Using a device based on this design, Kirchmair *et al.* (2013) were the first to conduct experiments on the single-photon Kerr effect. Explicitly, the authors observed the collapse and revival of an initially-prepared coherent cavity state due to the nonlinear Kerr-interactions between the photons in the cavity. In the course of the time evolution, highly non-classical superpositions of coherent (*i.e.* close to classical) states were formed, which the authors monitored both by measuring the Husimi Q function and, for some selected points in time, the Wigner function of the cavity (the Q function is a quasiprobability distribution more well-behaved and easier to measure than the Wigner

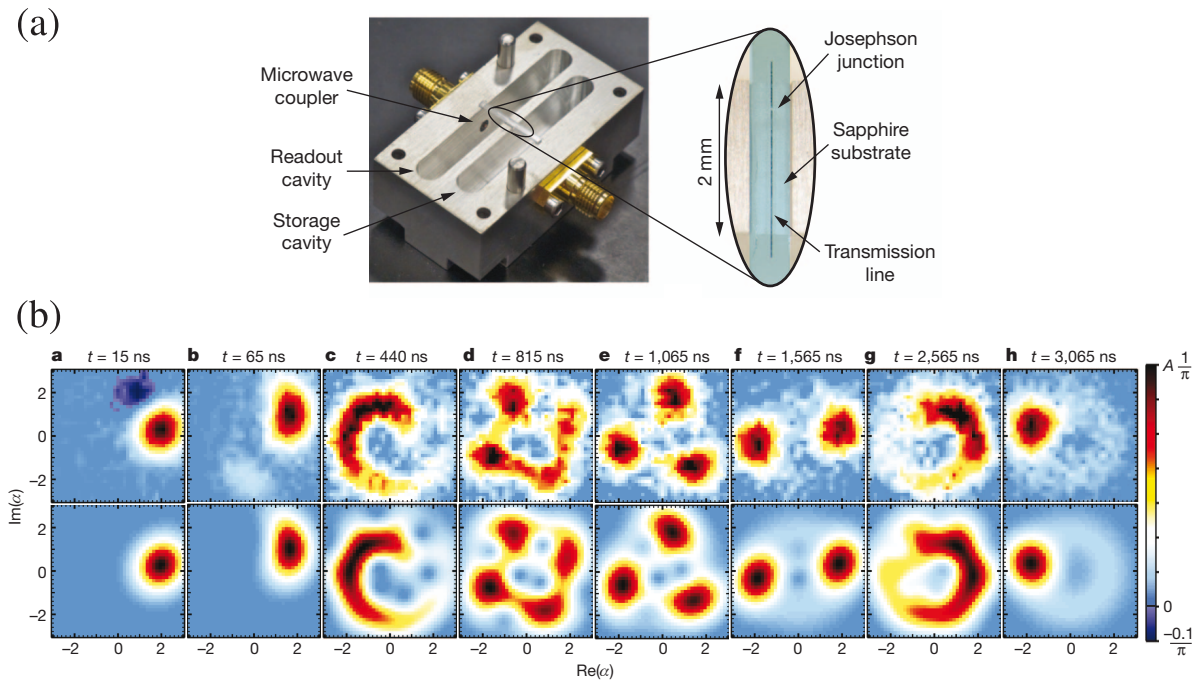

Figure 2.13: Experiments on the single photon Kerr effect by Kirchmair *et al.* (2013) (courtesy of R. Schoelkopf). (a) Experimental setup. The transmon qubit is formed by a Josephson junction embedded in a transmission line. The qubit is coupled to two 3D superconducting cavities. The storage cavity is used as nonlinear Kerr medium. The second resonator facilitates the read-out of the qubit state. (b) Husimi Q function of the storage cavity vs. complex cavity amplitude α as measured (upper row) and calculated (lower row) for different times after initializing the storage cavity in a coherent state with an average of four photons. After a complete phase collapse (panels **a**-**c**), structures re-emerge at specific (well-understood) later times. In panels **d**-**f**, the system is in superpositions of coherent states with $4, 3, 2$ components, respectively. A is a scaling parameter of order ~ 1.

function, see Walls and Milburn (1994). Their device consisted of two parallel 3D superconducting cavities and a perpendicular transmon qubit coupled dispersively to both cavities (see Figure 2.13(a)). One cavity, the storage cavity, was used as Kerr medium. The necessary Kerr nonlinearity was inherited from its interaction with the qubit (see Equation (2.32)). Because of the excellent coherence properties of the used device, both the (Kerr) photon-photon interaction and the dispersive shift of the qubit frequency per photon were at least one order of magnitude bigger than the decay rates of the system. The regime of strong Kerr interactions on the single-photon level had not been realized previously. The measurement of both the Q and the Wigner function of the storage cavity relied on a sequence of displacing this cavity and then measuring the probability of there being exactly n photons in the cavity. Unlike Hofheinz *et al.* (2009), who had used resonant qubit-cavity interactions for a similar purpose, Kirchmair *et al.* (2013) measured this probability by measuring if the dispersive shift of the qubit frequency is as large

as expected in the presence of n photons. This in turn could be determined by applying a photon-number selective π pulse to the qubit, that is, a pulse with frequency and duration matched to the qubit frequency in the presence of n photons, and by subsequently measuring whether the qubit got excited or not. This was done via the second resonator. The described scheme to determine if there are exactly n photons in the cavity had been demonstrated before by Johnson *et al.* (2010). The time-evolution of the Q function obtained by Kirchmair *et al.* (2013) is shown in Figure 2.13(b).

Quantum information processing with superconducting circuits

Regarding the processing of quantum information, circuit QED systems have reached a level where basic algorithms with a few qubits can be run with high fidelity and quantum error correction starts to come within reach. An outlook on the capabilities and likely near-future developments of quantum information processing with circuit QED was given by Devoret and Schoelkopf (2013).

An important step in the development so far was certainly the implementation of an entangling two-qubit interaction mediated by a cavity bus (Majer *et al.*, 2007), which we have already briefly discussed at the end of the last chapter. Some time later, DiCarlo *et al.* (2009) demonstrated the Grover search and the Deutsch-Jozsa algorithm with two transmon qubits in one cavity. The key to this experiment was a new entangling mechanism, based on the cavity-mediated interaction of the computational state $|1,1\rangle$ with the non-computational state $|0,2\rangle$. Here, $|i,j\rangle$ stands for a state in which the first (second) qubit is in its ith (jth) excited level. If the state $|0,2\rangle$ is brought adiabatically into resonance with $|1,1\rangle$, this will not change the population of the computational states $|i,j\rangle$ with $i,j \in 0,1$. However, since the energy of $|1,1\rangle$ is shifted by the interaction with $|0,2\rangle$ by an amount of, say, $-\xi$, this computational state picks up an additional dynamical phase $\delta_{11} = \phi_{11} - \phi_{01} - \phi_{10} = -\xi\tau$. Here, the $\phi_{i,j}$ are the dynamical phases acquired by the computational levels during the time τ the interaction of $|1,1\rangle$ and $|0,2\rangle$ is switched on. Suitably choosing τ, the authors realized a C-Phase (entangling) gate. In combination with single qubit rotations, the C-Phase gate allowed them to generate two-qubit Bell states on demand and to run the aforementioned quantum algorithms. Building on this work, DiCarlo *et al.* (2010) demonstrated deterministic generation of three-qubit entanglement. They were able to map the state $1/\sqrt{2}(|0\rangle + e^{i\varphi}|1\rangle)$ of one qubit onto the three-qubit state $1/\sqrt{2}(|000\rangle + e^{i\varphi}|111\rangle)$ with sufficient fidelity to witness three-qubit entanglement of the GHZ type via quantum state tomography (for a review on (witnessing) entanglement, see Horodecki *et al.* (2009)). This mapping can be seen as the first step of a repetition code and, hence, as a first step toward basic quantum error correction (Shor, 1995). The encoding protocol was based on an improved two-qubit C-Phase gate, which exploited non-adiabatically the interaction used in their previous work, supplemented by single-qubit rotations. In a related work, Neeley *et al.* (2010) employed a similar protocol of one-qubit and two-qubit iSWAP gates to create GHZ states of three phase qubits, and simultaneous three-qubit interactions to create W states. Also Neeley *et al.* (2010) were able to verify the creation of genuine three-qubit entanglement by means of quantum state tomography and entanglement witnesses. In an earlier work based on similar physics, the same group had measured the first violation of (the Clauser-Horne-Shimony-Holt version of) a Bell inequality

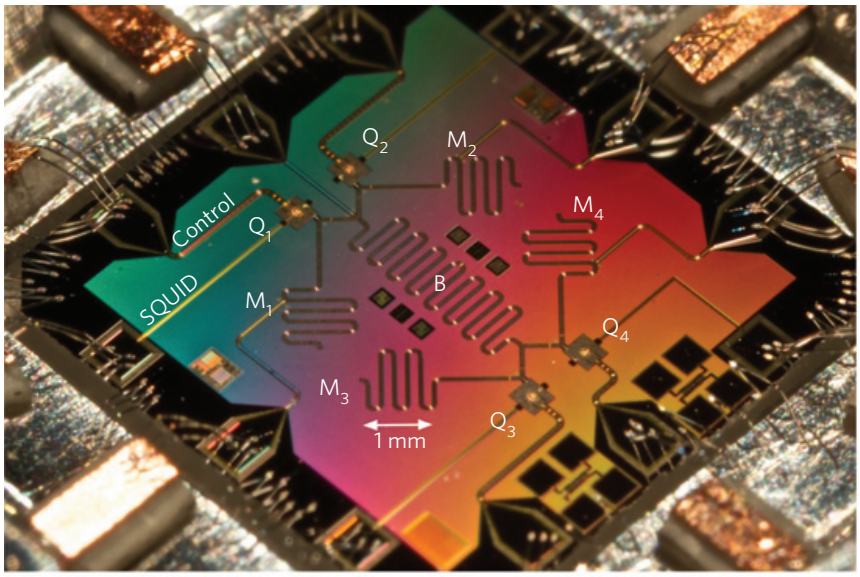

Figure 2.14: Experimental setup used by Lucero *et al.* (2012) to demonstrate Shor's algorithm (photo by E. Lucero; courtesy of A. Cleland). The device comprises four superconducting phase qubits Q_j, each coupled to a memory resonator M_j. The coupling resonator B facilitates multi-qubit gates. The lines for control and SQUID read-out of qubit Q_1 are indicated.

in a system with superconducting qubits (Ansmann *et al.*, 2009; Clauser *et al.*, 1969). We remark that, like the C-Phase gate, the iSWAP (and the $\sqrt{\text{iSWAP}}$) gate is sufficient for universal quantum computing if supplemented with single-qubit rotations. SWAP-type gates usually result from partial resonant exchange of excitations, *e.g.*, from a partial vacuum Rabi oscillation (see also Equation (2.48)). For phase qubits, they are easily implemented by sequentially bringing the qubits in resonance with a coupling resonator for a specific amount of time, or by coupling the qubits directly with a coupling capacitor.

Up to now, phase qubits do not have as good coherence times as other types of qubits. On the other hand, phase qubits have proved to be excellently suited to prepare non-classical states of a cavity. To work around the relatively short coherence times of phase qubits, researchers came up with the idea to store quantum information in long-lived (*i.e.*, low κ) microwave cavities and to extract the quantum information only for processing – just as in a classical von-Neumann architecture. As a first step in a series of publications towards that goal, Mariantoni *et al.* (2011a) demonstrated that they were able to coherently shuffle complex photonic quantum states in between three cavities and also to create entanglement between the cavities, using two phase qubits as connecting elements. They used essentially the same techniques as Hofheinz *et al.* (2009) for creating arbitrary photonic states in a resonator by means of manipulating a qubit, just with the qubits being coupled to two cavities each. In a next step, Mariantoni *et al.* (2011b) demonstrated a 'quantum von-Neumann architecture', comprised of seven elements: Two phase qubits connected through a coupling bus resonator formed the 'quantum central processing unit'. Each qubit was additionally connected to a 'quantum random access memory' resonator and a zeroing

register, the latter being a spurious two-level system used to reset qubits and memory. The quantum processing unit in their work was demonstrated to be capable of the entangling $\sqrt{\text{iSWAP}}$, iSWAP, and, using the interaction of the computational levels with higher levels similar to DiCarlo *et al.* (2009), C-Phase two-qubit gates. Using the lowest two Fock states $|0\rangle$ and $|1\rangle$ of the bus resonator as target bit, also three-qubit gates could be implemented. Finally, the ability to store, retrieve, and erase quantum information in the quantum memory was shown. In particular, the lifetime of entanglement deposited in the resonators was significantly enhanced compared to entanglement carried by the qubits. This line of research culminated so far in the work presented by Lucero *et al.* (2012). The authors scaled up the device further to four qubits, each coupled to a memory resonator. A quantum bus resonator facilitated (multi) qubit gates (see Figure 2.14). To demonstrate the potential of this architecture, the authors created multi-qubit entanglement and factorized the number 15 using Shor's algorithm.

Tools developed for further increasing the performance of quantum computations with superconducting circuits include the demonstration of tunable couplers for superconducting flux (Niskanen *et al.*, 2007), phase (Bialczak *et al.*, 2011), and charge (Srinivasan *et al.*, 2011) qubits. Fedorov *et al.* (2012) showed how the important, but experimentally challenging three-qubit Toffoli gate can be efficiently implemented with weakly anharmonic superconducting qubits (in their case, with transmons). The key idea in their approach was to 'hide' the population of the computational level $|1,1,1\rangle$ in the non-computational level $|2,0,1\rangle$. In this way, the entangling interaction they had at their disposal, which corresponded to the usual two-qubit C-Phase gate $|.,1,1\rangle \rightarrow -|.,1,1\rangle$, effectively affected only the computational level $|0,1,1\rangle$. With additional Hadamard transformations, one can put together the Toffoli gate. Bylander *et al.* (2011) used dynamical decoupling of a superconducting flux qubit to achieve the maximum dephasing time $T_2 = 2T_1 \approx 24\,\mu$s (with a pure dephasing time $T_\varphi > 0.1$ ms) and to characterize the environmental noise spectrum influencing the qubit. Two transmon qubits in two different resonators were directly coupled with a coupling capacitor by Dewes *et al.* (2012), and a two-qubit $\sqrt{\text{iSWAP}}$ gate was demonstrated. The peculiarity in this experiment was that both resonators had been made nonlinear by embedding a Josephson junction in the center traces. This allowed the experimenters to operate the resonators as Josephson parametric amplifiers, which enabled hitherto unrealized simultaneous single-shot read out of more than one transmon. Very recently, almost deterministic quantum teleportation (that is, with success probability approaching one) of arbitrary input states in a circuit QED architecture has been reported by Steffen *et al.* (2013). Teleportation might be relevant for transferring quantum states within larger networks of coupled cavities and qubits. Figure 2.15 shows the device used by Steffen *et al.* (2013), which relies on an architecture proposed by Helmer *et al.* (2009). Since the fidelity of the teleportation protocol depends not only on the degree of entanglement that can be created between the parties participating in the protocol, but also on the ability to measure in the two-qubit Bell basis, joint high-fidelity single-shot read-out of two qubits to had to be achieved also in this work. We remark that the last step of the teleportation protocol, the rotation of the target qubit conditioned on the outcome of the Bell-basis measurement, was not yet incorporated in the protocol of Steffen *et al.* (2013) and had to be compensated by post selection.

An interesting line of research with superconducting qubits with potential applications in quantum computing is the study of geometric phases. These were first observed by Leek *et al.*

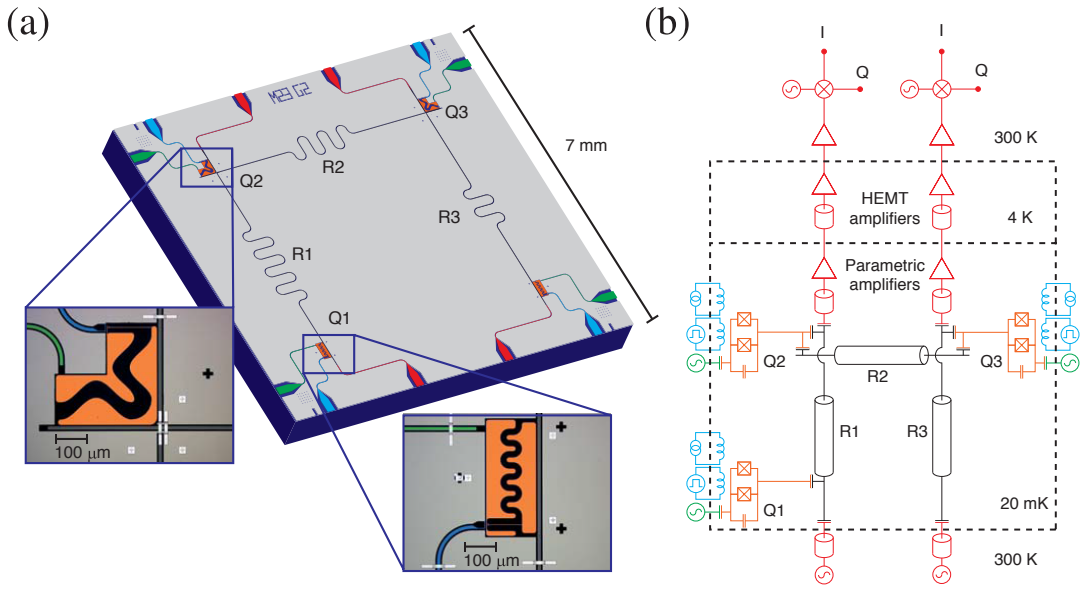

Figure 2.15: Circuit QED setup used for quantum teleportation by Steffen *et al.* (2013) (courtesy of A. Wallraff). (a) Rendered image of the setup. The transmon qubits Q_j participate in the protocol (a fourth qubit is unused). Each qubit is equipped with a microwave drive (green) for qubit rotations and a flux bias line (blue) for ns control of the qubit transition frequency. The qubits are coupled and dispersively read out via three cavities R_j. In the implemented teleportation protocol, Q_2 and Q_3 are entangled and Q_1 is prepared in the state to be teleported. If Q_1 and Q_2 are then measured in the Bell basis, Q_3 is, up to a rotation which is uniquely determined by the measurement result, in the same state as Q_1 at the beginning. (b) Schematics of the setup. The one- and two-qubit single-shot read-out is facilitated by amplifying the transmitted measurement tones through R_1 and R_3 with low-noise Josephson parametric amplifiers, which are then further amplified with linear HEMT amplifiers. The dashed boxes indicate the operation temperatures of the different circuit components.

(2007), using a Cooper-pair box dispersively coupled to a cavity. Adiabatic manipulations of the qubit Hamiltonian were implemented by means of off-resonant driving of the qubit according to the rules we have summarized in the last chapter. A echo technique similar to the Hahn echo was used to differentiate dynamical and geometric phase. As shown by Wilczek and Zee (1984), if a parameter-dependent Hamiltonian contains a degenerate subspace for all parameter values, non-Abelian holonomies can be obtained by adiabatic and cyclic changes of the parameters. This means essentially that the geometric phase picked up by a state is generalized to a mapping within the degenerate subspace, which in turn can be employed for implementing quantum gates (Zanardi and Rasetti, 1999). Only recently, non-Abelian holonomic single-qubit gates have been realized by Abdumalikov *et al.* (2013) with a 3D circuit QED system and utilizing a subtle non-adiabatic protocol (Sjöqvist *et al.*, 2012) which accommodates the limited coherence time of the system.

Given the high degree of control one has reached in performing different sorts of gate operations and elementary quantum protocols, the next step towards large-scale fault-tolerant quantum computing can now be seriously tackled (Devoret and Schoelkopf, 2013). This step consists in the implementation of error correction codes (Shor, 1995), in which a logical qubit is encoded in a larger number of physical qubits in a way that the coherence time of the logical qubit is significantly enhanced (ideally to infinity) compared to the physical qubits. Elementary quantum error correction codes were already implemented in circuit QED by Reed *et al.* (2012). These authors encoded a qubit state in three physical qubits and were able to show that their codes could correct artificial single-qubit bit-flip and phase-flip errors, respectively (bit-flip and phase-flip errors are equivalent up to a local change of basis). The codes were based on mapping the error syndrome to the state of the two ancilla qubits and correcting the error with a Toffoli gate. To undo arbitrary single-qubit errors, these codes had to be concatenated, *e.g.*, in Shor's code, which would require nine qubits. However, even for the elementary three-qubit codes of Reed *et al.* (2012), in the physically realistic situation where all qubits can be subject to errors, the limited gate fidelities prevented an actual enhancement of the robustness of the stored quantum information with respect to the artificially induced errors. With increasing complexity of the error-correction procedure, these problems will become even more severe. Thus, to reach the threshold for gainful error correction, further improvement of coherence times and gate fidelities is necessary. Finally, we remark that there is a variety of different error-correction schemes. Depending on the underlying circuit QED architecture, one or the other might be more promising to implement (Devoret and Schoelkopf, 2013).

Other applications of circuit QED

In this section, we point out some further achievements with circuit QED systems which do not straightforwardly fit into the above classification.

For completeness, we mention again that the immense improvement of the read-out in circuit QED systems owing to the emergence of low-noise Josephson junction based amplifiers (Siddiqi *et al.*, 2004; Castellanos-Beltran *et al.*, 2008; Mallet *et al.*, 2009; Bergeal *et al.*, 2010) made possible the study of interesting measurement physics. For instance, if a qubit is measured only weakly, the 'collapse' of its state vector is slowed down and it performs an erratic motion towards an eigenstate of the measured operator. Remarkably, if the measurement apparatus is fully efficient, that is, if none of the measurement's information content is lost, the evolution of the state vector can be entirely reconstructed from the measurement record. What is more, if the initial state of the qubit is known, its state after a weak measurement can be precisely determined. The information gained by continuous weak measurement of a 3D transmon qubit was used by Vijay *et al.* (2012) to stabilize Rabi oscillations indefinitely with a quantum feedback (which might be relevant for quantum error correction), and Hatridge *et al.* (2013) studied the measurement back-action on a (usual) transmon after variable-strength measurements. Weak measurements had been used before by Palacios-Laloy *et al.* (2010) to demonstrate the violation of the Leggett-Garg inequality (Leggett and Garg, 1985). Another important achievement concerning the measurement of superconducting qubits was the observation of quantum jumps of a transmon by Vijay *et al.* (2011).

Much effort is currently devoted to the investigation of hybrid quantum systems, in which superconducting qubits are coupled to other (potential) carriers of quantum information, usually via the electromagnetic field of the cavity. For example, Kubo *et al.* (2011) coupled a transmon qubit to an ensemble of nitrogen-vacancy centers in diamond and were able to store an initially prepared qubit state into the collective excitations of the ensemble and to retrieve it back later. Frey *et al.* (2012) and Petersson *et al.* (2012) coupled a double quantum dot to a microwave resonator in which superconducting qubits could be potentially integrated. Pirkkalainen *et al.* (2013) coupled a transmon qubit simultaneously to a microwave cavity and to a micromechanical resonator. The measurement of the first ground state cooling of a mechanical resonator was achieved by coupling the resonator to a phase qubit (Neeley *et al.*, 2010).

Finally, we mention the interesting experiments by Wilson *et al.* (2011), who observed the dynamical Casimir effect by rapidly changing the effective length of the cavity, by Johnson *et al.* (2011), who demonstrated quantum annealing with eight coupled flux qubits, and by Murch *et al.* (2012), who engineered the spectrum of the electromagnetic noise seen by a qubit so that it relaxed autonomously to an arbitrarily specified state.

2.4 Towards larger systems

In the face of the progress and the present state of circuit QED, it is timely to try and proceed to larger-scale circuit QED systems. For quantum computing applications of circuit QED, scaling is the central goal. An essential prerequisite for reaching this goal is the implementation of efficient quantum error correction. Despite the excellent coherence and controllability of circuit QED systems, quantum error correction will probably require a considerable increase of their complexity and, thus, certainly poses a formidable task. However, on the way to building a fully-fledged quantum computer, there might be interesting physics to discover with larger-scale multi-qubit, multi-resonator circuit QED setups, which is technically less challenging. This is where the new work presented in this thesis ties in. Potential applications of such circuit QED systems range from quantum simulations to, again, quantum optics. In the following, we first describe other theoretical work in this direction and then summarize the contribution made in this thesis. A general and more detailed account on quantum simulations will be given later. For the present purpose, it suffices to associate them with the purposeful implementation of a specific Hamiltonian in a well-controlled system.

The simplest circuit QED experiment with many qubits one could imagine would be to put a large number of qubits into a cavity and to probe the resonances of the system, *e.g.*, by spectroscopy. Such a scenario was first considered for fluxonium qubits at temperature $T = 0$ by Nataf and Ciuti (2010a). They found that, at a certain critical qubit density, one mode of the system becomes weak and the system undergoes a zero-temperature *superradiant phase transition* (Hepp and Lieb, 1973), which will be discussed in detail in Chapter 3. In a later work, Nataf and Ciuti (2010b) revisited this situation, replacing the fluxoniums by charge qubits, and found the same phase transition. The phenomenon superradiant phase transitions are named after, that is, *superradiance*, was predicted to be observable in circuit QED by Delanty *et al.* (2011). Superradiance is the enhancement of the peak intensity of the radiation emitted by N initially excited identical atoms, which can occur if the atoms are located in a region whose extent is of the order of the wavelength of the emitted radiation. For independently radiating (say, spatially sufficiently separated) atoms, the intensity of the emitted radiation is maximal immediately after the excitation of the atoms took place and scales in proportion to N. However, in a dense cloud of atoms, strong correlations between the atoms can build up during the radiation process so that the photon emission rate becomes drastically increased at some point in time. Its maximum scales in proportion to N^2 and gives rise to a peak of the detected radiation intensity $\propto N^2$ some time after the excitation of the atoms. One can say that, where the correlations between the atoms are strong, these radiate coherently like a single dipole with dipole operator $\propto N$. Hence, the intensity of the emitted radiation is $\propto N^2$. Note that the duration of this superradiant emission has to scale $\propto 1/N$ since the overall emitted energy has to be the same for independently and coherently radiating atoms. Superradiance was predicted by Dicke (1954) and first observed by Skribanowitz *et al.* (1973) (for reviews, see, *e.g.*, Gross and Haroche (1982); Brandes (2005)). Because of the exceptionally strong atom-field coupling in circuit QED, Delanty *et al.* (2011) predicted superradiance to be observable already with a small number of qubits (~ 5). The relation of superradiance and

superradiant phase transitions rests in the fact that at a superradiant phase transition, a system of atoms coupled to the electromagnetic field enters a highly collective phase in which all thermodynamically relevant states have the potential to superradiate (superradiant phase transitions can also occur if $T \neq 0$).

Intense theoretical and first experimental research is currently pursued on lattices of coupled cavities, made nonlinear by coupling each cavity to an (artificial) atom. Such systems are investigated primarily for quantum simulations of Bose-Hubbard type many-body physics, which was first suggested by Hartmann *et al.* (2006), Greentree *et al.* (2006), and Angelakis *et al.* (2007). Due to their exquisite experimental controllability, circuit QED systems are amongst the most promising candidate systems for implementing these ideas. The already comprehensive literature on this subject was reviewed by Houck *et al.* (2012) and Schmidt and Koch (2013). The central idea is to connect elementary circuit cavity QED systems containing one superconducting qubit each in a way that permits photon hopping at a rate κ from one cavity j to its nearest neighbors. Photons occupying the same site would then experience an effective photon-photon interaction owing to the Jaynes-Cummings nonlinearity. Ideally, such an array of coupled cavities would be described by the *Jaynes-Cummings-Hubbard Hamiltonian*

$$\mathcal{H}_{\mathrm{JCH}} = \sum_j \mathcal{H}_{\mathrm{JC},j} - \kappa \sum_{\langle i,j \rangle} (a_i^\dagger a_j + a_j^\dagger a_i), \tag{2.49}$$

where $\mathcal{H}_{\mathrm{JC},j}$ is the Jaynes-Cummings Hamiltonian describing the jth cavity (Equation (2.25)). The Hamiltonian $\mathcal{H}_{\mathrm{JCH}}$ has some similarities with the celebrated Bose-Hubbard model (Fisher *et al.*, 1989). In particular, in the limit of large lattices, it can undergo a quantum phase transition (Sachdev, 1999), whereby its ground state changes from a polariton superfluid to a polariton Mott insulator or vice versa.[10] Mean-field and other calculations for the phase diagram of $\mathcal{H}_{\mathrm{JCH}}$ reveal Mott lobes in close similarity to those obtained for the Bose-Hubbard model (Fisher *et al.*, 1989). The ratio of photon hopping and photon-photon interactions can be controlled *in situ* by varying the detuning of qubits and cavities and, thus, the strength of the Jaynes-Cummings nonlinearity. However, it must be emphasized that there are some important differences between $\mathcal{H}_{\mathrm{JCH}}$ and the Bose-Hubbard model. Most importantly, the 'particles' undergoing the superfluid-insulator transition in the case of $\mathcal{H}_{\mathrm{JHC}}$ are, in fact, circuit excitations and their chemical potential is therefore zero. Usually, one is optimistic enough to assume that an effective chemical potential of the polaritons can be engineered and still works in the grand-canonical ensemble (which is done in the calculations of the phase diagram mentioned above). Since the time that excitations injected into the system require to reach a quasi-equilibrium should be much shorter than the time it takes until the excitations are lost, this might indeed be possible. On the other hand, it could also be interesting to investigate the non-equilibrium steady state of a weakly driven cavity array, which should provide access to entirely different physics (Schmidt and Koch, 2013) than what is usually studied in systems described by the Bose-Hubbard model (such as ultracold atoms in optical lattices, see Section 4.2). Currently, small systems of a few coupled cavities are already studied in experiments. Even for small systems, interesting effects were predicted to be

10. In this context, it is convenient to refer to the local excitations of the system, that is, the excited states of the Jaynes-Cummings Hamiltonian, which have a photonic and an atomic part, as polaritons.

observable, such as the non-equilibrium transition of an initially imbalanced polariton population from delocalized to self-trapped (Schmidt *et al.*, 2010).

One-dimensional versions of the Jaynes-Cummings lattice have recently attracted some attention in the course of the current widespread interest in Majorana fermions. Majorana fermions, which are characterized by being their own anti-particles, were predicted to exist as pairs of spatially separated quasi-particles at the ends of certain quantum wires (Lutchyn *et al.*, 2010; Oreg *et al.*, 2010). Their superpositions correspond to usual fermionic states which, however, are largely immune to all sorts of local perturbations due to their nonlocal nature. Since these Majorana fermions are non-Abelian anyons, they are potentially useful for topological quantum computing (Kitaev, 2001, 2003). Several proposals have recently been put forward how Majorana fermions could be generated in a finite one-dimensional Jaynes-Cummings lattice (Bardyn and Imamoglu, 2012; Hwang and Choi, 2012; Kumar and Jalal, 2012). These rely essentially on the assumption that the qubit-cavity coupling can be made so strong that the polaritons become hard-core particles, which would shrink the local Hilbert spaces down to that of a two-level system. In this situation, the Hamiltonian of the lattice can be mapped onto that of a 1D spinless p-wave superconductor, which supports Majorana fermions (Kitaev, 2001). Different methods for their detection have also been proposed by Bardyn and Imamoglu (2012), Hwang and Choi (2012), and Kumar and Jalal (2012). However, it is important to note that the Majorana states in a Jaynes-Cummings chain would not enjoy topological protection. This is because the mapping of $\mathcal{H}_{\mathrm{JCH}}$ to the Hamiltonian of a p-wave superconductor involves a nonlocal (Jordan-Wigner) transformation. The escape of a photon from *one* site, for example, therefore translates into a *nonlocal* perturbation of the p-wave superconductor, to which the Majorana fermions are susceptible.

2.4.1 This thesis

The research presented in this thesis was pursued to push further the idea of circuit QED with multiple components, both with regard to quantum optics and quantum simulations, while being experimentally realistic in its proposals. It is concerned with two main topics.

First, we consider the simplest possible multi-qubit circuit QED scenario, the equilibrium behavior of many superconducting charge qubits coupled to a cavity. We re-examine the possibility of superradiant phase transitions in such a system. Our study is motivated by the following observation. On the basis of standard theory of circuit QED systems, which was introduced in the previous sections of this chapter, one is lead to the conclusion that superradiant phase transitions should be in principle observable in circuit cavity QED systems. However, for *real* atoms coupling to a bosonic mode, superradiant phase transitions cannot occur. Real atoms are subject to a no-go theorem discovered by Rzażewski *et al.* (1975), only shortly after superradiant phase transitions had been first discussed (Hepp and Lieb, 1973). This would mean that, in this one aspect, the otherwise well-established similarity of circuit cavity QED systems and atomic cavity QED systems fails.

In Chapter 3, we resolve this problem by employing a fundamental, microscopic description of the considered circuit QED system. This enables us to apply the no-go theorem to circuit QED systems as well and, thus, to reject the possibility of superradiant phase transitions in circuit QED systems with charge qubits. Although the standard description of circuit QED systems

has proved to be highly useful in many situations, and is certainly more convenient than our microscopic description, we may also conclude that the standard description can lead to even qualitatively incorrect predictions and can no longer be trusted when proceeding to large-scale circuit QED systems. In addition to that, we scrutinize the no-go theorem and generalize it to multi-level atoms so as to make it more applicable to realistic systems. Sections 3.1 - 3.3 provide detailed introductions to superradiant phase transitions, the no-go theorem, and previous discussions of this issue in the context of circuit QED, respectively. Our results on this topic have been published in a research article, which is reprinted in Section 3.4.

Second, we propose a circuit QED setup that simulates the quantum Ising chain in a time-dependent transverse magnetic field. In particular, we argue that our setup is suited for observing the non-equilibrium dynamics of the transverse-field Ising chain. Our proposal is motivated as follows. Non-equilibrium quantum physics is currently subject to much theoretical research. However, experimental platforms facilitating its time-resolved observation are rare and so far essentially limited to systems of cold atoms in optical lattices. Our proposal might help to alleviate this shortage. Moreover, based on a flexible design, its implementation might be an important benchmark for future circuit QED quantum simulators of non-integrable quantum many-body spin systems, whose dynamical behavior can no longer be predicted by a classical calculation. To measure the behavior of such quantum simulators and to obtain in that way the solutions of computationally intractable problems is the central goal of all quantum simulations. Compared to the circuit QED quantum simulators we have discussed previously in this section, the proposed system relies on a different and possibly simpler concept – the direct capacitive coupling of charge qubits – so that first results on its experimental implementation have already been obtained, as described below.

In Chapter 4, we introduce this setup, derive its Hamiltonian, and calculate its spectrum to facilitate its initial experimental characterization. Experiments for observing the non-equilibrium dynamics of the transverse-field Ising chain are suggested. The expected behavior is calculated for typical circuit QED parameters and interpreted using the tools developed in previous work on non-equilibrium physics. A systematic study of the influence of disorder on these experiments is provided. Small amounts of fabrication-induced disorder are shown not to spoil the predicted experimental results. Engineering the Ising chain with a larger degree of disorder would allow the study of interesting new effects such as Anderson localization of propagating excitations. We also describe the experimental implementation of our proposal, which we have pursued in collaboration with the group of Professor Irfan Siddiqi at UC Berkeley. We present preliminary results in this regard and compare them with our theory. Sections 4.1 and 4.2 provide a motivation of and an introduction to quantum simulations, with an emphasis being placed on the importance of simulating non-equilibrium systems. Arguments for pursuing quantum simulations in circuit QED are brought forward in Section 4.3. Some properties of the quantum Ising chain are summarized in Section 4.4, and its importance is highlighted. Reprints of our previously published research articles on the simulation of the non-equilibrium dynamics of the transverse-field Ising chain in circuit QED and on the influence of disorder on such simulations are contained in Sections 4.5 and 4.6, respectively. The experimental realization of our proposal is discussed in Section 4.7.

The thriving field of quantum computing triggered not only much research on potential quan-

tum technologies for implementing quantum protocols such as circuit QED but also intense fundamental investigations on the impact of quantum physics on information theory. The quantification and the classification of entanglement are an important part of this endeavour and formed a side project to the work presented in this thesis. The results obtained in this context are presented in Viehmann *et al.* (2011, 2012b).

Chapter 3

Superradiant phase transitions in circuit QED

3.1 Superradiant phase transitions

If, instead of a single two-level atom, N atoms couple resonantly to the electromagnetic field in a cavity, the splitting of the two excited states with a single excitation shared between cavity and atomic ensemble will increase in proportion to $\sqrt{N}$. This follows from the Tavis-Cummings model. Clearly, if the model remains valid, at some large N one of these excited state will no longer be separated by an energy gap from the ground state of the system, and a phase transition occurs.[1] This phase transition, which survives up to some nonzero temperature and is not tied to resonant atom field coupling, was first investigated by Hepp and Lieb (1973) and termed *superradiant phase transition* (SPT) because the occupied states in the new phase possess the potential to superradiate. A mathematically less rigorous but greatly simplified treatment was provided by Wang and Hioe (1973). The SPT persists if atoms and cavity are off-resonant and if the counter-rotating terms are included in the Hamiltonian, which cannot be neglected in this regime of strong coupling (Carmichael *et al.*, 1973). With counter-rotating terms, the Hamiltonian considered by these authors reads (from now on, we set $\hbar = 1$)

$$\mathcal{H}_{\mathrm{D},0} = \omega a^\dagger a + \frac{\Omega}{2}\sum_{j=1}^{N}\sigma_z^j + \frac{\lambda}{\sqrt{N}}\sum_{j=1}^{N}\sigma_x^j(a^\dagger + a), \tag{3.1}$$

which is usually called *Dicke Hamiltonian* in the context of superradiance and superradiant phase transitions. The notation is the same as for the Jaynes-Cummings Hamiltonian (2.25) except for $g \to \lambda/\sqrt{N}$ (see below) and $\omega_c \to \omega$ (to avoid confusion with critical quantities) throughout this chapter. The system is considered in the thermodynamic limit $N, V \to \infty$ with constant particle density N/V, where V is the quantization volume of the electromagnetic field. Therefore, it is convenient to pull out a factor of $1/\sqrt{N}$ from the coupling terms so that the coupling parameter λ (we adopt here the common notation) is a well-behaved function of the particle density N/V.

1. Mathematically, proper thermodynamic limits have to be taken, see below.

Explicitly, $\lambda \propto \Omega|\mathbf{e}\cdot\mathbf{d}|\sqrt{N/V}$. Here, $\mathbf{d} = \langle e|\sum_{i=1}^{n} q_i \mathbf{r}_i|g\rangle$ is the dipole matrix element between the kept two atomic levels $\{|g\rangle, |e\rangle\}$ of the atoms, which are assumed to be identical and to consist of n particles with charge q_i and coordinate $\mathbf{r}_i$, and $\mathbf{e}$ is the polarization vector of the vector potential $\mathbf{A}$. The Dicke Hamiltonian can be derived from Equations (2.26) and (2.27) under the same approximations as the Jaynes-Cummings Hamiltonian, and with the additional assumption that the N atoms are located in an area that is small compared to the wave length of the one considered field mode.

By direct evaluation of the system's partition function, it was shown that for $\lambda > \lambda_{c,0} = \sqrt{\omega\Omega}/2$, there is a critical temperature T_c at which a second-order phase transition occurs. This temperature satisfies

$$\tanh\left[\frac{\Omega}{2k_B T_c}\right] = \frac{\omega\Omega}{4\lambda^2}, \tag{3.2}$$

where k_B is the Boltzmann constant. For $\lambda < \lambda_{c,0}$, the system does not become critical. In the 'normal phase', characterized by $\lambda < \lambda_{c,0}$ or $\lambda > \lambda_{c,0}$ and $T > T_c$, there is no macroscopic population of the boson mode, $\langle a^\dagger a\rangle/N = 0$. In the 'superradiant phase' ($\lambda > \lambda_{c,0}$ and $T < T_c$), the bosonic mode is macroscopically occupied,

$$\frac{\langle a^\dagger a\rangle}{N} = 4\frac{\lambda^2}{\omega^2}x^2 - \frac{\Omega^2}{16\lambda^2}, \tag{3.3}$$

where x solves $2x = \tanh(4\lambda^2 x/(\omega k_B T)) > 0$.

In recent years, there has been much interest in the phase transition of the Dicke model, largely because Emary and Brandes (2003a,b) found exact results for the eigenvalues and eigenstates of the low-energy sector of $\mathcal{H}_{D,0}$ in the limit $N, V \to \infty$. This was achieved by deriving effective Hamiltonians for $\mathcal{H}_{D,0}$ for the cases $\lambda \lesseqgtr \lambda_{c,0}$ in a self-consistent procedure: For weak coupling, it is justified to assume that the low-lying states of the Hamiltonian do not exhibit a macroscopic population of the excited atomic levels, $\langle\sum_j \sigma_z^j\rangle/N = -1$. Thus, the atomic ensemble can be regarded as an effective harmonic oscillator since one can arbitrarily often excite a randomly chosen atom of the ensemble with one and the same quantum of energy without ever finding an atom already being in its excited state. Mathematically, this deliberation can be expressed by applying a *Holstein-Primakoff transformation* (Holstein and Primakoff, 1940) in Equation (3.1),

$$\sum_j \frac{\sigma_j^+}{\sqrt{N}} = b^\dagger\sqrt{1-\frac{b^\dagger b}{N}}, \qquad \sum_j \frac{\sigma_j^-}{\sqrt{N}} = \sqrt{1-\frac{b^\dagger b}{N}}\,b, \qquad \sum_j \frac{\sigma_z^j}{2} = b^\dagger b - \frac{N}{2}, \tag{3.4}$$

where b is bosonic, and dropping all terms with N in the denominator (Emary and Brandes, 2003a,b).[2] Equivalently, one can apply a *Hopfield transformation* (Hopfield, 1958), which we

2. We remark that Equations (3.4) presume that the atomic ensemble is in a state with maximum pseudo angular momentum (Emary and Brandes, 2003a).

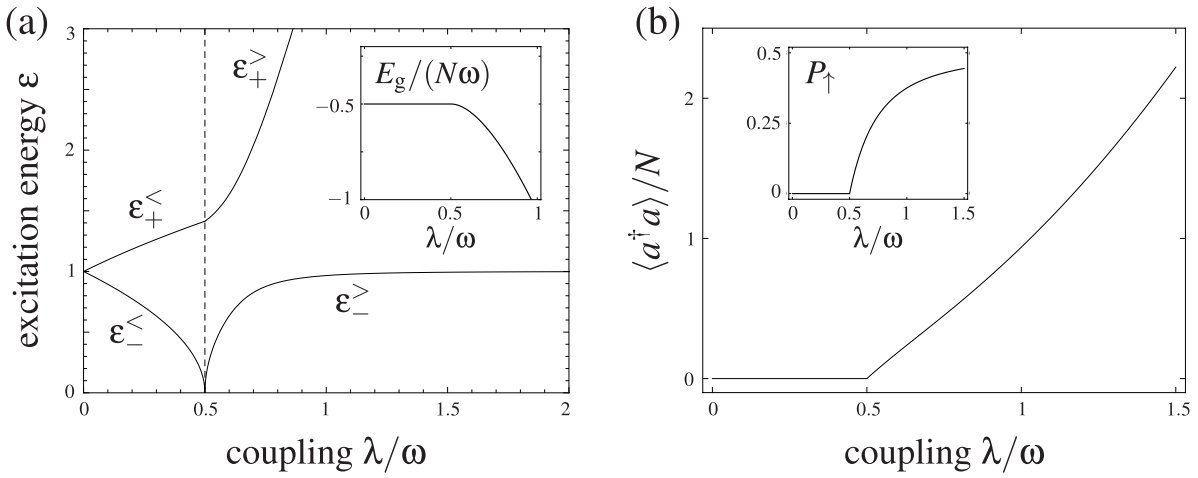

Figure 3.1: Properties of the Dicke Hamiltonian in the thermodynamic limit $N,V \to \infty$. For all plots, resonant atom-field coupling was assumed, $\omega = \Omega$. (a) Excitation energies ε vs. coupling λ. At $\lambda_c = \sqrt{\omega\Omega}/2$, the second-order superradiant phase transition occurs, indicated by the dashed line (only in this panel). The branches $\varepsilon_\pm^{\lessgtr}$ are the eigenmodes of the effective Hamiltonians for the low-energy sectors of the Dicke Hamiltonian in the two phases. The inset shows the scaled ground state energy E_g/N vs. λ, which is nonanalytic at the phase transition. (b) Scaled occupation of the bosonic mode, $\langle a^\dagger a\rangle/N$, vs. coupling λ. Inset, excitation probability $P_\uparrow$ of one specific atom vs. λ.

will make extensive use of (see later). Diagonalization of the resulting Hamiltonian gives the scaled ground state energy $E_g^</N = -\Omega/2$ and the eigenmodes $\varepsilon_\pm^<$,

$$2(\varepsilon_\pm^<)^2 = \omega^2 + \Omega^2 \pm \sqrt{(\omega^2-\Omega^2)^2 + 16\lambda^2\omega\Omega}, \tag{3.5}$$

which fully describe the low-energy spectrum of the Dicke Hamiltonian in the normal phase (Figure 3.1(a)). In particular, one realizes that one eigenmode of the system becomes gapless at $\lambda = \lambda_{c,0}$. At this point, the assumption of dilute atomic excitations breaks down. However, if one assumes instead of dilute atomic excitations that the photon field a and the Holstein-Primakoff field b are macroscopically displaced, one finds a new effective Hamiltonian for the low energy sector of $\mathcal{H}_{D,0}$ valid for $\lambda > \lambda_{c,0}$. Diagonalization yields the scaled ground state energy $E_g^>/N = -\lambda^2/\Omega + \omega\Omega^2/(16\lambda^2)$ and excitation energies

$$2(\varepsilon_\pm^>)^2 = \omega^2 + \Omega^2/\mu^2 \pm \sqrt{(\omega^2-\Omega^2/\mu^2)^2 + 4\omega^2\Omega^2}, \tag{3.6}$$

where $\mu = \omega\Omega/(4\lambda^2)$ (Figure 3.1(a)). In fact, there are two effective Hamiltonians for $\lambda > \lambda_c$, which are identical but result from two different possibilities to displace the fields a and b. This reflects the broken parity symmetry of $\mathcal{H}_{D,0}$ (which couples only states with an even or odd number of excitations, respectively) in the superradiant phase. Note also that the all states are

doubly degenerate for $\lambda > \lambda_{c,0}$, a consequence of the broken symmetry. The probability $P_\uparrow$ of finding an atom in an excited state, $P_\uparrow = \langle \sum_j \sigma_z^j \rangle / (2N) + 1/2$, and the macroscopic occupation of the photon mode, $\langle a^\dagger a \rangle / N$, are given by

$$P_\uparrow = \frac{1}{2} - \frac{\omega\Omega}{8\lambda^2}, \qquad \frac{\langle a^\dagger a \rangle}{N} = \frac{\lambda^2}{\omega^2} - \frac{\Omega^2}{16\lambda^2} \qquad \text{for} \qquad \lambda > \lambda_{c,0}, \tag{3.7}$$

and both are zero for $\lambda < \lambda_{c,0}$ (see Figure 3.1(b)). The RHSs of Equations (3.7) are the squared displacements of the fields b and a divided by N. We remark that the displacements increase $\propto \sqrt{\lambda - \lambda_{c,0}}$ close to the phase transition and can be regarded as order parameters. This approach allowed Emary and Brandes (2003a,b) to study in a very detailed way the zero-temperature phase transition of the Dicke Hamiltonian, which we will also focus on in the following.

3.2 The no-go theorem

Despite the simplicity of the situation described by the Dicke Hamiltonian, the equilibrium SPT is yet to be observed in an experiment. Indeed, for an atomic ensemble coupled to a bosonic mode, the existence of the SPT is questioned by a *no-go theorem* (Rzażewski *et al.*, 1975). The rationale behind the no-go theorem is the following. The Dicke Hamiltonian of Equation (3.1) is derived from minimal coupling of atoms and field (Equations (2.26) and (2.27)) under a number of approximations. In particular, a term $\propto \mathbf{A}^2$ was dropped from the minimal coupling Hamiltonian (2.26). This is a frequent simplification since the $\mathbf{A}^2$ term does not couple to the atomic degrees of freedom and would, in a single-mode approximation, just slightly renormalize the photon energy and the atom-photon coupling. However, for the energy balance of the SPT, this term might play a role. If photon energy and atom-photon coupling are modified, it might be energetically less favorable for the system to build up an electromagnetic field in order to minimize the coupling energy. Thus, for studying SPTs, the $\mathbf{A}^2$ term should be taken into account. This was done by Rzażewski *et al.* (1975). They considered a generalized version of the Dicke Hamiltonian,

$$\mathcal{H}_D = \omega a^\dagger a + \frac{\Omega}{2} \sum_{j=1}^N \sigma_z^j + \frac{\lambda}{\sqrt{N}} \sum_{j=1}^N \sigma_x^j (a^\dagger + a) + \kappa (a^\dagger + a)^2, \tag{3.8}$$

which retains the term

$$N \sum_{i=1}^n \frac{q_i^2 \mathbf{A}^2}{2m_i} \approx \left[N \sum_{i=1}^n \frac{q_i^2 A_0^2}{2m_i} \right] (a^\dagger + a)^2 \equiv \kappa (a^\dagger + a)^2 \tag{3.9}$$

present in the minimal coupling Hamiltonian for N atoms and one field mode. In Equations (3.8) and (3.9), we have employed the usual notation in this context and denoted the prefactor of $(a^\dagger + a)^2$ by κ, which however must not be confused with the cavity decay κ discussed in Chapter 2. Note that the approximation of a spatially invariant field in the region of the atoms, $\mathbf{A} \approx A_0 \mathbf{e}(a^\dagger +$

a), was already made in the derivation of $\mathcal{H}_{\mathrm{D},0}$. Applying the method of Wang and Hioe (1973) to $\mathcal{H}_{\mathrm{D}}$, Rzażewski *et al.* (1975) showed that the system would become critical at

$$\lambda_{\mathrm{c}}^2 = \frac{\omega\Omega}{4}\left(1+\frac{4\kappa}{\omega}\right). \tag{3.10}$$

Crucially, now the required coupling strength for reaching criticality depends on the particle density N/V via $\kappa \propto NA_0^2 \propto N/V$. Thus, increasing the coupling $\lambda \propto \sqrt{N/V}$ by increasing N/V does not help in realizing a SPT. Criticality would imply $\lambda^2 > \kappa\Omega$ where the particle density simply drops out. Even more, by inserting the explicit expressions for λ and κ derived from the full minimal coupling Hamiltonian, Rzażewski *et al.* (1975) noticed that this last inequality would violate the Thomas-Reiche-Kuhn sum rule (Thomas, 1925; Reiche and Thomas, 1925; Kuhn, 1925) (details of the sum rule and its violation will be discussed later). Therefore, a SPT cannot occur. This is known as the no-go theorem for SPTs.

The no-go theorem applies only to systems of mutually noninteracting atoms which couple minimally to the electromagnetic field and for which the approximations (i)-(iii) stated below Equation (2.27) can be made. Other systems, say, of atoms with intrinsic magnetic moment, are not subject to the no-go theorem. However, in atomic systems, a coupling of the order $\lambda \sim \omega$ is very difficult to achieve so that experimental tests of the possibility of SPTs in the relevant parameter regime are so far not available. We remark that the phase transition of the Dicke model was recently observed by Baumann *et al.* (2010) as the spontaneous spatial self-organization of a Bose-Einstein condensate coupled to a cavity and driven by an external pump laser field. Their experiment was related to theoretical work by Dimer *et al.* (2007). It is important note that the realized phase transition was dynamical and does not allow one to draw conclusions about the possibility of equilibrium SPTs.

3.3 What happens in circuit QED?

Circuit QED systems with multiple qubits are usually well described by the Dicke Hamiltonian $\mathcal{H}_{\mathrm{D},0}$. The coupling of the superconducting qubits and the electromagnetic field in circuit QED is several orders of magnitude stronger than the atom-field coupling in experiments with real atoms. Thus, multi-qubit circuit QED systems are potential candidates for entering the regime of SPTs. Assuming a single-qubit coupling strength $g/\omega \sim 0.05$, we can roughly estimate that $N \sim (g/\omega)^{-2} \sim 400$ qubits would need to couple collectively to a bosonic mode for that. Individual control of the qubits would not be essential for studying SPTs so that this number, while certainly challenging, does not seem to be entirely unattainable. Moreover, due to its quadratic dependence on g/ω, the minimum qubit number N would be considerably smaller if a larger ratio g/ω was achieved.

Indeed, SPTs have recently been predicted to be observable in circuit cavity QED systems with fluxoniums (Nataf and Ciuti, 2010a) and Cooper-pair boxes (Nataf and Ciuti, 2010b). For Cooper-pair boxes, this is quite surprising since their interaction with photons is very similar to the electric dipole coupling of atoms. It is of the form $\propto \hat{n}(a^\dagger + a)$, where $\hat{n} = \hat{Q}/(-2e)$ is the number operator (see the discussion around Equation (2.31)). Recalling that the charge

operator $\hat{Q}$ in quantum circuit theory corresponds to the momentum of a mechanical particle, one recognizes the analogy of this coupling and the minimal coupling term $\mathbf{p}\cdot\mathbf{A}$. We remark that $\mathbf{p}\cdot\mathbf{A} \propto [\mathbf{r}, \mathcal{H}_{\text{atom}}]\cdot\mathbf{A}$, which yields $\lambda \propto \Omega|\mathbf{e}\cdot\mathbf{d}|\sqrt{N/V}$ as cited in the previous section. We remark further that also transmons couple to the cavity field $\propto \hat{n}(a^\dagger + a)$, which results generally from capacitive qubit-cavity coupling. The inductive coupling of the fluxoniums and the cavity considered by Nataf and Ciuti (2010a) takes a different form, reminiscent of a spin coupled to a magnetic field.

Thus, one might suspect that circuit QED systems with many Cooper-pair boxes (or transmons) are subject to the no-go theorem. This was explicitly investigated by Nataf and Ciuti (2010b) and claimed not to be the case. Nataf and Ciuti (2010b) started from the standard description of such circuit QED systems as pioneered by Blais *et al.* (2004) and introduced in Section 2.2 of this thesis, and derived a generalized Dicke Hamiltonian $\mathcal{H}_{\text{D}}$ (Equation (3.8)) from it by keeping also all terms $\propto (a^\dagger + a)^2$. Astonishingly, the standard description suggest that the critical coupling λ_{c} (Equation (3.10)) causing a SPT can be reached in circuit QED. We will argue below, however, that this is an artefact of the standard description of circuit QED and due to an underrepresentation of the terms $\propto (a^\dagger + a)^2$ in this theory. Employing a more accurate, microscopic theory of circuit QED, we will show that the no-go theorem applies to circuit QED systems with charge qubits as well.

3.4 Publication: Superradiant phase transitions and the standard description of circuit QED

Our research building on the theory presented in the first parts of this chapter has been previously published as a Letter in the journal *Physical Review Letters* and its accompanying online supplemental material. This section contains a reprint of this publication. We remark that the generalization of the no-go theorem presented in our Letter implicitly assumes that a potential SPT would be of second order, which is the kind of transition predicted by Nataf and Ciuti (2010b). Our reasoning in the spirit of Emary and Brandes (2003a,b) relies on a perturbative stability analysis of the ground state and is therefore not capable of precluding novel types of first-order phase transitions that might exist in the system, which has been pointed out by Ciuti and Nataf (2012) and Baksic *et al.* (2013) (see also Viehmann *et al.* (2012a)).

PRL 107, 113602 (2011) PHYSICAL REVIEW LETTERS week ending 9 SEPTEMBER 2011

Superradiant Phase Transitions and the Standard Description of Circuit QED

Oliver Viehmann,[1] Jan von Delft,[1] and Florian Marquardt[2]

[1]*Physics Department, Arnold Sommerfeld Center for Theoretical Physics, and Center for NanoScience, Ludwig-Maximilians-Universität, Theresienstraße 37, 80333 München, Germany*

[2]*Institut for Theoretical Physics, Universität Erlangen-Nürnberg, Staudtstraße 7, 91058 Erlangen, Germany*

(Received 29 March 2011; published 8 September 2011)

We investigate the equilibrium behavior of a superconducting circuit QED system containing a large number of artificial atoms. It is shown that the currently accepted standard description of circuit QED via an effective model fails in an important aspect: it predicts the possibility of a superradiant phase transition, even though a full microscopic treatment reveals that a no-go theorem for such phase transitions known from cavity QED applies to circuit QED systems as well. We generalize the no-go theorem to the case of (artificial) atoms with many energy levels and thus make it more applicable for realistic cavity or circuit QED systems.

DOI: 10.1103/PhysRevLett.107.113602 PACS numbers: 42.50.Pq, 03.67.Lx, 64.70.Tg, 85.25.−j

Recent years have seen rapid progress in fabrication and experimental control of superconducting circuit QED systems, in which a steadily increasing number of artificial atoms interact with microwaves [1–4]. These developments set the stage to study collective phenomena in circuit QED. An interesting question in that context is whether a system with many artificial atoms undergoes an equilibrium phase transition as the coupling of artificial atoms and electromagnetic field is increased (at zero temperature). Phase transitions of this type have been intensely discussed for cavity QED systems [5–10] and are known as superradiant phase transitions (SPTs) [6]. However, in cavity QED systems with electric dipole coupling their existence is doubted due to a no-go theorem [8]. Recently, it has been claimed that SPTs are possible in the closely related circuit QED systems with capacitive coupling [10–12]. This would imply that the no-go theorem of cavity QED does not apply and challenges the well-established analogy of circuit and cavity QED.

Here, we show in a full microscopic analysis that circuit QED systems are also subject to the no-go theorem. We argue that such an analysis is necessary since the standard description of circuit QED systems by an effective model (EM) is deficient in the regime considered here. A toy model is used to illustrate this failure of an EM. Finally, we close a possible loophole of the no-go theorem by generalizing it from two-level to multilevel (artificial) atoms. Thus, our work restores the analogy of circuit and cavity QED and rules out SPTs in these systems under realistic conditions that have not been covered before.

Dicke Hamiltonian in cavity and circuit QED.—Both circuit QED systems and cavity QED systems with N (artificial) atoms (Fig. 1) are often described by the Dicke Hamiltonian [13] ($\hbar = 1$)

$$\mathcal{H}_{\mathrm{D}} = \omega a^\dagger a + \frac{\Omega}{2}\sum_{k=1}^{N}\sigma_z^k + \frac{\lambda}{\sqrt{N}}\sum_{k=1}^{N}\sigma_x^k(a^\dagger + a) + \kappa(a^\dagger + a)^2. \quad (1)$$

The (artificial) atoms are treated as two-level systems with energy splitting Ω between ground state $|g\rangle_k = \binom{0}{1}_k$ and excited state $|e\rangle_k = \binom{1}{0}_k$ (σ_x^k, σ_z^k are Pauli matrices). In the case of circuit QED, we assume Cooper-pair boxes as artificial atoms, which justifies the two-level approximation. Our main results, though, hold for any charge-based artificial atoms (capacitive coupling) [14]. Further, $a^\dagger$ generates a photon of energy ω. Matter and field couple with a strength λ. The κ term, often neglected in other contexts, will become crucial below. In cavity QED, $\mathcal{H}_{\mathrm{D}}$ derives from minimal coupling of atoms and electromagnetic field. For an atom (n electrons) at a fixed position,

$$\mathcal{H}^0_{\mathrm{cav}} = \sum_{i=1}^{n}\frac{[\mathbf{p}_i - e\mathbf{A}(\mathbf{r}_i)]^2}{2m} + V_{\mathrm{int}}(\mathbf{r}_1, \ldots, \mathbf{r}_n). \quad (2)$$

The $\mathbf{pA}$ and $\mathbf{A}^2$ terms in the analog N-atom Hamiltonian yield the λ and κ term in $\mathcal{H}_{\mathrm{D}}$, respectively. In circuit QED, $\mathcal{H}_{\mathrm{D}}$ arises from a widely used EM for a charge-based artificial atom in a transmission line resonator [15],

$$\mathcal{H}^0_{\mathrm{cir}} = 4E_C\sum_\nu(\nu - \bar{\nu})^2|\nu\rangle\langle\nu| - \frac{E_J}{2}\sum_\nu(|\nu+1\rangle\langle\nu| + \mathrm{H.c.}).$$

Here, ν counts the excess Cooper pairs on the island, E_J and $E_C = e^2/[2(C_G + C_J)]$ are the Josephson energy and

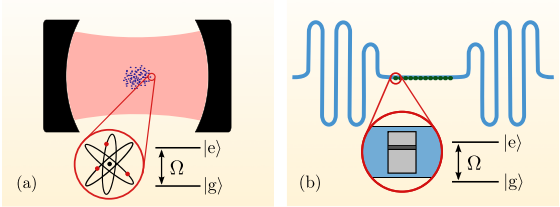

FIG. 1 (color online). Cavity QED system with N atoms (a) and circuit QED system with N Cooper-pair boxes as artificial atoms (b).

PRL 107, 113602 (2011) PHYSICAL REVIEW LETTERS week ending 9 SEPTEMBER 2011

the charging energy of the Cooper-pair box, and C_G and C_J are the coupling capacitance and the capacitance of the Josephson junction. Moreover, $\bar{\nu} = C_G(V_G + \mathcal{V})/2e$, V_G is an external gate voltage and $\mathcal{V}$ the quantum voltage due to the electromagnetic field in the resonator. The Cooper-pair box is assumed to be at its degeneracy point [15]. As it is described by macroscopic quantities (like E_C) and only 1 degree of freedom (ν), $\mathcal{H}_0^{\rm cir}$ is an EM for a Cooper-pair box in a transmission line. Starting either from $\mathcal{H}_{\rm cav}^0$ or $\mathcal{H}_{\rm cir}^0$, one obtains $\mathcal{H}_{\rm D}$ using the following approximations: The N (artificial) atoms are identical, noninteracting two-level systems with ground and excited states $|g\rangle$ and $|e\rangle$ which are strongly localized compared to the wavelength of the single considered field mode [i.e., $\mathbf{A}(\mathbf{r}_i^k) \approx \mathbf{A} \equiv A_0\boldsymbol{\epsilon}(a^\dagger + a)$, where $|\boldsymbol{\epsilon}| = 1$, and $\mathcal{V}(\mathbf{r}^k) \approx \mathcal{V} \equiv V_0(a^\dagger + a)$].

Superradiant phase transitions and no-go theorem.—In the limit $N \to \infty$, $\mathcal{H}_{\rm D}$ undergoes a second order phase transition at a critical coupling strength [6–8]

$$\lambda_c^2 = \frac{\omega\Omega}{4}\left(1 + \frac{4\kappa}{\omega}\right). \tag{3}$$

This phase transition was discovered for $\mathcal{H}_{\rm D}$ with $\kappa = 0$ and termed SPT [6]; see [9] for recent studies. At λ_c, the atoms polarize spontaneously, $\langle\sum_k \sigma_z^k\rangle/N \neq -1$, and a macroscopic photon occupation arises, $\langle a^\dagger a\rangle/N \neq 0$. A gapless excitation signals the critical point [Fig. 2(a)].

In cavity QED systems, however, λ_c cannot be reached if the κ term is not neglected [8]. That is because λ and κ are not independent of each other. Let us define a parameter α via $\kappa = \alpha\lambda^2/\Omega$. Then Eq. (3) becomes $\lambda_c^2(1-\alpha) = \omega\Omega/4$, and criticality requires $\alpha < 1$. With $A_0 = 1/\sqrt{2\epsilon_0\omega V}$ (V is the volume of the cavity) one finds

$$\lambda_{\rm cav} = \frac{\Omega|\boldsymbol{\epsilon}\cdot\mathbf{d}|}{\sqrt{2\epsilon_0\omega}}\sqrt{\frac{N}{V}}, \qquad \kappa_{\rm cav} = \frac{n}{2\epsilon_0\omega}\frac{e^2}{2m}\frac{N}{V}, \tag{4}$$

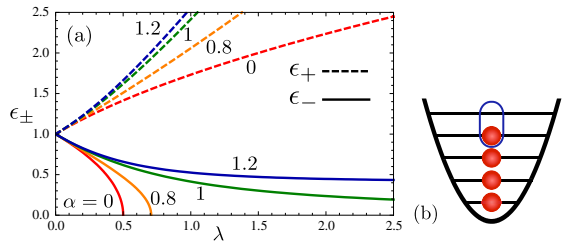

FIG. 2 (color online). (a) Excitation energies ϵ_+ and ϵ_- of the Dicke Hamiltonian $\mathcal{H}_{\rm D}$ versus coupling λ (in units of $\omega = \Omega$), for $\alpha = \kappa\Omega/\lambda^2 = 0, 0.8, 1, 1.2$. For $\alpha = 0$, ϵ_- vanishes at $\lambda = 0.5$, thus signaling a SPT. Only $\alpha \geq 1$ is compatible with the TRK sum rule. For these α, $\epsilon_- \to \sqrt{1 - 1/\alpha}$ and remains finite for all λ. The excitations $\epsilon_\pm(\lambda)$ of $\mathcal{H}_{\rm tm}$ correspond to $\alpha = 1$. (b) Toy model of an (artificial) atom. The oval line indicates the degree of freedom in the simplified effective model.

where $\mathbf{d} = \langle g|e\sum_{i=1}^n \mathbf{r}_i|e\rangle$ and $\alpha_{\rm cav}\Omega|\boldsymbol{\epsilon}\cdot\mathbf{d}|^2 = ne^2/2m$. But the Thomas-Reiche-Kuhn sum rule (TRK) ([16], Sec. A)

$$\sum_l (E_l - E_g)|\boldsymbol{\epsilon}\cdot\langle g|e\sum_{i=1}^n \mathbf{r}_i|l\rangle|^2 = n\frac{e^2}{2m} \tag{5}$$

for the Hamiltonian $H^0 = \sum_{i=1}^n \mathbf{p}_i^2/2m + V_{\rm int}(\mathbf{r}_1, \ldots, \mathbf{r}_n)$ of an uncoupled atom with spectrum $\{E_l, |l\rangle\}$ implies $\Omega|\boldsymbol{\epsilon}\cdot\mathbf{d}|^2 \leq ne^2/2m$, consequently $\alpha_{\rm cav} \geq 1$. This is known as the no-go theorem for SPTs [8,10]. Notice that $\alpha_{\rm cav}$ determines how strongly $\Omega|\boldsymbol{\epsilon}\cdot\mathbf{d}|^2$ exhausts the TRK. We remark that a direct dipole-dipole coupling between atoms (omitted here) can lead to a ferroelectric phase transition, which, however, occurs only at very high atomic densities [17].

Surprisingly, the no-go theorem was recently argued not to apply in circuit QED [10]. Indeed, the standard EM of circuit QED yields

$$\lambda_{\rm cir} = \frac{eC_G}{C_G + C_J}\sqrt{\frac{\omega N}{Lc}}, \qquad \kappa_{\rm cir} = \frac{C_G^2}{2(C_G + C_J)}\frac{\omega N}{Lc}, \tag{6}$$

where L denotes the length of the transmission line resonator, c its capacitance per unit length, and we have used $V_0 = (\omega/Lc)^{1/2}$ [15]. Here $\alpha_{\rm cir} = E_J/4E_C < 1$ is easily possible [1]. According to this argument, a SPT should be observable in a circuit QED system.

Effective models and superradiant phase transitions.—The EM has proved to be a very successful description of circuit QED whose predictions have been confirmed in numerous experiments. However, the circuit QED setups operated so far contained only few artificial atoms. It is not obvious that an EM also provides a good description of circuit QED systems with $N \gg 1$ atoms and, thus, a proper starting point to study SPTs in circuit QED. We now present a toy model illustrating how an EM similar to the one in circuit QED can erroneously predict a SPT.

The toy model consists of N harmonic oscillator potentials with frequency Ω, each trapping n noninteracting fermions of mass m and charge e, which all couple to a bosonic mode with frequency ω [Fig. 2(b)].

This toy model can be viewed as a very simplified description of (artificial) atoms with n microscopic constituents inside a resonator. It is governed by the Hamiltonian

$$\mathcal{H}_{\rm tm} = \omega a^\dagger a + \sum_{k=1}^N\sum_{i=1}^n \frac{(p_i^k - eA)^2}{2m} + \frac{m\Omega^2(x_i^k)^2}{2}, \tag{7}$$

where we assume again $A(x_i^k) \approx A = A_0(a^\dagger + a)$. Since A couples only to the center of mass coordinate of the kth oscillator, $\mathcal{H}_{\rm tm}$ can be diagonalized ([16], Sec. B):

$$\mathcal{H}_{\rm tm} = \epsilon_{\pm}\left(a_{\pm}^{\dagger}a_{\pm} + \frac{1}{2}\right) + \sum_{i=1}^{nN-1}\Omega\left(b_i^{\dagger}b_i + \frac{1}{2}\right),$$

$$2\epsilon_{\pm}^2(\lambda) = \omega^2 + 4\kappa\omega + \Omega^2 \pm \sqrt{(\omega^2 + 4\kappa\omega - \Omega^2)^2 + 16\lambda^2\omega\Omega}. \quad (8)$$

Here, $a_{\pm}^{\dagger}$ generate excitations that mix photon field with collective center of mass motion, the $b_i^{\dagger}$ excite the remaining degrees of freedom, $\lambda = A_0\Omega d\sqrt{N}$ and $\kappa = \lambda^2/\Omega$. As $d = \langle n|ex|n-1\rangle = e\sqrt{n/2m\Omega}$, the TRK is exhausted. Note that $\epsilon_{\pm}(\lambda)$ are also the relevant excitation energies of $\mathcal{H}_{\rm D}$ for $N \to \infty$, as can be shown using methods of Ref. [9] ([16], Sec. B), and demanding $\epsilon_{-} = 0$ yields Eq. (3). One sees that $\epsilon_{\pm}(\lambda)$ is real and nonzero for all λ and that the ground state energy is an analytic function of λ [Fig. 2(a)]. Hence, no phase transition is possible.

Let us now consider an EM for the toy model. Similar to the standard EM of circuit QED, we focus on the fermion with the highest energy in the kth harmonic oscillator and treat it as a two-level system with $|g_k\rangle = |n-1\rangle_k$ and $|e_k\rangle = |n\rangle_k$ [Fig. 2(b)]. Accounting only for one fermion per "atom," that is, expanding $\mathcal{H}_{\rm tm}^{\rm EM} = \omega a^{\dagger}a + \sum_{k=1}^{N}(p^k - eA)^2/2m + m\Omega^2(x^k)^2/2$ in the basis $\{|n-1\rangle_k, |n\rangle_k\}$, yields a Dicke Hamiltonian with $\lambda_{\rm EM} = \lambda$ and $\kappa_{\rm EM} = \kappa/n = Ne^2A_0^2/2m$. Crucially, only $\lambda_{\rm EM}$ depends on n. This allows $\lambda_{\rm EM}$ to be increased at constant $\kappa_{\rm EM}$; therefore, $\alpha_{\rm EM} = 1/n$ can be <1 and a SPT is possible. This failure of the EM can be interpreted as follows. The relation $\lambda = \lambda_{\rm EM} \propto d \propto \sqrt{n}$ reveals that the coupling of an "atom" to the bosonic mode is fully captured by the EM and grows with atom size n. However, in a proper description of the system, increasing the coupling by increasing n unavoidably also increases κ in proportion to n: all fermions of all atoms couple to the bosonic mode and each causes an A^2 term. This is lost in the EM with only 1 degree of freedom per atom. Interestingly, $\alpha_{\rm EM} < 1$ only if $n > 1$, i.e., as long as the effective description actually neglects degrees of freedom.

Microscopic description of circuit QED.—This example suggests not to rely on the standard description for investigating SPTs in circuit QED. Although the dipole coupling of field and qubit states might be fully represented by $\lambda_{\rm cir}$, $\kappa_{\rm cir}$ could still underestimate the A^2 terms of all charged particles in the Cooper-pair boxes. Instead, let us describe a circuit QED system with N artificial atoms by a minimal-coupling Hamiltonian that accounts for all microscopic degrees of freedom:

$$\mathcal{H}_{\rm mic} = \omega a^{\dagger}a + \sum_{k=1}^{N}\sum_{i=1}^{n_k}\frac{(\mathbf{p}_i^k - q_i^k\mathbf{A})^2}{2m_i^k} + V_{\rm int}(\mathbf{r}_1^k, \ldots, \mathbf{r}_{n_k}^k).$$

As we allow arbitrary charges q_i^k and masses m_i^k and an arbitrary interaction potential $V_{\rm int}$ of the n_k constituents of the kth artificial atom, $\mathcal{H}_{\rm mic}$ most generally captures the coupling of N arbitrary (but mutually noninteracting) objects to the electromagnetic field. We subject it to the same approximations that led from $\mathcal{H}_{\rm cir}^0$, the EM of circuit QED, to $\mathcal{H}_{\rm D}$. For identical artificial atoms $\{n_k, q_i^k, m_i^k\} \to \{n, q_i, m_i\}$. The Hamiltonian of an uncoupled artificial atom then reads $H_{\rm mic}^0 = \sum_{i=1}^{n}\mathbf{p}_i^2/2m_i + V_{\rm int}(\mathbf{r}_1, \ldots, \mathbf{r}_n)$. Its qubit states $|g\rangle$ and $|e\rangle$, which in the standard EM are superpositions of the charge states $|\nu\rangle$, are among the eigenstates $\{|l\rangle\}$ of $H_{\rm mic}^0$. Expanding $\mathcal{H}_{\rm mic}$ in the $\{|g\rangle_k, |e\rangle_k\}$ basis and taking $\mathbf{A}(\mathbf{r}_i^k) \approx \mathbf{A}$ gives the Dicke Hamiltonian $\mathcal{H}_{\rm D}$ with parameters generalizing those of cavity QED [Eq. (4)],

$$\lambda_{\rm cir}^{\rm mic} = \frac{\Omega|\boldsymbol{\epsilon}\cdot\mathbf{d}|}{\sqrt{2\epsilon_0\omega}}\sqrt{\frac{N}{V}}, \qquad \kappa_{\rm cir}^{\rm mic} = \frac{1}{2\epsilon_0\omega}\left(\sum_{i=1}^{n}\frac{q_i^2}{2m_i}\right)\frac{N}{V}, \quad (9)$$

where $\mathbf{d} = \langle g|\sum_{i=1}^{n} q_i\mathbf{r}_i|e\rangle$. This microscopic description of circuit QED facilitates the same line of argument which in Ref. [8] allowed the conclusion that there is no SPT in cavity QED: Criticality [Eq. (3)] requires $\Omega|\boldsymbol{\epsilon}\cdot\mathbf{d}|^2 > \sum_{i=1}^{n} q_i^2/2m_i$, which is ruled out by TRK for $H_{\rm mic}^0$,

$$\sum_l (E_l - E_g)|\boldsymbol{\epsilon}\cdot\langle g|\sum_{i=1}^{n} q_i\mathbf{r}_i|l\rangle|^2 = \sum_{i=1}^{n}\frac{q_i^2}{2m_i}. \quad (10)$$

Hence, the no-go theorem of cavity QED applies to circuit QED as well. This result confirms the analogy of cavity and circuit QED also with respect to SPTs. It has been obtained under the same approximations that led from the standard description of circuit QED, $\mathcal{H}_{\rm cir}^0$, to $\mathcal{H}_{\rm D}$ with $\lambda_{\rm cir}$ and $\kappa_{\rm cir}$. The discrepancy of the predictions of the microscopic and the standard description of circuit QED thus shows the limitations of the validity of the latter. This might be important for future circuit QED architectures with many artificial atoms in general, even for applications not related to SPTs. We emphasize, though, that our conclusion neither forbids SPTs in circuit QED systems with inductively coupling flux qubits [18] nor is it at odds with the great success of the standard description for few-atom systems: there, the deficiency of $\kappa_{\rm cir}$ does not manifest itself qualitatively as the κ term in $\mathcal{H}_{\rm D}$ mimics slightly renormalized system parameters $\tilde{\omega}$ and $\tilde{\lambda}$.

Possible loophole in the no-go theorem.—Although the two-level approximation for the anharmonic spectrum of (artificial) atoms is well justified in many cases, one might argue that higher levels should be taken into account in this context. Indeed, a SPT does not require $\Omega \approx \omega$, and thereby does not single out a particular atomic transition.

For a more profound reason for dropping the two-level assumption, consider the elementary question of how the presence of N mutually noninteracting atoms shifts a resonator's frequency ω. This situation is described by $\mathcal{H}_{\rm mic}$. It can be rewritten as $\mathcal{H}_{\rm mic} = \omega a^{\dagger}a + \sum_{k=1}^{N}(H_{\rm mic}^k + \mathcal{H}_{pA}^k + \mathcal{H}_{A^2}^k)$, where $\mathcal{H}_{pA}^k$ and $\mathcal{H}_{A^2}^k$ are the $\mathbf{pA}$ and $\mathbf{A}^2$ terms due to the kth atom ([16], Sec. C). Let us perturbatively calculate the frequency shift $\delta\omega = \delta\omega_{pA} + \delta\omega_{A^2}$ caused by $\sum \mathcal{H}_{pA}^k$ and $\sum \mathcal{H}_{A^2}^k$ ([16], Sec. C). To this end,

PRL 107, 113602 (2011) PHYSICAL REVIEW LETTERS week ending 9 SEPTEMBER 2011

take $\omega \ll \Omega_m^k$ for all m, k, where Ω_m^k is the mth excitation energy of $H_{\rm mic}^k$. Remarkably, it turns out ([16], Sec. C) that $\delta\omega_{pA}$ (<0) and $\delta\omega_{A^2}$ (>0) cancel almost exactly due to the TRK. The total frequency shift is small, $\delta\omega \sim (\omega/\Omega_m^k)^2$. As a SPT equates to $\delta\omega = -\omega$, the significance of both $\mathbf{pA}$ and $\mathbf{A}^2$ terms for its existence becomes clear. The $\mathbf{pA}$ terms cause a strong negative shift and favor a SPT, the $\mathbf{A}^2$ terms do the opposite. This means, most crucially, that one must not unequally truncate $\mathbf{pA}$ and $\mathbf{A}^2$ terms for assessing the possibility of a SPT by an approximate Hamiltonian. Dropping the $\mathbf{A}^2$ terms in $\mathcal{H}_{\rm D}$ ($\kappa = 0$) leads to the prediction of a SPT. In contrast, $\mathcal{H}_{\rm D}$ with $\kappa \neq 0$ fully incorporates the $\mathbf{A}^2$ terms of $\mathcal{H}_{\rm mic}$. But, due to the two-level approximation, it has only one matrix element of the $\mathbf{pA}$ terms per atom, thereby possibly underestimating the tendency towards a SPT. To exclude SPTs in cavity and circuit QED, a generalization of the no-go theorem to (artificial) atoms with more than two energy levels is necessary.

Generalized no-go theorem.—Let us consider $N \to \infty$ identical atoms coupled to a field mode with frequency ω. The atomic Hamiltonians $H_{\rm mic}^k$ may have an arbitrary spectrum $\{\Omega_l, |l_k\rangle = |l\rangle_k\}$, with $\Omega_0 = 0$ and μ excited states (Fig. 3).

With $d_{l,l'} = \boldsymbol{\epsilon} \cdot \langle l| \sum_{i=1}^n q_i \mathbf{r}_i |l'\rangle$, the full Hamiltonian of the system reads

$$\mathcal{H}_{\rm mic} = \omega a^\dagger a + \kappa(a^\dagger + a)^2 + \sum_{k=1}^{N} \sum_{l,l'=0}^{\mu} (\Omega_l \delta_{l,l'} |l_k\rangle\langle l_k| + iA_0(\Omega_{l'} - \Omega_l) d_{l,l'} (a^\dagger + a) |l_k\rangle\langle l'_k|). \quad (11)$$

We now follow a strategy similar to that of Refs. [9]: We derive a generalized Dicke Hamiltonian $\mathcal{H}_{\rm GD}$ having the same low-energy spectrum as $\mathcal{H}_{\rm mic}$ for a small density of atoms, $N/V \simeq 0$, using $A_0 \propto V^{-1/2}$ as small parameter. We then check whether $\mathcal{H}_{\rm GD}$ has a gapless excitation if the density is increased, which would signal a SPT and mark the breakdown of the analogy of $\mathcal{H}_{\rm GD}$ and $\mathcal{H}_{\rm mic}$.

Expanding the eigenstates and eigenenergies of $\mathcal{H}_{\rm mic}$ as $|\mathcal{E}\rangle \propto \sum_{s=0}^{\infty} A_0^s |\mathcal{E}_s\rangle$ and $\mathcal{E} \propto \sum_{ss'} A_0^{s+s'} \langle \mathcal{E}_s | \mathcal{H}_{\rm mic} | \mathcal{E}_{s'} \rangle$, we note that contributions from all $d_{l\neq 0, l'\neq 0}$ terms may be neglected: they are smaller than those retained by a factor of at least one power of A_0 (for $s + s' > 1$) or $\xi/N \ll 1$ (for $s + s' \leq 1$), where $\xi = \sum_k \sum_{l>0} |\langle l_k | \mathcal{E}_0 \rangle|^2$ is the number of atomic excitations in $|\mathcal{E}_0\rangle$, which is $\ll N$ for low-lying eigenstates ([16], Sec. D). We thus define $\mathcal{H}_{\rm GD}$ by setting $d_{l\neq 0, l'\neq 0} \to 0$ in $\mathcal{H}_{\rm mic}$. Up to a constant, we find ([16], Sec. D)

$$\mathcal{H}_{\rm GD} = \tilde{\omega} a^\dagger a + \sum_{l=1}^{\mu} \Omega_l b_l^\dagger b_l + \sum_{l=1}^{\mu} \tilde{\lambda}_l (b_l^\dagger + b_l)(a^\dagger + a), \quad (12)$$

by introducing $b_l^\dagger = \frac{1}{\sqrt{N}} \sum_{k=1}^N |l_k\rangle\langle 0_k|$ as collective excitation, omitting the energy of the "dark" collective excitations ([16], Sec. D), and removing the κ term by a Bogolyubov transformation yielding $\omega \to \tilde{\omega} = \sqrt{\omega^2 + 4\kappa\omega}$ and $\lambda_l \to \tilde{\lambda}_l = \sqrt{\frac{\omega}{\tilde{\omega}}}\lambda_l$, with $\lambda_l = A_0 \Omega_l |d_{0,l}| \sqrt{N}$. For dilute excitations, the b_l are bosonic, $[b_l, b_{l'}^\dagger] = \delta_{l,l'}$ [19]. The system undergoes a SPT if an eigenfrequency ϵ_i of $\mathcal{H}_{\rm GD}$ can be pushed to zero by increasing the couplings λ_l. We cannot calculate the ϵ_i's explicitly, but we will show that the assumption $\epsilon_i = 0$ contradicts the TRK. An ϵ_i solves the characteristic equation ([16], Sec. D)

$$\left(\prod_{l'=1}^{\mu} (\Omega_{l'}^2 - \epsilon^2)\right)\left((\tilde{\omega}^2 - \epsilon^2) - 4\tilde{\omega} \sum_{l=1}^{\mu} \frac{\Omega_l \tilde{\lambda}_l^2}{\Omega_l^2 - \epsilon^2}\right) = 0. \quad (13)$$

If ϵ_i were zero, this would imply

$$\frac{\omega}{4NA_0^2} = \sum_{l=1}^{\mu} \Omega_l |d_{0l}|^2 - \sum_{i=1}^{n} \frac{q_i^2}{2m_i} \quad (14)$$

and contradict the TRK for $H_{\rm mic}^0$ [Eq. (10)], which ensures that the right-hand side is negative even if the entire atomic spectrum is incorporated. This result is irrespective of the details of the atomic spectra. Note that for $\kappa = 0$, the negative term on the right-hand side of Eq. (14) vanishes, and one recovers the SPT for critical couplings λ_{lc} with $\sum_{l=1}^{\mu} \lambda_{lc}^2/\Omega_l = \omega/4$. This resembles Eq. (3) with $\kappa = 0$.

Experimental evidence for our conclusions could be gained by probing the shifted resonator frequency of a suitable circuit QED system. Consider a sample containing N artificial atoms with $\lambda/\sqrt{N} = 2\pi \times 120$ MHz and $\Omega/2\pi = \omega/2\pi = 3$ GHz. If $\alpha_{\rm cir} = E_J/4E_C = 0.1$, as predicted by the standard theory, there should be signatures of criticality for $N = 174$ [according to Eq. (3)], and the resonator frequency should be close to zero. But even if we assume $\alpha = 1$, the minimal value compatible with the TRK (that corresponds to ideal two-level atoms), we find the lowest excitation ϵ_- to be still at $\epsilon_- \approx 2\pi \times 2$ GHz. We have verified that these phenomena are insensitive to small fluctuations of the atomic parameters ([16], Sec. E; see also [18]) and hence experimentally observable.

We thank S. M. Girvin, A. Wallraff, J. Fink, A. Blais, J. Siewert, D. Esteve, J. Keeling, P. Nataf, and C. Ciuti for discussions. Support by NIM, the Emmy-Noether program, and the SFB 631 of the DFG is gratefully acknowledged.

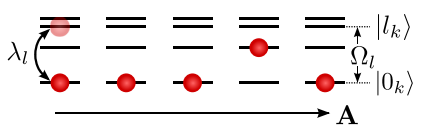

FIG. 3 (color online). Situation of the generalized no-go theorem. Many multilevel (artificial) atoms couple to the photon field. Transitions between excited atomic states are irrelevant for the low-energy spectrum of the system.

[1] A. Wallraff *et al.*, Nature (London) **431**, 162 (2004).
[2] J. M. Fink *et al.*, Phys. Rev. Lett. **103**, 083601 (2009).
[3] M. Neeley *et al.*, Nature (London) **467**, 570 (2010).
[4] L. DiCarlo *et al.*, Nature (London) **467**, 574 (2010).
[5] J. M. Raimond, M. Brune, and S. Haroche, Rev. Mod. Phys. **73**, 565 (2001).
[6] K. Hepp and E. H. Lieb, Ann. Phys. (N.Y.) **76**, 360 (1973).
[7] Y. K. Wang and F. T. Hioe, Phys. Rev. A **7**, 831 (1973).
[8] K. Rzążewski, K. Wódkiewicz, and W. Żakowicz, Phys. Rev. Lett. **35**, 432 (1975).
[9] C. Emary and T. Brandes, Phys. Rev. Lett. **90**, 044101 (2003); C. Emary and T. Brandes, Phys. Rev. E **67**, 066203 (2003).
[10] P. Nataf and C. Ciuti, Nature Commun. 1 (2010) 72.
[11] G. Chen, Z. Chen, and J. Liang, Phys. Rev. A **76**, 055803 (2007).
[12] N. Lambert *et al.*, Phys. Rev. B **80**, 165308 (2009).
[13] R. H. Dicke, Phys. Rev. **93**, 99 (1954).
[14] J. Clarke and F. Wilhelm, Nature (London) **453**, 1031 (2008).
[15] A. Blais *et al.*, Phys. Rev. A **69**, 062320 (2004).
[16] See Supplemental Material at http://link.aps.org/supplemental/10.1103/PhysRevLett.107.113602 for further explanation and details of the calculations.
[17] J. Keeling, J. Phys. Condens. Matter **19**, 295213 (2007).
[18] P. Nataf and C. Ciuti, Phys. Rev. Lett. **104**, 023601 (2010).
[19] J. J. Hopfield, Phys. Rev. **112**, 1555 (1958).

EPAPS: Supplementary Information for "Superradiant Phase Transitions and the Standard Description of Circuit QED"

Oliver Viehmann[1], Jan von Delft[1], and Florian Marquardt[2]

[1] *Physics Department, Arnold Sommerfeld Center for Theoretical Physics, and Center for NanoScience, Ludwig-Maximilians-Universität, Theresienstrasse 37, 80333 Munich, Germany*
[2] *Institut for Theoretical Physics, Universität Erlangen-Nürnberg, Staudtstraße 7, 91058 Erlangen, Germany*

We provide intermediate steps for the derivation of some important statements and equations of the main text (Secs. A-D). Furthermore, we discuss the influence of disorder in the parameters of artificial atoms on a possible experimental verification of our results (Sec. E). For clarity, formulas contained in the main text are typeset in blue.

A. Thomas-Reiche-Kuhn sum rule. We derive the TRK [1] for the Hamiltonian

$$H^0_{\rm mic} = \sum_{i=1}^{n} \frac{\mathbf{p}_i^2}{2m_i} + V_{\rm int}(\mathbf{r}_1, \ldots, \mathbf{r}_n), \tag{S1}$$

yielding Eq. (9) of the main text; Eq. (4) follows as a special case. The derivation of the TRK is based upon the identities

$$\sum_{i=1}^{n} \frac{q_i^2}{2m_i} = -i\Big[\boldsymbol{\epsilon}\cdot\sum_{i=1}^{n} q_i\mathbf{r}_i\,, \boldsymbol{\epsilon}\cdot\sum_{i'=1}^{n}\frac{q_{i'}\mathbf{p}_{i'}}{2m_{i'}}\Big], \qquad \sum_{i=1}^{n}\frac{q_i\mathbf{p}_i}{m_i} = i\Big[H^0_{\rm mic}, \sum_{i=1}^{n} q_i\mathbf{r}_i\Big], \tag{S2}$$

for a real unit vector $\boldsymbol{\epsilon}$. We denote the eigenspectrum of $H^0_{\rm mic}$ by $\{E_l, |l\rangle\}$. It comprises a ground state $|{\rm g}\rangle$ of energy $E_{\rm g}$. The TRK follows by combining the commutators of Eqs. (S2):

$$\sum_{i=1}^{n}\frac{q_i^2}{2m_i} = \langle{\rm g}|\Big[\boldsymbol{\epsilon}\cdot\sum_{i=1}^{n} q_i\mathbf{r}_i\,, \frac{\boldsymbol{\epsilon}}{2}\cdot\Big[H^0_{\rm mic}, \sum_{i'=1}^{n} q_{i'}\mathbf{r}_{i'}\Big]\Big]|{\rm g}\rangle \tag{S3a}$$

$$= \sum_l (E_l - E_{\rm g})|\boldsymbol{\epsilon}\cdot\langle{\rm g}|\sum_{i=1}^{n} q_i\mathbf{r}_i|l\rangle|^2. \tag{S3b}$$

B. Diagonalization of $\mathcal{H}_{\rm D}$ and $\mathcal{H}_{\rm tm}$. It is demonstrated that the diagonalization of both the Dicke Hamiltonian $\mathcal{H}_{\rm D}$ for $N \to \infty$ and the Hamiltonian $\mathcal{H}_{\rm tm}$ describing the toy model can be reduced to the diagonalization of special cases of $\mathcal{H}_{\rm gD}$, which appears in the context of the generalized no-go theorem. The characteristic equation of $\mathcal{H}_{\rm gD}$, which will be derived in Sec. D of these supplementary notes, is solvable for the special cases and yields the diagonal forms of $\mathcal{H}_{\rm D}$ and $\mathcal{H}_{\rm tm}$.

Diagonalization of $\mathcal{H}_{\rm D}$. First, we focus on the Dicke Hamiltonian

$$\mathcal{H}_{\rm D} = \omega a^\dagger a + \frac{\Omega}{2}\sum_{k=1}^{N}\sigma_z^k + \frac{\lambda}{\sqrt{N}}\sum_{k=1}^{N}\sigma_x^k(a^\dagger + a) + \kappa(a + a^\dagger)^2 \tag{S4a}$$

$$= \tilde{\omega} a^\dagger a + \frac{\Omega}{2}\sum_{k=1}^{N}\sigma_z^k + \frac{\tilde{\lambda}}{\sqrt{N}}\sum_{k=1}^{N}\sigma_x^k(a^\dagger + a) + C \tag{S4b}$$

with $\tilde{\omega} = \sqrt{\omega^2 + 4\kappa\omega}$, $\tilde{\lambda} = \sqrt{\omega/\tilde{\omega}}\lambda$, and $C = (\tilde{\omega} - \omega)/2$. The Hamiltonian (S4b) was diagonalized by means of a Holstein-Primakoff transformation in Refs. [2]. We employ here a closely related approach developed in [3], which is more convenient for a generalization beyond the two-level approximation and was also used in the derivation of $\mathcal{H}_{\rm gD}$. We drop C, set the energy of the atomic ground states to zero, introduce the operators

$$a_k^\dagger = |{\rm e}_k\rangle\langle{\rm g}_k|, \qquad b_{q_j}^\dagger = \frac{1}{\sqrt{N}}\sum_{k=1}^{N} e^{iq_j k}|{\rm e}_k\rangle\langle{\rm g}_k|, \tag{S5}$$

where $q_j = 2\pi(j/N)$ and $j \in \{0, 1, \ldots, N-1\}$, and obtain for $N \to \infty$

$$\mathcal{H}_{\rm D}' = \tilde{\omega} a^\dagger a + \Omega\sum_{k=1}^{N} a_k^\dagger a_k + \tilde{\lambda}(b_{q_0}^\dagger + b_{q_0})(a^\dagger + a) \tag{S6a}$$

$$= \tilde{\omega} a^\dagger a + \Omega\sum_{j=0}^{N-1} b_{q_j}^\dagger b_{q_j} + \tilde{\lambda}(b_{q_0}^\dagger + b_{q_0})(a^\dagger + a). \tag{S6b}$$

In the limit of dilute excitations, which is applicable as long as the excitation energies of the system are finite, the b_{q_j} obey bosonic commutation relations. Note that only the $j = 0$ collective mode couples to the radiation field. The $j \neq 0$ modes are 'dark' and will be omitted in the following. We write b instead of b_{q_0} and arrive at

$$\mathcal{H}_{\rm D}'' = \tilde{\omega} a^\dagger a + \Omega b^\dagger b + \tilde{\lambda}(b^\dagger + b)(a^\dagger + a), \tag{S7}$$

which corresponds to $\mathcal{H}_{\rm gD}$ (Eqs. (11) and (S28)) with $\mu = 1$. Later we will derive a characteristic equation for the eigenfrequencies of $\mathcal{H}_{\rm gD}$ (Eqs. (12) and (S32b)). For $\mu = 1$ this equation has the solutions

$$2\epsilon_\pm^2 = \omega^2 + 4\kappa\omega + \Omega^2 \pm \sqrt{(\omega^2 + 4\kappa\omega - \Omega^2)^2 + 16\lambda^2\omega\Omega}. \tag{S8}$$

Diagonalization of $\mathcal{H}_{\rm tm}$. Now we consider $\mathcal{H}_{\rm tm}$ (Eq. (6)). The coupling of the electromagnetic field and a single harmonic oscillator 'atom' is described by

$$\mathcal{H}^0_{\rm tm} = \sum_{i=1}^{n} \frac{(p_i - eA)^2}{2m} + \frac{m\Omega^2 x_i^2}{2}. \tag{S9}$$

Note that we drop the index k numbering the atoms in $\mathcal{H}_{\rm tm}$ for a moment. As usual, we assume $\mathbf{A}(\mathbf{r}) \approx \mathbf{A} = A_0(a^\dagger + a)$ in the region where the atoms are located. It is convenient to make the canonical transformation $\tilde{x}_i = -p_i/(m\Omega)$ and $\tilde{p}_i = m\Omega x_i$. This yields

$$\mathcal{H}^0_{\rm tm} = \sum_{i=1}^{n} \left(\frac{p_i^2}{2m} + \frac{m\Omega^2 x_i^2}{2} \right) + eA_0\Omega(a^\dagger + a) \sum_{i=1}^{n} x_i + \frac{ne^2A_0^2}{2m}(a^\dagger + a)^2, \tag{S10}$$

where we have written x_i and p_i instead of $\tilde{x}_i$ and $\tilde{p}_i$ to keep notation simple. Successively introducing relative and center-of-mass coordinates, $\{x_1, p_1, x_2, p_2\} \to \{\tilde{x}_1, \tilde{p}_1, X_1, P_1\}$, $\{X_1, P_1, x_3, p_3\} \to \{\tilde{x}_2, \tilde{p}_2, X_2, P_2\}$, …, leads to

$$\mathcal{H}^0_{\rm tm} = \sum_{i=1}^{n-1} \left(\frac{\tilde{p}_i^2}{2\mu_i} + \frac{\mu_i\Omega^2\tilde{x}_i^2}{2} \right) + \frac{\tilde{P}^2}{2M} + \frac{M\Omega^2X^2}{2} + eA_0\Omega(a^\dagger + a)nX + \frac{ne^2A_0^2}{2m}(a^\dagger + a)^2. \tag{S11}$$

Here, $X = X_n = \frac{1}{n}\sum_{j=1}^{n} x_j$ and $P = P_n = \sum_{j=1}^{n} p_j$ are the center-of-mass coordinates of all particles in the harmonic oscillator atom, and $M = nm$. The relative coordinates are given by $\tilde{x}_i = (1/i\sum_{j=1}^{i} x_j) - x_{i+1}$ and $\tilde{p}_i = 1/(i+1)(\sum_{j=1}^{i} p_j - ip_{j+1})$, and $\mu_i = mi/(i+1)$. Note that the electromagnetic field couples only to the center of mass. With this preliminary work done, one can write the full Hamiltonian as

$$\mathcal{H}_{\rm tm} = \tilde{\omega}a^\dagger a + \Omega\sum_{k=1}^{N} c_k^\dagger c_k + \tilde{\gamma}\sum_{k=1}^{N}(c_k^\dagger + c_k)(a^\dagger + a) + \Omega\sum_{i=1}^{N(n-1)}(b_i^\dagger b_i + \frac{1}{2}) + C'. \tag{S12}$$

The operator $c_k^\dagger$ excites the center-of-mass degree of freedom of the kth atom, and the creation operators for the $N(n-1)$ relative coordinates are denoted by $b_i^\dagger$. We have introduced

$$\gamma = eA_0\sqrt{\frac{n\Omega}{2m}}, \qquad \kappa = nN\frac{e^2A_0^2}{2m}, \tag{S13}$$

and removed the κ-term by means of $\tilde{\omega} = \sqrt{\omega^2 + 4\kappa\omega}$ and $\tilde{\gamma} = \sqrt{\omega/\tilde{\omega}}\gamma$ as before ($C' = (\tilde{\omega} - \omega + N\Omega)/2$). The first three terms are again a special case of $\mathcal{H}_{\rm gD}$ with $\Omega_l = \Omega$ and $\tilde{\lambda}_l = \tilde{\gamma}$ for all l, and $\mu = N$. Hence, their eigenvalues follow from the roots of the characteristic equation for $\mathcal{H}_{\rm gD}$ (Eq. (S32b)), simplified by the present conditions. They can be explicitly calculated and are the frequencies of the normal modes of field and center-of-mass coordinates. We find that $N-1$ eigenfrequencies are equal to Ω, and we represent the creation operators of the corresponding collective excitations also by $b_i^\dagger$. Only two eigenfrequencies $\epsilon_\pm$ are nondegenerate,

$$2\epsilon_\pm^2 = \omega^2 + 4\kappa\omega + \Omega^2 \pm \sqrt{(\omega^2 + 4\kappa\omega - \Omega^2)^2 + 16N\gamma^2\omega\Omega} \tag{S14a}$$

$$= \omega^2 + 4\kappa\omega + \Omega^2 \pm \sqrt{(\omega^2 + 4\kappa\omega - \Omega^2)^2 + 16\lambda^2\omega\Omega}. \tag{S14b}$$

We have defined $\lambda = \sqrt{N}\gamma$. Since the dipole element d of the transition from the ground state of an atom to its first excited state is given by $d = \langle n|ex|n-1\rangle = e\sqrt{n/2m\Omega}$, we can rewrite $\lambda = A_0\Omega d\sqrt{N}$ and $\kappa = \lambda^2/\Omega$. Denoting the operators of the $\epsilon_\pm$-modes by $a_\pm$, we arrive at

$$\mathcal{H}_{\rm tm} = \epsilon_\pm(a_\pm^\dagger a_\pm + \frac{1}{2}) + \sum_{i=1}^{nN-1}\Omega(b_i^\dagger b_i + \frac{1}{2}) - \frac{\omega}{2}. \tag{S15}$$

C. Shift of the resonator frequency due to the pA- and $\mathbf{A}^2$-terms. Consider a system of N mutually noninteracting objects (e.g. atoms) with Hamiltonians

$$H^k_{\rm mic} = \sum_{i=1}^{n_k}\frac{(\mathbf{p}_i^k)^2}{2m_i^k} + V_{\rm int}(\mathbf{r}_1^k,\ldots,\mathbf{r}_{n_k}^k) \tag{S16}$$

coupled to a field mode of frequency ω. It is described by

$$\mathcal{H}_{\rm mic} = \omega a^\dagger a + \sum_{k=1}^{N}\left(H^k_{\rm mic} + \mathcal{H}^k_{pA} + \mathcal{H}^k_{A^2}\right), \tag{S17}$$

where $H^k_{\rm mic} = \sum_{i=1}^{n_k}(\mathbf{p}_i^k)^2/2m_i^k + V_{\rm int}(\mathbf{r}_1^k,\ldots,\mathbf{r}_{n_k}^k)$, $\mathcal{H}^k_{pA} = -\sum_{i=1}^{n_k} q_i^k\mathbf{A}\mathbf{p}_i^k/m_i^k$, and $\mathcal{H}^k_{A^2} = \sum_{i=1}^{n_k}(q_i^k)^2\mathbf{A}^2/2m_i^k$. We denote the eigenspectrum of $H^k_{\rm mic}$ by $\{E^k_{m_k}, |m_k\rangle_k\}$ and the photon states by $|l\rangle$ and calculate the shifts $\delta\omega_{pA}$ and $\delta\omega_{A^2}$ of the resonator frequency due to $\sum\mathcal{H}^k_{pA}$ and $\sum\mathcal{H}^k_{A^2}$ using the first nonzero terms in a perturbation series for the energy of $|0,\ldots,0,l\rangle$. We take $\omega \ll (E^k_{m_k} - E^k_0) =: \Omega^k_{m_k}$ for $m_k > 0$ (otherwise, there would be no well-defined resonator frequency) and $\mathbf{A}(\mathbf{r}_i^k) \approx \mathbf{A}$. With $\mathbf{d}^k_{m_k,0} = {}_k\langle m_k|\sum_{i=1}^{n_k} q_i^k\mathbf{r}_i^k|0\rangle_k$, we find for the jth terms ΔE^j_{pA} and $\Delta E^j_{A^2}$ in the perturbation series for the perturbations $\sum\mathcal{H}^k_{pA}$ and $\sum\mathcal{H}^k_{A^2}$

$$\Delta E^1_{pA} = 0, \tag{S18a}$$

$$\Delta E^2_{pA} = -A_0^2\sum_{k=1}^{N}\sum_{m_k\neq 0}\Omega^k_{m_k}|\boldsymbol{\epsilon}\cdot\mathbf{d}^k_{m_k,0}|^2\left(\frac{(l+1)}{1+\frac{\omega}{\Omega^k_{m_k}}} + \frac{l}{1-\frac{\omega}{\Omega^k_{m_k}}}\right), \tag{S18b}$$

$$\approx -A_0^2\sum_{k=1}^{N}\sum_{m_k\neq 0}\Omega^k_{m_k}|\boldsymbol{\epsilon}\cdot\mathbf{d}^k_{m_k,0}|^2\left((2l+1) - \left(\frac{\omega}{\Omega^k_{m_k}}\right) + (2l+1)\left(\frac{\omega}{\Omega^k_{m_k}}\right)^2\right), \tag{S18c}$$

$$\Delta E^1_{A^2} = A_0^2(2l+1)\sum_{k=1}^{N}\sum_{i=1}^{n_k}\frac{(q_i^k)^2}{2m_i^k}. \tag{S18d}$$

Therefore,

$$\delta\omega_{pA} = -2A_0^2\sum_{k=1}^{N}\sum_{m_k\neq 0}\Omega^k_{m_k}|\boldsymbol{\epsilon}\cdot\mathbf{d}^k_{m_k,0}|^2\left(1+\frac{\omega^2}{(\Omega^k_{m_k})^2}\right), \tag{S19a}$$

$$\delta\omega_{A^2} = 2A_0^2\sum_{k=1}^{N}\sum_{i=1}^{n_k}\frac{(q_i^k)^2}{2m_i^k}. \tag{S19b}$$

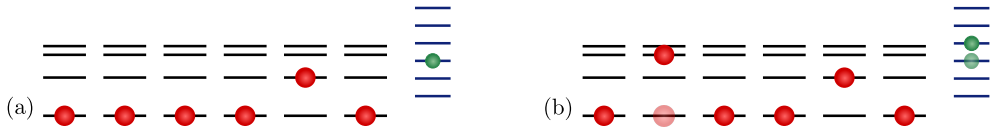

Figure S1: Situation of the generalized no-go theorem. Atomic spectra are drawn in black, eigenenergies of the free electromagnetic field in blue. (a) Structure of a low-energy state $|\mathcal{E}_0\rangle$ of the uncoupled system. For $N \to \infty$, the numbers of excited atoms ξ and of photons χ in $|\mathcal{E}_0\rangle$ are small compared to N, $\xi \ll N$ and $\chi \ll N$. (b) Structure of a component of $\mathcal{E}_1$. The coupling has induced one atomic transition and created or annihilated one photon (shown is an excitation of the second atom and the creation of a photon). The state $|\mathcal{E}_1\rangle$ is the sum of all such states. Their amplitude in the eigenstate of the coupled system is smaller than the amplitude of $|\mathcal{E}_0\rangle$ by a factor $\propto A_0 \propto V^{-1/2}$. In general, $|\mathcal{E}_s\rangle$ represents the sum over all states obtained from $|\mathcal{E}_0\rangle$ via s atomic transitions and s creations or annihilations of a photon. They contribute to the eigenstate of the coupled system by an amplitude $\propto A_0^s$.

The **pA**-terms cause a negative and the $\mathbf{A^2}$-terms a positive frequency shift. Note that $\delta\omega_{pA}$ and $\delta\omega_{A^2}$ almost cancel due to the TRK (applied for each k). The resulting total frequency shift $\delta\omega = \delta\omega_{pA} + \delta\omega_{A^2}$ is suppressed by $\sim (\omega/\Omega^k_{m_k})^2$ as compared with $\delta\omega_{pA}$ and $\delta\omega_{A^2}$.

D. The generalized Dicke Hamiltonian $\mathcal{H}_{\rm gD}$. In this section, we derive the Hamiltonian $\mathcal{H}_{\rm gD}$ (Eq. (11)) from $\mathcal{H}_{\rm mic}$ (in the form of Eq. (10)) for $N \to \infty$ and show how to obtain and evaluate its characteristic equation.

According to our strategy formulated in the main text, we start from low atomic densities and expand the eigenstates $|\mathcal{E}\rangle$ of $\mathcal{H}_{\rm mic}$ in powers of $A_0 \propto V^{-1/2}$,

$$|\mathcal{E}\rangle \propto \sum_{s=0}^{\infty} A_0^s |\mathcal{E}_s\rangle, \tag{S20}$$

where $|\mathcal{E}_s\rangle$ stands for a sum over components that each describe s transitions from $|\mathcal{E}_0\rangle$ both in its atomic and in its photonic part and hence has weight $\propto A_0^s$ (Fig. S1). The corresponding eigenenergies can be written as $\mathcal{E} \propto \sum_{ss'} A_0^{s+s'} \langle \mathcal{E}_s | \mathcal{H}_{\rm mic} | \mathcal{E}_{s'} \rangle$. We are interested only in the low-energy spectrum of $\mathcal{H}_{\rm mic}$. Thus, we assume that the number of atomic excitations $\xi = \sum_k \sum_{l>0} |\langle l_k | \mathcal{E}_0 \rangle|^2$ and the number of photons $\chi = \langle \mathcal{E}_0 | a^\dagger a | \mathcal{E}_0 \rangle$ in the uncoupled eigenstates $|\mathcal{E}_0\rangle$ are small compared to N, $\xi \ll N$ and $\chi \ll N$. We now calculate $\mathcal{E}$ by dropping all $s + s' \geq 2$ terms and show that for the low-energy spectrum of $\mathcal{H}_{\rm mic}$ all matrix elements that induce transitions in-between excited atomic states are irrelevant. To that end, we write

$$\mathcal{H}_{\rm mic} = \tilde{\omega} a^\dagger a + \sum_{k=1}^{N} \sum_{l,l'=0}^{\mu} \left(\Omega_l \delta_{l,l'} |l_k\rangle\langle l_k| + i A_0 \sqrt{\frac{\tilde{\omega}}{\omega}} (\Omega_{l'} - \Omega_l) d_{l,l'} (a^\dagger + a) |l_k\rangle\langle l'_k| \right) + C, \tag{S21}$$

with $\tilde{\omega} = \sqrt{\omega^2 + 4\kappa\omega}$ and $C = (\tilde{\omega} - \omega)/2$, and we define

$$H = \tilde{\omega} a^\dagger a + \sum_{k=1}^{N} \sum_{l=1}^{\mu} \Omega_l |l_k\rangle\langle l_k| \tag{S22a}$$

$$H_{\mathrm{cpl}} = (a^\dagger + a) \sum_{k=1}^{N} \sum_{l=1}^{\mu} A_0 \sqrt{\frac{\tilde{\omega}}{\omega}} \Omega_l \big(i d_{0,l} |0_k\rangle\langle l_k| - i d_{l,0} |l_k\rangle\langle 0_k| \big) \tag{S22b}$$

$$\Delta H = (a^\dagger + a) \sum_{k=1}^{N} \sum_{l>l' \geq 1}^{\mu} A_0 \sqrt{\frac{\tilde{\omega}}{\omega}} (\Omega_l - \Omega_{l'}) \big(i d_{l',l} |l'_k\rangle\langle l_k| - i d_{l,l'} |l_k\rangle\langle l'_k| \big). \tag{S22c}$$

Accordingly,

$$\mathcal{E} \propto \langle \mathcal{E} | \mathcal{H}_{\mathrm{mic}} | \mathcal{E} \rangle \tag{S23a}$$

$$\propto \langle \mathcal{E}_0 | H | \mathcal{E}_0 \rangle + A_0 \big(\langle \mathcal{E}_0 | H_{\mathrm{cpl}} | \mathcal{E}_1 \rangle + \langle \mathcal{E}_1 | H_{\mathrm{cpl}} | \mathcal{E}_0 \rangle + \langle \mathcal{E}_0 | \Delta H | \mathcal{E}_1 \rangle + \langle \mathcal{E}_1 | \Delta H | \mathcal{E}_0 \rangle \big). \tag{S23b}$$

Let us now compare the contributions of H_{cpl} and ΔH to $\mathcal{E}$. The photonic parts of H_{cpl} and ΔH are equal and do not need to be further considered. We write $\langle H_{\mathrm{cpl}} \rangle = \langle \mathcal{E}_0 | H_{\mathrm{cpl}} | \mathcal{E}_1 \rangle + \langle \mathcal{E}_1 | H_{\mathrm{cpl}} | \mathcal{E}_0 \rangle$ and $\langle \Delta H \rangle = \langle \mathcal{E}_0 | \Delta H | \mathcal{E}_1 \rangle + \langle \mathcal{E}_1 | \Delta H | \mathcal{E}_0 \rangle$, and we find

$$\frac{\langle \Delta H \rangle}{\langle H_{\mathrm{cpl}} \rangle} = \frac{\sum_{l>l' \geq 1}^{\mu} (\Omega_l - \Omega_{l'}) \mathrm{Im}\big[d_{l',l} \sum_{k=1}^{N} \big(\langle \mathcal{E}_0 | l'_k \rangle\langle l_k | \mathcal{E}_1 \rangle + \langle \mathcal{E}_1 | l'_k \rangle\langle l_k | \mathcal{E}_0 \rangle \big) \big]}{\sum_{l=1}^{\mu} \Omega_l \mathrm{Im}\big[d_{0,l} \sum_{k=1}^{N} \big(\langle \mathcal{E}_0 | 0_k \rangle\langle l_k | \mathcal{E}_1 \rangle + \langle \mathcal{E}_1 | 0_k \rangle\langle l_k | \mathcal{E}_0 \rangle \big) \big]} \tag{S24}$$

Since $N \to \infty$, the number of nonzero terms in the k-sums is decisive. For given l, l', the sum over k in the numerator has at most ξ nonzero terms, whereas the sum over k in the denominator has at least $N - \xi$ nonzero terms. Hence, we drop ΔH, which represents the matrix elements of $\mathcal{H}_{\mathrm{mic}}$ connecting the excited states of an atom, and keep H_{cpl} as the relevant coupling part of $\mathcal{H}_{\mathrm{mic}}$. We reintroduce the κ-term and call the resulting Hamiltonian *generalized Dicke Hamiltonian* $\mathcal{H}_{\mathrm{gD}}$,

$$\mathcal{H}_{\mathrm{gD}} = \omega a^\dagger a + \kappa (a^\dagger + a)^2 + \sum_{k=1}^{N} \sum_{l=1}^{\mu} \big(\Omega_l |l_k\rangle\langle l_k| - \Omega_l A_0 (a^\dagger + a) \big(i d_{l,0} |l_k\rangle\langle 0_k| + \mathrm{H.c.} \big) \big). \tag{S25}$$

It has the same low-energy spectrum as $\mathcal{H}_{\mathrm{mic}}$. Paralleling our treatment of $\mathcal{H}_{\mathrm{D}}$, we introduce

$$a^\dagger_{k,l} = |l_k\rangle\langle 0_k|, \qquad b^\dagger_{q_j,l} = \frac{1}{\sqrt{N}} \sum_{k=1}^{N} e^{i q_j k} |l_k\rangle\langle 0_k|, \tag{S26}$$

where $q_j = 2\pi(j/N)$ and $j \in \{0, 1, \ldots, N-1\}$ as before. With $\sum_{k=1}^{N} a^\dagger_{k,l} a_{k,l} = \sum_{j=0}^{N-1} b^\dagger_{q_j,l} b_{q_j,l}$, Eq. (S25) becomes

$$\mathcal{H}_{\mathrm{gD}} = \omega a^\dagger a + \kappa (a^\dagger + a)^2 + \sum_{l=1}^{\mu} \Big(\Omega_l \sum_{j=0}^{N-1} b^\dagger_{q_j,l} b_{q_j,l} - A_0 \Omega_l \sqrt{N} (a^\dagger + a) \big(i d_{l,0} b^\dagger_{q_0,l} + \mathrm{H.c.} \big) \Big). \tag{S27}$$

The operators $b_{q_j,l}$ are bosonic in the limit of dilute excitations ($\xi \ll N$)[3]. The $j > 0$ collective modes do not couple to the electromagnetic field. Again, we drop the energy of

these 'dark' modes, write b_l instead of $b_{q_0,l}$, define $\lambda = A_0\Omega_l|d_{0l}|\sqrt{N}$, and remove the κ-term by substituting $\omega \to \tilde{\omega} = \sqrt{\omega^2 + 4\kappa\omega}$ and $\lambda_l \to \tilde{\lambda}_l = \sqrt{\omega/\tilde{\omega}}\lambda_l$ and adding $C = (\tilde{\omega} - \omega)/2$. This gives

$$\mathcal{H}_{\mathrm{gD}} = \tilde{\omega}a^\dagger a + \sum_{l=1}^{\mu} \Omega_l b_l^\dagger b_l + \sum_{l=1}^{\mu} \tilde{\lambda}_l (b_l^\dagger + b_l)(a^\dagger + a) + C. \tag{S28}$$

In order to find the eigenfrequencies of $\mathcal{H}_{\mathrm{gD}}$, we introduce canonical coordinates by means of

$$x = \frac{1}{\sqrt{2\tilde{\omega}}}(a^\dagger + a), \quad p_x = i\sqrt{\frac{\tilde{\omega}}{2}}(a^\dagger - a), \quad y_l = \frac{1}{\sqrt{2\Omega_l}}(b_l^\dagger + b_l), \quad p_l = i\sqrt{\frac{\Omega_l}{2}}(b_l^\dagger - b_l), \tag{S29}$$

and define $\mathbf{X}^{\mathrm{T}} = (x, y_1, \ldots, y_\mu)$, $\mathbf{P}^{\mathrm{T}} = (p_x, p_1, \ldots, p_\mu)$, and $g_l = 2\tilde{\lambda}_l\sqrt{\tilde{\omega}\Omega_l}$. This yields

$$\mathcal{H}_{\mathrm{gD}} = \frac{\mathbf{P}^{\mathrm{T}}\mathbf{P}}{2} + \frac{1}{2}\mathbf{X}^{\mathrm{T}}\underline{\Omega}^2\mathbf{X} - \frac{1}{2}(\omega + \sum_{l=1}^{\mu}\Omega_l) \tag{S30}$$

where

$$\underline{\Omega}^2 = \begin{pmatrix} \tilde{\omega}^2 & g_1 & \cdots & g_\mu \\ g_1 & \Omega_1^2 & & \\ \vdots & & \ddots & \\ g_\mu & & & \Omega_\mu^2 \end{pmatrix} \tag{S31}$$

The orthogonal matrix G that diagonalizes $\underline{\Omega}^2$ induces a point transformation to the normal modes $\tilde{\mathbf{X}} = G\mathbf{X}$ and $\tilde{\mathbf{P}} = G\mathbf{P}$. The eigenvalues ϵ_i^2 of $\underline{\Omega}^2$ are the squared eigenfrequencies of the system. They solve the characteristic equation

$$0 = \Big(\prod_{l'=1}^{\mu}(\Omega_{l'}^2 - \epsilon^2)\Big)\Big((\tilde{\omega}^2 - \epsilon^2) - \sum_{l=1}^{\mu}\frac{g_l^2}{\Omega_l^2 - \epsilon^2}\Big) \tag{S32a}$$

$$= \Big(\prod_{l'=1}^{\mu}(\Omega_{l'}^2 - \epsilon^2)\Big)\Big((\tilde{\omega}^2 - \epsilon^2) - 4\tilde{\omega}\sum_{l=1}^{\mu}\frac{\Omega_l\tilde{\lambda}_l^2}{\Omega_l^2 - \epsilon^2}\Big). \tag{S32b}$$

None of them can be zero since this would imply

$$\frac{\omega}{4NA_0^2} = \sum_{l=1}^{\mu}\Omega_l|d_{0l}|^2 - \sum_{i=1}^{n}\frac{q_i^2}{2m_i}. \tag{S33}$$

We have used $\tilde{\omega} = \sqrt{\omega^2 + 4\kappa\omega}$, $\tilde{\lambda}_l = \sqrt{\omega/\tilde{\omega}}\lambda_l$, $\lambda_l = A_0\Omega_l|d_{0l}|\sqrt{N}$, and $\kappa = NA_0^2\sum_{i=1}^{n} q_i^2/2m_i$. However, the left side of Eq. (S33) is positive, whereas its right side is negative according to the TRK for H_{mic}^0 (Eqs. (S3) or Eq. (9) of the main text).

E. Influence of disorder in the atomic parameters. The unavoidable fluctuations of the transition frequencies and coupling strengths of the artificial atoms may be expected to weaken the tendency towards a SPT in a circuit QED system and thus should not jeopardize the assertion of the no-go theorem. However, the experimental verification of the failure of the standard description of circuit QED proposed in the main text requires that the coupling-induced shift of the resonator frequency and the SPT predicted by the standard description are robust with respect to some disorder in the atomic parameters. Further, for a coupling that is critical according to the standard description, the minimal excitation energy compatible with the TRK has to be well-separated form zero also for a disordered system.

In this section, we present numerical results showing that disorder in the atomic parameters does not have a significant influence on the lowest excitation energy of a circuit QED system with a large number of artificial atoms, both according to the standard description of circuit QED and according to a microscopic description that obeys the TRK. The proposed method for experimentally observing the failure of the standard description is consequently not affected by a small amount of disorder in the atomic parameters. Finally, we show that in the case of very strong coupling, the failure of the standard description of circuit QED can become measurable already for a system with $N = 10$.

Neither in the standard description nor in the microscopic description it is possible to numerically calculate the excitation energies for a system containing as many as $N \sim 200$ artificial atoms. One can therefore not demonstrate in this way that also for disordered systems the standard description predicts a SPT, whereas according to the microscopic description all excitation energies remain nonzero. Hence, we will follow a strategy pursued in a similar context in Ref. [4] and consider smaller systems with varying number of artificial atoms to study the effect of disorder under increasing system size. For non-identical artificial atoms, the Dicke Hamiltonian reads

$$\mathcal{H}_{\mathrm{D}} = \omega a^\dagger a + \sum_{k=1}^{N} \frac{\Omega_k}{2}\sigma_z^k + \sum_{k=1}^{N} \frac{\lambda_k}{\sqrt{N}}\sigma_x^k(a^\dagger + a) + \sum_{k=1}^{N} \kappa_k (a^\dagger + a)^2, \tag{S34}$$

where κ_k represents the $\mathbf{A}^2$-terms due to a single atom ($\kappa = \sum_{k=1}^{N} \kappa_k$). Note that Ω_k, λ_k, and κ_k depend on the properties of the kth atom and may slightly fluctuate in a way that has to be specified. The effective model for an artificial atom employed in the standard description leads to (cf. Eqs. (5) of the main text)

$$\lambda_{\mathrm{cir},k} = \frac{eC_{\mathrm{G}}^k}{C_{\mathrm{G}}^k + C_{\mathrm{J}}^k}\sqrt{\frac{\omega N}{Lc}}, \qquad \kappa_{\mathrm{cir},k} = \frac{(C_{\mathrm{G}}^k)^2}{2(C_{\mathrm{G}}^k + C_{\mathrm{J}}^k)}\frac{\omega}{Lc}, \tag{S35}$$

while the microscopic approach yields (cf. Eqs. (8) of the main text)

$$\lambda_{\mathrm{cir},k}^{\mathrm{mic}} = \frac{\Omega_k |\boldsymbol{\epsilon}\cdot\mathbf{d}^{\mathbf{k}}|}{\sqrt{2\epsilon_0\omega}}\sqrt{\frac{N}{V}}, \qquad \kappa_{\mathrm{cir},k}^{\mathrm{mic}} = \frac{1}{2\epsilon_0\omega V}\sum_{i=1}^{n_k}\frac{(q_i^k)^2}{2m_i^k}, \tag{S36}$$

and $\mathbf{d}^k = \langle \mathrm{e}_k | \sum_{i=1}^{n_k} q_i^k \mathbf{r}_i^k | \mathrm{g}_k \rangle$. We define a parameter α_k via $N\kappa_k = \alpha_k \lambda_k^2/\Omega_k$ and find

$$\alpha_{\mathrm{cir},k} = \frac{E_{\mathrm{J}}^k(C_{\mathrm{G}}^k + C_{\mathrm{J}}^k)}{2e^2} \equiv \frac{E_{\mathrm{J}}^k}{4E_{\mathrm{C}}^k}, \qquad \alpha_{\mathrm{cir},k}^{\mathrm{mic}} = \frac{\sum_{i=1}^{n_k}(q_i^k)^2/2m_i^k}{\Omega_k|\boldsymbol{\epsilon}\cdot\mathbf{d}^k|^2}, \tag{S37}$$

where $\alpha_{\mathrm{cir},k}^{\mathrm{mic}} \geq 1$ due to the TRK (Eq. (9) of the main text). We assume for the microscopic description $\alpha_{\mathrm{cir},k}^{\mathrm{mic}} = 1$, which corresponds to the strongest shift of the lowest excitation energy

allowed by the TRK (in other words, the atoms are taken to be perfect two-level systems). Now we implement disorder in the system and write $\Omega_k = \Omega\tau_k$, where we choose τ_k to be a random number following a normal distribution with mean 1 and standard deviation 0.1. To determine how disorder in the Ω_k affects λ_k and κ_k both in the standard and in the microscopic description of the system, it is further assumed that the artificial atoms have approximately the same shape and chemical composition, that the disorder is only due to imperfections in the fabrication of the Josephson junctions, and that $C_\mathrm{G} \gg C_\mathrm{J}^k$. Thus, $\kappa_{\mathrm{cir},k} = \kappa_\mathrm{cir}/N$ and $\kappa_{\mathrm{cir},k}^\mathrm{mic} = \kappa_\mathrm{cir}^\mathrm{mic}/N$ are taken to be independent of k. Under these conditions, $\lambda_{\mathrm{cir},k}^\mathrm{mic} = \lambda_\mathrm{cir}^\mathrm{mic}\sqrt{\tau_k}$, whereas $\lambda_{\mathrm{cir},k} = \lambda_\mathrm{cir}$ does not depend on the fluctuations of the atomic transition frequencies. Note that $\alpha_{\mathrm{cir},k} = E_{\mathrm{J},k}/4E_\mathrm{C} = \Omega_k/4E_\mathrm{C} = (E_\mathrm{J}/4E_\mathrm{C})\tau_k = \alpha_\mathrm{cir}\tau_k$. By fixing $\alpha_\mathrm{cir} = E_\mathrm{J}/4E_\mathrm{C} = 0.1$ as in the calculation for the ordered system, we have expressed Ω_k, λ_k and κ_k both in the standard and in the microscopic description of the disordered system by mean values Ω and λ and a disorder configuration $\{\tau_k\}$.

In our numerical analysis, we calculate the lowest excitation energies $\epsilon_-^{N,\mathrm{d}}$ of disordered circuit QED systems with $N = 3, 5, 7$ artificial atoms as functions of λ according to the standard and the microscopic description. It will be necessary to consider couplings of the same order of magnitude as Ω. Even though with present-day technologies such couplings are not realistic for $N = 3, 5, 7$, this gives us the evolution of the lowest excitation energy with increasing N under strong coupling and allows us to infer the behavior of a system with larger N, for which $\lambda \sim \Omega$ is possible ($\lambda \propto \sqrt{N}$), but which would be numerically intractable. All calculations are done for $\omega = \Omega$, and we have used 100 disorder configurations for each system size to calculate mean values $\langle\epsilon_-^{N,\mathrm{d}}\rangle$ and standard deviations σ_N. Numerical experiments show that restricting the photonic part of the Hilbert space to maximally seven photons provides a good compromise between accuracy and numerical effort. We have also calculated the lowest excitation energies ϵ_-^N of the corresponding ordered systems ($\tau_k = 1$ for all k), and we compare our results with ϵ_-^∞ (for varying α), the exact lowest excitation energy of an infinitely large ordered system (Eq. (7) and Fig. 2(a) of the main text, there denoted simply by ϵ_-).

Figure S2 is our main numerical result. We plot in black the excitation energies of the homogeneous systems, ϵ_-^N, for $N = 3, 5, 7$. The upper three black curves are calculated according to the microscopic description of circuit QED, the lower ones according to the standard description of circuit QED. In both cases, the frequency shift for given λ increases with N. For comparison, we plot the corresponding analytically found excitation energies for the infinitely large homogeneous system, $\epsilon_-^\infty|_{\alpha=0.1}$ (dark red) and $\epsilon_-^\infty|_{\alpha=1}$ (dark green). The latter curve already appeared in Fig. 2(a) of the main text. Indeed, as N increases, ϵ_-^N approaches $\epsilon_-^\infty|_{\alpha=0.1}$ (or $\epsilon_-^\infty|_{\alpha=1}$) if calculated according to the standard (or microscopic) description of circuit QED.

We plot further the averaged lowest excitation energies $\langle\epsilon_-^{N,\mathrm{d}}\rangle$ (dashed blue, dashed green, and dashed magenta for $N = 3, 5, 7$, respectively), again both according to the microscopic description (upper three curves) and according to the standard description (lower three curves). The figure clearly demonstrates that the mean excitation energies of the disordered systems are similar to the excitation energies of the homogeneous systems. The dashed lines for $\langle\epsilon_-^{N,\mathrm{d}}\rangle$ gained from the standard description are hardly visible for $\lambda/\Omega \gtrsim 0.5$ as they coincide, in the resolution of Fig. S2, with the corresponding ϵ_-^N-lines and are plotted underneath.

The solid colored curves enclosing the color-shaded regions represent $\langle\epsilon_-^{N,\mathrm{d}}\rangle \pm \sigma_N$ as calculated from the microscopic and the standard description of circuit QED. We use again blue, green, and magenta for $N = 3, 5, 7$, respectively.

According to the microscopic description, the standard deviation does not appreciably

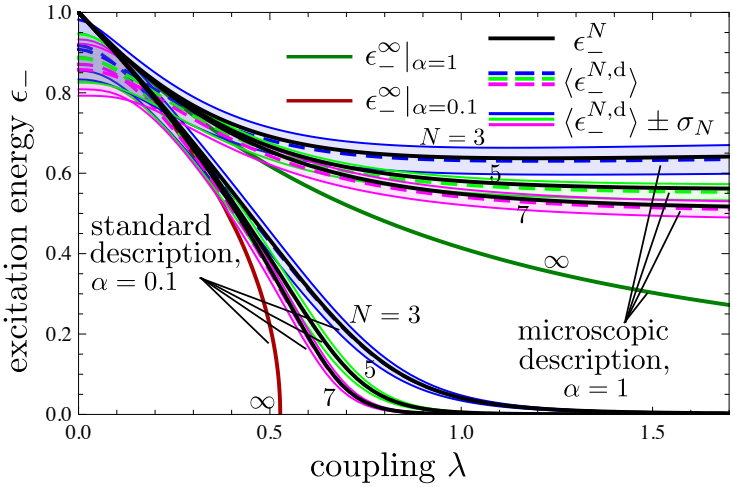

Figure S2: Lowest excitation energies of (dis-)ordered circuit QED systems with varying number of artificial atoms vs. coupling λ. The figure shows the predictions both of the standard description of circuit QED and of a microscopic description that is compatible with the Thomas-Reiche-Kuhn sum rule. Scales are in units of $\omega = \Omega$. Black lines: lowest excitation energies of ordered circuit QED systems with $N = 3, 5, 7$ artificial atoms according to the microscopic description (upper three curves) and according to the standard description (lower three curves). Blue, green, and magenta lines: results for ensembles of corresponding disordered systems. Mean excitation energies are represented by dashed lines, while the solid lines stand for the mean values plus and minus the standard deviation. Furthermore, analytical results for a homogeneous system with $N \to \infty$ according to the standard description (dark red) and according to the microscopic description (dark green). The standard description predicts precursors of the superradiant phase transition for the disordered finite-size systems. For couplings that produce a quasi-degenerate ground state according to the standard description, the microscopic description predicts a nonzero energy gap, irrespective of the presence of disorder in the atomic parameters.

decrease with increasing λ. However, the standard deviation is small compared to the mean lowest excitation energy $\langle\epsilon_-^{N,\mathrm{d}}\rangle$ and decreases with N, $\sigma_3 > \sigma_5 > \sigma_7$ for all λ. Disorder, thus, does not have a significant effect on the lowest excitation energy of a circuit QED system containing many artificial atoms according to the microscopic description. The lower bound derived in the main text for the shifted resonator frequency of a homogeneous circuit QED system that undergoes a SPT according to the standard description will remain basically unchanged if a small amount of disorder in the atomic parameters is admitted.

According to the standard description, the effect of disorder is strongly suppressed for large λ. The lowest excitation energies of the disordered systems do not only coincide on average with the excitation energies of the homogeneous systems, also the standard deviation from the mean rapidly shrinks with λ and N. For instance, for $N = 7$ and $\lambda/\Omega = 1.5$, we find by means of the standard description $\epsilon_-^7/\Omega \approx 10^{-5}$, $\langle\epsilon_-^{7,\mathrm{d}}\rangle/\Omega \approx 10^{-5}$, and $\sigma_7/\Omega \approx 2 \times 10^{-6}$. This means that the ground states of the systems become quasi-degenerate for strong coupling λ, irrespective of the presence of disorder. Hence, in the standard description of circuit QED, precursors of the SPT are visible for finite-size disordered systems and get more pronounced with increasing N. The effect of disorder is much weaker than the coupling-induced frequency

shift and vanishes where the corresponding ordered systems become gapless. Consequently, our estimate on the basis the standard description of how many artificial atoms are required to see signatures of a SPT in a homogeneous circuit QED system with realistic parameters (see main text) will not be affected by small fluctuations of the atomic parameters.

Taken together, our numerical results for the microscopic and the standard description ensure – this is the central conclusion of this section – that the method for experimentally observing the failure of the standard description of circuit QED systems that we have proposed in the main text is insensitive to a small amount of disorder in the atomic parameters.

We remark that we have done the same analysis of (dis-)ordered finite-size circuit QED systems as above on the basis of the microscopic description, but with $\alpha = 0$ (Fig. S3). This shows how the SPT emerges in a (dis-)ordered circuit or cavity QED system according to the microscopic picture if the κ-term is disregarded (recall that the dependence of λ_j on Ω_j differs between standard and microscopic description). One finds very similar results as for the standard description of circuit QED: the mean lowest excitation energies (dashed colored lines) converge to those of the homogeneous systems (black lines) as λ increases, the standard deviation (solid colored lines, plotted relative to the mean values) shrinks even faster than in the standard description, and the (mean) excitation energies approach $\epsilon_-^{\infty}|_{\alpha=0}$ (red line) if N is increased. The latter curve already appeared in Fig. 2(a) of the main text. These findings imply that if a SPT occurred in a homogeneous system (this would happen if $\alpha < 1$ according to Eq. (3)), it would be not affected by some disorder in the atomic parameters, not only according to the standard description but also according to the microscopic description of circuit QED.

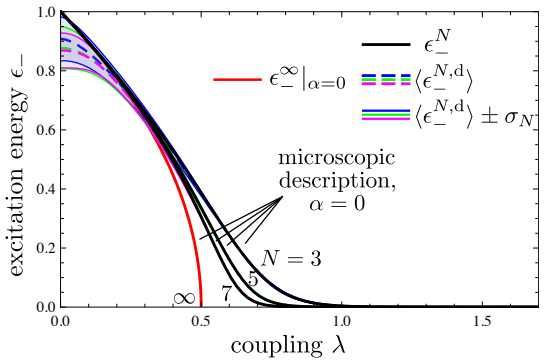

Figure S3: Lowest excitation energies of (dis-)ordered circuit QED systems with varying number of artificial atoms vs. coupling λ (in units of $\omega = \Omega$). The figure shows the predictions the microscopic description if the κ-term is neglected ($\alpha = 0$). The color code is the same as in Fig. S2. Furthermore, the analytical result for a homogeneous system with $N \to \infty$ if the κ-term is neglected (red).

Finally, we numerically estimate the deviation of the prediction of the standard description of circuit QED from the actual value for the lowest excitation energy of a circuit QED system with only 10 artificial atoms but with very strong coupling. Suppose an artificial atom couples with a strength $\lambda/\Omega = 0.1$ to the resonator field. This has been already achieved with flux qubits [5] and is referred to as "ultrastrong coupling". Since we have seen that disorder plays only a minor role for the lowest excitation energy of a circuit QED systems with $N \gg 1$, we consider for simplicity a homogeneous system. We assume again $\omega = \Omega$, include up to 10 photons in our calculations, and obtain, by taking the $\sqrt{N}$-scaling of the coupling into account, excitation energies of $\epsilon_-^{10}|_{\alpha=0.1}/\Omega \approx 0.63$ (corresponding to the standard description with $\alpha_{\mathrm{cir}} = E_{\mathrm{J}}/4E_{\mathrm{C}} = 0.1$, cf. Eqs. (S37)) and $\epsilon_-^{10}|_{\alpha=1}/\Omega \approx 0.74$ ($\alpha = 1$ corresponds to the strongest frequency shift compatible with the TRK, i.e., to the microscopic description of ideal two-level artificial atoms, cf. Eqs. (S37) and Eq. (9) of the main text). This means that, if the coupling is ultrastrong, already for systems with ~ 10 artificial atoms the standard

description can be measurably inaccurate: in the case considered here, the actually measured lowest excitation energy will be at least 17% greater than predicted by the standard description. Measuring the excitation energy of such a system hence could be an alternative viable way to experimentally verify our conclusions. Ultimately, these deliberations may give an improved idea of the required system sizes and coupling strengths that render the mistakes made by the standard description manifest.

References

[1] W. Thomas, Naturwissenschaften **13**, 627 (1925); F. Reiche and W. Thomas, Z. Phys. **34**, 510 (1925); W. Kuhn, *ibid.* **33**, 408 (1925).

[2] C. Emary and T. Brandes, Phys. Rev. Lett. **90**, 044101 (2003); C. Emary and T. Brandes, Phys. Rev. E **67**, 066203 (2003).

[3] J. J. Hopfield, Phys. Rev. **112**, 1555 (1958).

[4] P. Nataf and C. Ciuti, Phys. Rev. Lett. **104**, 023601 (2010).

[5] T. Niemczyk *et al.*, Nature Phys. **6**, 772 (2010).

Chapter 4

Quantum simulations of non-equilibrium spin chains in circuit QED

In this chapter, we propose and analyze a circuit QED design that implements the quantum transverse-field Ising chain. The setup is argued to provide a new platform for observing the non-equilibrium dynamics of spin systems. Disorder effects on its (dynamical) behavior are studied. First results on the realization of our proposal are discussed. Sections 4.1 - 4.4 prepare and motivate our work, which is then presented in Sections 4.5 - 4.7.

4.1 Quantum simulations and non-equilibrium dynamics

"Nature isn't classical, dammit, and if you want to make a simulation of nature, you'd better make it quantum mechanical" – It is difficult to resist quoting the closing words of Richard Feynman's influential talk on simulating physics with computers (Feynman, 1982). He alludes to the problem that the computational resources for simulating a quantum mechanical system on a classical computer generically increase exponentially with the number N of the system's constituents. This makes such simulations usually intractable as soon as there are more than, say, a few tens of them, even today. The need for simulations of quantum many-body systems, however, is omnipresent, not only in physics but also in chemistry or biology. For instance, the quest for an explanation of high-temperature superconductivity would greatly profit if one could simulate the behavior of candidate models for this phenomenon. Feynman envisioned that the problem stated above could be bypassed by using a *universal quantum simulator*, a quantum device consisting of discrete entities with tunable local interactions such that arbitrary or large classes of quantum systems could be efficiently simulated with it. Feynman's hypothesis was proved by Lloyd (1996). He showed that all quantum systems without long-range interactions can be efficiently simulated (so that the required resources increase polynomially in N) already with a spin one-half lattice equipped with a universal (Barenco *et al.*, 1995) set of nearest-neighbor interactions – which is essentially a quantum computer in the sense of DiVincenzo (2000).

To get an idea of the functioning of a quantum computer as universal quantum simulator, let us briefly sketch Lloyd's simulation protocol, which is also known as a *digital quantum sim-*

ulation. We assume that we want to simulate the time evolution generated by a Hamiltonian $\mathcal{H} = \sum_j^m H_j$ with local H_j. According to Lloyd's protocol, this time evolution is decomposed into many small steps by virtue of the Trotter formula (Trotter, 1959)

$$e^{-i\mathcal{H}t} \approx \left(e^{-iH_1 t/n} \cdot \ldots \cdot e^{-iH_m t/n}\right)^n, \tag{4.1}$$

for some large n. The action of $e^{-iH_j t/n}$ on the corresponding subspace of $\mathcal{H}$ is modeled by a number of quantum gates on an equivalent subspace of the quantum simulator. This is done for all j, n times in a row. For given t and desired simulation precision ($\sim n$), the time required for the simulation increases with N only as fast as m. The protocol can be extended to time-dependent Hamiltonians or to Liouvillian time evolution. Adiabatic or annealing protocols also allow one to investigate the ground state of a system of interest. In any case, we can state that the digital quantum simulation of a quantum many-body system requires the implementation of many coherent external state manipulations with a high fidelity.

Nevertheless, achieving a practically relevant quantum speed-up with a quantum computer still appears to be much easier in the simulation of quantum many-body systems than in non-quantum tasks such as number factorization or database search. The latter can be reasonably performed also with classical computers. To get a practical use of one of the few known quantum algorithms for such tasks, one would need to carry out millions of quantum operations without errors. On the other hand, performing, say, a few tens of Trotter steps on a quantum many-body system with 50 interacting spins does not seem to be hopelessly beyond the current experimental capabilities and would probably already outperform classical simulations. What is more, in a physical context we are often interested in system properties that are relatively robust with respect to perturbations, such as phase transitions. Therefore, one may hope that also the outcome of a corresponding quantum simulation is irrespective of small errors that might occur during the simulation, and that some relevant open physical questions can be addressed with quantum simulators even without the need to perform quantum error correction (Cirac and Zoller, 2012; Blatt and Roos, 2012). First digital quantum simulations of the dynamics generated by Hamiltonians describing up to six spins have been implemented by Lanyon *et al.* (2011).

However, there is a second approach to quantum simulations, which does not rely on the algorithmic operation of a quantum computer and which might be an easier, but still highly rewarding short-term goal for quantum technologies (Buluta and Nori, 2009; Cirac and Zoller, 2012) – so-called *analog quantum simulations*. The key idea of analog quantum simulations is to engineer the Hamiltonian of interest (which defies an analysis with classical computers) in an experimentally well-controlled system, and to obtain the solution to the problem at hand by appropriate measurements of the quantum simulator. Assuming that the desired Hamiltonian is implemented with a sufficient degree of accuracy, which to verify is a nontrivial task, the operation of an analog quantum simulator is relatively easy. Since external state manipulations and time-slicing are not necessary, an analog quantum simulator should be even less prone to errors than a digital quantum simulator. For these reasons, most efforts in the field of quantum simulations are currently directed to analog quantum simulations. Our work presented in this chapter also follows this approach. The main disadvantage of analog quantum simulations is the lack of universality. For each problem one is interested in, one has to find a suitable quantum

simulator. This will probably not always be possible. In fact, currently there are only a few quantum technologies with good enough experimental control to qualify as potential quantum simulators.

Up to now, answering a relevant open question by means of a quantum simulation has not yet been accomplished, despite impressive experimental progress in this regard (see later). To achieve this ultimate goal of quantum simulations, it is reasonable to focus on classes of quantum many-body problems to which none of the elaborate and powerful classical simulation techniques, such as Monte-Carlo simulations (Pollet, 2012) or the density matrix renormalization group (Schollwöck, 2011), to name just two, can be successfully applied. These typically involve strongly interacting fermions in more than one spatial dimension, frustrated spins, or non-equilibrium dynamics (Cirac and Zoller, 2012). The quantum simulator we will propose is intended to simulate the non-equilibrium dynamics of a quantum many-body system.

Generic non-equilibrium scenarios are not only difficult to simulate classically but also physically highly relevant (for a review on non-equilibrium dynamics, see Polkovnikov *et al.* (2011)). A question of fundamental importance is if there are universal features in the non-equilibrium dynamics of a quantum many-body system. One may ask, for instance, if or under which circumstances a quantum many-body system out of equilibrium will thermalize, that is, evolve into a state that looks locally as if the system was in thermal equilibrium. How do different types of observables behave under such dynamics? How do (quasi-)particles propagate in non-equilibrium situations? Can we understand the defect creation and associated processes when tuning the system through a quantum critical point? These questions have been intensely studied during the last years (see Polkovnikov *et al.* (2011) and our discussion below). To approach the general aspects of non-equilibrium dynamics, oftentimes concrete example systems are considered. However, for practical reasons, these have to be either analytically solvable or small enough to be accessible to numerical simulations. The exciting theory of non-equilibrium physics would likely profit a lot if it was possible to gain access to the dynamics of generic, non-integrable systems by means of quantum simulations. The work presented in this chapter might help to get closer to that. Before we go on and discuss the details of our proposed quantum simulator, we briefly summarize what has been achieved in the field of quantum simulations so far.

4.2 State of the art in quantum simulations

The conditions a quantum system has to fulfill to qualify as a potential quantum simulator have been cast into a concise list similar to the DiVincenzo criteria by Cirac and Zoller (2012). To put it crudely, but even more concisely, one can say that a potential quantum simulator is a quantum system with many precisely known degrees of freedom and a set of externally controllable parameters for which high-fidelity initialization and read-out is available. Among the most successful platforms for quantum simulations are currently systems of trapped ions (Blatt and Roos, 2012) and cold atomic gases (Bloch *et al.*, 2012). It has been argued by others (see Section 2.4), and will also be suggested in this chapter, that circuit QED could be a promising framework for quantum simulations as well.

Early experiments on quantum simulations have been conducted with liquid state nuclear

magnetic resonance (Somaroo *et al.*, 1999; Vandersypen and Chuang, 2005). Also some experiments on Josephson-junction arrays (Fazio and van der Zant, 2001) can be interpreted as going into this direction since these artificial systems enabled experimental studies of several interesting and otherwise hardly accessible phenomena. For instance, a Mott phase of strongly interacting bosons (vortices) was demonstrated by van Oudenaarden and Mooij (1996).

Both experimental and theoretical research on quantum simulations and related topics was greatly intensified through a series of seminal experiments with ultracold atoms in optical lattices, which demonstrated unprecedented control of a quantum many-body system: Greiner *et al.* (2002a) observed the quantum phase transition of the Bose-Hubbard Hamiltonian (Fisher *et al.*, 1989), realizing a proposal by Jaksch *et al.* (1998). The externally controllable depth of the optical lattice controls the ratio of the kinetic energy and the on-site interaction of the atoms and was used to tune the system from a superfluid to a Mott insulating phase (the same effects can be obtained by employing Feshbach resonances). In follow-up experiments, Greiner *et al.* (2002b) observed the collapse and the revival of the matter wave field of the Bose-Einstein condensate (akin to the circuit QED experiment by Kirchmair *et al.* (2013) discussed in Section 2.3), and Paredes *et al.* (2004) realized a Tonks-Girardeau gas of strongly repulsive bosons. With advancing state preparation and measurement techniques, it became possible, for example, to simulate the phase transition of the antiferromagnetic Ising model in a longitudinal field by identifying the spin components with lattice site occupation numbers (Simon *et al.*, 2011), to simulate negative temperatures for the motional degrees of freedom by melting a Mott insulator with inverted parameters of the Bose-Hubbard Hamiltonian (Braun *et al.*, 2013), or to simulate gauge fields interacting with the charge neutral atoms by generating a geometric (effective Aharonov-Bohm) phase for the moving particles with Raman lasers (Lin *et al.* (2009); no optical lattice was used there). Also experiments on non-equilibrium quantum many-body dynamics were conducted with cold bosonic gases, exploiting the excellent isolation of these systems from their environment. For instance, Kinoshita *et al.* (2006) observed the absence of thermalization of a near-integrable Bose gas out of equilibrium. The time evolution towards equilibrium following a quantum quench of the Bose-Hubbard Hamiltonian was measured by Trotzky *et al.* (2012). And the light-cone like spreading of correlations after a quench within the Mott phase of this Hamiltonian was seen by Cheneau *et al.* (2012), indicating the presence of a Lieb-Robinson bound in the system (Lieb and Robinson, 1972). Finally, we mention that there have been amazing experiments also with ultracold fermions (DeMarco and Jin, 1999), including the crossover from a Bose-Einstein condensate to a Bardeen-Cooper-Schrieffer superconductor for attractive interactions (Greiner *et al.*, 2003; Regal *et al.*, 2004) or the formation of a fermionic Mott insulator for repulsive interactions in the presence of an optical lattice (Jördens *et al.*, 2008; Schneider *et al.*, 2008). However, because of the required extremely low entropies, the regime of quantum magnetism in the Fermi-Hubbard model, which would be highly interesting for quantum simulations, started to come within reach only recently (Greif *et al.*, 2013). In a nutshell, the achievements listed above underline the distinguished role of cold atomic gases in the context analog quantum simulations.

Systems of ions in a linear trap are suited both for analog and digital quantum simulations, in particular, for systems that can be represented by interacting spins. Thereby, the internal electronics states of the ions are identified with the spins. There are several ways to generate

controlled interactions between the internal states of the ions. According to the groundbreaking proposal by Cirac and Zoller (1995), the motional sidebands of an individual ion can be externally driven to map the internal state of the ion to a collective vibrational state. Conditioned on the vibrational state, a second ion the trap is excited or not. The entangling part in this excitation consists in adding a sign to only one of the product states of collective motion and the spin of the second ion. To do so, this one state is selectively cycled through an auxiliary state. If after the conditional excitation of the second ion the motional state is swapped back to the first ion, one ends up with a CNOT gate between the two ions, which was first implemented by Schmidt-Kaler *et al.* (2003). Simpler techniques to obtain such interactions, ideally suited for simulating spin Hamiltonians (Porras and Cirac, 2004), involve simultaneous driving of the ions with two tones (Sørensen and Mølmer, 1999). Based on this, two spins with an (adiabatically) variable Ising coupling in a transverse field were simulated by Friedenauer *et al.* (2008) (in the sense of an analog quantum simulation). In a similar experiment with up to nine ions and long-range Ising coupling, Islam *et al.* (2011) were able to observe the precursors of a quantum phase transition from paramagnetic to ferromagnetic. Gerritsma *et al.* (2010) simulated the one-dimensional free Dirac equation and were able to observe Zitterbewegung. The two-component spinor was encoded in two internal levels of an ion and the ion's motional state. In a subsequent work, Gerritsma *et al.* (2011) included various scattering potentials for the Dirac particle in their quantum simulation, which allowed them to study Klein tunneling. An interacting spin system of potentially computational relevant scale was recently simulated by Britton *et al.* (2012). The authors used a Penning trap to create a two-dimensional Coulomb crystal of about 300 ions. Again, by coupling the internal states of the ions simultaneously to collective vibrational modes of the ion crystal, both ferromagnetic and anti-ferromagnetic Ising coupling of tunable range could be demonstrated. With improvements in the read-out and the implementation of a competing term in the Hamiltonian, this approach is highly promising for analog quantum simulations. Digital quantum simulations with trapped ions were impressively demonstrated by Lanyon *et al.* (2011). To simulate, for instance, the time evolution of a two-qubit state under the Hamiltonian $\mathcal{H} = H_1 + H_2 = \Omega/2(\sigma_z^1 + \sigma_z^2) + J\sigma_x^1\sigma_x^2$, the authors programmed quantum gates implementing H_1 and H_2 separately. By propagating a two-qubit state sequentially under H_1 and H_2, the authors showed that the measured time evolution converged to the calculated one upon decreasing the size of the Trotter steps (cf. Equation (4.1)). The authors successfully carried out digital quantum simulations of this type for more complicated Hamiltonians for up to six spins. Other works in the same spirit which also included the simulation of dissipative processes were conducted by Barreiro *et al.* (2011) and Schindler *et al.* (2013).

Finally, we remark that also all-optical quantum simulations have yielded promising results (O'Brien, 2007; Aspuru-Guzik and Walther, 2012). All-optical (*i.e.*, with no other particles than photons) quantum computations and simulations were initiated by an astonishing observation by Knill *et al.* (2001). These authors realized that entangling gates on usually barely interacting photonic qubits (encoded in the polarization states of photons) can be realized just by linear optical circuits if supplemented with appropriate measurements. Such and related measurement-induced photon-photon interactions were used to simulate, for instance, frustrated Heisenberg interactions of four spins in an analog quantum simulation (Ma *et al.*, 2011) or the time evolution of the eigenstates of the hydrogen molecule in a digital quantum simulation with two qubits,

which then facilitated the extraction of the energies of the eigenstates via a quantum phase estimation algorithm (Abrams and Lloyd, 1997; Aspuru-Guzik *et al.*, 2005; Lanyon *et al.*, 2010). A second type of experiments with photons having potential for quantum simulations is the implementation of quantum walks (Perets *et al.*, 2008; Broome *et al.*, 2010; Peruzzo *et al.*, 2010).

4.3 So why use circuit QED?

Thus, regarding quantum simulations, much has already been done with systems other than circuit QED. Trapped ions, ultracold atoms, or optical photons are still much better isolated from their environment and decoherence is much less of an issue, despite the tremendous evolution of circuit QED systems. What is more, ultracold atoms are naturally in the 'many-body regime' and trapped ions are about to reach it (Britton *et al.*, 2012), while circuit QED systems with more than four qubits are yet to be operated. Certainly, circuit QED is a very promising platform for quantum computing. If the rapid progress in this regard continues, digital quantum simulations might become possible with these systems in the long run. However, it is fair to ask what might be the benefit of attempting analog quantum simulations in circuit QED, which we and others (see Houck *et al.* (2012) and Schmidt and Koch (2013)) propose as a short-term goal.

Among the technologies discussed above, each one has it own advantages and weaknesses. For a certain class of problems to be simulated, one or the other might be suited better (if at all), and, as long as we do not have a universal quantum simulator at our disposal, there is much room for other quantum technologies to complement the currently most successful approaches to analog quantum simulations. Circuit QED systems, in particular, possess some features that might be advantageous for quantum simulations. For instance, they can be equipped with fast, local control lines for each of their constituents. The read-out is non-destructive. Coupling between different constituents can be engineered almost arbitrarily (potentially even tunable *in situ*). All these features are difficult to obtain, *e.g.*, with cold atoms. Drawbacks of other technologies that are not present or less severe in circuit QED include the following. In the case of ultracold atoms, both the parabolic confining potential and the currently attainable minimum temperatures set some limitations on possible experiments, in particular with regard to spin physics (Esslinger, 2010). Photonic quantum simulators suffer primarily from the lack of controlled single photon sources, which makes it difficult to proceed to larger systems (O'Brien, 2007; Aspuru-Guzik and Walther, 2012). Also ions in linear traps will probably face scalability issues at some point. Whether state-initialization, ion-ion coupling, and read-out in alternative, potentially scalable trap architectures reach the required level of performance remains to be seen.

Finally, as soon as quantum simulators are able to provide answers to questions that cannot be tackled by means of classical simulations, one is left with the problem to verify that these are sufficiently accurate. A good indication for that would be that the quantum simulation yields correct outcomes for special cases of the problem at hand which can be solved analytically or on a classical computer. For this reason, we will propose a circuit QED quantum simulator of an elementary (but nontrivial) many-body quantum system which can be solved exactly. If the simulation of this system succeeds, as seen by comparison of experiment and theoretical predictions, it will be easy in the flexible framework of circuit QED to implement integrability-

breaking interactions. However, a higher degree of reliability of a quantum simulation of a complex quantum many-body system would be obtained if the simulation was repeated with a second quantum simulator, based on an entirely different quantum technology. This alone justifies looking for new platforms for quantum simulations.

In the following sections, we will argue that circuit QED systems are suited for simulating quantum many-body spin systems and their non-equilibrium dynamics. Our proposal is based on a different concept than the earlier proposals on circuit QED quantum simulations of Bose-Hubbard physics, which we have reviewed in Section 2.4. Explicitly, we propose a quantum simulator of the quantum transverse-field Ising chain (TFIC). Despite the enormous importance of this system as a model example system (see next section), time-resolved experimental studies of its free non-equilibrium dynamics seem to be elusive – Lanyon *et al.* (2011) performed a digital quantum simulation of the time evolution generated by small Ising spin chains and, very recently, Fukuhara *et al.* (2013) made an analog quantum simulation of the non-equilibrium dynamics of the closely related one-dimensional Heisenberg model with ultracold bosonic atoms in an optical lattice. The essential properties of the TFIC and the tools for its mathematical treatment are described in our publications reprinted in Sections 4.5 and 4.6. Nevertheless, we provide a very brief non-technical account of the TFIC in the next section, primarily to explain its importance as a theoretical example system.

4.4 The quantum transverse-field Ising chain

The Hamiltonian of the quantum transverse-field Ising chain reads

$$\mathcal{H}_{\mathrm{I}} = \frac{\Omega}{2}\sum_{j=1}^{N}\sigma_z^j - J\sum_{j=1}^{N-1}\sigma_x^j\sigma_x^{j+1}. \tag{4.2}$$

It describes the elementary situation of N spin-$1/2$ particles sitting at sites j, coupled to their nearest neighbors with a strength J and to a transverse magnetic field of strength $\Omega/2 > 0$. Let us assume ferromagnetic coupling in this section, $J > 0$. In the limit $N \to \infty$, the TFIC undergoes a second-order quantum phase transition ($T = 0$) at critical normalized transverse field strength $\xi \equiv \Omega/2J = \xi_{\mathrm{c}} \equiv 1$. In the ferromagnetic phase, $\xi < 1$, there is long-range order in σ_x, which vanishes at the transition to the paramagnetic phase (for details, see below). Far in the ferromagnetic phase, the spins will point either the $+x$ or the $-x$ direction (the Z_2 symmetry $\Pi_j\sigma_z^j$ of $\mathcal{H}_{\mathrm{I}}$ is broken in this phase). Far in the paramagnetic phase, the spins point in the $-z$ direction. Non-zero temperatures destroy the sharp quantum phase transition. As long as the temperature is smaller than the energy gap present in both phases, the local system properties are preserved (characteristic spatial or temporal correlations have an extent exponential in the gap-temperature ratio). In the vicinity of ξ_{c}, the system is described by a universal quantum critical theory (as long as $k_{\mathrm{B}}T \ll \Omega, J$ (Sachdev, 1999)).

The TFIC can be exactly diagonalized by means of a Jordan-Wigner transformation (Jordan and Wigner, 1928; Lieb *et al.*, 1961; Pfeuty, 1970). This transformation maps $\mathcal{H}_{\mathrm{I}}$ to a quadratic fermion Hamiltonian. Pictorially, the transformation associates a flipped spin with the presence

of a particle which is destroyed by flipping the spin twice and therefore a fermion. The quadratic Hamiltonian can be brought into the form, $\mathcal{H}_{\mathrm{I}} = \sum_k \Lambda_k \eta_k^\dagger \eta_k$, where the η_k are fermionic. The excitation energies Λ_k can be analytically calculated up to a trigonometric equation, which can be solved either numerically or approximately for small π/N. However, we remark that the integrability of the model is lost as soon as one includes, say, next-nearest-neighbor interactions.

Because of the simplicity of the physical scenario, the availability of an exact solution and its quantum critical point, the TFIC was used as an example system in countless theoretical considerations, primarily in the fields of quantum phase transitions and non-equilibrium thermodynamics. An implementation of the TFIC in circuit QED might allow one to realize some of the obtained results in an experiment and is therefore certainly worthwhile beyond the prospect of benchmarking future quantum simulators of more complex spin systems.

4.5 Publication: Observing the nonequilibrium dynamics of the transverse-field Ising chain in circuit QED

Our proposal on implementing the quantum transverse-field Ising chain in circuit QED, motivated in the first parts of this chapter, has been previously published as a Letter in the journal *Physical Review Letters* and its accompanying online supplemental material. This section contains a reprint of this publication.

PRL 110, 030601 (2013) PHYSICAL REVIEW LETTERS week ending 18 JANUARY 2013

Observing the Nonequilibrium Dynamics of the Quantum Transverse-Field Ising Chain in Circuit QED

Oliver Viehmann,[1] Jan von Delft,[1] and Florian Marquardt[2]

[1]*Physics Department, Arnold Sommerfeld Center for Theoretical Physics, and Center for NanoScience, Ludwig-Maximilians-Universität, Theresienstraße 37, 80333 München, Germany*

[2]*Institut for Theoretical Physics, Universität Erlangen-Nürnberg, Staudtstraße 7, 91058 Erlangen, Germany*

(Received 9 August 2012; published 15 January 2013)

We show how a quantum Ising spin chain in a time-dependent transverse magnetic field can be simulated and experimentally probed in the framework of circuit QED with current technology. The proposed setup provides a new platform for observing the nonequilibrium dynamics of interacting many-body systems. We calculate its spectrum to offer a guideline for its initial experimental characterization. We demonstrate that quench dynamics and the propagation of localized excitations can be observed with the proposed setup and discuss further possible applications and modifications of this circuit QED quantum simulator.

DOI: 10.1103/PhysRevLett.110.030601 PACS numbers: 05.70.Ln, 03.67.Lx, 42.50.Pq, 75.10.Jm

The promising idea of tackling complex quantum many-body problems by quantum simulations [1,2] has become even more compelling recently, due to the widespread current interest in nonequilibrium dynamics. Indeed, experiments with cold atoms in optical lattices [3–6] and ions [7–10] have already made impressive progress in this regard. At the same time, the capabilities of scalable, flexible solid-state platforms are developing rapidly. In particular, circuit quantum electrodynamics (cQED) architectures of superconducting artificial atoms and microwave resonators [11–19] are now moving toward multiatom, multiresonator setups with drastically enhanced coherence times, making them increasingly attractive candidates for quantum simulations [20]. Here, we propose and analyze a cQED design that simulates a quantum transverse-field Ising chain with current technology. Our setup can be used to study quench dynamics, the propagation of localized excitations, and other nonequilibrium features in a field theory exhibiting a quantum phase transition (QPT) [21] and based on a design that could easily be extended to break the integrability of the system.

The present Letter takes a different path than the proposals for simulating Bose-Hubbard-type many-body physics in cavity arrays, which might be also realizable in cQED [20,22–26]. It is based on a possibly simpler concept—direct coupling of artificial atoms—that naturally offers access to quantum magnetism. The transverse-field Ising chain (TFIC) is a paradigmatic quantum many-body system. It is exactly solvable [27,28] and thus serves as a standard theoretical example in the context of nonequilibrium thermodynamics and quantum criticality [21,29–34]. Our proposal to simulate the TFIC and its nonequilibrium dynamics might help to mitigate the lack of experimental systems for testing these results. Moreover, the experimental confirmation of our predictions for various nonequilibrium scenarios in this integrable many-body system would serve as an important benchmark and allow one to proceed to variations of the design that break integrability or introduce other features.

Implementation of the TFIC.—A charge-based artificial atom (such as the Cooper-pair box or the transmon) [35] in a superconducting microwave resonator can be understood as an electric dipole (with dipole operator σ_x) that couples to the quantized electromagnetic field in the resonator [36]. Consider the system of Fig. 1, at first, without resonator B. Only the first artificial atom couples to resonator A. However, all atoms couple directly (not mediated by a quantized field) to their neighbors via dipole-dipole coupling $\propto \sigma_x^i \sigma_x^j$ (for details, see Ref. [37]). Coupling of this type has already been demonstrated with two Cooper-pair boxes [38] and two transmons [19]. Since this interaction is short ranged, we model our system by

$$\mathcal{H} = \omega_0(a^\dagger a + 1/2) + g(a^\dagger + a)\sigma_x^1 + \mathcal{H}_I, \quad (1)$$

where $\mathcal{H}_I$ is the Hamiltonian of the TFIC,

$$\mathcal{H}_I = \frac{\Omega}{2}\sum_{j=1}^{N}\sigma_z^j - J\sum_{j=1}^{N-1}\sigma_x^j\sigma_x^{j+1}. \quad (2)$$

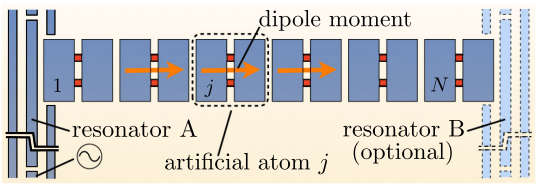

FIG. 1 (color online). Circuit QED implementation of the Ising model with a transverse magnetic field. The dipole moments of the artificial atoms tend to align. Resonator A (B) facilitates initialization and readout of the first (Nth) artificial atom by standard circuit QED techniques.

PRL 110, 030601 (2013) PHYSICAL REVIEW LETTERS week ending 18 JANUARY 2013

Here, $a^\dagger$ generates a photon with frequency ω_0, and $\sigma^j_{x/z}$ is a Pauli matrix. That is, we consider the artificial atoms as two-level systems (qubits). This is justified even for weakly anharmonic transmons since the experiments proposed below involve only low atomic excitation probabilities or well controllable excitation techniques (π pulses). Qubit 1 and the resonator couple with strength g. The qubit level spacing $\Omega > 0$ is tunable rapidly (~ 1 ns) via the magnetic flux through the qubits' SQUID loops [11–14]. It corresponds to the transverse magnetic field in the usual TFIC. In our geometry, the qubit-qubit coupling strength J is positive (ferromagnetic; the antiferromagnetic coupling $J < 0$ arises by rotating each qubit in Fig. 1 by 90° and is discussed in Ref. [37]). Estimates based on the typical dimensions of a cQED system yield $J/2\pi \sim 100$ MHz. Interdigitated capacitors between the qubits might significantly increase J. In general, tuning Ω will also affect J in a way that depends on the tuning mechanism and on the fundamental qubit parameters [37]. Using standard technology, upon variation of the magnetic flux, $J \propto \Omega$ for transmons, whereas, for Cooper-pair boxes, J is independent of Ω. Resonator A facilitates the initialization and readout of qubit 1 (with standard techniques [11]). Resonator B would allow one to measure end-to-end correlators. However, for simplicity, we consider a system with one resonator unless otherwise noted. We mention that the proposed setup should also be implementable using the novel, high-coherence 3d cQED devices [39]. Superconducting flux and phase qubits [35] can also be coupled to implement $\mathcal{H}_I$ and related Hamiltonians [15,17]. For different proposals on the implementation of and mean-field-type experiments with the TFIC in cQED, see Refs. [40,41], respectively.

In our calculations [37], we frequently use the spin-free-fermion mapping for $\mathcal{H}_I$ from Refs. [27,28]. It yields $\mathcal{H}_I = \sum_k \Lambda_k(\eta_k^\dagger \eta_k - 1/2)$, where $\eta_k^\dagger$ generates a fermion of energy $\Lambda_k = 2J\sqrt{1 + \xi^2 - 2\xi \cos k}$ and $\xi = \Omega/2J$ is the normalized transverse field. The allowed values of k satisfy $\sin kN = \xi \sin k(N+1)$. For $N \to \infty$, $\mathcal{H}_I$ undergoes the second order QPT at $\xi = 1$ from a ferromagnetic phase ($\xi < 1$) with long-range order in σ_x to a disordered, paramagnetic phase (for details, see Refs. [21,27,28,37]).

Spectrum of the system.—An initial experiment would likely characterize the setup by measuring the transmission spectrum S of the resonator as a function of probe frequency ω and qubit frequency Ω. For definiteness, we now assume that J is fixed and that the transverse field $\xi = \Omega/2J$ is tunable via Ω, as is the case for Cooper-pair boxes. A system with standard transmons can be shown to be confined to the paramagnetic phase (with fixed $\xi > 1$), but its spectrum as a function of ω and $J \propto \Omega$ otherwise displays the same features [37]. To calculate S, we first focus on the spectrum of the bare TFIC, $\tilde{\rho}(\omega) = \int dt e^{i\omega t} \langle \sigma_x^1(t)\sigma_x^1(0)\rangle$. It shows at which frequencies a field coupled to σ_x^1 can excite the chain. Assuming $g/\omega_0 \ll 1$, we then approximate the chain as a linear bath, coupled to the resonator: We replace it by a set of harmonic oscillators with the spectrum $\tilde{\rho}(\omega)$ of the TFIC. This allows us to compute S. Our calculations are for zero temperature. Except near the QPT, where $\mathcal{H}_I$ becomes gapless, this is experimentally well justified.

For finite N, the calculated spectrum $\tilde{\rho}(\omega)$ would consist of discrete peaks. In an experiment, they would be broadened by decay and, for large N, the measured spectrum would be continuous. This can be modeled by taking $N \to \infty$ in our calculations. In that case,

$$\tilde{\rho}(\omega) = 2\pi\delta(\omega)\Theta(1-\xi)(1-\xi^2) + \frac{4\xi}{\omega}\,\mathrm{Re}\sqrt{1-\cos^2 k(\omega)} \tag{3}$$

for $\omega \geq 0$, and $\tilde{\rho}(\omega < 0) = 0$. Here, $\Theta(x)$ is the Heaviside step function, and $\cos k(\omega) = [1 + \xi^2 - (\frac{\omega}{2J})^2]/2\xi$. The delta function for $\xi < 1$ is due to the nonzero mean value of $\mathrm{Re}\langle\sigma_x^1(t)\sigma_x^1(0)\rangle$ in this phase. We plot $\tilde{\rho}(\omega)$ for several ξ in Fig. 2(a). For $\xi > 1$ ($\xi < 1$), $\tilde{\rho}$ has a width of $4J$ ($4J\xi$), the bandwidth of the Λ_k. This might be helpful to measure J. At $\xi = 1$, $\tilde{\rho}$ becomes gapless and, thus, carries a clear signature of the QPT. The loss of normalization for $\xi = 0.5$ is compensated by the delta function in (3). This is required by a sum rule for $\tilde{\rho}$ and can be understood: In the ordered phase, the ground state $|0\rangle$ of the TFIC becomes similar to a σ_x eigenstate. Thus, driving via σ_x^1 is less efficient in causing excitations out of $|0\rangle$, but a static force on σ_x^1 will change the energy of $|0\rangle$. We note that, for all ξ, $\tilde{\rho}(\omega)$ has its maximum where the band Λ_k has zero curvature (and maximum slope). Thus, most η_k excitations

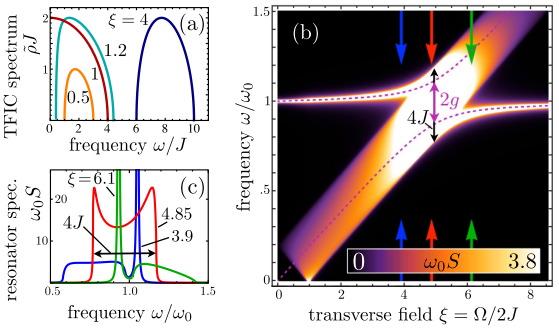

FIG. 2 (color online). Spectrum of the system. (a) Spectrum $\tilde{\rho}(\omega) = \int dt e^{i\omega t}\langle\sigma_x^1(t)\sigma_x^1(0)\rangle$ of an isolated transverse-field Ising chain for $N \to \infty$ and normalized transverse fields $\xi = \Omega/2J = 4, 1.2, 1, 0.5$. (b) Spectrum S of a resonator coupled to a TFIC (as in Fig. 1), plotted vs ξ and ω (for $N \to \infty$). The parameters used are $g = 0.12$, $J = 0.1$, and $\kappa = 10^{-4}$ (in units of ω_0). For better visibility of the features, values >3.8 are plotted in white. The dashed lines represent the excitation energies of $\mathcal{H}$ for $N = 1$. (c) S vs ω for $\xi = 3.9, 4.85, 6.1$ (blue, red, and green lines, respectively). These lines correspond to cuts along the arrows in (b).

of the TFIC have a nearly uniform velocity $v_0 = \max[d\Lambda_k/dk]$ ($v_0 = 2J\xi$ for $\xi < 1$ and $v_0 = 2J$ for $\xi > 1$), which will be important below.

We obtain resonator spectrum $S(\omega)$ in terms of $\tilde{\rho}(\omega)$,

$$S(\omega) = \frac{4\Theta(\omega)[\kappa + g^2\tilde{\rho}(\omega)]}{[\omega^2/\omega_0 - \omega_0 - 4g^2\chi(\omega^2)]^2 + [\kappa + g^2\tilde{\rho}(\omega)]^2}. \quad (4)$$

Here, $\chi(\omega^2)$ denotes the principal value integral $\chi(\omega^2) = 1/(2\pi)\int d\Omega\tilde{\rho}(\Omega)\Omega/(\omega^2 - \Omega^2)$ and κ is the full linewidth at half maximum of the Lorentzian spectrum of the uncoupled ($g = 0$) resonator. Our calculation uses tools that are explained, e.g., in Ref. [42]. It actually also applies when the resonator couples to a different system, with another spectrum $\tilde{\rho}(\omega)$. We plot S as function of ω and ξ in Fig. 2(b). For comparison, we also plot the resonances of the Jaynes-Cummings model, as they have been observed in numerous cQED experiments (dashed lines; case $N = 1$ in $\mathcal{H}$). As long as the spectrum $\tilde{\rho}(\omega)$ of the chain does not overlap the resonator frequency ω_0, there is a dispersive shift analogous to the off-resonant single-qubit case. Here, the chain causes only a small but broad side maximum and hardly modifies the dominant Lorentzian [green and blue lines in Fig. 2(c)]. If the chain comes into resonance, this changes dramatically, and $S(\omega)$ takes on large values over a region of width $\sim 4J$. For our choice of parameters, $S(\omega)$ develops a slightly asymmetric double-peak structure [red line in Fig. 2(c)]. This is again reminiscent of the Jaynes-Cummings doublet, but now the peaks are split by $4J$ rather than $2g$. We emphasize that the shape of the spectrum on resonance depends significantly on the ratio g/J. The larger $g/J > 1$, the closer the system resembles the single-qubit case (corresponds to $J = 0$). If $g/J < 1$, the double peak vanishes and one observes a Lorentzian around ω_0 with width $2g^2/J$ (for $g^2/J \gg \kappa$). This is because the resonator irreversibly decays into the chain, whose inverse bandwidth $\propto 1/J$ sets the density of states at $\omega \approx \omega_0$ and so determines the decay rate (for plots on both limiting cases and for finite N, see Ref. [37]).

Propagation of a localized excitation.—Off resonance, chain and resonator are essentially decoupled. In this situation, our setup allows one to study nonequilibrium dynamics in the TFIC. The resonator can be used to dispersively read out the first qubit. For measurements, this qubit must be detuned (faster than $2\pi/J$) from the chain so that it dominates the dispersive shift of the resonator [11] and decouples from the chain's dynamics.

First, we focus on the nonequilibrium dynamics of the chain after a local excitation has been created. As the resonator couples only to one qubit, the initialization of the system is easy. We assume that the chain is far in the paramagnetic phase ($\xi \gg 1$). Hence, $\langle\sigma_z^j\rangle \approx -1$ in its ground state. By applying a fast (~ 1 ns) π pulse, the first spin of the chain can be flipped without affecting the state of the other qubits (if $J/2\pi \ll 1$ GHz$/2\pi$ or if the first qubit is detuned from the others for initialization). We model the state of the system immediately after the π pulse by $\sigma_x^1|0\rangle$, where $|0\rangle$ is the ground state of the TFIC. The time evolution of the qubit excitations $\langle\sigma_z^j\rangle$,

$$\langle\sigma_z^j\rangle(t) = \langle 0|\sigma_x^1 e^{i\mathcal{H}_I t}\sigma_z^j e^{-i\mathcal{H}_I t}\sigma_x^1|0\rangle, \quad (5)$$

is plotted in Fig. 3 for a chain with $N = 20$ and $\xi = 8$ (right panel). The experimentally measurable trace of $\langle\sigma_z^1\rangle(t)$ is singled out on the left-hand side. Due to the qubit-qubit coupling, the excitation propagates through the chain, is reflected at its end, and leads to a distinct revival of $\langle\sigma_z^1\rangle$ at $Jt_R \approx N$. Assuming $J/2\pi = 50$ MHz, we find $t_R \approx 64$ ns for $N = 20$, which is safely below transmon coherence times. Note that the excitation propagates with velocity $v_0 = 2J$. This is because it consists of many excitations in k space, and most of them have velocity v_0.

Quench dynamics.—An appealing application of our system would be to observe its nonequilibrium dynamics after a sudden change of the transverse field $\xi = \Omega/2J$. By using fast flux lines, changes of Ω have been achieved practically instantaneously on the dynamical time scale of a cQED system (without changing the wave function) [12–14]. In our setup, such a change amounts to a (global) quantum quench of ξ if $J \neq \Omega$. This condition can be fulfilled by using qubits whose Josephson and charging energies [35] have a ratio $E_J/E_C \lesssim 10$ [37], that is, Cooper-pair boxes or transmons slightly out of their optimal parameter ratio [43]. In this regime, the tuning of J with Ω is weak (vanishes for Cooper-pair boxes). Since it would only lead to a rescaling of time by a factor ~ 1, we assume in the following that J is independent of Ω and consider quantum quenches of ξ in our system. Quantum quenches in the TFIC have been studied theoretically, e.g., in Refs. [30–33]. One usually assumes that for $t < 0$ the system is in the ground state $|0\rangle_a$ of the Hamiltonian $\mathcal{H}_{I,a}$

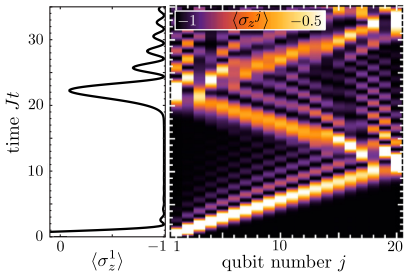

FIG. 3 (color online). Propagation of a localized excitation. Right: nonequilibrium time evolution of $\langle\sigma_z^j\rangle$ for all qubits j of a transverse Ising chain of length $N = 20$ in a normalized transverse field $\xi = \Omega/2J = 8$ (paramagnetic phase) after the first spin has been flipped. Values > -0.5 are plotted in white. Left: separate plot of $\langle\sigma_z^1\rangle$ on the same time scale. This quantity can be measured in the setup of Fig. 1.

PRL 110, 030601 (2013) PHYSICAL REVIEW LETTERS week ending 18 JANUARY 2013

at some initial value $\xi_a = \Omega_a/2J$. At $t = 0$, ξ is changed to $\xi_b = \Omega_b/2J$, and the time evolution under the action of $\mathcal{H}_{I,b}$ is investigated.

In the following, we focus on the dynamics of the experimentally easily accessible observable $\langle\sigma_z^1\rangle$ after quenches within the paramagnetic phase. This corresponds to our estimates for realistic values of J. The main difference of quenches involving the ferromagnetic phase would be a modified dynamical time scale due to the different value of v_0. Figure 4 shows the magnetization $\langle\sigma_z^j\rangle(t)$ after quenching ξ (center). In region I (see schematic plot, right), the magnetization first increases and then oscillates with decreasing amplitude. Here, it is virtually identical with the overall magnetization of a cyclic TFIC with $N \to \infty$ calculated in Ref. [30] and would, for $N \to \infty$, approach a constant value. This is in line with predictions from conformal field theory [32]. However, at $t = j/v_0$ and $t = (N - j)/v_0$ (dashed red lines in the schematic plot), where $v_0 = 2J$ as before, the magnetization has dips. They are followed (in regions II and III) by a relaxation similar as in region I to the same asymptotic value (see Ref. [37] for a zoomed-in plot). Near the system boundaries, the magnetization reaches and stays at this value for a considerable time before undergoing a revival. A sharp oscillation across the entire chain at $T = N/v_0$ subsequently decays. Revivals reoccur (quasi-)periodically with period T (region IV), but this behavior is smeared out for large times (not plotted). These phenomena are reflected in the measurable observable $\langle\sigma_z^1\rangle(t)$ (left panel) and take place on a time scale of ~ 0.1 μs for $N = 30$ and $J/2\pi = 50$ MHz.

Our results can be qualitatively understood in a simplifying quasiparticle (QP) picture that has already been used to calculate or interpret the (quench) dynamics of different quantities in the TFIC [31–34]. In the paramagnetic phase, the QPs correspond to spins pointing in the $+z$ direction. They are created in pairs by the quench and ballistically move with velocities $\pm v_0$ with reflections at the boundaries. Further, only contiguously generated QPs are correlated. After an initial transient, any given site will be visited only by uncorrelated QPs, originating from distant places. This leads to the relaxation of the magnetization to a steady-state value in region I that would be characterized by a certain static density of uncorrelated QPs. However, once correlated QPs meet again due to reflections at the boundaries, coherences are recreated and show up in oscillation revivals. This happens, first, at multiples of T (black solid lines in the schematic plot) when all QP trajectories cross their momentum-inverted counterparts (the solid red lines show an example) and, second, along the trajectories of QP pairs generated at the boundaries. Such QPs travel together as one partner is reflected at $t \approx 0$ (dashed red lines, not plotted in region IV for clarity). The periodicity of the trajectories should lead to periodic revivals for $t > T$. This is indeed observed approximately, although finally the velocity dispersion of the QPs renders the time evolution quasiperiodic. Finally, QP trajectories cannot intersect at $j = 1, N$. The density of (incoherent) QPs is thus lower here than for bulk sites, yielding an appreciably lower quasistationary value.

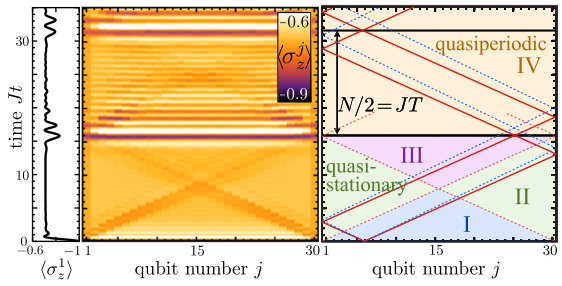

FIG. 4 (color online). Behavior after a quench: time evolution of the magnetization $\langle\sigma_z^j\rangle$ in a TFIC of length $N = 30$ after a quench of the normalized transverse field $\xi = 8 \to 1.2$ (center) with a schematic plot (right) and the measurable observable $\langle\sigma_z^1\rangle$ singled out (left) on the same time scale. Values < -0.9 (> -0.6) are plotted in black (white).

Discussion and outlook.—The setup and the experiments we have proposed might help to establish the simulation of interacting quantum many-body systems as a new paradigm in circuit QED and to bring parts of the theoretical discourse in nonequilibrium physics closer to observation. The phenomena discussed here are based on realizable system parameters and should occur within the system's coherence time. Given the readout capabilities in cQED (e.g., Ref. [16]), their measurement should be feasible, for instance, because single-shot readout is not required. Once an actual implementation sets some boundary conditions, the choice of system parameters can be further optimized. We have numerically verified that all presented results are robust against disorder up to a few percent in Ω and J [44]. Detuning individual qubits, however, would allow one to create arbitrary potentials for the excitations, study the interplay of Anderson localization and many-body physics, or change the effective chain length. Using a second resonator, the dynamics of the end-to-end correlator $\langle\sigma_x^1\sigma_x^N\rangle$ (indicating long-range order) could be measured (see Ref. [37]). Many other experiments are conceivable with our setup, such as suddenly coupling two isolated chains (and other local quenches) or even parameter ramps through the QPT, with Kibble-Zurek defect creation. We note also that hitherto unexplored measurement physics could be studied when the first qubit is not detuned from the chain, like resolving many-body eigenstates or the quantum Zeno effect in a many-body system. Once the setup is properly understood, it will be easy to break the integrability of our model in a controlled way (e.g., via longer-range couplings). This would push our cQED quantum simulator into a regime beyond classical computational capabilities, where further open questions about nonequilibrium

dynamics can be addressed, such as thermalization and diffusive transport. Furthermore, going to 2d or 3d introduces new design options, for instance, frustrated lattices.

We thank I. Siddiqi, R. Vijay, A. Schmidt, and N. Henry for discussions. O. V. thanks the QNL group at UC Berkeley for their hospitality. Support by NIM, the Emmy-Noether Program, and the SFB 631 of the DFG is gratefully acknowledged.

[1] R. Feynman, Int. J. Theor. Phys. **21**, 467 (1982).
[2] I. Buluta and F. Nori, Science **326**, 108 (2009).
[3] D. Jaksch, C. Bruder, J. I. Cirac, C. W. Gardiner, and P. Zoller, Phys. Rev. Lett. **81**, 3108 (1998).
[4] M. Greiner, O. Mandel, T. Esslinger, T. W. Hänsch, and I. Bloch, Nature (London) **415**, 39 (2002).
[5] J. Simon, W. S. Bakr, R. Ma, M. E. Tai, P. M. Preiss, and M. Greiner, Nature (London) **472**, 307 (2011).
[6] S. Trotzky, Y.-A. Chen, A. Flesch, I. P. McCulloch, U. Schollwöck, J. Eisert, and I. Bloch, Nat. Phys. **8**, 325 (2012).
[7] A. Friedenauer, H. Schmitz, J. T. Glueckert, D. Porras, and T. Schaetz, Nat. Phys. **4**, 757 (2008).
[8] R. Islam *et al.*, Nat. Commun. **2**, 377 (2011).
[9] B. P. Lanyon, C. Hempel, D. Nigg, M. Muller, R. Gerritsma, F. Zahringer, P. Schindler, J. T. Barreiro, M. Rambach, G. Kirchmair, M. Hennrich, P. Zoller, R. Blatt, and C. F. Roos, Science **334**, 57 (2011).
[10] J. W. Britton, B. C. Sawyer, A. C. Keith, C.-C. J. Wang, J. K. Freericks, H. Uys, M. J. Biercuk, and J. J. Bollinger, Nature (London) **484**, 489 (2012).
[11] A. Wallraff, D. I. Schuster, A. Blais, L. Frunzio, R.-S. Huang, J. Majer, S. Kumar, S. M. Girvin, and R. J. Schoelkopf, Nature (London) **431**, 162 (2004).
[12] L. DiCarlo, M. D. Reed, L. Sun, B. R. Johnson, J. M. Chow, J. M. Gambetta, L. Frunzio, S. M. Girvin, M. H. Devoret, and R. J. Schoelkopf, Nature (London) **467**, 574 (2010).
[13] A. Fedorov, L. Steffen, M. Baur, M. P. da Silva, and A. Wallraff, Nature (London) **481**, 170 (2012).
[14] M. D. Reed, L. DiCarlo, S. E. Nigg, L. Sun, L. Frunzio, S. M. Girvin, and R. J. Schoelkopf, Nature (London) **482**, 382 (2012).
[15] R. McDermott, R. W. Simmonds, M. Steffen, K. B. Cooper, K. Cicak, K. D. Osborn, S. Oh, D. P. Pappas, J. M. Martinis, Science **307**, 1299 (2005).
[16] R. Vijay, D. H. Slichter, and I. Siddiqi, Phys. Rev. Lett. **106**, 110502 (2011).
[17] M. W. Johnson *et al.*, Nature (London) **473**, 194 (2011).
[18] M. Mariantoni *et al.*, Science **334**, 61 (2011).
[19] A. Dewes, F. Ong, V. Schmitt, R. Lauro, N. Boulant, P. Bertet, D. Vion, and D. Esteve, Phys. Rev. Lett. **108**, 057002 (2012).
[20] A. A. Houck, H. E. Türeci, and J. Koch, Nat. Phys. **8**, 292 (2012).
[21] S. Sachdev, *Quantum Phase Transitions* (Cambridge University Press, Cambridge, England, 1999).
[22] M. J. Hartmann, F. G. S. L. Brandao, and M. B. Plenio, Nat. Phys. **2**, 849 (2006).
[23] A. D. Greentree, C. Tahan, J. H. Cole, and L. C. L. Hollenberg, Nat. Phys. **2**, 856 (2006).
[24] J. Koch and K. L. Hur, Phys. Rev. A **80**, 023811 (2009).
[25] M. Schiró, M. Bordyuh, B. Öztop, and H. E. Türeci, Phys. Rev. Lett. **109**, 053601 (2012).
[26] M.-J. Hwang and M.-S. Choi, arXiv:1207.0088.
[27] E. Lieb, T. Schultz, and D. Mattis, Ann. Phys. (N.Y.) **16**, 407 (1961).
[28] P. Pfeuty, Ann. Phys. (N.Y.) **57**, 79 (1970).
[29] A. Polkovnikov, K. Sengupta, A. Silva, and M. Vengalattore, Rev. Mod. Phys. **83**, 863 (2011).
[30] E. Barouch, B. McCoy, and M. Dresden, Phys. Rev. A **2**, 1075 (1970).
[31] F. Iglói and H. Rieger, Phys. Rev. Lett. **85**, 3233 (2000).
[32] P. Calabrese and J. Cardy, Phys. Rev. Lett. **96**, 136801 (2006); J. Stat. Mech. (2007) P06008.
[33] H. Rieger and F. Iglói, Phys. Rev. Lett. **106**, 035701 (2011); Phys. Rev. B **84**, 165117 (2011).
[34] S. Sachdev and A. P. Young, Phys. Rev. Lett. **78**, 2220 (1997).
[35] J. Clarke and F. Wilhelm, Nature (London) **453**, 1031 (2008).
[36] R. J. Schoelkopf and S. M. Girvin, Nature (London) **451**, 664 (2008).
[37] See Supplemental Material at http://link.aps.org/supplemental/10.1103/PhysRevLett.110.030601 for our explicit calculations and some additional details.
[38] Yu. A. Pashkin, T. Yamamoto, O. Astafiev, Y. Nakamura, D. V. Averin, and J. S. Tsai, Nature (London) **421**, 823 (2003).
[39] H. Paik *et al.*, Phys. Rev. Lett. **107**, 240501 (2011).
[40] Y.-D. Wang, F. Xue, Z. Song, and C.-P. Sun, Phys. Rev. B **76**, 174519 (2007).
[41] L. Tian, Phys. Rev. Lett. **105**, 167001 (2010).
[42] F. Marquardt and D. S. Golubev, Phys. Rev. A **72**, 022113 (2005).
[43] J. Koch, T. Yu, J. Gambetta, A. Houck, D. Schuster, J. Majer, A. Blais, M. Devoret, S. Girvin, and R. Schoelkopf, Phys. Rev. A **76**, 042319 (2007).
[44] O. Viehmann, J. von Delft, and F. Marquardt (to be published).

Supplementary Material for "Observing the nonequilibrium dynamics of the quantum transverse-field Ising chain in circuit QED"

Oliver Viehmann,[1] Jan von Delft,[1] and Florian Marquardt[2]
[1]*Physics Department, Arnold Sommerfeld Center for Theoretical Physics, and Center for NanoScience, Ludwig-Maximilians-Universität, Theresienstraße 37, 80333 München, Germany and*
[2]*Institut for Theoretical Physics, Universität Erlangen-Nürnberg, Staudtstraße 7, 91058 Erlangen, Germany*

CONTENTS

I. THE QUBIT-QUBIT COUPLING HAMILTONIAN

In this section, our goal is to derive the Hamiltonian of a chain of capacitively coupled charge-based artificial atoms as in Fig. 1 of the main text from circuit theory. Both for Cooper-pair boxes (CPBs) and for transmons (for reviews on superconducting artificial atoms, see [1, 2]), this Hamiltonian takes on the form of $\mathcal{H}_I$ [Eq. (2) of the main text]. Our derivation of the Hamiltonian on the basis of circuit theory enables us to analyze the dependence of Ω and J (and thus of $\xi = \Omega/2J$) on the fundamental, engineerable parameters of the artificial atoms and on an externally applied, in-situ tunable magnetic flux.

We model the chain of artificial atoms in Fig. 1 of the main text by the circuit diagram of Fig. S1. The SQUID-like loop of the jth artificial atom can be threaded by a (classical) external magnetic flux bias Φ_j. Its identical Josephson junctions are characterized each by a Josephson energy $\epsilon_{J,j}$. For simplicity, we absorb the capacitances of the Josephson junctions into the capacitance C_j between the islands of the artificial atom (which shunts the SQUID loop). Moreover, we take into account only coupling capacitances $\mathcal{C}_j$ between the right island of the jth artificial atom and the left island of the $j+1$st artificial atom. The mediated capacitive coupling between the artificial atoms corresponds to the electrostatic coupling of the electric dipole operators of charge distributions in atomic QED [3], which we have employed in the main text to motivate the Hamiltonian $\mathcal{H}_I$. In order to be able to compare our results with previous ones [4, 5], we do not assume that the artificial atoms are identical for the moment.

We begin by considering the conceptionally important case $N = 2$. This case has been already studied for CPBs [4] and transmons [5] in similar setups. Using the standard approach to circuit quantization [6, 7], one obtains $H^{(2)} = \sum_{j=1}^{2}(q_j^2/2\tilde{C}_j - E_{J,j}^{\Phi}\cos 2e\phi_j) + q_1 q_2/\tilde{\mathcal{C}}$. Here, $\hbar = 1$, ϕ_j and q_j are the conjugate quantum flux and charge variables, $[\phi_j, q_j] = i$, and e is the elementary charge. We have defined $\tilde{C}_j = C_*^2/(C_j + \mathcal{C})$, $\tilde{\mathcal{C}} = C_*^2/\mathcal{C}$, and $C_*^2 = C_1C_2 + C_1\mathcal{C} + C_2\mathcal{C}$ (for $N = 2$, we drop the index 1 from $\mathcal{C}_1$ and related quantities like $\tilde{\mathcal{C}}_1$). Furthermore, $E_{J,j}^{\Phi} = E_{J,j}(\Phi_j) = 2\epsilon_{J,j}\cos(\pi\Phi_j/\Phi_0)$, where Φ_0 is the superconducting flux quantum. As usual, we introduce charging energies $E_{C,j} = e^2/2\tilde{C}_j$, number and phase operators $\hat{n}_j = -q_j/2e$ and $\varphi_j = -2e\phi_j$ (see, e.g., [7]), and a coupling energy $E_{\mathcal{C}} = e^2/2\tilde{\mathcal{C}}$. The effects of possible gate voltages that might bias the superconducting islands of an artificial atom are taken into account by introducing offset charges $n_{b,j} \in \mathbb{R}$ (in units of $2e$) and substituting $\hat{n}_j \to \hat{n}_{b,j} \equiv \hat{n}_j - n_{b,j}$ (possible gate capacitances are assumed to be absorbed in $E_{C,j}$ and $E_{\mathcal{C}}$). With these substitutions,

$$H^{(2)} = h_1 + h_2 + 8E_{\mathcal{C}}\hat{n}_{b,1}\hat{n}_{b,2}. \tag{S.1}$$

The $h_j = 4E_{C,j}\hat{n}_{b,j}^2 - E_{J,j}^{\Phi}\cos\varphi_j$ describe the energies of two isolated artificial atoms. The eigenfunctions (in the φ_j-basis) and eigenvalues of h_j are Mathieu's functions and characteristic values [8–10]. Their numerical values can be determined with arbitrary precision for all parameters $E_{C,j}$, $E_{J,j}^{\Phi}$, and $n_{b,j}$ (and all φ_j) and are implemented in standard math programs. Taking the ground state $|g_j\rangle$ and the first excited state $|e_j\rangle$ of h_j to be eigenstates of σ_z^j and restricting the Hilbert space to these

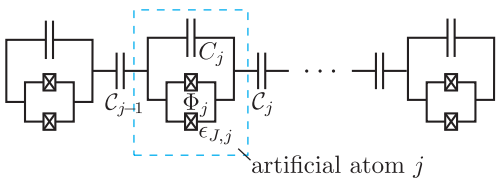

FIG. S1. Circuit diagram of a chain of capacitively coupled charge-based artificial atoms as in Fig. 1 of the main text.

qubit bases, the Hamiltonian of the system becomes (up to a constant)

$$H^{(2)} = \sum_{j=1}^{2} \frac{\Omega_j}{2}\sigma_z^j + 8E_{\mathcal{C}} \prod_{j=1}^{2} \sum_{m_j,n_j} (\hat{n}_{b,j})_{m,n} |m_j\rangle\langle n_j|. \tag{S.2}$$

Here, Ω_j is the difference between the qubit eigenenergies, $(\hat{n}_{b,j})_{m,n} = \langle m_j|\hat{n}_{b,j}|n_j\rangle$, and $m_j, n_j \in \{g_j, e_j\}$. Using the explicit forms of $\langle\varphi_j|m_j\rangle$ from [8–10] and $\hat{n}_j = -i\partial/\partial\varphi_j$, the $(\hat{n}_{b,j})_{m,n}$ are found to be real and can be numerically calculated. In general, the $\hat{n}_{b,j}$ have diagonal elements in our choice of basis. However, for the most common types of charge-based artificial atoms, CPBs and transmons, $H^{(2)}$ takes on the form of $\mathcal{H}_I$ for $N = 2$, which is insightful to consider before returning to the general case.

CPBs are characterized by $4E_{C,j} \gg E_{J,j}^{\Phi}$. Since we are interested only in the low-energy sector of the Hilbert space of (S.1), this condition allows us, in good approximation, to restrict the Hilbert space to the number states $\{|n_j\rangle, |(n+1)_j\rangle\}$. Here, $n_j = \lfloor n_{b,j} \rfloor$ [1]. Without loss of generality, one can choose $n_{b,j} \in [0, 1[$. This restriction leads from Eq. (S.1) to

$$\begin{aligned} H_{CPB}^{(2)} = \sum_{j=1}^{2} \Big[& 4E_{C,j}(n_{b,j}^2 |0_j\rangle\langle 0_j| + (1-n_{b,j})^2 |1_j\rangle\langle 1_j|) \\ & - \frac{E_{J,j}^{\Phi}}{2}(|0_j\rangle\langle 1_j| + \text{H.c.})\Big] \\ & + 8E_{\mathcal{C}} \prod_{j=1}^{2} \sum_{n_j=0}^{1} (n_j - n_{b,j}) |n_j\rangle\langle n_j|, \end{aligned} \tag{S.3}$$

in close similarity to the Hamiltonian derived in [4]. If the CPBs are operated as usual at the charge degeneracy points $n_{b,j} = 1/2$ (to decrease charge noise), $|g_j\rangle$ ($|e_j\rangle$) is an (anti-)symmetric superposition of $|0_j\rangle$ and $|1_j\rangle$. We drop constants, identify $|0_j\rangle\langle 1_j| = \sigma_-^j$, and rotate the coordinate system by $\pi/2$ around the y-axis (clockwise). This brings $H_{CPB}^{(2)}$ into the form of Eq. (S.2),

$$H_{CPB}^{(2)} = \sum_{j=1}^{2} \frac{E_{J,j}^{\Phi}}{2}\sigma_z^j + 2E_{\mathcal{C}}\sigma_x^1\sigma_x^2. \tag{S.4}$$

This Hamiltonian also has the form of $\mathcal{H}_I$ for $N = 2$ (since $\hat{n}_{b,j}$ transforms into $\sigma_x^j/2$ under the present assumptions). That is, in the case of CPBs, the transition frequencies Ω_j are simply given by $E_{J,j}^{\Phi}$ and flux-tunable. The qubit-qubit coupling $J = 2E_{\mathcal{C}}$ depends only on the capacitances of the system and is independent of Φ_j and the qubit transition frequencies ($\mathrm{d}J/\mathrm{d}\Omega_j = 0$). Thus, the normalized transverse field $\xi = \Omega/2J$ (for $\Omega_1 = \Omega_2$) is strictly linear in Ω.

For transmons-qubits [10], which are characterized by $4E_{C,j} \ll E_{J,j}^{\Phi}$, (i) expanding the $\cos\phi_j$ terms in h_j of Eq. (S.1) and (ii) dropping the boundary condition $\psi_{j,m}(\varphi_j) = \psi_{j,m}(\varphi_j + 2\pi)$ on the eigenfunctions of h_j provides a good approximation [10]. Note that due to (ii), the effect of the offset charges $n_{b,j}$ is completely suppressed since the $\hat{n}_j$ and the biased number operators $\hat{n}_{b,j}$ are equivalent canonical variables, $[\varphi_j, \hat{n}_{b,j}] = [\varphi_j, \hat{n}_j] = i$. This is justified as the dependence of the qubit properties on the offset charges is exponentially suppressed with increasing ratio $E_{J,j}^{\Phi}/E_{C,j}$ [10] (in reality, gate voltages do not have to be applied to transmons). Thus, we now aim to derive the parameters Ω_j and $(\hat{n}_{b,j})_{m,n}$ occuring in Eq. (S.2) from Eq. (S.1) with

$$\begin{aligned} h &\approx 4E_C\hat{n}_b^2 - E_J^{\Phi}(1 - \varphi^2/2! + \varphi^4/4!) \\ &= \Omega_0(a^\dagger a + 1/2) - \alpha\Omega_0(a^\dagger + a)^4/4! + \text{const.}, \end{aligned} \tag{S.5}$$

in a perturbation expansion in $\alpha = (E_C/2E_J^{\Phi})^{1/2} \ll 1$. Here and in the following, we drop the index j where not essential. Note that α is proportional to an approximate expression for a transmon's 'relative anharmonicity' [10]. We have defined $\Omega_0 = (8E_J^{\Phi}E_C)^{1/2}$, $\varphi = \sqrt{2\alpha}(a^\dagger + a)$, $\hat{n}_b = i/\sqrt{8\alpha}(a^\dagger - a)$, and $[\phi, \hat{n}_b] = i$ requires a to be bosonic. This approach has been used in [10] to study a single transmon and its coupling to a microwave resonator. To first order in α, $|g_\alpha\rangle = |0\rangle + \alpha/4!(3\sqrt{2}|2\rangle + \sqrt{3/2}|4\rangle)$ and $|e_\alpha\rangle = |1\rangle + \alpha/4!(5\sqrt{6}|3\rangle + \sqrt{15/2}|5\rangle)$, where $|m\rangle$ is now an eigenstate of $a^\dagger a$. We substitute Eq. (S.5) and the above expression for $\hat{n}_b$ into Eq. (S.1) and expand the resulting transmon-approximation $H_t^{(2)}$ of $H^{(2)}$ in the qubit basis spanned by $|g_\alpha\rangle$ and $|e_\alpha\rangle$. Dropping constants and all terms $\propto \alpha^x$ with $x > 1$, and rotating the coordinate system counter-clockwise by $\pi/2$ around the z-axis leads to

$$H_t^{(2)} = \sum_{j=1}^{2} \frac{\Omega_{0,j}(1-\alpha_j/2)}{2}\sigma_z^j + E_{\mathcal{C}} \prod_{j=1}^{2} \frac{(1-\alpha_j/4)}{\sqrt{\alpha_j}}\sigma_x^j.$$

This transmon approximation of Eq. (S.2) also has the form of $\mathcal{H}_I$ for $N = 2$. We remark that in 0th order perturbation theory, where the transmons are harmonic oscillators, the terms in parentheses in $H_t^{(2)}$ are equal to 1. However, the term $1/\sqrt{\alpha_1\alpha_2}$, stemming from the product of the $\hat{n}_{b,j}$ operators, is present. The 0th order result corresponds to the Hamiltonian derived in [5] for their system of coupled transmons. To first order in α, the transmon transition frequencies are given by $\Omega_j = \Omega_{0,j}(1-\alpha_j/2) = (8E_{J,j}^{\Phi}E_{C,j})^{1/2} - E_C$ [10]. They are flux-tunable via $(E_{J,j}^{\Phi})^{1/2}$ (rather than $\Omega_j \propto E_{J,j}^{\Phi}$ as for CPBs). For transmons, the qubit-qubit coupling is given by $J = E_{\mathcal{C}}\prod(1-\alpha_j/4)/\sqrt{\alpha_j}$. Importantly, this J depends also on external fluxes via $\alpha_j \propto (E_{J,j}^{\Phi})^{-1/2}$ (and on the transition frequencies via $\alpha_j = 2E_{C,j}/\Omega_{0,j}$). Since the physical properties of a uniform TFIC are essentially determined by the normalized transverse field $\xi = \Omega/2J$ (the absolute values of Ω and J only set the dynamical time scales), we use our perturbative results to study the tunability of ξ for identical transmons. We

insert our first-order results for Ω and J into ξ and expand $\xi \approx (\Omega_0/2E_\mathcal{C})[\alpha - \alpha^3/16 + \mathcal{O}(\alpha^4)]$, where we have set $E_{C(J),1} = E_{C(J),2}$. The overall factor α comes from the nominator of J and is not due to the nonlinear perturbation of the system as argued above. Factoring out $\alpha = 2E_C/\Omega_0$ yields

$$\xi \approx \frac{E_C}{E_\mathcal{C}}(1 - \alpha^2/16 + \mathcal{O}(\alpha^3)) \approx \frac{E_C}{E_\mathcal{C}}. \qquad \text{(S.6)}$$

That is, the first order corrections to Ω and J in α exactly cancel. For transmons, flux-tunability of ξ is a second-order effect, via $\alpha^2 = E_C/2E_J^\Phi$. To roughly estimate the strength of this effect, we consider the contribution of the first-order approximations of Ω and J to it. Note that the second-order approximations of Ω and J actually also contribute to the leading flux-dependent term ($\propto \alpha^2$) of ξ. If one requires the transmons to remain in their optimal working regime $20 \lesssim E_J^\Phi/E_C$ [10], this contribution leads to a tunability $\Delta\xi/\xi \approx \alpha^2/(16-\alpha^2) < 0.2\%$. Thus, one may expect that strongly tuning ξ by changing the flux bias will require to leave the optimal transmon working regime, and possibly even to go beyond the validity regime of Eq. (S.5). Therefore, we now come back to the general case of Eq. (S.1). Before doing so, we remark that $\xi \approx E_C/E_\mathcal{C} = (C + \mathcal{C})/\mathcal{C} > 1$. This indicates that the ferromagnetic phase ($\xi < 1$) cannot be reached with transmons.

It turns out that at the charge degeneracy point $n_b = 1/2$, the biased charge operator $\hat{n}_b = \hat{n} - n_b$ has only off-diagonal elements in the basis chosen in Eq. (S.2). Consequently, $H^{(2)}$ has the form of $\mathcal{H}_I$ (at $N = 2$) for all ratios $E_{J,j}^\Phi/E_{C,j}$. This enables us to interpolate between the charge-degenerate CPB case and the transmon case (where the $n_{b,j}$ become irrelevant): Assuming identical qubits, we vary the ratio E_J^Φ/E_C at $n_b = 1/2$. We numerically calculate $J = 8E_\mathcal{C}[(\hat{n}_b)_{g,e}]^2$ and Ω as functions of E_J^Φ/E_C. Then we plot J vs. Ω [Fig. S2(a)] and ξ vs. Ω [Fig. S2(b)]. Additionally, we plot the approximate results that we have gained analytically for CPBs and transmons. To obtain J as a function of Ω from our analytical results for transmons, we employ our approximation for J to first order in α. In this approximation, we replace $\alpha \approx 2E_C/(\Omega + E_C)$, making use of the first order approximation for Ω. The plots show that for $E_J^\Phi/E_C \gtrsim 10$, the qubit-qubit coupling J becomes proportional to Ω, and the normalized transverse field ξ ceases to be flux-tunable. For quenching ξ by changing the flux bias one therefore has to engineer $E_J^\Phi/E_C \lesssim 10$. In this regime, the artificial atoms start to loose their insensitivity to charge noise, which is a distinguishing property of transmons. For instance, at $E_J^\Phi/E_C = 10$, $[\max\Omega(n_b) - \min\Omega(n_b)]/\overline{\Omega(n_b)} \approx 3\%$. Here, $\overline{\Omega(n_b)}$ denotes the mean qubit transition frequency, averaged over all possible bias charges n_b. However, the characteristic features of the quench dynamics of our circuit QED quantum simulator occur on short timescales (see main text), so that one should get along with the reduced dephasing times of charge qubits in this regime (compared to usual transmons). For example, an energy relaxation time T_1 of $\sim 7\mu$s and a dephasing time T_2 of ~ 500ns have been reported even for a CPB (at the charge degeneracy point) [11]. We remark that, depending on the charge bias n_b, Ω can be equal to the energy difference between second and first excited state of the artificial atom, $E_{2,1}$, which would invalidate the two-level approximation for the artificial atoms. For instance, if $n_b = 0.5$ as considered here, this happens at $E_J^\Phi/E_C \approx 9.03$ [10]. However, the difference of these transitions crosses zero very steeply as a function of E_J^Φ/E_C [10]. Thus, the two-level approximation for the artificial atoms is justified as long as start or end point of the quench are not too close to this value. We finally remark that working with tunable coupling capacitances [12] might provide an alternative to working with transmons out of their optimal parameter range. This would allow one to tune ξ via tuning $E_\mathcal{C}$.

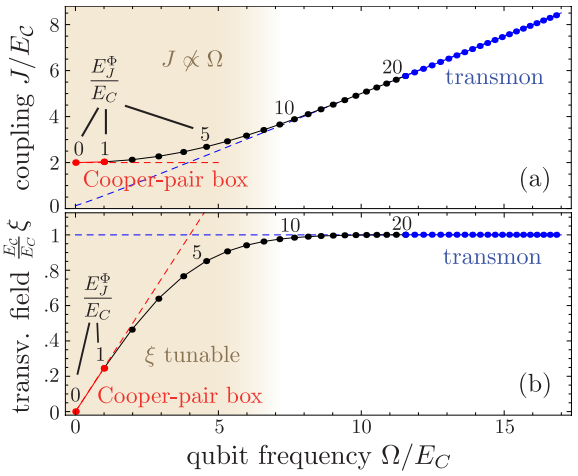

FIG. S2. (a) Qubit-qubit coupling J and (b) normalized transverse field $\xi = \Omega/2J$ vs. qubit transition frequency Ω for two identical charge qubits operated at the charge degeneracy point. The system is characterized by the charging energy E_C and the flux-tunable total Josephson energy E_J^Φ of a qubit, and by the capacitive coupling energy $E_\mathcal{C}$. The ratio E_J^Φ/E_C fully determines a point on each axis (i.e., the quantities Ω/E_C, J/E_C, and $\frac{E_C}{E_C}\xi$). The dots correspond to the integer values $0, 1, \ldots, 40$ of E_J^Φ/E_C. The solid lines are a guide to the eye. Dashed, approximate analytical results for the limits $E_J^\Phi/4E_C \ll 1$ (Cooper-pair boxes) and $E_J^\Phi/4E_C \gg 1$ (transmons).

Coming now to the general case of a chain of artificial atoms of arbitrary length, it turns out that we can directly apply our results for $N = 2$. Having written the Lagrangian of such a system in terms of the classical variables ϕ_j and $\dot{\phi}_j$ [6, 7], one finds that the canonical charge variables q_j are given by $\mathbf{q} = \underline{C}\dot{\boldsymbol{\phi}}$. Here, we have

defined $\mathbf{q} = (q_1, \ldots, q_N)^T$, $\dot{\boldsymbol{\phi}} = (\dot{\phi}_1, \ldots, \dot{\phi}_M)^T$, and

$$\underline{C} = \begin{pmatrix} C+\mathcal{C} & -\mathcal{C} & 0 & & \cdots & 0 \\ -\mathcal{C} & C+2\mathcal{C} & -\mathcal{C} & & & \\ 0 & -\mathcal{C} & C+2\mathcal{C} & -\mathcal{C} & & \\ \vdots & & \ddots & \ddots & \ddots & \\ & & & -\mathcal{C} & C+2\mathcal{C} & -\mathcal{C} \\ 0 & & & & -\mathcal{C} & C+\mathcal{C} \end{pmatrix},$$

and we have assumed that the artificial atoms are identical, $C_j = C$ and $\mathcal{C}_j = \mathcal{C}$. Inverting $\underline{C}$ yields $\ddot{\boldsymbol{\phi}}(\mathbf{q})$. With that, one obtains the Hamiltonian H of the system, which is then quantized as usual [6, 7]. To first order in $\mathcal{C}/C$,

$$H = \sum_{j=1}^{N} \left(\frac{q_j^2}{2C} - E_J^{\Phi} \cos 2e\phi_j \right) + \frac{\mathcal{C}}{C} \left(\frac{-q_1^2 - q_N^2 - \sum_{j=2}^{N-1} 2q_j^2 + \sum_{j=1}^{N-1} 2q_j q_{j+1}}{2C} \right). \tag{S.7}$$

The same steps as for $N = 2$ now lead to a straightforward generalization of Eq. (S.1), where artificial atoms with Hamiltonian h_j are coupled to their nearest neighbours via $\hat{n}_{b,j}\hat{n}_{b,j+1}$ [for $N = 2$, Eq. (S.7) equals the first order expansion of $H^{(2)}$ above Eq. (S.1)]. To first order in $\mathcal{C}/C$, the only difference for $N > 2$ is that the effective charging energies of the artificial atoms in the bulk of the chain ($j \neq 1, N$) are slightly reduced compared to those at the surface ($j = 1, N$). This is because the bulk artificial atoms couple to two neighbours. In reality, this surface inhomogeneity should be negligible already because the capacitance of the surface artificial atoms is also increased by their coupling to other parts of the circuit. Therefore, to first order in $\mathcal{C}/C$, our derivation of the Hamiltonian $\mathcal{H}_I$ of the TFIC from the circuit theory of two artificial atoms also holds for larger chains, only with a slightly renormalized E_C. The same is true for our corresponding deliberations on the dependence of Ω, J, and ξ on the fundamental circuit quantities. We remark that taking into account terms of order $(\mathcal{C}/C)^l$ introduces coupling terms $\propto q_j q_{j+l}$ in Eq. (S.7) (and, for $l > 1$, renormalizes also the nearest neighbour coupling energies $E_{\mathcal{C}}$ compared to the case $N = 2$). Hence, the integrability-breaking longer-range coupling decays exponentially with distance l in our system and is therefore neglected in this work. We finally remark that nonperturbative numerical calculations strongly suggest that also the renormalized values of E_C and $E_{\mathcal{C}}$ for $N > 2$ do not allow one to achieve $E_C/E_{\mathcal{C}} < 1$. This means that the ferromagnetic phase cannot be reached with transmons in the limit of large E_J^{Φ}/E_C [cf. Eq. (S.6)].

II. DIAGONALIZATION AND SPECTRUM OF THE TRANSVERSE-FIELD ISING CHAIN

In this section, we diagonalize the Hamiltonian $\mathcal{H}_I$ [Eq. (2) of the main text] and calculate the qubit autocorrelator $\rho(t) = \langle \sigma_x^1(t)\sigma_x^1(0)\rangle$ and the corresponding spectrum $\tilde{\rho}(\omega) = \int dt e^{i\omega t}\rho(t)$. Our method and notation follow Ref. [13].

In the main text, we have focussed on a circuit QED system with ferromagnetic qubit-qubit coupling $J > 0$. Since setups with antiferromagnetic coupling are also conceivable, we generalize in the remainder of these supplementary notes the Hamiltonian of the transverse-field Ising chain to

$$\mathcal{H}_I = \frac{\Omega}{2} \sum_{j=1}^{N} \sigma_z^j - \mathcal{J} \sum_{j=1}^{N-1} \sigma_x^j \sigma_x^{j+1}, \tag{S.8}$$

where $\mathcal{J}$ may be negative ($\Omega > 0$ as before). We define $J = |\mathcal{J}|$. Applying the Jordan-Wigner transformation $\sigma_j^+ = c_j^\dagger \exp(i\pi \sum_{k=1}^{j-1} c_k^\dagger c_k)$ to $\mathcal{H}_I$ leads to

$$\mathcal{H}_I = -\frac{N\Omega}{2} + \Omega \sum_{j=1}^{N} c_j^\dagger c_j - \mathcal{J} \sum_{j=1}^{N-1} [c_j^\dagger c_{j+1}^\dagger + c_j^\dagger c_{j+1} + \text{H.c.}], \tag{S.9}$$

with fermionic c_j. In this form, $\mathcal{H}_I$ can be diagonalized using the method for diagonalizing quadratic fermionic Hamiltonians of the form

$$H = \sum_{i,j=1}^{N} [c_i^\dagger A_{i,j} c_j + 1/2(c_i^\dagger B_{i,j} c_j^\dagger + \text{H.c.})] \tag{S.10}$$

of Ref. [13]. In our case,

$$A = \begin{pmatrix} \Omega & -\mathcal{J} & 0 & & \cdots & 0 \\ -\mathcal{J} & \Omega & -\mathcal{J} & & & \\ 0 & -\mathcal{J} & \Omega & -\mathcal{J} & & \\ \vdots & & \ddots & \ddots & \ddots & \\ & & & -\mathcal{J} & \Omega & -\mathcal{J} \\ 0 & & & & -\mathcal{J} & \Omega \end{pmatrix}, \tag{S.11}$$

and B is obtained by substituting $A_{i,i} = \Omega \to 0$ and $A_{i+1,i} = -\mathcal{J} \to \mathcal{J}$ in A. H is diagonalized by introducing new fermions $\eta_k = \sum_{j=1}^{N} g_{k,j} c_j + h_{k,j} c_j^\dagger$. The components $g_{k,j}$ and $h_{k,j}$ of the vectors g_k and h_k and the eigenvalues Λ_k of H are determined by defining normalized vectors $\phi_k = g_k + h_k$ and $\psi_k = g_k - h_k$ and solving the equations

$$\phi_k(A - B) = \Lambda_k \psi_k, \qquad \psi_k(A + B) = \Lambda_k \phi_k. \tag{S.12}$$

For $\Lambda_k \neq 0$, this is most easily done by solving, e.g.,

$$(A - B)(A + B)\phi_k = \Lambda_k^2 \phi_k \tag{S.13}$$

and calculating ψ_k via Eqs. (S.12). Note that since $A^T = A$ and $B^T = -B$, $\Lambda_k^2 \geq 0$ and the ϕ_k and ψ_k can be chosen real and orthogonal for different k, $\sum_j \phi_{k,j}\phi_{k',j} = \sum_j \psi_{k,j}\psi_{k',j} = \delta_{k,k'}$. For A and B as defined above, one

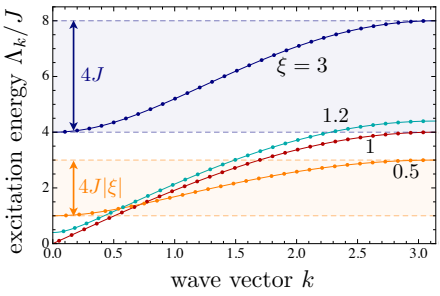

FIG. S3. Excitation energies Λ_k vs. the allowed real wave vectors k of a transverse-field Ising chain with $N = 30$ and $\xi = 0.5, 1, 1.2, 3$ (dots). For $\xi = 0.5$, there is also one imaginary wave vector (see text). The solid lines are a guide to the eye. The shaded regions indicate the bandwidth of the Ising chain for $\xi = 0.5$ (ferromagnetic phase, orange) and for $\xi = 3$ (paramagnetic phase, blue).

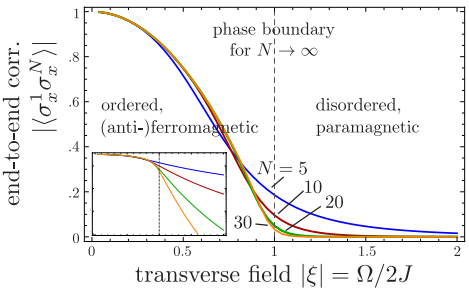

FIG. S4. End-to-end correlator $|\langle\sigma_x^1\sigma_x^N\rangle|$ vs. normalized magnetic field $|\xi| = \Omega/2J$ for $N = 5, 10, 20, 30$ (blue, red, green, orange). The signs of $\langle\sigma_x^1\sigma_x^N\rangle(\xi)$ and ξ agree except that N is odd and $\xi < 0$. Inset, same plot but $|\langle\sigma_x^1\sigma_x^N\rangle|$ on a logarithmic scale covering values from 10^{-7} to 1.

obtains

$$\mathcal{H}_I = \sum_k \Lambda_k(\eta_k^\dagger\eta_k - 1/2), \tag{S.14}$$

$$\Lambda_k = 2J\sqrt{1+\xi^2-2\xi\cos k}, \tag{S.15}$$

$$\phi_{k,j} = A_k \sin k(N+1-j), \tag{S.16}$$

$$\psi_{k,j} = \mathrm{sign}\Big[\frac{\mathcal{J}\sin k}{\sin k(N+1)}\Big] A_k \sin kj, \tag{S.17}$$

$$A_k = 2\big(2N+1-\sin[k(2N+1)]/\sin k\big)^{-1/2}. \tag{S.18}$$

Here, $\xi = \Omega/2\mathcal{J}$ is the normalized transverse field, and the possible values of k are solutions of

$$\frac{\sin kN}{\sin k(N+1)} = \xi. \tag{S.19}$$

If $|\xi| \geq N/(N+1)$ ($|\xi| < N/(N+1)$), Eq. (S.19) has N ($N-1$) real solutions $\in [0,\pi]$. If $|\xi| < N/(N+1)$, there is also one imaginary solution $k' = i\kappa$ ($k' = \pi + i\kappa$) for positive (negative) ξ with $\sinh\kappa N/\sinh\kappa(N+1) = |\xi|$. These solutions exhaust the eigenmodes of the system. Note that $\Lambda_{k'} \to 0$ if $|\xi| \to 0$ or $N \to \infty$.

For $N \to \infty$, $\mathcal{H}_I$ undergoes a second order QPT at $\xi = \pm 1$ from a ferromagnetic [$\xi \in (0,1)$] or an antiferromagnetic [$\xi \in (-1,0)$] ordered phase with doubly degenerate eigenstates ($\Lambda_{k'} \to 0$) to a paramagnetic disordered phase ($|\xi| > 1$) with $\Lambda_k > 0$ for all k. This QPT is signaled by correlators of the order parameter σ_x. Note, though, that $\langle\sigma_x^j\rangle \equiv 0$ for all ξ. Since $\mathcal{H}_I$ commutes with $\prod_j \sigma_z^j$, all eigenstates of $\mathcal{H}_I$ formally obey this symmetry that maps $\sigma_x^j \to -\sigma_x^j$.

Fig. S3 shows the excitation energies Λ_k of $\mathcal{H}_I$ vs. the allowed (real) wave vectors k for $N = 30$ and various ξ (for $\xi = 0.5$, there is one imaginary wave vector $k' \approx 0.693i$, and $\Lambda_{k'} \approx 0$). In the limit $N \to \infty$, the Λ_k form a continuous band. Its gap is given by $|1-|\xi||$ and vanishes at the quantum critical point $|\xi| = 1$. In the disordered phase ($|\xi| > 1$), the bandwidth is $4J$ (indicated for $\xi = 3$ in Fig. S3) and independent of ξ. In the ordered phase ($|\xi| < 1$), the bandwidth is given by $4J|\xi|$.

Signatures of the QPT are already present for relatively small system sizes. This is evident from Fig. S4 where we plot the end-to-end correlator $\langle\sigma_x^1\sigma_x^N\rangle$, an order parameter of the QPT for $N \to \infty$, as function of ξ for different (finite) N (at zero temperature; see Sec. V and [13] for calculations). Already for $N \gtrsim 10$, the end-to-end correlator becomes very small at $|\xi| \approx 1$ and displays a distinct transition from algebraic to exponential decay (see inset of Fig. S3). This illustrates that even small Ising chains of a comparable size exhibit interesting quantum many-body physics. For more details on the transverse-field Ising chain and its QPT, see, e.g., [13–15].

Assuming zero temperature, the qubit autocorrelator $\rho(t) = \langle\sigma_x^1(t)\sigma_x^1(0)\rangle$ can now be easily calculated using

$$\sigma_x^1 = c_1^\dagger + c_1 = \sum_k \phi_{k,1}(\eta_k^\dagger + \eta_k). \tag{S.20}$$

One obtains

$$\rho(t) = \sum_k \phi_{k,1}^2 e^{-it\Lambda_k}. \tag{S.21}$$

The Fourier transform $\tilde{\rho}(\omega)$ of $\rho(t)$ is a sum of delta peaks. In order to obtain a continuous spectrum $\tilde{\rho}(\omega)$, we have to take the limit $N \to \infty$ in Eq. (S.21). As its RHS contains rapidly oscillating terms for $N \to \infty$ (like $\sin Nk$), it cannot be straightforwardly transformed into an integral via a Riemann sum. We therefore write $k_l = \pi/N(l-\nu_l)$ for $l = 1, \ldots, N$ [13] and find, by means of Eq. (S.19),

$$\nu_l = \frac{1}{\pi}\arctan\Big[\frac{\xi\sin(\pi l/N)}{\xi\cos(\pi l/N)-1}\Big] + \mathcal{O}(1/N). \tag{S.22}$$

With these expressions for k_l and ν_l, $\rho(t)$ can be transformed into an integral $\int_1^N \mathrm{d}l$ for $N \to \infty$. Substituting $\mathrm{d}l \to \mathrm{d}k$ (k as defined above, $\mathrm{d}k/\mathrm{d}l \approx \pi/N$) and dropping

all terms $\mathcal{O}(1/N)$ finally leads to

$$\rho(t) = \Theta(1-|\xi|)(1-|\xi|^2) + \frac{2}{\pi}\int_0^\pi \mathrm{d}k \frac{\xi^2 \sin^2 k}{1+\xi^2-2\xi\cos k} e^{-it\Lambda(k)}, \quad \text{(S.23)}$$

where $\Theta(x)$ is the Heaviside step function and $\Lambda(k)$ stands for Λ_k with continuous k. The first term on the RHS of Eq. (S.23) is the k'-term in Eq. (S.21) for $N \to \infty$, which must be treated separately. It causes a nonzero mean value of $\mathrm{Re}\rho(t)$ in the ordered phase. Taking the Fourier transform of Eq. (S.23) yields

$$\tilde{\rho}(\omega) = 2\pi\delta(\omega)\Theta(1-|\xi|)(1-|\xi|^2) + \Theta(\omega - 2J|1-|\xi||)\,\Theta(2J|1+|\xi|| - \omega) \times \frac{4|\xi|}{\omega}\sqrt{1-\cos^2 k(\omega)}, \quad \text{(S.24)}$$

where $\cos k(\omega) = [1+\xi^2-(\frac{\omega}{2J})^2]/(2\xi)$. Note that this result does not depend on the sign of $\mathcal{J}$ (and the sign of $\xi = \Omega/2\mathcal{J}$). For ferromagnetic coupling $\mathcal{J} > 0$ (and $\xi > 0$), Eq. (S.24) can be simplified to the form of Eq. (3) and is plotted in Fig. 2(a) of the main text. For antiferromagnetic coupling $\mathcal{J} < 0$ (and $\xi < 0$), one just has to replace $\xi \to |\xi|$ in Eq. (3). Thus, with this replacement, our discussion of $\tilde{\rho}(\omega)$ below Eq. (3) and the plots in Fig. 2 of the main text hold for antiferromagnetic coupling as well.

III. SPECTRUM OF THE RESONATOR

In this section, we calculate the spectrum $S(\omega)$ of the resonator of our system, which is coupled to the Ising chain. Complementary to Figs. 2(b) and 2(c) of the main text, we plot $S(\omega)$ in the limiting cases $g/J \ll 1$ and $g/J \gg 1$, and for finite N. In these plots, we vary the transverse field ξ at fixed qubit-qubit coupling J, as experimentally realistic for Cooper-pair boxes (see Sec. I of these supplementary notes). However, if the proposed setup is implemented with standard transmons instead of Cooper-pair boxes, then ξ will be constant and J will be flux-tunable. We also provide plots of $S(\omega)$ for this scenario. We remark that, like $\tilde{\rho}(\omega)$, $S(\omega)$ turns out to be independent of the sign of $\mathcal{J}$ (and of the sign of $\xi = \Omega/2\mathcal{J}$). For ease of notation, we will therefore refer to J as the qubit-qubit coupling and identify $\xi = |\xi| = \Omega/2J$ where appropriate throughout this section.

In order to calculate $S(\omega)$, we assume $g/\omega_0 \ll 1$ and linearize the Hamiltonian $\mathcal{H}$ [Eq. (1) of the main text]. That is, we now consider the Hamiltonian

$$\tilde{\mathcal{H}} = \frac{1}{2}(p_0^2 + \omega_0^2 x_0^2) + x_0 \sum_{j=1}^N \lambda_j x_j + \mathcal{H}_h, \quad \text{(S.25)}$$

where $\lambda_j = \sqrt{2g^2\omega_0}\tilde{\lambda}_j$ and $\mathcal{H}_h = \sum_{j=1}^N (p_j^2 + w_j^2 x_j^2)/2$. It is obtained by substituting the coupling term in Eq. (1) by $g(a^\dagger + a)\sum_{j=1}^N \tilde{\lambda}_j x_j$ ($\tilde{\lambda}_j$ is a coupling constant) and $\mathcal{H}_I$ by $\mathcal{H}_h$, the Hamiltonian of a set of harmonic oscillators with frequencies w_j, and by introducing canonical coordinates for the resonator via $x_0 = 1/\sqrt{2\omega_0}(a^\dagger + a)$ and $p_0 = i\sqrt{\omega_0/2}(a^\dagger - a)$. Note that x_0 couples to a force $F_h(t) = \sum_{j=1}^N \lambda_j x_j(t)$ in Eq. (S.25). By writing $\mathcal{H}$ [Eq. (1)] in terms of x_0 and p_0, one finds that here x_0 couples to a force $F_I(t) = \sqrt{2g^2\omega_0}\sigma_x^1(t)$. The parameters $\tilde{\lambda}_j$ and w_j in $\tilde{\mathcal{H}}$ can be chosen such that

$$\langle F_h(t)F_h(0)\rangle = \sum_{j=1}^N \frac{\lambda_j^2}{2w_j} e^{-iw_j t} = \langle F_I(t)F_I(0)\rangle \quad \text{(S.26)}$$

(in this case also the spectra of the forces will agree). Indeed, $w_j = \Lambda_{k_j}$ and $\tilde{\lambda}_j^2 = 2w_j A_{k_j}^2 \sin^2 Nk_j$ guarantee Eq. (S.26). We now calculate $S(\omega)$, the Fourier transform of $2\omega_0\langle\tilde{0}|x_0(t)x_0|\tilde{0}\rangle$, where $|\tilde{0}\rangle$ is the ground state of $\tilde{\mathcal{H}}$. To that end, we first reformulate

$$\tilde{\mathcal{H}} = \frac{1}{2}(\mathbf{P}^T\mathbf{P} + \mathbf{X}^T\underline{\Omega}^2\mathbf{X}), \quad \text{(S.27)}$$

with $\mathbf{X}^T = (x_0, x_1, \ldots, x_N)$, $\mathbf{P}^T = (p_0, p_1, \ldots, p_N)$, and

$$\underline{\Omega}^2 = \begin{pmatrix} \omega_0^2 & \lambda_1 & \ldots & \lambda_N \\ \lambda_1 & w_1^2 & & \\ \vdots & & \ddots & \\ \lambda_N & & & w_N^2 \end{pmatrix}. \quad \text{(S.28)}$$

There is an orthogonal matrix G for which

$$\tilde{\mathcal{H}} = \frac{1}{2}(\tilde{\mathbf{P}}^T\tilde{\mathbf{P}} + \tilde{\mathbf{X}}^T\underline{\tilde{\Omega}}^2\tilde{\mathbf{X}}), \quad \text{(S.29)}$$

where $\tilde{\mathbf{X}} = G^T\mathbf{X}$, $\tilde{\mathbf{P}} = G^T\mathbf{P}$, and $\underline{\tilde{\Omega}}^2$ is diagonal with $\tilde{\Omega}_j^2 \equiv (\underline{\tilde{\Omega}}^2)_{jj}$ being an eigenvalue of $\underline{\Omega}^2$. We calculate

$$\langle\tilde{0}|x_0(t)x_0|\tilde{0}\rangle = \sum_{j,j'=0}^N G_{0,j}G_{0,j'}\langle\tilde{0}|\tilde{x}_j(t)\tilde{x}_{j'}|\tilde{0}\rangle \quad \text{(S.30)}$$

$$= \sum_{j=0}^N \frac{G_{0,j}^2}{2\tilde{\Omega}_j} e^{-it\tilde{\Omega}_j} \quad \text{(S.31)}$$

and obtain with that

$$S(\omega) = 2\pi\omega_0 \sum_{j=0}^N \frac{G_{0,j}^2}{\tilde{\Omega}_j}\delta(\omega - \tilde{\Omega}_j) \quad \text{(S.32)}$$

$$= 4\Theta(\omega)\omega_0 \mathrm{Im}\big[\mathcal{R}(\underline{\Omega}^2, \omega^2 - i0^+)_{0,0}\big]. \quad \text{(S.33)}$$

In the last line, the matrix element of the resolvent $\mathcal{R}(\underline{\Omega}^2, \omega^2) = (\omega^2 - \underline{\Omega}^2)^{-1}$ is to be taken in the basis in that $\underline{\Omega}^2$ has the form of Eq. (S.28). It can be calculated following Ref. [16]. The result is

$$S(\omega) = \frac{4\Theta(\omega)\omega_0[\langle F_h F_h\rangle_\omega/2 + 0^+]}{[\omega^2 - \omega_0^2 - 2\tilde{\chi}(\omega^2)]^2 + [0^+ + \langle F_h F_h\rangle_\omega/2]^2}, \quad \text{(S.34)}$$

$$\tilde{\chi}(\omega^2) = \frac{1}{2\pi}\int d\Omega \frac{\Omega\langle F_h F_h\rangle_\Omega}{\omega^2 - \Omega^2}. \quad \text{(S.35)}$$

Thus, we have expressed the spectrum of the resonator $S(\omega)$ in terms of the spectrum $\langle F_h F_h\rangle_\omega$ of the bath of harmonic oscillators which is the Fourier transform of $\langle F_h(t)F_h(0)\rangle$ [Eq. (S.26)]. Note that in the limit $N\to\infty$, $\langle F_h F_h\rangle_\omega$ can become continuous and then $\tilde\chi(\omega^2)$ is a principal value integral. If we now assume that we have chosen $\tilde\lambda_j$ and w_j in $\tilde{\mathcal{H}}$ [Eq. (S.25)] such that Eq. (S.26) holds, we can substitute $\langle F_h F_h\rangle_\omega \to \langle F_I F_I\rangle_\omega = 2g^2\omega_0\tilde\rho(\omega)$. This leads to

$$S(\omega)=\frac{4\Theta(\omega)\omega_0[g^2\omega_0\tilde\rho(\omega)+0^+]}{[\omega^2-\omega_0^2-4g^2\omega_0\chi(\omega^2)]^2+[0^++g^2\omega_0\tilde\rho(\omega)]^2}, \tag{S.36}$$

where $\chi(\omega^2)$ is the principal value integral

$$\chi(\omega^2)=\frac{1}{2\pi}\int \mathrm{d}\Omega\frac{\tilde\rho(\Omega)\Omega}{\omega^2-\Omega^2}. \tag{S.37}$$

Note that $S(\omega)|_{g=0}=2\pi\delta(\omega-\omega_0)$. However, the spectrum of any realistic microwave resonator at $g=0$ will be a Lorentzian with full linewidth κ at half maximum. We use the case $g=0$ to relate the so far infinitesimal real number 0^+ in Eq. (S.36) to κ by demanding

$$S(\omega)|_{g=0}=\frac{4\Theta(\omega)\omega_0 0^+}{(\omega^2-\omega_0^2)^2+(0^+)^2}\approx\frac{\kappa}{(\omega-\omega_0)^2+(\kappa/2)^2}. \tag{S.38}$$

For $\kappa\ll\omega_0$, it is sufficient to focus on the vicinity of the strongly pronounced peak of $S(\omega)|_{g=0}$ at $\omega=\omega_0$ (i.e., on $\omega-\omega_0\ll\omega_0$), and we find that here Eq. (S.38) is fulfilled for $0^+=\kappa\omega_0$. Inserting this expression in Eq. (S.36) finally leads to Eq. (4) of the main text. Note that the properties of the TFIC enter our result for $S(\omega)$ only via the spectrum $\tilde\rho(\omega)$ of the bare TFIC. Therefore, Eq. (4) also holds if the resonator is coupled to a different system than the TFIC, with some other spectrum. Note further that $S(\omega)$ is independent of the sign of $\mathcal{J}$ (and the sign of $\xi=\Omega/2\mathcal{J}$) because the spectrum $\tilde\rho(\omega)$ of the TFIC has this property.

Fig. S5 complements Figs. 2(b) and 2(c) of the main text by showing $S(\omega)$ in the limiting cases $g/J\ll1$ [Fig. S5(a)] and $g/J\gg1$ [Fig. S5(b)]. In Fig. S5(a), we choose the parameters J/ω_0 and κ/ω_0 as in Fig. 2(b), but $g/\omega_0=0.05$. Where the Ising chain is off-resonant with ω_0, the spectrum is qualitatively similar to the one of Fig. 2(b). Also here one observes the dispersive shift ($\propto g^2$) of the resonator frequency in analogy to the $N=1$ case and a broad side maximum of width $\sim 4J$ (blue and green lines in the inset). Both are less pronounced than in Fig. 2(b) due to the lower value of g. On resonance ($\xi\approx\omega_0/2J$), though, the double peak structure reminiscent of the $N=1$ case is no longer visible. Instead, $S(\omega)$ is a Lorentzian around ω_0 with full width at half maximum given by $2g^2/J$ (as long as $\kappa\ll g^2/J$ and ω is within the band of the Ising chain). Indeed, assuming small g/J, one may replace $\tilde\rho(\omega)$ by its maximum $2/J$ and take $\chi(\omega^2)\approx0$ in

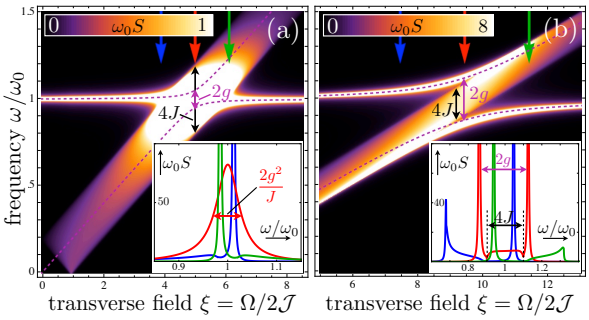

FIG. S5. Spectrum S of a resonator coupled to the first spin of an Ising chain ($N\to\infty$) vs. frequency ω and normalized transverse field ξ. (a) The case $g/J\ll1$ (the parameters are $g=0.05$, $J=0.1$, and $\kappa=10^{-4}$). Inset, $S(\omega)$ for $\xi=3.9,5,6.1$ (blue, red, green). (b) The case $g/J\gg1$ (the parameters are $g=0.12$, $J=0.05$, and $\kappa=10^{-4}$). Inset, $S(\omega)$ for $\xi=7.8,10,12.2$ (blue, red, green). All parameters are measured in units of ω_0. The dashed lines are the first two excitation energies of $\mathcal{H}$ for the same parameters, but $N=1$. For better visibility of the features, values of $S(\omega)>1$ [$S(\omega)>8$] in the density plot of (a) [(b)] are plotted in white. The lines in the insets correspond to cuts along the arrows in the main plots.

Eq. (S.36). One can then verify

$$S(\omega)|_{\xi\approx\omega_0/2J}\approx\frac{2g^2/J}{(\omega-\omega_0)^2+(g^2/J)^2}. \tag{S.39}$$

In Fig. S5(b), we choose the parameters g/ω_0 and κ/ω_0 as in Fig. 2(b), but $J/\omega_0=0.05$. This case has already much similarity with the usual single-qubit case. Off resonance, the resonator experiences again the same dispersive shift as for $N=1$. On resonance, the broad double peak structure of Figs. 2(b,c) with width $4J$ has developed into two sharp Lorentzians separated by $\approx 2g$ as for $N=1$ (red line in the inset). The chain is visible only as faint band of width $4J$ in between these peaks.

In order to illustrate finite-size effects on the resonator spectrum $S(\omega)$, we calculate the spectrum $\tilde\rho(\omega)$ of a finite transverse-field Ising chain. It is given by the Fourier transform of Eq. (S.21) and reads $\tilde\rho(\omega)=2\pi\sum_k\phi_{k,1}^2\delta(\omega-\Lambda_k)$. We assume that the delta peaks in $\tilde\rho$ are broadened by decay processes and replace them with Lorentzians centered around Λ_k and having a full width at half maximum of γ. Together with Eq. (4) of the main text, this yields the spectrum $S(\omega)$ of a resonator coupled to a TFIC of finite length. In Fig. S6, we plot $S(\omega)$ for similar system parameters as in Fig. 2 of the main text ($g/J\approx1$), but $N=20$. Signatures of the QPT at $\xi=1$, the dispersive shift of the resonator frequency, and the double-peak structure on resonance with $4J$ separation of the peaks (rather than $2g$ as in the case $N=1$) are present also for $N=20$. We remark that compared to the case $N\to\infty$ (Fig. 2), the ratio g/J has to be slightly increased for $N=20$ (Fig. S6) such that the double peak structure of $S(\omega)$ on resonance is clearly

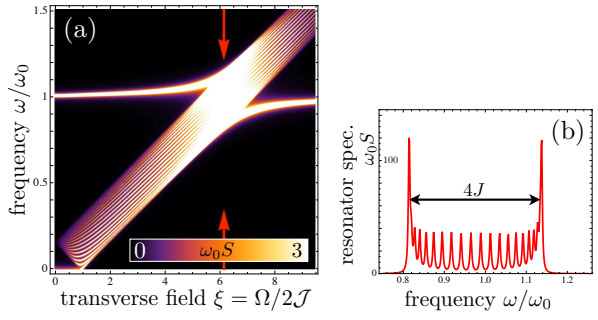

FIG. S6. (a) Spectrum S of a resonator coupled to the first spin of a finite Ising chain ($N = 20$) vs. frequency ω and normalized transverse field ξ. The parameters are $g = 0.12$, $J = 0.08$, $\kappa = 10^{-4}$, and $\gamma = 5 \times 10^{-3}$ (in units of ω_0). (b) $S(\omega)$ for $\xi = 6.1$. This curve corresponds to a cut along the arrows in (a).

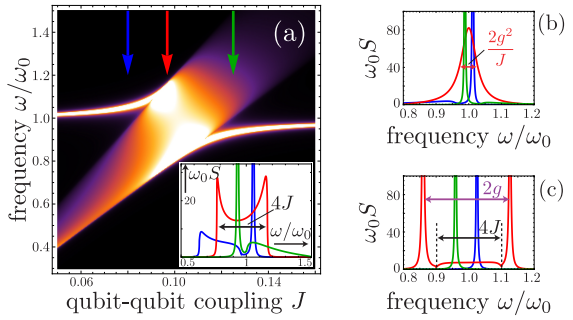

FIG. S7. (a) Spectrum S of a resonator coupled to the first spin of an Ising chain ($N \to \infty$) vs. probe frequency ω and qubit-qubit coupling J. The normalized transverse field ξ is constant ($\xi = 5$). This corresponds to an implementation of the Ising chain with standard transmons. Here, the resonator and the first spin couple with a strength $g = 0.12$. The color scale covers values of S from 0 (black) to 15 (white), and values > 15 are also plotted in white. Inset, $S(\omega)$ for the same parameters and $J = 0.08, 0.096, 0.125$ (blue, red, green). These curves correspond to cuts along the arrows through the density plot of (a). (b) Spectrum S as in (a) in the limiting case $g/J \ll 1$. The plot shows $S(\omega)$ for $\xi = 5$, $g = 0.05$, and $J = 0.08, 0.1, 0.13$ (blue, red, green). (c) Spectrum S as in (a) in the limiting case $g/J \gg 1$. The plot shows $S(\omega)$ for $\xi = 10$, $g = 0.12$, and $J = 0.03, 0.05, 0.07$ (blue, red, green). For all plots we have chosen the resonator linewidth $\kappa = 10^{-4}$. All parameters are measured in units of the resonator frequency ω_0.

visible. This is because the weight of the edges of the band of the Ising chain in the spectrum $\tilde{\rho}(\omega)$ increases with N.

Finally, we plot $S(\omega)$ for varying values of the qubit-qubit coupling J and keep the normalized transverse field $\xi = \Omega/2J$ constant. This corresponds to an implementation of our proposal with usual flux-tunable transmons. In such an implementation, J and Ω change with the external flux approximately in the same proportion. Thus, J is tunable and ξ is constant (see Sec. I of these supplementary notes).

An Ising chain with tunable J but constant ξ is confined to one phase. If implemented with transmons, this has to be the paramagnetic phase ($\xi > 1$; see Sec. I). Thus, when plotted as function of J at constant ξ, the resonator spectrum $S(\omega)$ will not carry signatures of a phase transition. Moreover, the bandwidth of the chain ($4J\xi$ for $\xi < 1$ and $4J$ for $\xi > 1$) will not be constant. Otherwise $S(\omega)$ displays the same features for transmons as before for CPBs, as Fig. S7 demonstrates. Before discussing Fig. S7, we remark that the tunability of J for transmons implies that ratio g/J is not constant. We have seen that shape of the spectrum S depends crucially on the ratio g/J if the Ising chain is resonant with the resonator. Therefore, we differentiate the cases $g/J \ll 1$, $g/J \approx 1$, and $g/J \gg 1$ (as for CPBs) for the Ising chain formed by transmons being resonant with the resonator frequency ω_0.

Under these conditions, Fig. S7(a) corresponds to Figs. 2(b) and 2(c) of the main text. That is, these figures illustrate the situation where the qubit-qubit coupling J in a semi-infinite chain of transmons resonant with ω_0 [Fig. S7(a)] and in a semi-infinite chain of CPBs [Figs. 2(b,c)] is comparable to the coupling g of the respective first artificial atom and the resonator. Explicitly, like in Figs. 2(b,c), we have chosen $g/\omega_0 = 0.12$ in Fig. S7(a). Moreover, the choice $\xi = 5$ (a realistic value for transmons) ensures that the center of the band of the Ising chain ($2J\xi$) formed by transmons is on resonance with the resonator at $J/\omega_0 = 0.1$ [like in Figs. 2(b,c)]. As expected, the bandwidth of the TFIC increases linearly with J in Fig. S7(a). Out of resonance, one observes the usual dispersive shift of the resonator frequency. On resonance, the spectrum exhibits the characteristic double-peak structure with $4J$ separation of the peaks, which is also present for Cooper-pair boxes [Fig. 2(c)].

Also in the limiting cases $g/J \ll 1$ and $g/J \gg 1$ (on resonance), a chain of transmons displays the same behavior that we have found before for CPBs: Fig. S7(b) shows $S(\omega)$ for $\xi = 5$ as in (a), but with $g/\omega_0 = 0.05$. For the different curves, J is chosen such that the TFIC is below (blue), on resonance with (red), and above (green) the resonator frequency ω_0. This plot corresponds to the inset of Fig. S5(a). The spectrum of a chain of transmons weakly coupled to a resonator is essentially identical to the one for a chain of CPBs, and its features can be explained in the same manner. In order to study the limiting case $g/J \gg 1$ for transmons, we chose $g = 0.12$ and $\xi = 10$ for the curves in Fig. S7(c). With this choice of ξ, the Ising chain formed by transmons is on resonance with the resonator at $J = 0.05$. This was also the case in Fig. S5(b), where we have studied the limiting case $g/J \gg 1$ for CPBs. As Fig. S7(b), Fig. S7(c) shows $S(\omega)$ for J chosen such that the TFIC is below (blue), on resonance with (red), and above (green) the resonator frequency ω_0.

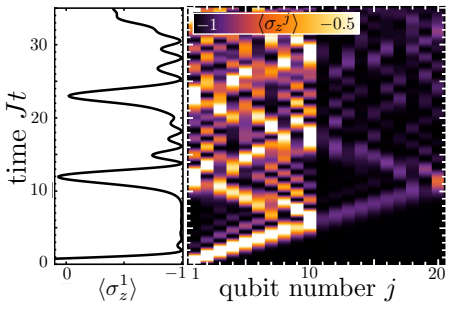

FIG. S8. Nonequilibrium time evolution of $\langle\sigma_z^j\rangle$ after a π-pulse on the first qubit in a transverse-field Ising chain of length $N = 20$ in the paramagnetic phase (normalized transverse field $\xi = 8$). Qubit 11 is strongly detuned from the rest of the chain. Values > -0.5 are plotted in white. The measurable observable $\langle\sigma_z^1\rangle$ is singled out left.

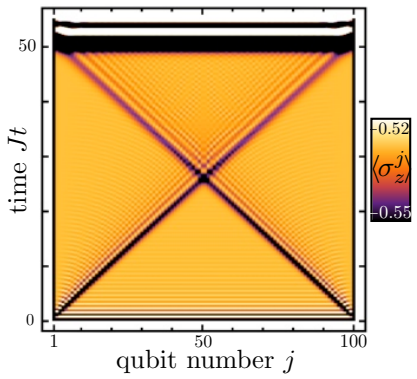

FIG. S9. Time evolution of $\langle\sigma_z^j\rangle$ in a transverse-field Ising chain of length $N = 100$ after a quench of the normalized transverse field $\xi = 8 \to 1$. Values < -0.55 (> -0.52) are plotted in black (white).

Like for CPBs, one can clearly see how the usual Jaynes-Cummings spectrum (corresponding to the case $N = 1$) emerges as limiting case.

IV. PROPAGATION OF A LOCALIZED EXCITATION IN THE ISING CHAIN

This section contains the explicit evaluation of the RHS of Eq. (5) of the main text. Further, it is shown that by deliberately detuning the transition frequency of one qubit, the effective length of the TFIC can be modified. With

$$L_j \equiv c_j^\dagger + c_j = \sum_k \phi_{k,j}(\eta_k^\dagger + \eta_k) \tag{S.40}$$

$$M_j \equiv c_j^\dagger - c_j = \sum_k \psi_{k,j}(\eta_k^\dagger - \eta_k), \tag{S.41}$$

where $\phi_{k,j}$ and $\psi_{k,j}$ are determined by Eqs. (S.12) [and explicitly given in Eqs. (S.16) and (S.17)], we reformulate Eq. (5) in terms of fermions,

$$\langle\sigma_z^j\rangle(t) = \langle 0|L_1 M_j(t) L_j(t) L_1|0\rangle. \tag{S.42}$$

The RHS of this equation can be evaluated using Wick's theorem, which was first used in this context in Ref. [13]. One finds

$$\langle\sigma_z^j\rangle(t) = -\sum_k \psi_{k,j}\phi_{k,j} + \sum_{k,k'} e^{i(\Lambda_k - \Lambda_{k'})t}\big[\phi_{k,1}\phi_{k',1} \times (\psi_{k,j}\phi_{k',j} + \psi_{k',j}\phi_{k,j})\big]. \tag{S.43}$$

This formula was used for the plots in Fig. 3 of the main text.

If the transition frequencies Ω_j of the qubits can be tuned individually, one can intentionally detune one qubit from the rest of the chain and observe how the system dynamics changes depending on the detuning. Fig. S8 shows the time evolution of $\langle\sigma_z^j\rangle(t)$ after a local excitation has been created on the first site for the same system parameters as in Fig. 3, but with qubit 11 strongly detuned from the others, explicitly $\Omega_{11} = 1.3\Omega_j$ for $j \neq 11$. This local inhomogeneity acts as a barrier for the propagating excitation and leads to its reflection. The revival of the measurable observable $\langle\sigma_z^1\rangle(t)$ takes place at $t \approx N/2J$ rather than at $t \approx N/J$ as in Fig. 3 of the main text. Thus, strongly detuning one qubit from the others effectively changes the length of the chain.

V. QUENCH DYNAMICS OF THE MAGNETIZATION AND THE END-TO-END CORRELATIONS

We calculate the time evolution of $\langle\sigma_z^j\rangle$ and $\langle\sigma_x^1\sigma_x^N\rangle$ that follows a sudden change from $\xi = \xi_a$ to $\xi = \xi_b$ at $t = 0$. We plot and discuss the result for $\langle\sigma_x^1\sigma_x^N\rangle$ and provide a plot of $\langle\sigma_z^j\rangle$ in addition to Fig. 4 of the main text. In the following, quantities belonging to $\mathcal{H}_{I,a}$ are labelled by a (like Λ_k^a), and analogously for $\mathcal{H}_{I,b}$.

First, we focus on

$$\langle\sigma_z^j\rangle(t) = {}_a\langle 0|e^{i\mathcal{H}_{I,b}t}\sigma_z^j e^{-i\mathcal{H}_{I,b}t}|0\rangle_a. \tag{S.44}$$

To evaluate the RHS, we use the usual mapping to free fermions [13, 14]: We express σ_z^j by η_k^b and $\eta_k^{b\dagger}$ whose time dependence is trivial. Then we express these operators by η_k^a and $\eta_k^{a\dagger}$ whose action on $|0\rangle_a$ is known. One obtains

$$\langle\sigma_z^j\rangle(t) = -\sum_k \psi_{k,j}^b\phi_{k,j}^b + 2\sum_{k,k'}\{\psi_{k,j}^b\phi_{k',j}^b \times [X_{k,k'}\cos t(\Lambda_k^b + \Lambda_{k'}^b) + Y_{k,k'}\cos t(\Lambda_k^b - \Lambda_{k'}^b)]\}. \tag{S.45}$$

Here,

$$X_{k,k'} = \big[(g_k^b)^T H^a + (h_k^b)^T G^a\big]\big[(G^a)^T g_{k'}^b + (H^a)^T h_{k'}^b\big],$$
$$Y_{k,k'} = \big[(g_k^b)^T H^a + (h_k^b)^T G^a\big]\big[(H^a)^T g_{k'}^b + (G^a)^T h_{k'}^b\big],$$

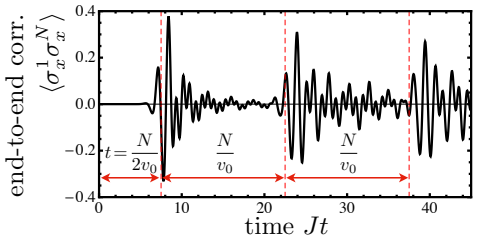

FIG. S10. Time evolution of the end-to-end correlator $\langle\sigma_x^1\sigma_x^N\rangle$ in a transverse-field Ising chain of length $N = 30$ after a quench of the normalized transverse field $\xi = 8 \to 1.5$.

and G and H are matrices containing the g_k and h_k as columns, respectively. Complementary to Fig. 4 of the main text, we plot in Fig. S9 $\langle\sigma_z^j\rangle(t)$ for a quench $\xi_a = 8 \to \xi_b = 1$ in a transverse-field Ising chain with length $N = 100$. We focus here on $t \leq T$ and choose a relatively large chain to strongly contrast the initial approach of $\langle\sigma_z^j\rangle$ to a constant value with the effects of the finite system size. The choice of the non-generic value $\xi_b = 1$ minimizes dispersion of Λ_k and, thus, of the velocities of the quasiparticles. The features of $\langle\sigma_z^j\rangle(t)$ for $t \leq T$ described in the main text are more pronounced and clearly visible in Fig. S9.

Let us now turn to the quench dynamics of the end-to-end correlator

$$\langle\sigma_x^1\sigma_x^N\rangle(t) = {}_a\langle 0|e^{i\mathcal{H}_{I,b}t}\sigma_x^1\sigma_x^N e^{-i\mathcal{H}_{I,b}t}|0\rangle_a. \quad \text{(S.46)}$$

We remark that similar quantities have been studied in [17]. To evaluate the RHS of (S.46), we use that $\mathcal{H}_I$ commutes with $e^{i\pi\sum_{k=1}^N c_k^\dagger c_k}$ for all ξ. Consequently, $|0\rangle_a$ is also an eigenstate of the latter operator [13]. It is now easy to see that

$$\sigma_x^N(t)|0\rangle_a = [c_N^\dagger(t) - c_N(t)]e^{i\pi\sum_{k=1}^N c_k^\dagger c_k}|0\rangle_a \quad \text{(S.47)}$$
$$= [c_N^\dagger(t) - c_N(t)]|0\rangle_a, \quad \text{(S.48)}$$

where $\mathcal{O}(t) = e^{i\mathcal{H}_{I,b}t}\mathcal{O}e^{-i\mathcal{H}_{I,b}t}$ for an operator $\mathcal{O}$. The same strategy as for $\langle\sigma_z^j\rangle$ leads to

$$\langle\sigma_x^1\sigma_x^N\rangle(t) = \sum_k \phi_{k,1}^b\psi_{k,N}^b + 2\sum_{k,k'}\{\phi_{k,1}^b\psi_{k',N}^b\times$$
$$[X_{k,k'}\cos t(\Lambda_k^b + \Lambda_{k'}^b) - Y_{k,k'}\cos t(\Lambda_k^b - \Lambda_{k'}^b)]\}, \quad \text{(S.49)}$$

with $X_{k,k'}$ and $Y_{k,k'}$ defined above. This result is plotted in Fig. S10 for a quench within the paramagnetic phase. The observable $\langle\sigma_x^1\sigma_x^N\rangle$ is an order parameter of the Ising chain in equilibrium and does not develop a nonzero mean value for quenches within the paramagnetic phase. However, at $t \approx N/2v_0 = T/2$, where $v_0 = 2J$ in the paramagnetic phase, oscillations of $\langle\sigma_x^1\sigma_x^N\rangle$ arise. After an abrupt increase, their amplitude decreases again, and this pattern quasiperiodically repeats with period $T = N/v_0$. The observed behavior of the end-to-end correlator can, again, be understood in the QP picture (see [17] for a related analysis). Among the pairs of momentum-inverted QP trajectories with the same origin only those originating at $j = N/2$ have trajectories hitting the system boundaries simultaneously. Since only contiguously generated QPs carry quantum correlations, only the QPs generated at $j = N/2$ can build up correlations between the surface spins which will manifest themselves in a nonzero value of $\langle\sigma_x^1\sigma_x^N\rangle$. These QPs arrive for the first time at the surface spins at $t = N/2v_0 = T/2$, are then reflected, and build up correlations between the surface spins each time they have travelled through the whole chain, that is, after multiples of $T = N/v_0$. This explains the two different time scales $T/2$ and T and the quasiperiodicity (for $t > T/2$) of the end-to-end correlator $\langle\sigma_x^1\sigma_x^N\rangle(t)$. Slower QPs generated at $j = N/2$ will also arrive simultaneously but delayed at the surface spins. They are responsible for the slow decay of the oscillations of the correlator for $t \gtrsim T/2$ and will, for large t, eventually smear out the quasiperiodic structure.

[1] Y. Makhlin, G. Schön, and A. Shnirman, Rev. Mod. Phys. **73**, 357 (2001)
[2] J. Clarke and F. K. Wilhelm, Nature **453**, 1031 (2008).
[3] C. Cohen-Tannoudji, J. Dupont-Roc, and G. Grynberg, *Photons & Atoms* (Wiley-VCH, Weinheim, Germany, 2004).
[4] Yu. A. Pashkin *et al*, Nature **421**, 823 (2003).
[5] A. Dewes *et al.*, Phys. Rev. Lett. **108**, 057002 (2012).
[6] B. Yurke and J. S. Denker, Phys. Rev. A **29**, 1419 (1984).
[7] M. H. Devoret, in *Quantum Fluctuations (Les Houches Session LXIII)*, edited by S. Reynaud, E. Giacobino, and J. Zinn-Justin (Elsevier, New York, 1997), pp. 351–386.
[8] A. Cottet, Implementation of a quantum bit in a superconducting circuit, PhD Thesis, Universite Paris, 2002.
[9] M. H. Devoret, A. Wallraff, and J. M. Martinis, e-print arXiv:cond-mat/0411174.
[10] J. Koch *et al.*, Phys. Rev. A **76**, 042319 (2007).
[11] A. Wallraff *et al.*, Phys. Rev. Lett. **95**, 060501 (2005).
[12] D. V. Averin and C. Bruder, Phys. Rev. Lett. **91**, 057003 (2003).
[13] E. Lieb, T. Schultz, and D. Mattis, Ann. Phys. **16**, 407 (1961).
[14] P. Pfeuty, Ann. Phys. **57**, 79 (1970).
[15] S. Sachdev, *Quantum Phase Transitions* (Cambridge Univ. Press, Cambridge, England, 1999).
[16] F. Marquardt and D. S. Golubev, Phys. Rev. A **72**, 022113 (2005).
[17] F. Iglói, and H. Rieger, Phys. Rev. Lett. **85**, 3233 (2000).

4.6 Publication: The quantum transverse-field Ising chain in circuit quantum electrodynamics: effects of disorder on the nonequilibrium dynamics

In this section, we study the effects of disorder on the (dynamical) behavior of our quantum simulator. Small amounts of disorder in the system parameters have to be expected in an actual implementation of our circuit QED setup, caused by imperfections in the fabrication process. We address the question whether this disorder would spoil the experimental results predicted in the previous section and how much disorder can be tolerated. We also study the regime of strong disorder, which leads to qualitatively new effects such as the Anderson localization of propagating quasiparticles. The crossover between weak and strong disorder should be directly accessible in our setup by detuning individual qubits *in situ*. Our work in this regard has been previously published as an article in *New Journal of Physics*. This section contains a reprint of this publication.

New Journal of Physics
The open access journal for physics

The quantum transverse-field Ising chain in circuit quantum electrodynamics: effects of disorder on the nonequilibrium dynamics

Oliver Viehmann[1], **Jan von Delft**[1] **and Florian Marquardt**[2]

[1] Physics Department, Arnold Sommerfeld Center for Theoretical Physics, and Center for NanoScience, Ludwig-Maximilians-Universität, Theresienstraße 37, D-80333 München, Germany

[2] Institut for Theoretical Physics, Universität Erlangen-Nürnberg, Staudtstraße 7, D-91058 Erlangen, Germany

E-mail: oliver.viehmann@physik.lmu.de, vondelft@lmu.de and Florian.Marquardt@physik.uni-erlangen.de

New Journal of Physics **15** (2013) 035013 (25pp)
Received 19 November 2012
Published 12 March 2013
Online at http://www.njp.org/
doi:10.1088/1367-2630/15/3/035013

Abstract. We study several dynamical properties of a recently proposed implementation of the quantum transverse-field Ising chain in the framework of circuit quantum electrodynamics (QED). Particular emphasis is placed on the effects of disorder on the nonequilibrium behavior of the system. We show that small amounts of fabrication-induced disorder in the system parameters do not jeopardize the observation of previously predicted phenomena. Based on a numerical extraction of the mean free path of a wave packet in the system, we also provide a simple quantitative estimate for certain disorder effects on the nonequilibrium dynamics of the circuit QED quantum simulator. We discuss the transition from weak to strong disorder, characterized by the onset of Anderson localization of the system's wave functions, and the qualitatively different dynamics it leads to.

Contents

1. Introduction

Circuit quantum electrodynamics (QED) systems consist of superconducting artificial atoms coupled to the electromagnetic field in a microwave resonator [1]. Such systems have been successfully used for the implementation of elementary quantum optical Hamiltonians [2, 3] and basic quantum information processing [4–7]. The rapid technological development in the field of circuit QED will soon facilitate experiments with highly coherent multi-atom, multi-resonator circuit QED architectures. This makes circuit QED a promising platform for observing interesting multi-atom quantum optical effects [8–10] and even for simulating genuinely interacting quantum many-body systems from solid state physics [11–20].

In [20], we have proposed and analyzed a circuit QED design that implements the quantum transverse-field Ising chain (TFIC) coupled to a microwave resonator for readout. The TFIC is an elementary example of an integrable quantum many-body system. Despite its simplicity, it still exhibits interesting features, e.g. a quantum phase transition (QPT), and therefore serves as a model example system in the theory of quantum criticality [21] and nonequilibrium thermodynamics [22]. Our circuit QED quantum simulator can be used to study quench dynamics, the propagation of localized excitations and other nonequilibrium phenomena in the TFIC, based on a design that could easily be extended to break the integrability of the system. While in [20] we have focused on an idealized implementation of the TFIC with perfectly uniform parameters, the main purpose of the present paper is to investigate the effects of disorder in the system parameters on the dynamical behavior of our quantum simulator.

The study of disorder effects on quantum simulators is relevant for two reasons. Firstly, on the more practical level, any real experimental system will come with a degree of unwanted disorder (especially in condensed matter settings). In the case of circuit QED systems, inhomogeneities of the system parameters are caused by fabrication issues as well as by static noise fields (e.g. produced by defects). It is important to verify that the basic behavior of a quantum simulator survives the amounts of disorder which are present in realistic systems or

even to estimate the amount of disorder that can be tolerated. Secondly, on a more fundamental level, simulating quantum many-body systems with built-in (potentially tunable) disorder is interesting in its own right. Many physical phenomena, from free propagation of wave packets to quench dynamics to (quantum) phase transitions, can be affected in significant ways by disorder, and this leads to phenomena such as Anderson localization or disorder-induced phases.

To prepare for our study, we briefly review the system (section 2.1), discuss sources of disorder and how disorder scales with the tunable system parameters (section 2.2) and explain the mathematical approach to and some properties of the quantum Ising chain (section 2.3). We start our main discussion by considering the time-dependent correlations of the order parameter of the chain, where the finite-size effects and the long-time behavior will be analyzed in the absence of disorder (section 3.1). Based on this, we will move on to the spectrum of the resonator coupled to the quantum Ising chain in our system, which is closely related to the aforementioned time-dependent correlations. To that end, we employ a very useful approximation which we have introduced in [20] and which will presumably become important also for future studies of quantum many-body systems coupled to resonators. In this approximation, the full quantum many-body system is replaced by a bath of harmonic oscillators with an identical spectrum. We show here that this approximation actually works very well under appropriate circumstances (section 3.2). We then calculate the spectrum of the resonator coupled to a slightly disordered Ising chain and find that the effects of disorder on the spectrum are small (section 3.3). The Ising chain in our circuit-QED quantum simulator can be driven out of equilibrium in several ways. This allows one to perform various types of nonequilibrium experiments, a particularly appealing application of our setup. In our previous work, we have suggested to observe the propagation of a localized excitation through the chain or the nonequilibrium dynamics of the system after a quantum quench. Here, we show that the predicted phenomena are insensitive to a small amount of disorder in the system parameters (sections 4.1 and 4.2, respectively). Moreover, we provide a simple estimate of the amount of disorder that will qualitatively change the wave functions and, thus, strongly affect the dynamics even of small systems (that is, on the scale of neighboring artificial atoms). However, as argued above, it would be highly desirable to possess also a quantitative theory of disorder effects. Since the nonequilibrium dynamics of the uniform TFIC is determined by the ballistic propagation of quasiparticles (QPs; wave packets), we formulate and numerically verify for the weakly disordered case a relation between the mean free path of the latter and the parameters of the system and the disorder potential. By means of this relation we are able to predict the dynamical behavior of our quantum simulator given a certain disorder strength, and to estimate the amount of disorder that a particular experiment can tolerate (section 4.1).

2. The quantum transverse-field Ising chain in circuit quantum electrodynamics

2.1. Setup

We consider a circuit QED quantum simulator of the TFIC as proposed in [20]. It consists of a chain of N capacitively coupled charge-based superconducting artificial atoms [23], such as transmons or Cooper-pair boxes (the latter have to be biased to their charge degeneracy point [23] to properly simulate the TFIC). For a review on superconducting artificial atoms, see [23]. The first artificial atom is capacitively coupled to a microwave resonator (see figure 1). This resonator A is required for initialization and readout of the first artificial atom. For

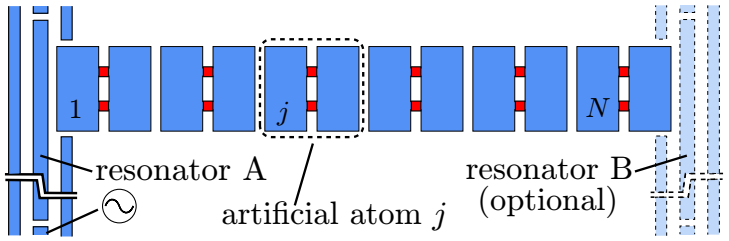

Figure 1. Circuit QED implementation of the quantum TFIC (adapted from [20]). Charge-based artificial atoms are capacitively coupled to their nearest neighbors. Coupling the first (Nth) artificial atom to resonator A (B) allows one to use standard circuit QED techniques for initialization and read-out of the first (Nth) artificial atom.

certain types of experiments, e.g. for measuring end-to-end correlators, one also needs a second resonator B, coupled to the Nth artificial atom. For details of the implementation and the theoretical description of the system, see [20]. The system (at first, only with resonator A) can be approximately described by the Hamiltonian

$$\mathcal{H} = \omega_0 a^\dagger a + g(a^\dagger + a)\sigma_x^1 + \mathcal{H}_{\mathrm{I}}, \tag{1}$$

and $\mathcal{H}_{\mathrm{I}}$ is the Hamiltonian of the TFIC,

$$\mathcal{H}_{\mathrm{I}} = \sum_{j=1}^{N} \frac{\Omega_j}{2}\sigma_z^j - \sum_{j=1}^{N-1} \mathcal{J}_j \sigma_x^j \sigma_x^{j+1}. \tag{2}$$

Here, $\sigma_{x/z}^j$ is a Pauli matrix. That is, the artificial atoms are considered as two-level systems (qubits), and their two states are described as spin states. The operators $a^\dagger$ and a generate and annihilate a photon of energy ω_0. The transition frequency $\Omega_j > 0$ of the jth qubit corresponds to a local magnetic field acting on the jth spin in the usual interpretation of the TFIC. As such, it would be transverse to the direction of the qubit–qubit coupling $\mathcal{J}_j$. The latter can be either ferromagnetic ($\mathcal{J}_j > 0$, as in the geometry of figure 1) or anti-ferromagnetic ($\mathcal{J}_j < 0$, if the qubits in figure 1 are rotated by 90°). While in our previous work we have focused on the uniform case $\mathcal{J}_j = \mathcal{J}$ and $\Omega_j = \Omega$ for all j, here we are often interested in the case where these system parameters are explicitly nonuniform. This is because, on the one hand, a slight nonuniformity of the Ω_j and $\mathcal{J}_j$ has to be expected from imperfections of the fabrication process. On the other hand, one can also intentionally detune one or several qubits (by threading the SQUID-like loops of the qubits with different fluxes) and observe how the system's properties change depending on the detuning.

2.2. Disorder and tunability of the system parameters

Let us discuss the flux tunability and the undesired disorder of the system parameters in some more detail. We will argue that the qubit transition frequencies Ω_j and the qubit–qubit couplings $\mathcal{J}_j$, when normalized to their respective mean values, may be assumed to be flux independent. This will be relevant for our theoretical description of the disorder in the system.

In reality, it should be possible to engineer the geometry of the qubits essentially uniform. That is, the areas of the qubits' SQUID loops, their charging energies and the coupling capacitances between the qubits will only vary weakly in the chain. However, the (flux-tunable) total Josephson energies $E_{\mathrm{J}}(\Phi)$ of the artificial atoms should be experimentally harder to control since these depend exponentially on the properties of the Josephson junctions. For a flux-tunable (i.e. SQUID-type) artificial atom with two Josephson junctions [24],

$$E_{\mathrm{J}}(\Phi) = (\epsilon_{\mathrm{J}}^1 + \epsilon_{\mathrm{J}}^2)\cos\left(\frac{\Phi\pi}{\Phi_0}\right)\left(1 + d^2\tan^2\left(\frac{\Phi\pi}{\Phi_0}\right)\right)^{1/2}. \tag{3}$$

Here, ϵ_{J}^i is the Josephson coupling energy of one Josephson junction, Φ_0 is the superconducting flux quantum, Φ is the tunable external flux threading the SQUID loop, and $d = (\epsilon_{\mathrm{J}}^1 - \epsilon_{\mathrm{J}}^2)/(\epsilon_{\mathrm{J}}^1 + \epsilon_{\mathrm{J}}^2)$. Assuming equal qubit geometries, Φ can be chosen identical for all qubits (e.g. by using a common flux line) and only the ϵ_{J}^i can give rise to disorder. Even if one allows for $|d| \sim 0.1$, this still means that $d^2 \ll 1$, and one can approximate the total Josephson energy of the jth artificial atom by $E_{\mathrm{J}j}(\Phi) \approx (\epsilon_{\mathrm{J}j}^1 + \epsilon_{\mathrm{J}j}^2)\cos(\Phi\pi/\Phi_0)$ (as long as $|\Phi| \not\approx \Phi_0/2$). Now, for Cooper-pair boxes at the charge degeneracy point $\Omega_j(\Phi) \approx E_{\mathrm{J}j}(\Phi)$, and for transmons $\Omega_j(\Phi) \approx [8E_{\mathrm{J}j}(\Phi)E_{\mathrm{C}}]^{1/2}$ [24]. Thus, under the assumption of identical geometry, both for Cooper-pair boxes and for transmons the transition frequencies $\Omega_j(\Phi)$ of all qubits j scale with a j-independent function $\alpha(\Phi)$ of the (global) flux Φ, $\Omega_j(\Phi) = \alpha(\Phi)\Omega_j(0)$. Here, $\alpha(\Phi) = \cos(\Phi\pi/\Phi_0)$ for Cooper-pair boxes and $\alpha(\Phi) = [\cos(\Phi\pi/\Phi_0)]^{1/2}$ for transmons. This result implies that the qubit transition frequencies, when normalized to their flux-dependent mean value, do not depend on Φ and, hence, have the same statistical properties for all Φ. Explicitly, the mean value of the Ω_j is given by $\overline{\Omega_j(\Phi)} = \alpha(\Phi)\overline{\Omega_j(0)}$. Thus, the mean value of the Ω_j is flux tunable. However, the normalized qubit transition frequencies $\Omega_j(\Phi)/\overline{\Omega_j(\Phi)}$ are independent of Φ, which must also be the case, for instance, for their standard deviation. This will become important for our numerical implementation of disorder in the Ω_j when we consider changes of the external magnetic flux Φ.

The qubit–qubit couplings $\mathcal{J}_j$ can also depend on the $E_{\mathrm{J}j}(\Phi)$ and, thus, on the Ω_j. This is the case for transmons, where approximately $\mathcal{J}_j \propto (\Omega_j\Omega_{j+1})^{1/2} \propto (E_{\mathrm{J}j}E_{\mathrm{J}j+1})^{1/4}$ [20, 25]. That is, the disorder in the Ω_j and the $\mathcal{J}_j$ will not be independent for transmons. Moreover, Ω_j, $\mathcal{J}_j$ and their mean values $\overline{\Omega_j}$ and $\overline{\mathcal{J}_j}$ change with the external flux Φ approximately in the same proportion ($\propto [\cos(\Phi\pi/\Phi_0)]^{1/2}$). For Cooper-pair boxes, on the other hand, the $\mathcal{J}_j$ depend only on charging energies and not on the $E_{\mathrm{J}j}(\Phi)$ [20]. This means that the $\mathcal{J}_j$ are not affected by changes of the external flux. Furthermore, the disorder in the $\mathcal{J}_j$ should be less pronounced than and hardly correlated with the disorder in the Ω_j. Concerning the relative strength and the correlation of the disorder in the $\mathcal{J}_j$ and the Ω_j, we remark that also static noise fields can play a role, producing some disorder also in the various charging energies of the system (in particular for Cooper-pair boxes, which have small electrostatic capacitances). Apart from that, disorder in the $\mathcal{J}_j$ will turn out to have a much weaker effect than disorder in the Ω_j. These deliberations allow us to assume for simplicity that, both for Cooper-pair boxes and for transmons, disorder in the Ω_j and $\mathcal{J}_j$ can be present to a comparable degree and that disorder in the Ω_j ($\mathcal{J}_j$) would be uncorrelated with the disorder possibly present in the $\mathcal{J}_j$ (Ω_j). We finally remark that many properties of the TFIC are determined by the ratio $\overline{\Omega_j}/\overline{\mathcal{J}_j}$, since this ratio essentially (in the limit of weak disorder) determines the eigenstates of the system (see below). For standard transmons, the ratio $\overline{\Omega_j}/\overline{\mathcal{J}_j}$ is not straightforwardly flux tunable. One of the experiments we suggest to perform with our quantum simulator relies on the possibility to

change the eigenfunctions of the system (cf section 4.2), which can be done only by changing the ratio $\overline{\Omega_j}/\overline{\mathcal{J}_j}$. All other possible experiments discussed in this paper can be performed, in principle, with Cooper-pair boxes and transmons equally well, irrespective of the $\mathcal{J}_j$ being flux-dependent or not [20]. Therefore, when plotting our results as a function of a flux-tunable system parameter, we will assume for definiteness that our circuit-QED quantum simulator of the TFIC is implemented with Cooper-pair boxes and that the $\mathcal{J}_j$ do not change with the external magnetic flux.

2.3. The transverse-field Ising chain

The Hamiltonian (2) can be exactly diagonalized by means of a Jordan–Wigner transformation, which was first used in this context in [26, 27]. This transformation maps the spin degrees of freedom to fermionic operators $c_j, c_j^\dagger$ via $\sigma_j^+ = c_j^\dagger \exp(\mathrm{i}\pi \sum_{k=1}^{j-1} c_k^\dagger c_k)$ and yields

$$\mathcal{H}_\mathrm{I} = -\sum_{j=1}^{N} \frac{\Omega_j}{2} + \sum_{j=1}^{N} \Omega_j c_j^\dagger c_j - \sum_{j=1}^{N-1} \mathcal{J}_j [c_j^\dagger c_{j+1}^\dagger + c_j^\dagger c_{j+1} + \mathrm{H.c.}]. \tag{4}$$

Up to a constant $-\sum_j \Omega_j/2$, this Hamiltonian is of the form

$$H = \sum_{i,j=1}^{N} [c_i^\dagger A_{i,j} c_j + 1/2 (c_i^\dagger B_{i,j} c_j^\dagger + \mathrm{H.c.})]. \tag{5}$$

Note that the conditions $H = H^\dagger$ and $\{c_j, c_j^\dagger\} = 1$ require that $A = A^\dagger$ and $B = -B^\mathrm{T}$. By introducing new fermions $\eta_k = \sum_{j=1}^{N} g_{k,j} c_j + h_{k,j} c_j^\dagger$, such Hamiltonians can be transformed into the diagonal form $H = \sum_k \Lambda_k (\eta_k^\dagger \eta_k - 1/2) + \sum_j A_{j,j}/2$ [26]. The components $g_{k,j}$ and $h_{k,j}$ of the vectors g_k and h_k and the excitation energies Λ_k of H are determined by defining normalized vectors $\phi_k = g_k + h_k$ and $\psi_k = g_k - h_k$ and by solving the equations

$$\phi_k (A - B) = \Lambda_k \psi_k, \quad \psi_k (A + B) = \Lambda_k \phi_k. \tag{6}$$

In our case

$$A = \begin{pmatrix} \Omega_1 & -\mathcal{J}_1 & 0 & & \cdots & 0 \\ -\mathcal{J}_1 & \Omega_2 & -\mathcal{J}_2 & & & \\ 0 & -\mathcal{J}_2 & \Omega_3 & -\mathcal{J}_3 & & \\ \vdots & & \ddots & \ddots & \ddots & \\ & & & -\mathcal{J}_{N-2} & \Omega_{N-1} & -\mathcal{J}_{N-1} \\ 0 & & & & -\mathcal{J}_{N-1} & \Omega_N \end{pmatrix}, \tag{7}$$

and B is obtained by substituting $A_{j,j} = \Omega_j \to 0$ and $A_{j+1,j} = -\mathcal{J}_j \to \mathcal{J}_j$ into A. For uniform Ω_j and $\mathcal{J}_j$, the ϕ_k, ψ_k and Λ_k can be analytically calculated from equations (6) (see, e.g., [20]). For nonuniform system parameters, these quantities have to be determined numerically. In both cases, the Hamiltonian $\mathcal{H}_\mathrm{I}$ of the TFIC can be written in the form

$$\mathcal{H}_\mathrm{I} = \sum_k \Lambda_k (\eta_k^\dagger \eta_k - 1/2), \tag{8}$$

and knowledge of the ϕ_k and ψ_k allows one to express spin observables in terms of the η_k-fermions, which is the basis of many of our calculations. For instance,

$$\sigma_z^j = (c_j^\dagger + c_j)(c_j - c_j^\dagger) = \sum_{k,k'} \phi_{k,j} \psi_{k',j} (\eta_k^\dagger + \eta_k)(\eta_{k'} - \eta_{k'}^\dagger). \tag{9}$$

We collect some important facts about the TFIC. In the uniform case,

$$\Lambda_k = 2J\sqrt{1+\xi^2-2\xi\cos k}. \tag{10}$$

Here, $J = |\mathcal{J}|$ and $\xi = \Omega/2\mathcal{J}$ is the normalized transverse field. The possible values of k are solutions of $\sin kN = \xi \sin k(N+1)$. For $N \to \infty$, the uniform TFIC undergoes a second-order QPT at $\xi = \pm 1$ from a ferromagnetic [$\xi \in (0, 1)$] or an anti-ferromagnetic [$\xi \in (-1, 0)$] ordered phase with doubly degenerate eigenstates (one $\Lambda_k \to 0$) to a paramagnetic disordered phase with $\Lambda_k > 0$ for all k. The QPT is signaled by the disappearance of long-range correlations in σ_x. This QPT will also occur in a nonuniform system (at some mean transverse field strength $\overline{\Omega_j}$) [21]. However, there can be weakly (dis)ordered Griffith–McCoy 'phases' in the vicinity of the critical point [28–31].

Finally, we introduce a convenient notation for nonuniform Ω_j and $\mathcal{J}_j$. In this case, we will frequently write $\Omega_j = \Omega\tau_j$ and $\mathcal{J}_j = \mathcal{J}\tau'_j$, where τ_j and τ'_j usually have mean 1, or, if Ω_j and $\mathcal{J}_j$ follow probability distributions, expectation value 1. We will refer to Ω as the 'mean' qubit transition frequency, even if $\Omega = \langle\Omega_j\rangle$ is the expectation value of a probability distribution and the actual mean value $\overline{\Omega_j}$ is (for finite N) in general different from Ω. We use the same convention for the qubit–qubit coupling $\mathcal{J}$. Furthermore, we define the local and the 'mean' normalized transverse magnetic field, $\xi_j = \Omega_j/2\mathcal{J}_j$ and $\xi = \Omega/2\mathcal{J}$. Note that in general both $\xi \neq \overline{\xi_j}$ and $\xi \neq \langle\xi_j\rangle$ (but for the probability distributions we will consider, $(\xi - \langle\xi_j\rangle)/\langle\xi_j\rangle < 1\%$). We usually characterize $\mathcal{H}_1$ by the parameters ξ, J, τ_j and τ'_j. Under the assumptions formulated in section 2.1, Ω and thus ξ are flux-tunable without changing the τ_j in the proposed circuit-QED quantum simulator of the TFIC.

3. Spectrum of the system

In order to provide a guideline for the initial experimental characterization of our setup, we have calculated in [20] the transmission spectrum S of the resonator as a function of the probe frequency ω and the flux-tunable qubit transition frequency Ω (see below equation (28)). To that end, we have first calculated the spectrum of the bare TFIC for coupling to the first qubit via σ_x^1,

$$\tilde{\rho}(\omega) = \int \mathrm{d}t\, \mathrm{e}^{\mathrm{i}\omega t}\langle\sigma_x^1(t)\sigma_x^1(0)\rangle, \tag{11}$$

which is the Fourier transform of the qubit autocorrelator $\rho(t) = \langle\sigma_x^1(t)\sigma_x^1(0)\rangle$. We have argued that for sufficiently large (but finite) N, qubit decay processes will render the measured spectrum continuous and akin to the spectrum one would obtain by taking the limit $N \to \infty$ in the calculation of ρ. Assuming small coupling $g/\omega_0 \ll 1$ of the first qubit and the resonator, we have then considered the TFIC as a linear bath for the resonator, and this approximation allowed us to calculate the resonator spectrum S in the coupled system. In this section, we add some remarks on the interpretation of the autocorrelator, the transition $N \to \infty$ and the linear approximation. Moreover, we discuss how a small amount of disorder in the qubit parameters due to imperfections in the fabrication process affects the resonator spectrum S.

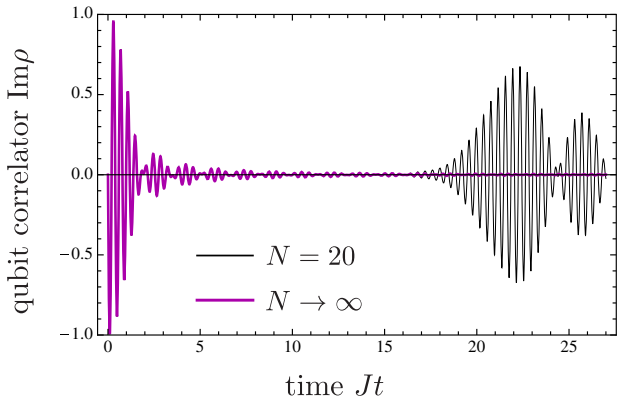

Figure 2. Imaginary part of the qubit autocorrelator $\rho(t) = \langle\sigma_x^1(t)\sigma_x^1(0)\rangle$ of the TFIC with normalized transverse field $\xi = \Omega/2\mathcal{J} = 8$ in the cases $N = 20$ (black) and $N \to \infty$ (magenta).

3.1. Time-dependent correlations in the transverse-field Ising chain

By means of the spin–free-fermion mapping described in section 2.3, one readily finds that

$$\rho(t) = \langle\sigma_x^1(t)\sigma_x^1(0)\rangle = \sum_k \phi_{k,1}^2\, \mathrm{e}^{-\mathrm{i}t\Lambda_k}. \tag{12}$$

Here and in the following, expectation values are calculated under the assumption of zero temperature. This is justified because the band gap of the Ising chain is of the same order of magnitude as the qubit transition frequencies $\Omega \sim 5\,\mathrm{GHz}$ (except near the critical point) and, thus, much bigger than the usual mK temperatures of a cryogenic environment. In the uniform case $\Omega_j = \Omega$ and $\mathcal{J}_j = \mathcal{J}$, where explicit expressions for ϕ_k and Λ_k can be found, the limit $N \to \infty$ can be taken analytically and yields [20]

$$\rho(t) = \Theta(1-|\xi|)(1-|\xi|^2) + \frac{2}{\pi}\int_0^\pi \mathrm{d}k \frac{\xi^2 \sin^2 k}{1+\xi^2-2\xi\cos k}\mathrm{e}^{-\mathrm{i}t\Lambda(k)}. \tag{13}$$

Here, $\Theta(x)$ is the Heaviside step function and $\Lambda(k)$ stands for Λ_k with continuous k (equation (10)). The first term on the rhs of (13) causes a nonzero mean value of $\mathrm{Re}\,\rho(t)$ in the ordered phase. Figure 2 shows $\mathrm{Im}\,\rho(t)$ for $\xi = 8$ in the cases $N = 20$ (equation (12)) and $N \to \infty$ (equation (13)) (the time evolutions of $\mathrm{Re}\,\rho$ and $\mathrm{Im}\,\rho$ are qualitatively similar and agree for $|\xi| \gg 1$ up to a phase). For small times, the curves coincide (the second covers the first). However, the finite size of the TFIC with $N = 20$ causes a revival of ρ at $T_\mathrm{r} \approx 2N/v$ with $v = \max[\mathrm{d}\Lambda(k)/\mathrm{d}k]$ ($v = 2J|\xi|$ for $\xi < 1$ and $v = 2J$ for $|\xi| > 1$). This can be understood in the following way. The autocorrelator ρ is related to the linear response $\Delta\langle\sigma_x^1\rangle(t)$ of the TFIC to a perturbation $\propto \delta(t)\sigma_x^1$ relative to the equilibrium value $\langle\sigma_x^1\rangle = 0$. Indeed, Kubo's formula predicts that $\Delta\langle\sigma_x^1\rangle(t) \propto \mathrm{Im}\,\rho(t)$. The δ-pulse at $t = 0$ forces the first spin in the $-x$-direction. This local excitation in position space is composed of many excitations in k-space. Since most of them have velocity v [20], the local excitation propagates with velocity v through the system, is reflected at the far end of the chain and causes revivals of ρ at multiples of $T_\mathrm{r} = 2N/v$. To further clarify the transition $N \to \infty$, we note that for large t, ρ has a standard deviation from

its mean $\propto 1/\sqrt{N}$. This can be expected from (12) since $|\rho(t)|^2 \sim 1/N^2 \sum_{k,k'} \mathrm{e}^{\mathrm{i}t(\Lambda_k - \Lambda_{k'})}$ and, for $t \to \infty$, all terms in the sum except for those with $k = k'$ will cancel. In general, the $t \to \infty$ fluctuations that we find for all time-dependent observables considered in this work are due to the finite system size and decrease with N (but not all of them behave like $\propto 1/\sqrt{N}$).

3.2. Spectrum of the resonator—the linear approximation

Taking the Fourier transform of equations (12) and (13) yields the spectrum $\tilde{\rho}(\omega)$ of the TFIC for a force that couples to σ_x^1 for finite N and $N \to \infty$, respectively. In order to calculate the spectrum S of the resonator, whose coordinate $(a^\dagger + a)$ couples to σ_x^1 (cf equation (1)), we have suggested [20] a useful approximation: we consider the TFIC as a linear bath for the resonator. That is, we replace the TFIC by a set of harmonic oscillators having the spectrum $\tilde{\rho}$ of the TFIC. This approximation can be straightforwardly generalized to other contexts, where a different many-body system couples to a resonator. It is justified in the limit of small qubit–resonator coupling $g/\omega_0 \ll 1$, as we discuss in the following.

The linear approximation for the TFIC-bath fails as soon as probing the resonator sufficiently excites the TFIC so that its nonlinearity becomes important. Thus, the linear approximation requires a small coupling g and is worst if the TFIC is on resonance with the resonator (ω_0 within the band Λ_k of the TFIC). The 'most nonlinear' bath possible for the resonator, that is, the bath whose nonlinearity becomes important for the smallest value of g, is a bath consisting of only a single qubit on resonance with the resonator. If the linear approximation is adequate for such a system in the limit $g/\omega_0 \ll 1$, it will be also sufficient for our purposes. Therefore, we now consider the case $N = 1$ and $\Omega = \omega_0$ of equation (1) and calculate the spectrum of the resonator by linearizing the single-qubit bath. Since the atomic Hilbert space is small for $N = 1$, we can then numerically check the accuracy of our approximation. We also compare our approximation with the resonator spectrum calculated analytically within the rotating wave approximation (RWA), which is the standard approximation of $\mathcal{H}$ in this specific situation.

For $N = 1$ and $\Omega = \omega_0$, the Hamiltonian $\mathcal{H}$ (equation (1)) becomes

$$\mathcal{H}_{N=1} = \omega_0 a^\dagger a + g(a^\dagger + a)\sigma_x + \frac{\omega_0}{2}\sigma_z. \tag{14}$$

That is, the resonator coordinate $(a^\dagger + a)$ couples to a single-qubit bath with the Hamiltonian $\mathcal{H}_\mathrm{q} = \frac{\omega_0}{2}\sigma_z$ via a force $g\sigma_x$. The spectrum of this force is

$$\tilde{F}_\mathrm{q}(\omega) = \int \mathrm{d}t\, \mathrm{e}^{\mathrm{i}\omega t}\, {}_\mathrm{q}\langle g\sigma_x(t)\, g\sigma_x(0)\rangle_\mathrm{q} = 2\pi g^2 \delta(\omega - \omega_0), \tag{15}$$

where the time evolution of σ_x and the expectation value ${}_\mathrm{q}\langle\,.\,\rangle_\mathrm{q}$ are to be calculated with respect to (the ground state of) $\mathcal{H}_\mathrm{q}$. Now we linearize the system and replace $\mathcal{H}_{N=1}$ by

$$\mathcal{H}_\mathrm{lin} = \omega_0 a^\dagger a + g'(a^\dagger + a)(b^\dagger + b) + w b^\dagger b \tag{16}$$

with bosonic $b, b^\dagger$ and parameters g' and w to be determined. In (16), the resonator couples to a force $g'(b^\dagger + b)$ exerted by a bath that consists of a single harmonic oscillator with the Hamiltonian $\mathcal{H}_\mathrm{ho} = w b^\dagger b$. The spectrum of this force reads

$$\tilde{F}_\mathrm{ho}(\omega) = 2\pi (g')^2 \delta(\omega - w). \tag{17}$$

Thus, we choose $g' = g$ and $w = \omega_0$ such that $\tilde{F}_\mathrm{ho} = \tilde{F}_\mathrm{q}$. With this substitution, we now calculate the autocorrelator of the resonator coordinate

$$\rho_\mathrm{lin}(t) = {}_\mathrm{lin}\langle [a^\dagger(t) + a(t)][a^\dagger(0) + a(0)]\rangle_\mathrm{lin}, \tag{18}$$

and its Fourier transform, the resonator spectrum

$$\tilde{\rho}_{\mathrm{lin}}(\omega) = \int \mathrm{d}t\, \mathrm{e}^{\mathrm{i}\omega t} \rho_{\mathrm{lin}}(t), \tag{19}$$

according to equation (16). To that end, we express the resonator coordinate $(a^\dagger + a)$ in terms of the (bosonic) eigenmodes $\tilde{c}_\pm$ with frequencies $\tilde{\omega}_\pm = \sqrt{\omega_0^2 \pm 2\, g\omega_0}$ of $\mathcal{H}_{\mathrm{lin}}$,

$$(a^\dagger + a) = \sqrt{\frac{\omega_0}{2}} \left(\frac{\tilde{c}_+^\dagger + \tilde{c}_+}{\sqrt{\tilde{\omega}_+}} + \frac{\tilde{c}_-^\dagger + \tilde{c}_-}{\sqrt{\tilde{\omega}_-}} \right). \tag{20}$$

Using (20), one readily finds that

$$\rho_{\mathrm{lin}}(t) = \frac{\omega_0}{2} \left[\frac{\mathrm{e}^{-\mathrm{i}\tilde{\omega}_+ t}}{\tilde{\omega}_+} + \frac{\mathrm{e}^{-\mathrm{i}\tilde{\omega}_- t}}{\tilde{\omega}_-} \right], \tag{21}$$

$$\tilde{\rho}_{\mathrm{lin}}(\omega) = \pi \left[\frac{\omega_0}{\tilde{\omega}_+} \delta(\omega - \tilde{\omega}_+) + \frac{\omega_0}{\tilde{\omega}_-} \delta(\omega - \tilde{\omega}_-) \right]. \tag{22}$$

Before we go on and compare these approximate analytical results with numerical finite-size calculations for $\mathcal{H}_{N=1}$ (equation (14)), we calculate the same quantities on the basis of the standard approximation to $\mathcal{H}_{N=1}$ for $g/\omega_0 \ll 1$, the RWA (see, e.g., [32]). This will be a helpful benchmark for estimating the quality of the linear approximation. In the RWA, the Hamiltonian $\mathcal{H}_{N=1}$ reduces to the Jaynes–Cummings Hamiltonian

$$\mathcal{H}_{\mathrm{RWA}} = \omega_0 a^\dagger a + g(a^\dagger \sigma^- + a\sigma^+) + \frac{\omega_0}{2}\sigma_z. \tag{23}$$

This Hamiltonian can be straightforwardly diagonalized, and one can therefore analytically calculate the autocorrelator $\rho_{\mathrm{RWA}}(t)$ and the spectrum $\tilde{\rho}_{\mathrm{RWA}}(\omega)$ of the resonator in the approximation provided by $\mathcal{H}_{\mathrm{RWA}}$,

$$\rho_{\mathrm{RWA}}(t) = \frac{1}{2} \left[\mathrm{e}^{-\mathrm{i}t(\omega_0 + g)} + \mathrm{e}^{-\mathrm{i}t(\omega_0 - g)} \right], \tag{24}$$

$$\tilde{\rho}_{\mathrm{RWA}}(\omega) = \pi [\delta(\omega - (\omega_0 + g)) + \delta(\omega - (\omega_0 - g))]. \tag{25}$$

On the basis of (23), the results (24) and (25) are exact.

The autocorrelator and the spectrum of the resonator can also be calculated numerically after truncating the photonic Hilbert space. This is achieved by expanding $\mathcal{H}_{N=1}$ and the resonator coordinate $(a^\dagger + a)$ in the product basis $\{|s_z, \nu\rangle\}$, where $s_z = \uparrow, \downarrow$ and $\nu \in \mathbb{N}_0$, and dropping all matrix elements with $\nu > \nu_{\max}$. In this finite-size approximation, the eigenvalues E_n and eigenvectors $|n\rangle$ of $\mathcal{H}_{N=1}$ can be numerically calculated ($n = 0, \ldots, n_{\max} = 2\nu_{\max} + 1$) and give $\rho(t)$ and $\tilde{\rho}(\omega)$ according to

$$\rho(t) = \sum_{n=0}^{n_{\max}} \mathrm{e}^{-\mathrm{i}(E_n - E_0)t}\, |\langle 0|(a^\dagger + a)|n\rangle|^2, \tag{26}$$

$$\tilde{\rho}(\omega) = 2\pi \sum_{n=0}^{n_{\max}} \delta(\omega - (E_n - E_0))\, |\langle 0|(a^\dagger + a)|n\rangle|^2. \tag{27}$$

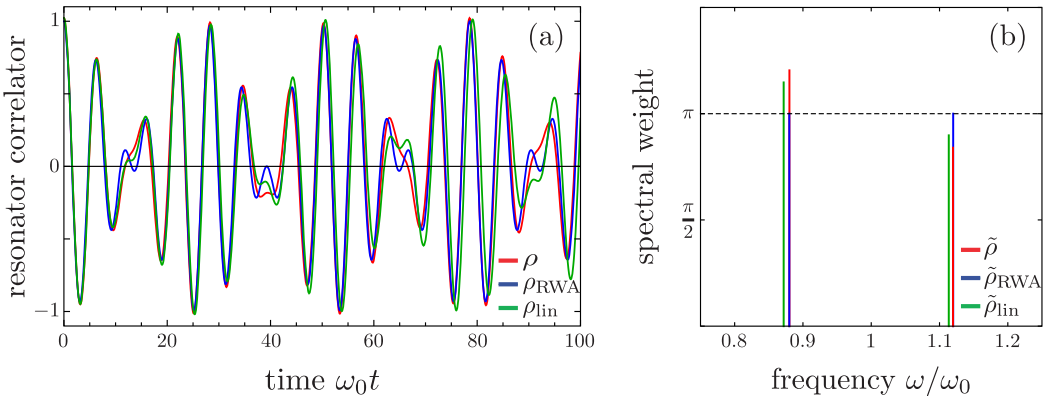

Figure 3. Comparison of the RWA and the linear approximation with highly accurate finite-size numerics for a resonator with frequency ω_0 resonantly coupled to a single qubit with coupling strength $g/\omega_0 = 0.12$. (a) The autocorrelator $\rho(t) = \langle [a^\dagger(t) + a(t)][a^\dagger(0) + a(0)] \rangle$ of the resonator (red), and the same quantity calculated within the RWA (ρ_{RWA}, blue) and the linear approximation (ρ_{lin}, green). (b) The spectrum $\tilde{\rho}(\omega) = \int \mathrm{d}t\, \mathrm{e}^{\mathrm{i}\omega t} \rho(t)$ of the resonator (red), and the same quantity calculated within the RWA ($\tilde{\rho}_{\mathrm{RWA}}$, blue) and the linear approximation ($\tilde{\rho}_{\mathrm{lin}}$, green). The dashed line is a guide to the eye.

Even for a relatively strong coupling $g/\omega_0 = 0.3$, the numerical results for $\rho(t)$ and $\tilde{\rho}(\omega)$ are already converged if $\nu_{\max} = 3$ photonic excitations are taken into account. However, to be on the safe side, we choose $\nu_{\max} = 10$ in our calculations, which is still numerically easily tractable.

Our results for the autocorrelator $\rho(t)$ and the spectrum $\tilde{\rho}(\omega)$ of the resonator in $\mathcal{H}_{N=1}$ are plotted, respectively, in figure 3(a) (equations (21), (24), (26)) and figure 3(b) (equations (22), (25), (27)). In both plots, we choose $g/\omega_0 = 0.12$, which is the largest ratio of g/ω_0 used in this work and in [20]. The autocorrelator $\rho(t)$ of the resonator (red) is well approximated both by the RWA (ρ_{RWA}, blue) and the linear approximation (ρ_{lin}, green), and the quality of these approximations is essentially equal. For small t, the linear approximation might be even more accurate than the RWA, but becomes worse at large t. This can be understood in the frequency domain. In figure 3(b), we plot the spectral weights of the delta peaks in the spectra $\tilde{\rho}$, $\tilde{\rho}_{\mathrm{RWA}}$ and $\tilde{\rho}_{\mathrm{lin}}$ (red, blue and green) at the corresponding peak positions. The spectrum $\tilde{\rho}$ contains also delta peaks at higher frequencies than the ones plotted, but their weight is virtually zero ($2\pi |\langle 0|(a^\dagger + a)|n\rangle|^2 < 10^{-7}$ for all $n \neq 1, 2$). Both approximations yield good predictions for the positions and the spectral weights of the peaks in $\tilde{\rho}$. The RWA is more precise in predicting the peak positions and the linear approximation in predicting the spectral weights (note, however, that the peak positions in $\tilde{\rho}_{\mathrm{lin}}$ and $\tilde{\rho}_{\mathrm{RWA}}$ agree up to first order in g/ω_0). Thus, the linear approximation is more precise for small t, in particular at $t \approx 0$ and where the envelope of $\rho(t)$ has a minimum, but becomes worse for large t. In summary, we conclude that even for the situation $N = 1$ and $\Omega = \omega_0$, the linear approximation yields good results for the autocorrelator and the spectrum of the resonator in the limit $g/\omega_0 \ll 1$ that are qualitatively comparable to the usual RWA in this context. This implies that the linear approximation is well justified in our calculation of the spectrum of a resonator coupled to a TFIC.

3.3. Spectrum of the resonator—disorder effects

The linear approximation for the TFIC allows one to express the spectrum $S(\omega)$ of the (coupled) resonator as a function of the spectrum $\tilde{\rho}(\omega)$ of the TFIC [20],

$$S(\omega) = \frac{4\Theta(\omega)[\kappa + g^2\tilde{\rho}(\omega)]}{[\omega^2/\omega_0 - \omega_0 - 4g^2\chi(\omega^2)]^2 + [\kappa + g^2\tilde{\rho}(\omega)]^2}. \tag{28}$$

Here, κ is the full-linewidth at half-maximum of the Lorentzian spectrum of the uncoupled ($g = 0$) resonator and $\chi(\omega^2)$ denotes the principal-value integral $\chi(\omega^2) = 1/(2\pi)\int \mathrm{d}\Omega\tilde{\rho}(\Omega)\Omega/(\omega^2 - \Omega^2)$. This result is actually general and holds for any linear bath coupled to a resonator, with an arbitrary spectrum $\tilde{\rho}$. Plots of S, with $\tilde{\rho}(\omega)$ being the Fourier transform of (13), are presented in [20]. However, in an actual implementation of the proposed setup, the qubit parameters $\mathcal{J}_j$ and Ω_j will not be perfectly uniform, due to imperfections in the fabrication process. We now investigate how this modifies the characteristic features of the spectrum S of the uniform system. It is known in the field of random-matrix theory that disorder would have to be very strong in order to have a dominant effect on (average) spectra. We will observe the same here, in this concrete model system.

For a nonuniform TFIC, no closed analytical expressions for $\tilde{\rho}(\omega)$ are available. Thus, we have to consider finite system sizes and calculate numerically the relevant quantities, specifically, the spectrum of a finite-size nonuniform TFIC,

$$\tilde{\rho}(\omega) = 2\pi \sum_k \phi_{k,1}^2 \delta(\omega - \Lambda_k), \tag{29}$$

which is the Fourier transform of equation (12). To take the effect of qubit decay processes into account, we phenomenologically broaden the delta peaks in (29) and replace them by Lorentzians of width γ around the Λ_k. We model the nonuniformity of the qubit parameters by writing $\Omega_j = \Omega\tau_j$ and $\mathcal{J}_j = \mathcal{J}\tau'_j$ and choosing τ_j and τ'_j to be random variables, which follow Gaussian distributions with means 1 and standard deviations $\sigma_\tau = \sigma_{\tau'} = 0.02$. Uniformity of the qubit parameters Ω_j and $\mathcal{J}_j$ of this degree will turn out to be sufficient for all proposed experiments. Much stronger disorder is not generally tolerable, as we will see below. However, from the experimental data for a sample with three (even spatially separated) qubits presented in [33], we calculate a standard deviation of the qubit transition frequencies from their mean of 0.8% (for zero flux bias). Thus, the requirements on the uniformity of Ω_j and $\mathcal{J}_j$ appear to be attainable. With a typical set of system parameters that was also used in [20], we numerically calculate $\tilde{\rho}(\omega)$ according to (29) and the corresponding resonator spectrum S according to (28). In order to judge the effects of disorder, we also reproduce our calculation of S for the corresponding uniform system [20] (figure S6). Figure 4 shows S as a function of ω and the (mean) normalized transverse field $\xi = \Omega/2\mathcal{J}$ for the uniform system (figures 4(a) and (b)) and for a typical disorder configuration (figures 4(c) and (d)). In the uniform case, the signatures of the QPT at $\xi = 1$, the dispersive shift of the resonator frequency and, on resonance, the double peak with a separation of $4J$ (rather than $2g$ as in the case $N = 1$) that we have discussed in detail for $N \to \infty$ in [20] are clearly visible also for $N = 20$. These characteristic features are insensitive with respect to a small amount of disorder in the system parameters, as figures 4(c) and (d) demonstrate.

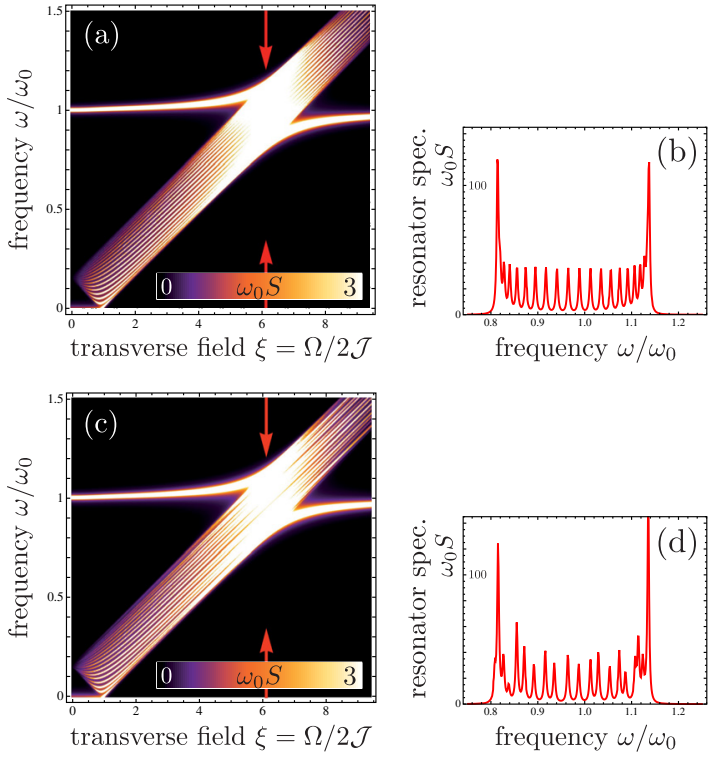

Figure 4. (a) Spectrum S of a resonator coupled to a finite uniform TFIC with $N = 20$ versus probe frequency ω and normalized transverse field $\xi = \Omega/2\mathcal{J}$. The parameters are $g = 0.12$, $J = 0.08$, $\kappa = 10^{-4}$ and $\gamma = 5 \times 10^{-3}$ (in units of ω_0). For better visibility of the features, values > 3 are plotted in white. (b) Spectrum $S(\omega)$ for $\xi = 6.1$. This curve corresponds to a cut along the arrows in (a). (c) The same as in (a) but with Ω_j and $\mathcal{J}_j$ following a Gaussian distribution with a standard deviation of 2% around their mean values. (d) Cut along the arrows in (c).

We remark that in several recent circuit QED experiments the qubits have been found to be unexpectedly hot [34–36]. A corresponding non-negligible equilibrium population of the excited many-body eigenstates of the Ising chain in our setup would lead to additional lines in the described spectroscopy experiment, at frequencies smaller than the bandwidth of the Ising chain. In the experimentally realistic case that the Ising chain is deeply in the paramagnetic phase ($\Omega \gg 2J$), these resonances at $\omega \lesssim 4J$ (the bandwidth of the chain in the paramagnetic phase) would be well below the lower band edge $\Omega - 2J$. Thus, they would be distinguishable from the band of the Ising chain as plotted in figure 4, and their intensity might allow one to estimate the spurious population of the excited states. However, for the proposed time-domain experiments with our circuit QED quantum simulator that we discuss in the following sections, a non-negligible equilibrium excitation of the Ising chain might necessitate post-selection or initialization techniques.

4. Disorder effects on the system dynamics

A particularly interesting application of the proposed system would be to simulate the nonequilibrium dynamics of the TFIC. In [20], we have suggested to experimentally track the propagation of a localized excitation in the (uniform) TFIC that can be easily created in our system and to measure the system dynamics after quenching the transition frequencies of all qubits. In this section, we show that none of the predicted experimental results changes qualitatively if the parameters of the TFIC are slightly disordered, as has to be expected in reality. Stronger disorder, accessible, e.g., by deliberately detuning individual qubits, is shown to produce qualitatively different physics in the previously proposed experiments, like Anderson localization of the propagating excitation. For the realistic case $\Omega \gg J$, we give an estimate of the corresponding disorder strength. Finally, we develop a quantitative theory of the effects of weak disorder on the system's nonequilibrium dynamics that explains the results of numerical experiments with the disordered TFIC. This theory might be helpful for experimentalists to estimate system and disorder parameters for successfully performing nonequilibrium experiments with the TFIC (e.g. for a given measurement resolution) without having to do numerical simulations.

4.1. Propagation of localized excitations

For the first type of experiments we have suggested in [20], it is assumed that the TFIC is deeply in the paramagnetic phase ($\xi \gg 1$) and detuned from the resonator. In this situation, the TFIC is essentially decoupled from the resonator and its ground state is characterized by $\langle \sigma_z^j \rangle \approx -1$. Applying a fast π-pulse to the first qubit thus creates a localized excitation in the system that subsequently propagates through the chain due to the qubit–qubit coupling $\mathcal{J}$. The time evolution of the observable $\langle \sigma_z^j \rangle$ after the π-pulse can be approximately described by [20]

$$\langle \sigma_z^j \rangle(t) = -\sum_k \psi_{k,j}\phi_{k,j} + \sum_{k,k'} \mathrm{e}^{\mathrm{i}(\Lambda_k - \Lambda_{k'})t}\left[\phi_{k,1}\phi_{k',1}(\psi_{k,j}\phi_{k',j} + \psi_{k',j}\phi_{k,j})\right]. \tag{30}$$

We plot this result in figure 5(a) for all j in a chain of length $N = 20$ and for a mean normalized transverse field $\xi = \Omega/2\mathcal{J} = 8$ (the same system parameters as in [20]) and, again, we randomly choose $\Omega_j = \Omega\tau_j$ and $\mathcal{J}_j = \mathcal{J}\tau'_j$ according to Gaussian distributions with standard deviations of 2% from the mean values Ω and $\mathcal{J}$ as before (right panel). The experimentally measurable observable $\langle \sigma_z^1 \rangle(t)$ is singled out in the left panel. The propagation of a localized excitation through the chain, and its reflection at the far end of the chain that leads to a distinct revival of $\langle \sigma_z^1 \rangle(t)$ at $t \approx N/J$, are still clearly visible in this slightly nonuniform system.

If the transition frequencies Ω_j of the qubits can be tuned individually, the effective length of the TFIC has been shown to be adjustable by strongly detuning one qubit from the others [20]. This holds true also for a slightly nonuniform system: figure 5(b) shows the typical result for a system with the same parameters and disorder strength as in (a), but with qubit 11 strongly detuned by setting $\tau_{11} = 1.3$. This result is qualitatively identical with the result for the corresponding nondisordered system [20]. The strong nonuniformity at $j = 11$ acts as a barrier for the propagating excitation and leads to its reflection. Thus, it effectively changes the length of the TFIC.

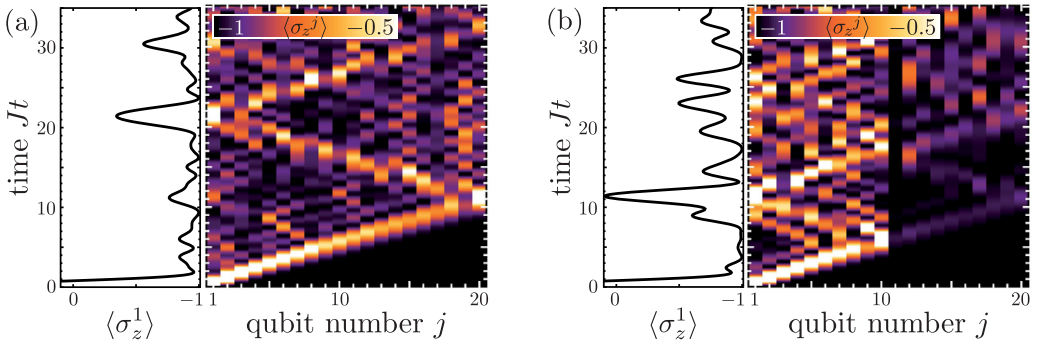

Figure 5. Propagation of a localized excitation in a slightly disordered TFIC of length $N = 20$. Specifically, the density plots show the nonequilibrium time evolution of $\langle\sigma_z^j\rangle$ for all j after a π-pulse on the first qubit while the system is in the paramagnetic phase (mean normalized transverse field $\xi = 8$). For better visibility of the features, values > -0.5 are plotted in white. The experimentally accessible observable $\langle\sigma_z^1\rangle$ is singled out in the left panels. (a) The qubit transition frequencies Ω_j and qubit–qubit couplings $\mathcal{J}_j$ are randomly chosen according to Gaussian distributions with standard deviations of 2% from the mean values. (b) The same as in (a) but with qubit 11 strongly detuned.

Having shown that the experiments with propagating localized excitations proposed in [20] yield qualitatively the same results for ordered and slightly disordered systems, we now proceed and study disorder effects on this type of experiment quantitatively. Parts of the following analysis also apply to other nonequilibrium experiments with the TFIC, as will be discussed in the context of quantum quenches (section 4.2).

Since it is assumed that the system is deeply in the paramagnetic phase, the mean qubit transition frequency Ω is larger than the modulus of the mean qubit–qubit coupling J, $\Omega/J \gg 1$. As before, we further assume uncorrelated disorder of the system parameters via $\Omega_j = \Omega\tau_j$ and $\mathcal{J}_j = \mathcal{J}\tau'_j$, where τ_j and τ'_j follow Gaussian distributions with standard deviations σ_τ and $\sigma_{\tau'}$ from 1. That is, for $\sigma_\tau = \sigma_{\tau'}$, the absolute variation of the Ω_j will be larger than the absolute variation of the $\mathcal{J}_j$. Therefore, the dynamics of the system may be expected to be much more sensitive to increasing σ_τ than $\sigma_{\tau'}$. Moreover, one may expect that disorder effects start to qualitatively affect the system dynamics even of small systems (that is, on the scale of neighboring qubits j and $j+1$) when the disorder in the qubit transition frequencies becomes comparable to the modulus of the mean qubit–qubit coupling, $\Omega\sigma_\tau = J$. These deliberations are confirmed by numerical experiments: we first consider the wave functions $g_{k,j}$ and $h_{k,j}$ in position space ($\eta_k = \sum_{j=1}^{N} g_{k,j}c_j + h_{k,j}c_j^\dagger$). For zero disorder, they are extended over the whole chain (except for the mode with $\Lambda_k \to 0$ in the ordered phase [37]). Increasing σ_τ localizes the wave functions much more strongly than increasing $\sigma_{\tau'}$, and the localization length of the wave functions indeed reduces from many ($\gg 1$) sites to a few ($\gtrsim 1$) sites at $\Omega\sigma_\tau \approx J$. Correspondingly, the propagation of an excitation initially localized at site 1 is only weakly affected by disorder in $\mathcal{J}$. However, if $\sigma_\tau \gtrsim J/\Omega$, it propagates only a few sites before becoming completely trapped due to the disorder. This manifestation of Anderson localization [38] is

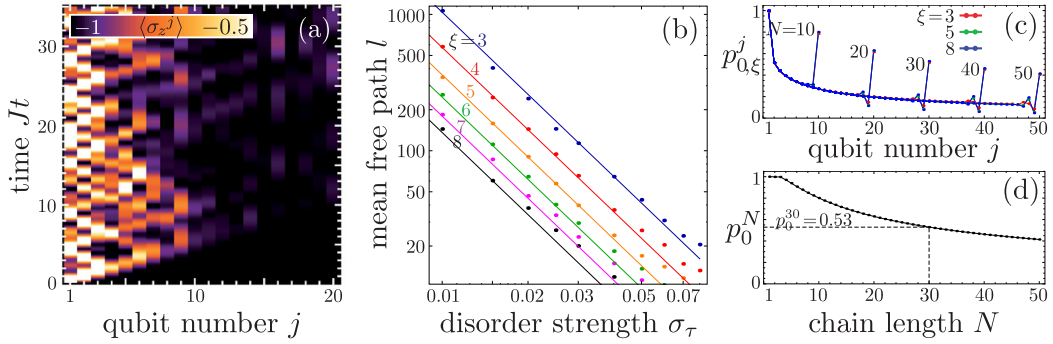

Figure 6. (a) Propagation of an initially localized excitation in a strongly disordered TFIC. Initialization and system parameters are identical to figure 5(a), but the Ω_j and $\mathcal{J}_j$ are randomly chosen according to Gaussian distributions with standard deviations of 6.5% from the mean values. The plot clearly shows that strong localization of the excitation prohibits its propagation through the chain. (b) Mean free path l of the propagating excitation (defined in the main text) versus normalized standard deviation σ_τ of the qubit transition frequencies for different values of the normalized transverse field ξ on the log–log scale. The points are $l_{\sigma_\tau,\xi}$ as gained by numerically averaging many disorder configurations. The lines are best fits of $1/\sigma_\tau^a \xi^b$ to these data. (c), (d) Behavior of a nondisordered system, with uniform $\Omega_j = \Omega$ and $\mathcal{J}_j = \mathcal{J}$, for comparison. (c) Maximum excitation probabilities $p^j_{0,\xi}$ of the jth qubits in the nonequilibrium time evolution of uniform TFICs of lengths $N = 10, 20, 30, 40, 50$ after the first qubit has been flipped. For each chain length, $p^j_{0,\xi}$ is plotted for $\xi = 3, 5, 8$ (red, green, blue). Apart from boundary effects, the decay of $p^j_{0,\xi}$ with j is slower than $\propto 1/j$. The maximum excitation probabilities $p^N_{0,\xi}$ of the last qubits of the chains are significantly enhanced compared to nearby bulk sites. (d) Maximum excitation probability p^N_0 of the Nth qubit versus chain length N (for any $\xi \gg 1$).

illustrated in figure 6(a), where we have used the same system parameters as in figure 5, but we have randomly chosen τ_j and τ'_j according to Gaussian distributions around 1 with standard deviations $\sigma_\tau = J/\Omega = 0.0625 = \sigma_{\tau'}$. For definiteness, we always choose $\sigma_{\tau'} = \sigma_\tau$ in the following.

We have seen that for $|\xi| \gg 1$ (paramagnetic phase) the effective disorder strength in the quantum Ising chain is set by $\sigma_\tau \Omega/J \propto \sigma_\tau |\xi|$. Now we try to determine how the relevant observables in the currently considered type of experiment depend on this quantity. The observable we focus on in the following is the maximum excitation probability (maximized over time) of the jth qubit caused by the propagation of the localized excitation through the disordered chain. In an experiment, one would for instance create an excitation of the first qubit and measure the excitation probability of some other (e.g. the Nth) qubit as a function of time. The maximum excitation probability of the jth qubit is an important quantity since it will determine whether the effect of the propagating excitation can be measured at site j, given a certain measurement resolution. In a single disordered system, the maximum excitation

probability of qubit j will depend on the specific (random) disorder configuration of this system. Therefore, a study of the effect of disorder as characterized by the statistical quantity $\sigma_\tau|\xi|$ can only refer to the statistical average of the maximum excitation probability of qubit j in one disordered system over an ensemble of many disordered systems (disorder configurations), all chosen according to the same probability distribution. Stated as a formula, this ensemble average of the maximum excitation probability of qubit j is given by

$$p^j_{\sigma_\tau,|\xi|} = \frac{1}{2}\Big(\overline{\overline{\max_t[\langle\sigma_z^j\rangle(t)]}} + 1\Big). \tag{31}$$

Here, the double overbar $\overline{\overline{\cdot}}$ denotes the ensemble average over many disordered systems (disorder configurations) with the same system and disorder parameters ξ, J and $\sigma_\tau = \sigma_{\tau'}$. This average is taken after one has maximized $\langle\sigma_z^j\rangle(t)$ for a specific disordered system over time. Our goal is to find the explicit functional dependence of $p^j_{\sigma_\tau,|\xi|}$ on σ_τ and $|\xi|$ (in fact, we expect dependence only on the product $\sigma_\tau|\xi|$). Note that we assume that $p^j_{\sigma_\tau,|\xi|}$ depends neither on the sign of ξ nor explicitly on the mean qubit–qubit coupling J, but only on the ratio of Ω and J (via $|\xi|$). This is strictly true for $\sigma_\tau = \sigma_{\tau'} = 0$. By explicitly solving equations (6) for this case [20], one can show that after substituting $\xi \to -\xi$, the new allowed wave vectors are $q = \pi - k$ with $\Lambda_q = \Lambda_k$, $\phi_{q,j} = (-1)^{N-j}\phi_{k,j}$, and $\psi_{q,j} = (-1)^{N-j}\psi_{k,j}$. With that one can easily see that equation (30) does not depend on the sign of ξ. Moreover, ϕ_k and ψ_k are independent of J (which also follows from equations (6)), and $\Lambda_k \propto J$ such that changing J corresponds only to a rescaling of time. The influence of disorder, however, is essentially set by $\sigma_\tau|\xi|$ (for $|\xi| \gg 1$), as we have argued above. Consequently, we may take p^j to be independent of J and of the sign of ξ. Nevertheless, to keep notation short, we write ξ instead of $|\xi|$ for the remainder of this section. For simplicity, we first focus on a semi-infinite system ($N \to \infty$) and discuss later the increase of p^j at the end of the chain (due to the refocusing of the dispersed wave packet of the propagating excitation).

As usual for disordered systems (e.g. [39]), we will try to characterize the disorder effects on the ensemble-averaged maximum qubit excitation $p^j_{\sigma_\tau,\xi}$ via a mean free path. To that end, it pays to first discuss in more detail the uniform case, $p^j_{0,\xi}$. Even there, analyzing the propagation of the dispersive wave packet that determines the maximum excitation probability of a qubit requires some care. For $\xi \gg 1$, this excitation probability does not depend on ξ. This is because the dispersion relation of the TFIC becomes that of the tight binding model, $\Lambda_k = 2J\sqrt{1+\xi^2-2\xi\cos k} \approx 2J\,\mathrm{sign}(\xi)(\xi - \cos k)$. Thus, ξ only sets the band gap but does not influence the shape of the dispersion relation. Except for the aforementioned boundary effects, $p^j_{0,\xi}$ also does not depend on N. This is evident from figure 6(c), where we plot $p^j_{0,\xi}$ for several ξ and N. The curves for different ξ but the same N lie almost on top of each other (henceforth, we drop the index ξ from $p^j_{0,\xi}$), and curves for different N can be distinguished only by the boundary effects, that is, by the strong increase of p^j_0 at $j = N$ (which will be discussed later). The decay of the p^j_0 with j is relatively slow (slower than $1/j$), which should considerably simplify the experiments proposed in [20]. This slow decay of p^j_0 can be understood from the dispersion relation Λ_k of the system which, for $\xi \gg 1$, is quadratic in k at $k \approx 0, \pi$, and linear at $k \approx \pi/2$: if an initially localized wave packet with width s and momentum q, $\psi(x,0) = \alpha\,\mathrm{e}^{-x^2/2s^2+iqx}$, $\alpha = (s^2\pi)^{-1/4}$, is evolved in time by the Hamiltonians $H_1 = h_1 k$ and $H_2 = h_2 k^2$, respectively, one finds that

$$|\psi(x,t)|^2_{H_1} = |\psi(x - h_1 t, 0)|^2 = \alpha^2 \mathrm{e}^{-(x-h_1 t)^2/s^2}, \tag{32}$$

$$|\psi(x,t)|^2_{H_2} = \frac{\alpha^2 s^2}{\sqrt{s^4+4h_2^2t^2}} \exp\left(-\frac{(x-2h_2tq)^2}{s^4+4h_2^2t^2}\right). \tag{33}$$

That is, for H_1, the maximum and width of the probability distribution for finding the particle at a position x are constant, while for H_2 and strong initial localization (or large times) the width is $\propto t$ and the maximum is $\propto 1/t$. As the dispersion relation of the TFIC interpolates between these two cases, one may expect a decay of p_0^j slower than $1/j$.

Coming back now to the disordered case, one might suspect that the ensemble-averaged maximum qubit excitation $p^j_{\sigma_\tau,\xi}$ is related to the corresponding quantity for a nondisordered system p_0^j via an exponential decay, governed by a finite mean free path $l_{\sigma_\tau,\xi}$ for the propagation of the localized excitation,

$$p^j_{\sigma_\tau,\xi} = p_0^j \, \mathrm{e}^{-j/l_{\sigma_\tau,\xi}}. \tag{34}$$

If (34) holds,

$$\frac{1}{l_{\sigma_\tau,\xi}} = \frac{1}{j} \ln\left(\frac{p_0^j}{p^j_{\sigma_\tau,\xi}}\right) \tag{35}$$

should be independent of j. This observation can be used to check our assumption (34). We numerically calculate $p^j_{\sigma_\tau,\xi}$ for all combinations of $\xi = 3,\ldots,8$ and $100\times\sigma_\tau \in \{1, 1.5, 2, 2.5, 3, 4, 5, 6, 7, 8\}$ in a chain of length $N = 20$, and we average over 100 disorder configurations. This turns out to be a good compromise between calculation time and ensemble and system size as long as the effective disorder $\sigma_\tau\xi$ is not too small (see below). With these $p^j_{\sigma_\tau,\xi}$, we calculated the rhs of (35) for $j = 5,\ldots,16$. Other j are not considered, in order to minimize boundary effects. Our results for $j = 5,\ldots,16$ are approximately equal, with the ratio of standard deviation to mean value being < 0.1 for given σ_τ and ξ. We note that for very weak effective disorder $\sigma_\tau\xi \lesssim 0.1$ we have to average over 500 disorder configurations such that this ratio is < 0.1, because with decreasing ratio $p_0^j/p^j_{\sigma_\tau,\xi}$ the slope of the logarithm on the rhs of (35) increases. Thus, the numerical data seem to confirm our assumption (34), and the influence of disorder on the considered experiment is captured by a mean free path $l_{\sigma_\tau,\xi}$. In our subsequent analysis, we try to find simple expressions for this quantity.

The propagation of the localized excitation in the Gaussian disordered TFIC is akin to the propagation of a particle in an uncorrelated random potential $V(r)$ with $\langle V(r)V(r')\rangle = V_0^2\delta(r-r')$. To lowest order in perturbation theory (Fermi's golden rule, e.g. [39]), the mean free path of the latter decreases as the inverse square of the disorder strength, $\propto 1/V_0^2$. In our case, the effective disorder strength is determined by the dimensionless quantity $\sigma_\tau\xi$. Therefore, we expect that

$$l_{\sigma_\tau,\xi} = \frac{1}{(\sigma_\tau\xi)^2}. \tag{36}$$

To check this, we calculate $l_{\sigma_\tau,\xi}$ for the same combinations of σ_τ and ξ as before by averaging the rhs of (35) over $j = 5,\ldots,16$. Then we fit the function $l(\sigma_\tau,\xi) = 1/\sigma_\tau^a\xi^b$ to our data for $l_{\sigma_\tau,\xi}$. We find the exponents $a \approx 2.002$ and $b \approx 2.071$, which comes close to our expectation of $a = b = 2$. Numerical data and fit are plotted on the log–log scale in figure 6(b). As long as the effective disorder strength is not too big ($\sigma_\tau\xi \lesssim 0.2$), $l(\sigma_\tau,\xi)$ with the fit values of a and b reproduces the numerically (by ensemble-averaging) extracted mean free path $l_{\sigma_\tau,\xi}$. Here,

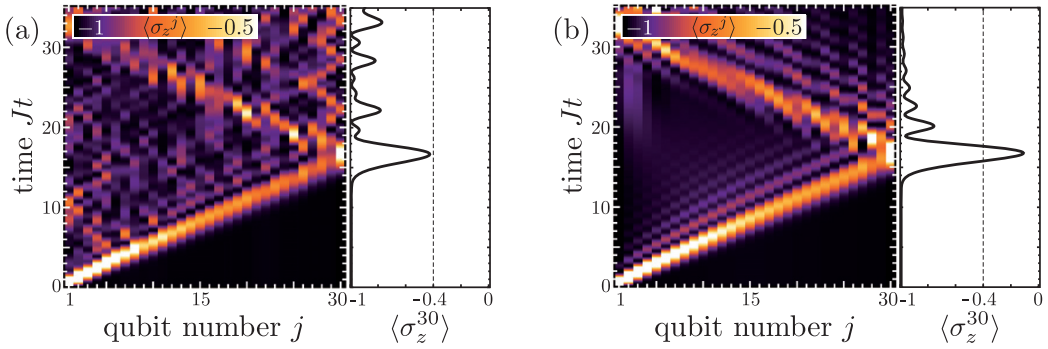

Figure 7. Propagation of a localized excitation in a nonuniform TFIC of length $N = 30$ and with normalized transverse field $\xi = 4$. (a) The qubit transition frequencies Ω_j and qubit–qubit couplings $\mathcal{J}_j$ are randomly chosen according to Gaussian distributions with standard deviations of 3.4% from the mean values. (b) the same as in (a) but with a cosine modulation of the qubit transition frequencies Ω_j with standard deviation $\approx 3.4\%$, instead of uncorrelated disorder of Ω_j and $\mathcal{J}_j$.

one may attribute the deviations of a and b from 2 to the finite ensemble sizes. For stronger disorder, however, the fit of $l(\sigma_\tau, \xi) = 1/\sigma_\tau^a \xi^b$ begins to deviate from $l_{\sigma_\tau,\xi}$. Thus, higher-order effects (beyond Fermi's golden rule) and/or the disorder in J seem to be no longer negligible.

Finally, in setups with a second readout resonator (cf figure 1), the maximum population $p^N_{\sigma_\tau,\xi}$ of the Nth qubit will be an experimentally relevant quantity. Since the dispersed wave packet of the propagating excitation is refocused at the end of the chain, the maximum excitation probability of the Nth qubit is considerably enhanced compared to nearby bulk qubits (see figure 6(c)). It turns out that $p^N_{\sigma_\tau,\xi}$ can also be estimated by means of (34), the mean free path (36), and the value of p_0^N for the corresponding nondisordered system, which we plot for $N = 1, \ldots, 50$ in figure 6(d).

Summing up, equations (34) and (36), together with figures 6(c) and (d), allow one to easily estimate suitable system and disorder parameters for successfully implementing the presently considered type of experiment. For instance, if in a system with $N = 30$ and $\xi = 4$ the Nth qubit should get a population of $p^{30}_{\sigma_\tau,\xi} = 0.3$ (which corresponds to $\max\left[\langle\sigma_z^{30}\rangle(t)\right] = -0.4$), then one can roughly (i.e. averaged over many systems) afford a standard deviation of the qubit transition frequencies from their mean of $\sigma_\tau = \left[(N\xi^2)^{-1}\log\left(p_0^{30}/0.3\right)\right]^{1/2} \approx 0.034$, where we have extracted $p_0^{30} \approx 0.53$ from figure 6(d). A typical result for these parameters is plotted in figure 7(a). Here, the maximum excitation probability is found to be $p^{30}_{0.034,4} \approx 0.29$ (since $\max_t\left[\langle\sigma_z^{30}\rangle(t)\right] \approx -0.43$).

We remark that the foregoing deliberations only hold for uncorrelated disorder of the system parameters and do not take into account qubit decay. Correlated disorder can yield qualitatively different results and has to be studied explicitly via equation (30). We also remark that if the Ω_j are individually tunable, it becomes possible to study the propagation of localized excitations in arbitrary potentials. For instance, it might be interesting to choose $\Omega_j = \Omega[1 + \sqrt{2}\sigma_\tau \cos(2\pi j/N)]$ and to compare the system dynamics with the Gaussian disordered case.

For large N, both distributions of Ω_j have the same mean and the same standard deviation, but in the former case the system is not disordered and the localization of the propagating excitation is much weaker than in the genuinely disordered case. Figure 7(b) shows the propagating excitation in such a system with N, ξ and σ_τ as in figure 7(a) (with uniform $\mathcal{J}_j$).

4.2. Quench dynamics

The second type of nonequilibrium experiment we have proposed in [20] relies on the possibility to rapidly change the transition frequency Ω of a superconducting qubit in a circuit QED system by tuning the magnetic flux through its SQUID loop. This has been shown to be possible virtually instantaneously on the dynamical time scale of a circuit QED system [4, 6, 7], without changing the system's wave function. Let us now assume that the circuit QED quantum simulator of the (uniform) TFIC proposed in [20] is implemented with Cooper-pair boxes. For this system, such a sudden change of all $\Omega_j = \Omega$ corresponds to a global quantum quench of the normalized transverse magnetic field $\xi = \Omega/2\mathcal{J}$. We remark that one can also produce quenches of ξ by using transmons in a non-standard parameter regime instead of Cooper-pair boxes, or by using usual transmons with tunable coupling capacitances [20, 40]. We also remark that the observation of the phenomena described in the following will set higher requirements on the energy relaxation and phase coherence times of the collective many-body quantum states of the Ising chain than the experiments proposed in sections 3.3 and 4.1. The global quantum quench brings the Ising chain in a globally excited state whose time evolution has to be coherent on the time scale N/J of these phenomena (see below). Nevertheless, meeting this constraint seems feasible, since even for $N = 30$ and a moderate coupling strength $J/2\pi = 100\,\mathrm{MHz}$, we find that $N/J \sim 50\,\mathrm{ns}$, which is far below the energy relaxation times $T_1 \sim 7.3\,\mu\mathrm{s}$ and coherence times $T_2 \sim 500\,\mathrm{ns}$ achieved for individual Cooper-pair boxes [41].

The nonequilibrium dynamics of the TFIC following a quantum quench is currently subject to much theoretical research, e.g. [22, 42–53], and should be experimentally observable with our circuit QED quantum simulator. In this context it is usually assumed that for $t < 0$ the system is in the ground state $|0\rangle_a$ of a Hamiltonian $\mathcal{H}_{\mathrm{I},a}$ (characterized by ξ_a). At $t = 0$, the overall transverse field is changed, $\xi_a \to \xi_b$, and the nonequilibrium time evolution of some observable $\mathcal{O}$ under $\mathcal{H}_{\mathrm{I},b}$ is investigated,

$$\langle \mathcal{O}\rangle(t) = {}_a\langle 0|\mathrm{e}^{\mathrm{i}t\mathcal{H}_{\mathrm{I},b}}\mathcal{O}\,\mathrm{e}^{-\mathrm{i}t\mathcal{H}_{\mathrm{I},b}}|0\rangle_a. \tag{37}$$

In [20] we have focused on the time evolution of the local transverse magnetization $\langle\sigma_z^j\rangle$ and the end-to-end correlator $\langle\sigma_x^1\sigma_x^N\rangle$ (indicating long-range order) after quenching ξ within the paramagnetic phase. These quantities should be experimentally easily accessible in our system. In this section, we show that also for such quantum quenches the predicted experimental results of our earlier work are insensitive to a small amount of fabrication-induced disorder.

In general, two sets of the Ω- and $\mathcal{J}$-parameters, $\{\Omega_j^{a/b}\}$ and $\{\mathcal{J}_j^{a/b}\}$, fully specify the Hamiltonians $\mathcal{H}_{\mathrm{I},a/b}$ (equation (2)). Given these parameters, the time evolution (37) of the local magnetization and the end-to-end correlator can be written as [20]

$$\langle\sigma_z^j\rangle(t) = -\sum_k \psi_{k,j}^b\phi_{k,j}^b + 2\sum_{k,k'}\{\psi_{k,j}^b\phi_{k',j}^b[X_{k,k'}\cos t(\Lambda_k^b+\Lambda_{k'}^b) + Y_{k,k'}\cos t(\Lambda_k^b-\Lambda_{k'}^b)]\}, \tag{38}$$

$$\langle\sigma_x^1\sigma_x^N\rangle(t) = \sum_k \phi_{k,1}^b\psi_{k,N}^b + 2\sum_{k,k'}\{\phi_{k,1}^b\psi_{k',N}^b[X_{k,k'}\cos t(\Lambda_k^b+\Lambda_{k'}^b) - Y_{k,k'}\cos t(\Lambda_k^b-\Lambda_{k'}^b)]\}. \tag{39}$$

Here,

$$X_{k,k'} = \left[(g_k^b)^{\mathrm{T}} H^a + (h_k^b)^{\mathrm{T}} G^a\right]\left[(G^a)^{\mathrm{T}} g_{k'}^b + (H^a)^{\mathrm{T}} h_{k'}^b\right], \tag{40}$$

$$Y_{k,k'} = \left[(g_k^b)^{\mathrm{T}} H^a + (h_k^b)^{\mathrm{T}} G^a\right]\left[(H^a)^{\mathrm{T}} g_{k'}^b + (G^a)^{\mathrm{T}} h_{k'}^b\right], \tag{41}$$

and G and H are matrices that, respectively, contain the g_k and h_k as columns. In these equations, a quantity carrying the index a or b is to be calculated from equations (6) with parameter set a or b.

To implement disorder of the system parameters before the quantum quench, we write again $\Omega_j^a = \Omega^a \tau_j$ and $\mathcal{J}_j = \mathcal{J}\tau_j'$, and we randomly choose τ_j and τ_j' according to Gaussian distributions with standard deviations σ_τ and $\sigma_{\tau'}$ from 1. As we have argued in section 2.1, tuning the flux Φ through the SQUID loops of the qubits only changes the mean qubit transition frequency $\Omega^a \to \Omega^b$ (and, thus, the mean transverse field $\xi_a = \Omega^a/2\mathcal{J} \to \xi_b = \Omega^b/2\mathcal{J}$), but leaves τ_j, $\mathcal{J}$ and τ_j' unaffected. Hence, by fixing $\xi_{a/b}$ and $\sigma_{\tau/\tau'}$, the system is fully specified before and after the quench (as in section 4.1, the absolute values of $\Omega^{a/b}$ and $\mathcal{J}$ can be absorbed in the time scale Jt of the dynamics), and we are ready to evaluate equations (38) and (39).

Figure 8(a) shows the local magnetization $\langle\sigma_z^j\rangle(t)$ for all j and for the same system parameters as in figure 4 of [20], but with $\Omega_j^{a/b}$ and $\mathcal{J}_j$ having standard deviations $\sigma_\tau = \sigma_{\tau'} = 2\%$ around their mean values (right panel). The experimentally easily measurable trace of $\langle\sigma_z^1\rangle$ is singled out in the left panel (black). For comparison, we also plot (green) the local magnetization of the first qubit $\langle\sigma_z^1\rangle$ of the uniform system (as plotted in the left panel of figure 4 of [20]). Correspondingly, figure 8(b) shows (39) for a uniform system as in figure S6 of [20] (green), and with 2% disorder in $\Omega_j^{a/b}$ and $\mathcal{J}_j$ (black). The plots demonstrate that the quench dynamics of the considered observables is not qualitatively affected by the presence of a small amount of disorder.

For a more systematic analysis of the disorder effects on the quench experiments considered here, we make use of our findings for the mean free path of a propagating localized excitation from the previous section. This is possible because the quench dynamics of the TFIC is governed by the propagation of QPs through the system [20, 43, 44, 46, 48, 54]. These correspond to flipped spins, essentially like the localized excitation of the previous section. Indeed, if the system is initially in the paramagnetic phase, the time evolution immediately after the quantum quench $\mathrm{e}^{-\mathrm{i}t\mathcal{H}_b}|0\rangle_a \propto \prod_j \mathrm{e}^{-\mathrm{i}t\mathcal{J}(\xi_b-\xi_a)/\xi_a\sigma_x^j\sigma_x^{j+1}}|0\rangle_a$ flips pairs of adjacent spins so that they point in the $+z$-direction. Due to the qubit–qubit coupling, these local excitations propagate as QPs with velocity $v \approx 2J$ through the chain. For an interpretation of the quench dynamics and the time scales indicated in the plots (all of which scale as N/J) in terms of these QPs, see [20]. If ξ_b is in the paramagnetic phase, the mean free path l of the QPs in a disordered TFIC can be estimated by $l = 1/(\sigma_\tau \xi_b)^2$ according to the previous section. The characteristic quasi-T-periodic behavior ($T = N/v$) of the local magnetization after the quench in the nondisordered TFIC can be understood as a revival of coherence each time QPs initially generated at the same spot meet again [20, 48]. This happens when the QPs have traveled multiples of the chain length N. If there should be a significant probability that two contiguously generated QPs meet again at least once before being scattered and thus decrease the local magnetization at $t = T$, the mean free path has to be sufficiently large, $l > 2N$. The appearance of significant end-to-end correlations after the quench (that are stronger than those for $t \to \infty$) requires that QPs

IOP Institute of Physics DEUTSCHE PHYSIKALISCHE GESELLSCHAFT

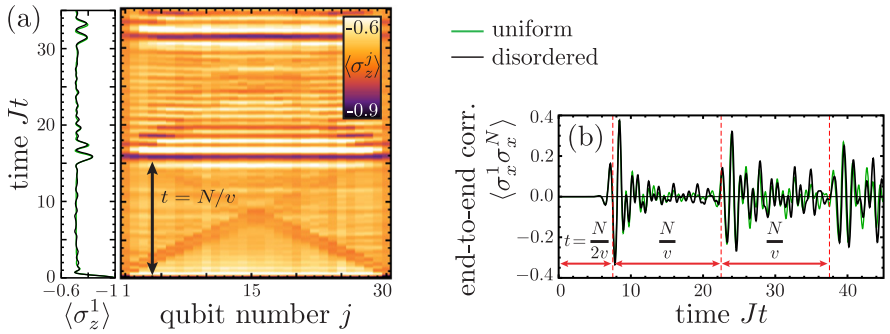

Figure 8. (a) Time evolution of the magnetization $\langle\sigma_z^j\rangle$ in a disordered TFIC of length $N = 30$ after a quench of the mean normalized transverse field $\xi = \Omega/2\mathcal{J} = 8 \to 1.2$ (right). Values < -0.9 (> -0.6) are plotted black (white). The measurable observable $\langle\sigma_z^1\rangle$ is plotted separately in the left panel (black), along with the corresponding trace for a uniform system (green). (b) Time evolution of the end-to-end correlator $\langle\sigma_x^1\sigma_x^N\rangle$ in a disordered TFIC of length $N = 30$ after a quench of the mean normalized transverse field $\xi = 8 \to 1.5$ (black), along with the corresponding trace for a uniform system (green). In both plots the qubit transition frequencies Ω_j and qubit–qubit couplings $\mathcal{J}_j$ are randomly chosen according to Gaussian distributions with standard deviations of 2% from the mean values Ω and $\mathcal{J}$.

generated in the middle of the chain reach the edges of the chain without being scattered, hence $l > N$. We have performed numerical experiments which indeed suggest that the corresponding values of σ_τ mark the transition to a degree of disorder where the described phenomena are no longer present. In that sense, the distinctive features of the quench dynamics of the end-to-end correlator are less sensitive to disorder than those of the local magnetization (and, due to the shorter time scale, less sensitive to decoherence or decay). We finally note that also here the effective chain length can be adjusted by strongly detuning individual qubits (this can also be used to create local quantum quenches by 'joining' two initially independent chains) and arbitrary effective potentials Ω_j can be chosen.

5. Conclusion

In the quest for controllable large-scale quantum systems, the framework of circuit QED offers several advantages, such as fast, high-fidelity readout, a great flexibility in design and steadily increasing coherence times. However, a potentially significant disadvantage arises from the hardly avoidable static noise and disorder sources in these man-made devices. The central result of this work is that also in this respect, there is reason to be optimistic: the requirements on the homogeneity of the system parameters for observing interesting (and predictable) many-body physics in a circuit QED system are not too high to be achievable with present-day or near-future technology. This underlines the prospects of circuit QED as a promising platform for implementing quantum simulations of complex quantum many-body Hamiltonians. In addition,

we have shown that circuit QED quantum simulators could be used to study deliberately the effects of tunable disorder on quantum many-body dynamics.

Acknowledgments

We thank I Siddiqi, R Vijay, A Schmidt and N Henry for discussions. OV thanks the QNL group at UC Berkeley for their hospitality. Support from the NIM and the SFB 631 of the DFG is gratefully acknowledged.

References

[1] Schoelkopf R J and Girvin S M 2008 Wiring up quantum systems *Nature* **451** 664–9

[2] Blais A *et al* 2004 Cavity quantum electrodynamics for superconducting electrical circuits: an architecture for quantum computation *Phys. Rev.* A **69** 062320

[3] Wallraff A *et al* 2004 Strong coupling of a single photon to a superconducting qubit using circuit quantum electrodynamics *Nature* **431** 162–7

[4] DiCarlo L *et al* 2010 Preparation and measurement of three-qubit entanglement in a superconducting circuit *Nature* **467** 574–8

[5] Mariantoni M *et al* 2011 Implementing the quantum von Neumann architecture with superconducting circuits *Science* **334** 61–5

[6] Fedorov A, Steffen L, Baur M, da Silva M P and Wallraff A 2012 Implementation of a Toffoli gate with superconducting circuits *Nature* **481** 170–2

[7] Reed M D *et al* 2012 Realization of three-qubit quantum error correction with superconducting circuits *Nature* **482** 382–5

[8] Nataf P and Ciuti C 2010 Vacuum degeneracy of a circuit QED system in the ultrastrong coupling regime *Phys. Rev. Lett.* **104** 023601

[9] Delanty M, Rebić S and Twamley J 2011 Superradiance and phase multistability in circuit quantum electrodynamics *New J. Phys.* **13** 053032

[10] Viehmann O, von Delft J and Marquardt F 2011 Superradiant phase transitions and the standard description of circuit QED *Phys. Rev. Lett.* **107** 113602

[11] Romito A, Fazio R and Bruder C 2005 Solid-state quantum communication with Josephson arrays *Phys. Rev.* B **71** 100501

[12] Hartmann M J, Brandao F G S L and Plenio M B 2006 Strongly interacting polaritons in coupled arrays of resonators *Nature Phys.* **2** 849–55

[13] Greentree A D, Tahan C, Cole J H and Hollenberg L C L 2006 Quantum phase transitions of light *Nature Phys.* **2** 856–61

[14] Wang Y D, Xue F, Song Z and Sun C P 2007 Detection mechanism for quantum phase transition in superconducting qubit array *Phys. Rev.* B **76** 174519

[15] Koch J and Le Hur K 2009 Superfluid–Mott-insulator transition of light in the Jaynes–Cummings lattice *Phys. Rev.* A **80** 023811

[16] Tian L 2010 Circuit QED and sudden phase switching in a superconducting qubit array *Phys. Rev. Lett.* **105** 167001

[17] Schiró M, Bordyuh M, Öztop B and Türeci H E 2012 Phase transition of light in cavity QED lattices *Phys. Rev. Lett.* **109** 053601

[18] Houck A A, Türeci H E and Koch J 2012 On-chip quantum simulation with superconducting circuits *Nature Phys.* **8** 292–9

[19] Hwang M J and Choi M S 2012 Large-scale Schrödinger-cat states and majorana bound states in coupled circuit-QED systems arXiv:1207.0088 (in preparation)

[20] Viehmann O, von Delft J and Marquardt F 2013 Observing the nonequilibrium dynamics of the quantum transverse-field Ising chain in circuit QED *Phys. Rev. Lett.* **110** 030601

[21] Sachdev S 1999 *Quantum Phase Transitions* (Cambridge: Cambridge University Press)

[22] Polkovnikov A, Sengupta K, Silva A and Vengalattore M 2012 Colloquium: nonequilibrium dynamics of closed interacting quantum systems *Rev. Mod. Phys.* **83** 863–83

[23] Clarke J and Wilhelm F K 2008 Superconducting quantum bits *Nature* **453** 1031–42

[24] Koch J *et al* 2007 Charge-insensitive qubit design derived from the Cooper pair box *Phys. Rev.* A **76** 042319

[25] Dewes A *et al* 2012 Characterization of a two-transmon processor with individual single-shot qubit readout *Phys. Rev. Lett.* **108** 057002

[26] Lieb E, Schultz T and Mattis D 1961 Two soluble models of an antiferromagnetic chain *Ann. Phys.* **16** 407–66

[27] Pfeuty P 1970 The one-dimensional Ising model with a transverse field *Ann. Phys.* **57** 79–90

[28] Griffiths R B 1969 Nonanalytic behavior above the critical point in a random Ising ferromagnet *Phys. Rev. Lett.* **23** 17–9

[29] McCoy B M 1969 Incompleteness of the critical exponent description for ferromagnetic systems containing random impurities *Phys. Rev. Lett.* **23** 383–86

[30] Fisher D S 1992 Random transverse field Ising spin chains *Phys. Rev. Lett.* **69** 534–37

[31] Fisher D S 1995 Critical behavior of random transverse-field Ising spin chains *Phys. Rev.* B **51** 6411–61

[32] Walls D F and Milburn G J 2008 *Quantum Optics* (Berlin: Springer)

[33] Fink J M *et al* 2009 Dressed collective qubit states and the Tavis–Cummings model in circuit QED *Phys. Rev. Lett.* **103** 083601

[34] Córcoles A D *et al* 2011 Protecting superconducting qubits from radiation *Appl. Phys. Lett.* **99** 181906

[35] Murch K W *et al* 2012 Cavity-assisted quantum bath engineering *Phys. Rev. Lett.* **109** 183602

[36] Geerlings K *et al* Demonstrating a driven reset protocol of a superconducting qubit arXiv:1211.0491 (in preparation)

[37] Kitaev A Y 2001 Unpaired Majorana fermions in quantum wires *Phys.—Usp.* **44** 131–36

[38] Anderson P W 1959 Absence of diffusion in certain random lattices *Phys. Rev.* **109** 1492–505

[39] Akkermans E and Montambaux G 2007 *Mesoscopic Physics of Electrons and Photons* (Cambridge: Cambridge University Press)

[40] Averin D V and Bruder C 2004 Variable electrostatic transformer: controllable coupling of two charge qubits *Phys. Rev. Lett.* **91** 057003

[41] Wallraff A *et al* 2005 Approaching unit visibility for control of a superconducting qubit with dispersive readout *Phys. Rev. Lett.* **95** 060501

[42] Barouch E, McCoy B and Dresden M 1970 Statistical mechanics of the *XY* model I *Phys. Rev.* A **2** 1075–92

[43] Iglói F and Rieger H 2000 Long-range correlations in the nonequilibrium quantum relaxation of a spin chain *Phys. Rev. Lett.* **85** 3233–36

[44] Calabrese P and Cardy J 2006 Time dependence of correlation functions following a quantum quench *Phys. Rev. Lett.* **96** 136801

[45] Rossini D, Silva A, Mussardo G and Santoro G E 2009 Effective thermal dynamics following a quantum quench in a spin chain *Phys. Rev. Lett.* **102** 127204

[46] Iglói F and Rieger H 2011 Quantum relaxation after a quench in systems with boundaries *Phys. Rev. Lett.* **106** 035701

[47] Calabrese P, Essler F H L and Fagotti M 2011 Quantum quench in the transverse-field Ising chain *Phys. Rev. Lett.* **106** 227203

[48] Rieger H and Iglói F 2011 Semiclassical theory for quantum quenches in finite transverse Ising chains *Phys. Rev.* B **84** 165117

[49] Heyl M, Polkovnikov A and Kehrein S 2012 Dynamical quantum phase transitions in the transverse field Ising model arXiv:1206.2505

[50] Calabrese P, Essler F H L and Fagotti M 2012 Quantum quench in the transverse field Ising chain: I. Time evolution of order parameter correlators *J. Stat. Mech.* **2012** P07016

[51] Calabrese P, Essler F H L and Fagotti M 2012 Quantum quenches in the transverse field Ising chain: II. Stationary state properties *J. Stat. Mech.* **2012** P07022

[52] Marino J and Silva A 2012 Relaxation, prethermalization and diffusion in a noisy quantum Ising chain *Phys. Rev.* B **86** 060408

[53] Essler F H L, Evangelisti S and Fagotti M 2012 Dynamical correlations after a quantum quench *Phys. Rev. Lett.* **109** 247206

[54] Sachdev S and Young A P 1997 Low temperature relaxational dynamics of the Ising chain in a transverse field *Phys. Rev. Lett.* **78** 2220–23

4.7 Experimental implementation

For the experimental realization of our proposal, we have established a collaboration with the group of Professor Irfan Siddiqi at UC Berkeley. In this section, we report and analyze the experimental results obtained so far. The experimental data and the photographs of the circuit QED devices shown in this section were taken by Edward Henry and Andrew Schmidt, who are carrying out the experiments.

Device description

The samples studied so far are based on the 3D circuit QED technology (Paik *et al.*, 2011). This avoids the modification of the standard cavity design necessary in 2D architectures and promises lower decoherence. Figure 4.1(a) shows the two halves of a typical 3D cavity used in the experiments. The photograph also shows a chip on which qubit chains of different lengths are patterned. The chains of lengths $N = 4$ and $N = 6$ are shown magnified in the inset. One such chain is placed inside the 3D cavity. To create a situation where only the first qubit of the chain is coupled to the cavity, the 3D transmons simulating the spins $j > 1$ are made relatively small and are rotated by $\pi/2$ relative to the large 3D transmon simulating the spin $j = 1$. That is, two neighboring small islands in the inset of Figure 4.1(a) form one transmon and are connected by a Josephson junction. This can be seen in Figure 4.1(b), which shows a minimal test system, a chain of length $N = 2$, further magnified. We remark that the bridge between the islands of the small transmon, which contains the Josephson junction, is twisted so that all junctions in the device have the same 'orientation' and can be fabricated in one step.

The chain of qubits is placed inside the resonator such that the polarisation vector $\mathbf{e}$ of the cavity mode closest in frequency to the qubits is parallel to the axis of the first qubit and orthogonal to the axes of the $j > 1$ qubits. This minimizes the qubit-cavity coupling $\sim \mathbf{e} \cdot \mathbf{d}_j$ for $j > 1$ and maximizes the qubit-cavity coupling for $j = 1$. Here, $\mathbf{d}_j$ is the transition dipole matrix element of qubit j, which will have a significantly larger magnitude for $j = 1$ than for $j > 1$ because of the size difference of the qubits. Using a 3D cavity makes it difficult to flux bias the qubits individually with separate flux lines. In all samples studied so far, only the first qubit was fabricated with a split Josephson junction and therefore tunable *in-situ* from a maximum transition frequency $\Omega_1 = \Omega_{1,\max}$ to lower Ω_1. The transition frequencies $\Omega_{j>1}$ of all other qubits are fixed by design and chosen to be far below the cavity frequency ω_c. Typical values for the samples studied so far are $\Omega_{1,\max} \approx 5.5$ GHz, $\Omega_{j>1} \approx 4$ GHz and $\omega_c \approx 7$ GHz. To tune the first qubit, the cavity is made of copper (instead of superconducting material), and the whole device is threaded by the flux from an external bias coil. The line width of a copper cavity is significantly larger than for superconducting cavities. To protect the qubits from Purcell decay, a large detuning from the cavity resonance is necessary. Using an external coil, the tuning the first qubit can be done only slowly compared to all frequencies appearing in the Ising Hamiltonian. However, by employing a Stark-pulse technique (*e.g.*, as used by Majer *et al.* (2007)), it seems feasible to bring the first qubit non-adiabatically into and out of resonance with the other qubits (see below).

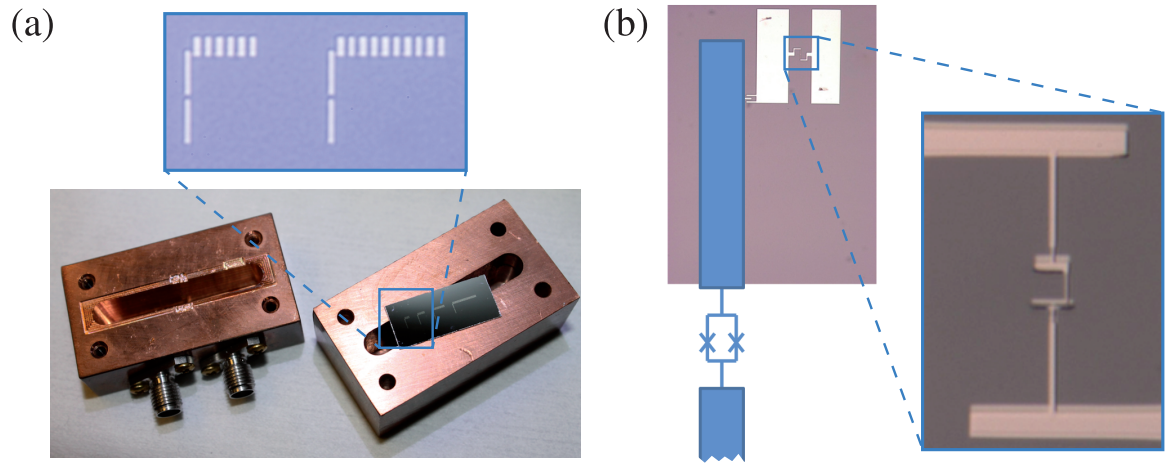

Figure 4.1: Experimental implementation of the transverse-field Ising chain in circuit QED (photos by E. Henry and A. Schmidt). (a) 3D cavity and chip on which qubit chains of different lengths are laid out. The inset shows a zoom-in on the chains with $N = 4$ and $N = 6$ 3D transmon qubits. The two large, vertically aligned islands on the left end of each chain form the qubit that couples to the cavity. All other qubits, each of which is formed by two smaller islands, are rotated by $\pi/2$ relative to this qubit and couple to the cavity only marginally. The bridges between the islands, which contain the Josephson junctions, are not visible on this scale. See main text for further details. (b) Rendered image of a minimal Ising chain of length $N = 2$ in the same design. Also shown is the magnification of a Josephson junction equivalent to that of the small qubit. Only the large qubit is fabricated with a split junction and flux-tunable.

Theoretical description

Our theoretical description of the system is based on the Hamiltonian

$$\mathcal{H} = \omega_c a^\dagger a + \sum_{j=1}^{N} \left(\frac{\Omega_j}{2} \sigma_z^j + g_j (a^\dagger + a) \sigma_x^j \right) - \sum_{j=1}^{N-1} J_j \sigma_x^j \sigma_x^{j+1}. \tag{4.3}$$

Far in the dispersive regime, the cavity hybridizes only weakly with the qubits. Given the large cavity line width, the marginal qubit-induced Kerr-nonlinearity of the cavity will be indiscernible and can be neglected. Ideally, $g_{j>1} \approx 0$. To see if is the case, we keep the $g_{j>1}$ in the Hamiltonian. If the system is driven by ν different tones of frequencies ω_l (see below), we describe it by

$$\mathcal{H}_\nu = \mathcal{H} + \sum_{l=1}^{\nu} F_l (a e^{i\omega_l t} + a^\dagger e^{-i\omega_l t}), \tag{4.4}$$

where we assume drive amplitudes $F_l \in \mathbb{R}$ for simplicity. In the case of $\nu = 1$, we define $F = F_1$ and $\omega = \omega_1$. In this case, in a frame rotating at ω (cf. Equation (2.44) and below),

$$\mathcal{H}_1' = \delta_c a^\dagger a + \sum_{j=1}^{N} \left(\frac{\delta_q^j}{2} \sigma_z^j + g_j (a \sigma_+^j + a^\dagger \sigma_-^j) \right) - \sum_{j=1}^{N-1} J_j (\sigma_+^j \sigma_-^{j+1} + \sigma_-^j \sigma_+^{j+1}) + F(a^\dagger + a), \tag{4.5}$$

where $\delta_c = \omega_c - \omega$, $\delta_q^j = \Omega_j - \omega$, and we have dropped all counter-rotating terms. The Lindblad master equation (Walls and Milburn, 1994)

$$\frac{d}{dt}\rho = -i[\mathcal{H}_\nu, \rho] + \sum_l \Gamma_l (R_l \rho R_l^\dagger - \frac{1}{2} R_l^\dagger R_l \rho - \frac{1}{2} \rho R_l^\dagger R_l) \tag{4.6}$$

for the density matrix ρ of the system has the same form in the laboratory frame and in the rotating frame. One only has to replace $\mathcal{H}_\nu \to \mathcal{H}'_\nu$ and $\rho \to \rho' = U\rho U^\dagger$ (U is the straightforward generalization of Equation (2.44) to N qubits), but the Lindblad operators $R_l = a, \sigma_-^j, \sigma_z^j$ for cavity decay, qubit decay and pure dephasing, respectively, remain unaffected. As usual, we denote the corresponding rates Γ_l by κ, γ_j, and $\gamma_{\varphi,j}/2$. Recall that these are related to the qubit energy relaxation and dephasing times via $T_1^{-1} = \gamma$ and $T_2^{-1} = \gamma/2 + \gamma_\varphi$, where the index j is implicit (see Section 2.2). Since the RHS of Equation (4.6) is linear in ρ, one can find an operator $\mathcal{L}$ so that the Liouville equation

$$\frac{d}{dt}\rho = -i\mathcal{L}(t)\rho \tag{4.7}$$

is equivalent to the Lindblad master equation (4.6). This is useful for the numerical implementation of the dissipative dynamics since Equation (4.7) allows one to easily map ρ to a column vector and the Liouvillian $\mathcal{L}(t)$ to a usual (generally non-hermitian) matrix. Note that if one can remove the time dependence from the Hamiltonian, for instance, by going into a rotating frame and dropping the counter-rotating terms as in Equation (4.5), a steady state $\rho(t \to \infty)$ of the system is an eigenvector of $\mathcal{L}$ with eigenvalue 0. Often one is interested only in these steady states, in which case one can utilize the efficient numerical algorithms available for finding the eigenvalue of smallest magnitude and the corresponding eigenstate of $\mathcal{L}$ (*e.g.*, Arnoldi iteration).

To gain some insight into the properties of the system, we return to $\mathcal{H}$ (Equation (4.3)) and consider the experimentally realistic case that all couplings g_j and J_j are much smaller than ω_c, Ω_j, and all detunings $\omega_c - \Omega_j$. In this situation, the cavity remains approximately harmonic but its frequency is dispersively shifted from ω_c to ω'_c due to the perturbation $\sum_j g_j(a^\dagger + a)\sigma_x^j - \sum_j J_j \sigma_x^j \sigma_x^{j+1}$. We can calculate perturbatively the shifted cavity frequency according to $\omega'_c = E(|\nu+1, \mathbf{s}\rangle) - E(|\nu, \mathbf{s}\rangle)$, using $|\nu, \mathbf{s}\rangle$ as unperturbed basis and the mean value of the couplings divided by one of the large energies as a small parameter. Here, $|\nu\rangle$ is a photon Fock state and $|\mathbf{s}\rangle = |s_1, \ldots, s_N\rangle$ encodes the qubit states, $s_i = \uparrow, \downarrow$. The first-order correction to ω_c vanishes. The second-order correction is seen to consist of two sums, one ν-independent sum stemming from the J_j terms and one ν-dependent sum from the g_j terms. Thus, the dispersive (direct) qubit-qubit coupling contributes only in third order perturbation theory to ω'_c. The second-order result reads

$$\omega'_c = \omega_c + \sum_j \left(\frac{g_j^2}{-\omega_c + \langle \sigma_z^j \rangle \Omega_j} + \frac{g_j^2}{\omega_c + \langle \sigma_z^j \rangle \Omega_j} \right) \tag{4.8}$$

$$\approx \omega_c - \sum_j \frac{g_j^2 \langle \sigma_z^j \rangle}{\omega_c - \Omega_j}, \tag{4.9}$$

where $\langle\sigma_z^j\rangle = \langle \nu, \mathbf{s}|\sigma_z^j|\nu,\mathbf{s}\rangle$ and the approximation in the second line corresponds to making the rotating-wave approximation. Thus, the dispersive cavity shift of our quantum simulator is expected to depend on the qubit states in straightforward generalization of the single-qubit case of Equation (2.42) (note that ideally only $g_1 \neq 0$, though). The same result can be obtained in a more cumbersome way by applying the transformation $U = \exp[a^\dagger \sum_i \varepsilon_i \sigma_i^- - a\sum_i \varepsilon_i \sigma_i^+]$ to $\mathcal{H}$, which generalizes the single-qubit dispersive transformation (Equation (2.41)). Keeping terms to second order in ε_i and making the rotating-wave approximation yields

$$\begin{aligned}\mathcal{H}_{\text{disp.}} = &\left(\omega_c - \sum_{j=1}^{N} \frac{g_j^2 \sigma_z^j}{\omega_c - \Omega_j}\right) a^\dagger a + \sum_{j=1}^{N}\left(\Omega_j - \frac{g_j^2}{\omega_c - \Omega_j}\right)\frac{\sigma_z^j}{2} \\ &- \sum_{j=1}^{N-1} J_j[\sigma_j^-\sigma_{j+1}^+ + \sigma_j^+\sigma_{j+1}^- - \varepsilon_j\sigma_z^j(a\sigma_{j+1}^+ + a^\dagger\sigma_{j+1}^-) - \varepsilon_{j+1}\sigma_z^{j+1}(a\sigma_j^+ + a^\dagger\sigma_j^-)] \\ &+ \sum_{j\neq j'}^{N}[\varepsilon_j\varepsilon_{j'}(\omega_c - \Omega_j/2 - \Omega_{j'}/2)\sigma_j^+\sigma_{j'}^- - g_j\varepsilon_{j'}(\sigma_{j'}^-\sigma_j^+ + \sigma_j^-\sigma_{j'}^+)],\end{aligned} \tag{4.10}$$

if $\varepsilon_j = g_j/(\omega_c - \Omega_j)$. In this dispersive approximation to $\mathcal{H}$, the linear coupling of cavity and qubits is removed. We recognize the dispersively shifted cavity, the photon-number dependent qubit transitions, and the Lamb shift as the diagonal part of the Hamiltonian (first line). The direct nearest-neighbor qubit-qubit coupling (second line) remains strong in this dispersive approximation to $\mathcal{H}$ (linear in J if the qubits are resonant). There is a residual off-resonant mixing of the cavity and the qubits (last two terms in the second line), which slightly contributes to the direct qubit-qubit coupling and also slightly modifies the cavity frequency of the first line. However, these effects do no occur in proportion to the corresponding (second-order) coupling $J_j\varepsilon_{j'}$, as we have already discussed for the cavity frequency above. The third line describes the purely cavity-mediated qubit-qubit coupling (weaker than the direct nearest-neighbor coupling by a factor $\sim \varepsilon_{j'}$). In the ideal case $g_{j>0} = 0$, this third line vanishes from the Hamiltonian. We also remark that in the case of $N = 2$, $J_j = 0$, $g_j = g$, and $\Omega_j = \Omega$, Equation (4.10) reduces to the Hamiltonian of Equation (2.48).

Spectroscopy

For an initial characterization of this previously unexplored type of setup, spectroscopy on different samples with small N (ranging form $N = 2$ to $N = 6$) and varying chain designs is currently being performed. The main goals of these experiments are to determine (I) the qubit-qubit coupling strength J and its dependence on the design features of the sample such as the qubit-qubit spacing or the presence or absence of additional interdigitated capacitors between the qubits, (II) the undesired residual coupling of the qubits $j > 1$ to the cavity, (III) the homogeneity of the qubit parameters, (IV) the undesired residual longer-range qubit-qubit coupling.

Since the qubit system is off-resonant with the cavity for all values of the bias flux Φ_{ext}, spectroscopy experiments are done using a two-tone technique, a one-qubit variant of which was first used by Schuster *et al.* (2005). In a first step, one measures the dispersively shifted cavity

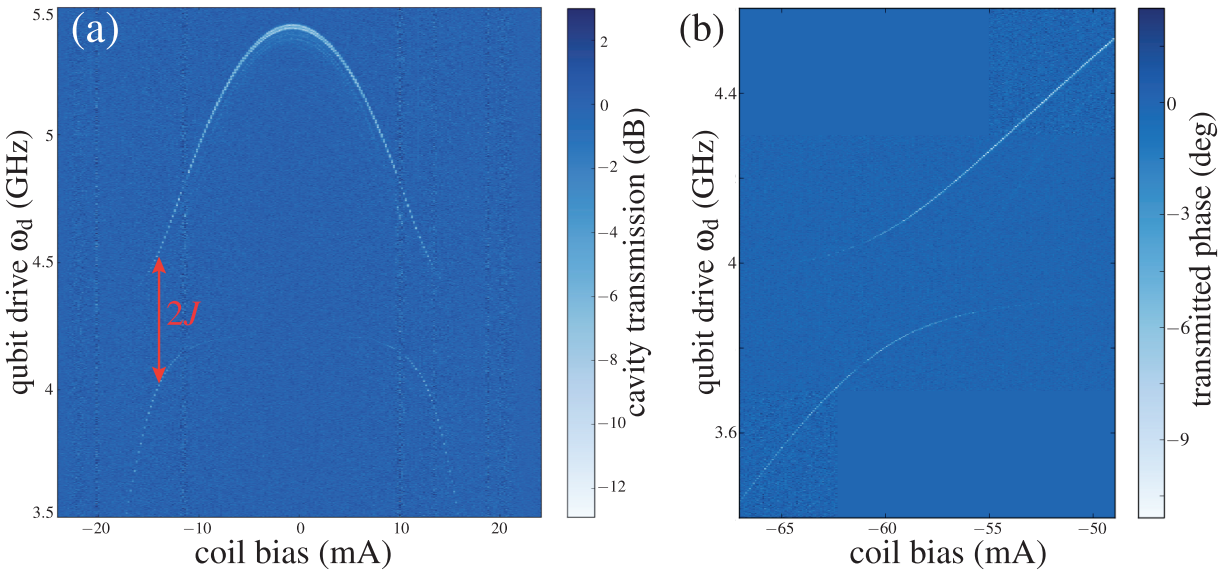

Figure 4.2: Two-tone spectroscopy of two-qubit samples (data by E. Henry and A. Schmidt). (a) Measured transmitted intensity of the cavity probe tone as a function of the current through the external flux bias coil and the drive frequency ω_d for the sample shown in Figure 4.1(b). The avoided crossing has a width of $2J$. In this case, $J/2\pi = 270$ MHz. The vertical streaks in the plot are due to imperfections in the readjustment of the cavity probe tone with varying flux (see main text). Note that for minimal detuning of the first qubit from the cavity, the lines of this first qubit slightly split up since they are photon-number resolved in this region and there is a nonzero cavity population. The point of minimal detuning is slightly shifted from zero bias current due to a small amount of trapped flux. (b) High-resolution spectroscopy of the avoided crossing of a different two-qubit sample with $J/2\pi = 135$ MHz. Plotted is the measured phase of the transmitted signal.

frequency $\omega_c'(\Phi_{ext})$ as a function of Φ_{ext} by one-tone transmission spectroscopy. The dependence of ω_c' on Φ_{ext} stems from the flux-dependent detuning $\omega_c - \Omega_1(\Phi_{ext})$ between the bare cavity frequency ω_c and the frequency of the first qubit $\Omega_1(\Phi_{ext})$. Note that the qubit system remains essentially in its ground state during this measurement. In a second step, the cavity is weakly probed with a probe tone of frequency $\omega_p = \omega_c'(\Phi_{ext})$, while a second tone with frequency ω_d strongly drives the system in the vicinity of the frequencies of the qubits. If this second tone excites the qubit system, the dispersive shift of the cavity frequency changes in accordance with Equations (4.9) and (4.10). This then leads to a drop of the transmission of the probe and to a phase shift in both the reflected and transmitted probe signal, each of which can be detected. Note that the transmitted intensity only drops significantly if the qubit-state dependent frequency shift of the cavity is larger than the cavity line width. Therefore, for the described situation of strongly detuned qubits and copper cavities, phase measurements oftentimes yield a higher visibility of the features of the spectrum.

Regarding goal (I), two-qubit samples are measured with the described spectroscopy tech-

nique (see Figure 4.2). As expected, the capacitive qubit-qubit coupling is found to be strong. For the sample shown in Figure 4.1(b), the avoided crossing reveals $J/2\pi = 260$ MHz (Figure 4.2(a)). It is likely that this value can be further increased by using larger coupling capacitances. However, for time-domain experiments on the basis of Stark-pulses on the first qubit, smaller coupling seems to be favorable. While Stark pulses are fast enough for non-adiabatic pulses under couplings of this strength, sufficiently large frequency shifts into and out of the avoided crossing are difficult to obtain with this technique. Therefore, samples with significantly reduced J (down to ~ 40 MHz) have been fabricated and measured as well, which should allow for time-domain measurements soon.

It can also be estimated from Figure 4.2 that the spurious coupling (II) of the second, small qubit and the cavity is weak. This is indicated by the fact that in regions of the flux bias, where this second qubit is only weakly hybridized with the first qubit, it is hardly visible in the spectroscopy experiments. The dependence of the visibility of the spectroscopy lines on the degree of the hybridization can be seen well in Figure 4.2(b), which shows the avoided crossing of a two-qubit sample with $J/2\pi = 135$ MHz in high resolution.

The simplest way to compare the measured two-tone spectroscopy with theory is to calculate the transition rates of the system from its ground state to its excited states due to the qubit drive tone ω_d. These rates are a measure for the visibility (or the intensity) of the corresponding transitions in a spectroscopy experiment. Explicitly, we consider the qubit drive as a perturbation to $\mathcal{H}$ and evaluate numerically the induced transition rates $\Gamma(\mathrm{g} \to f)$ from the ground state $|\mathrm{g}\rangle$ to the excited states $|f\rangle$ of $\mathcal{H}$ as predicted by Fermi's golden rule,

$$\Gamma(\mathrm{g} \to f) = 2\pi F^2 \delta(E_f - E_\mathrm{g} - \omega) |\langle f|a^\dagger|\mathrm{g}\rangle|^2. \tag{4.11}$$

Figure 4.3 shows the transition frequencies of $\mathcal{H}$ for $N = 2$ and varying values of the residual coupling g_2. The corresponding transition rates, calculated according to Equation (4.11), are encoded in the color of the curves. Explicitly, for each plot, we calculate the squared matrix element $|\langle f|a^\dagger|\mathrm{g}\rangle|^2$ of each plotted data point. Since these strongly increase where Ω_1 approaches ω_c (except for $g_1 = g_2$), we apply a color scale only for these squared matrix elements that lie within a range of 0% (blue) to 10% (red) of the maximum squared matrix element. All other data points are plotted in red. Only for the leftmost plot ($g_2 = g_1$) the color scale is applied to all data points. The parameters used in the numerical calculations roughly correspond to those measured for the sample studied in Figure 4.2(b). If $g_2 = g_1$, the second excitation of the resonant qubit system ($\Omega_1 = \Omega_2$) is dark. The reason for this will be explained in the next paragraphs. With decreasing ratio g_2/g_1, the dark spot shifts to the off-resonant regime, but is still distinct at $g_2/g_1 = 1/2$. Upon decreasing this ratio to $1/4$, the intensity of the spectroscopy lines becomes strongly asymmetric with respect to $|\Omega_1 - \Omega_2|$. For smaller residual coupling, this asymmetry vanishes and, except in the vicinity of the avoided crossing, only the first qubit is bright. For $g_2/g_1 \geq 1/4$, the calculated intensity of the spectroscopy lines is qualitatively different from the measured one, in that neither a dark spot nor an asymmetry as described above is observed experimentally. Since this holds true also if g_1, Ω_2, and J differ from the values assumed for Figure 4.3 within some range, it should be safe to assume that the residual cavity coupling of the second qubit in the experiment of Figure 4.2(b) is smaller than the cavity coupling of the first qubit at least by a factor of $1/4$.

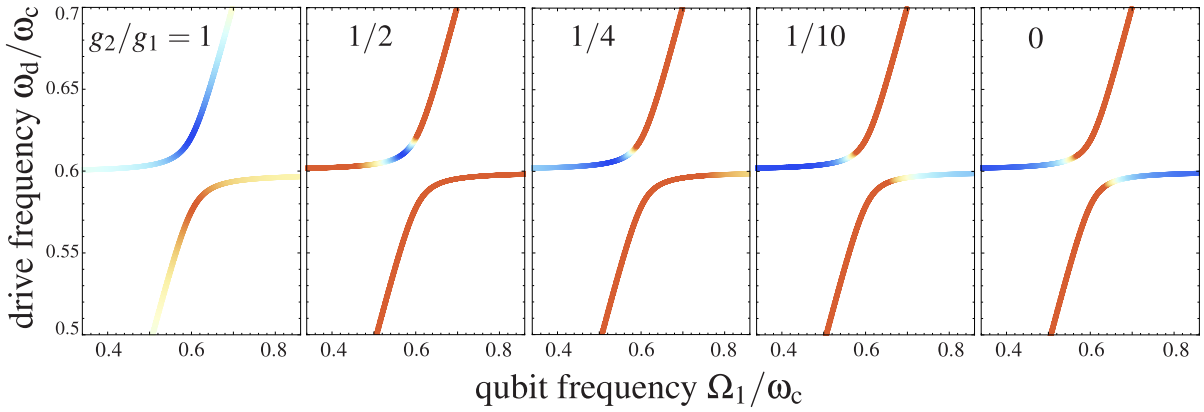

Figure 4.3: Calculated excitation frequencies and their visibility in a spectroscopy experiment of a circuit QED system with two Ising-coupled qubits for different residual couplings g_2 in the vicinity of the avoided crossings of the qubits. In all plots, the frequency of the first qubit Ω_1 varies on the horizontal axes while the frequency of the second qubit is constant at $\Omega_2/\omega_c = 0.6$. The coupling of the first qubit and the cavity, g_1, and the qubit-qubit coupling J are the same for all plots, $g_1/\omega_c = 0.03$ and $J/\omega_c = 0.02$. The coupling of the second qubit g_2 varies as indicated in the plots. The color of the curves encodes the visibility in a spectroscopy experiment according to Fermi's golden rule (blue: low, red: high). The color coding of the leftmost plot is on a different scale than that of the other plots. The calculated visibility for $g_2/g_1 \geq 1/4$ is incompatible with the experimental data of Figure 4.2(b). See text for details.

To strengthen and possibly to further decrease this upper bound, more detailed studies are necessary. For instance, one might compare the Rabi frequencies ($\propto g_j$) of the bright and the dark qubit. Also high-resolution measurements of the shapes of the spectroscopy lines might be helpful (see below). On the theory side, an accurate modelling of such experiments will also have to take dissipation into account. To prepare further studies with our quantum simulator and to deepen our understanding of it, we model the experimental two-tone spectroscopy once again and include dissipation.

Bearing in mind the experimental situation of the two-tone spectroscopy, we assume that the visibility (or the intensity) of the spectroscopy signal is proportional to the shift of the cavity frequency due to the driving of the qubit system. We calculate this shift according to Equation (4.9), which we evaluate (i) in the ground state of the coupled system and (ii) in the steady state of the system in the presence of a qubit drive tone with amplitude F and frequency ω_d and qubit and cavity decay rates γ_j and κ. Subtracting the result of (ii) from (i) gives the cavity shift caused by the qubit drive in the long-time limit. Our results are plotted in Figure 4.4 for (a) the ideal case of zero residual cavity coupling of the second qubit, $g_2 = 0$, and (b) equally strong cavity coupling of the two qubits, $g_1 = g_2$. The qubit parameters used are the same as in Figure 4.3. The decay rates used roughly correspond to the experimentally measured cavity quality factor $Q = \omega_c/\kappa \sim 3 \times 10^3$ and an conservative estimate for the qubit energy relaxation time of $T_1 \sim 1\,\mu$s. We remark that the actual qubit relaxation time in the sample studied in Figure 4.2 is

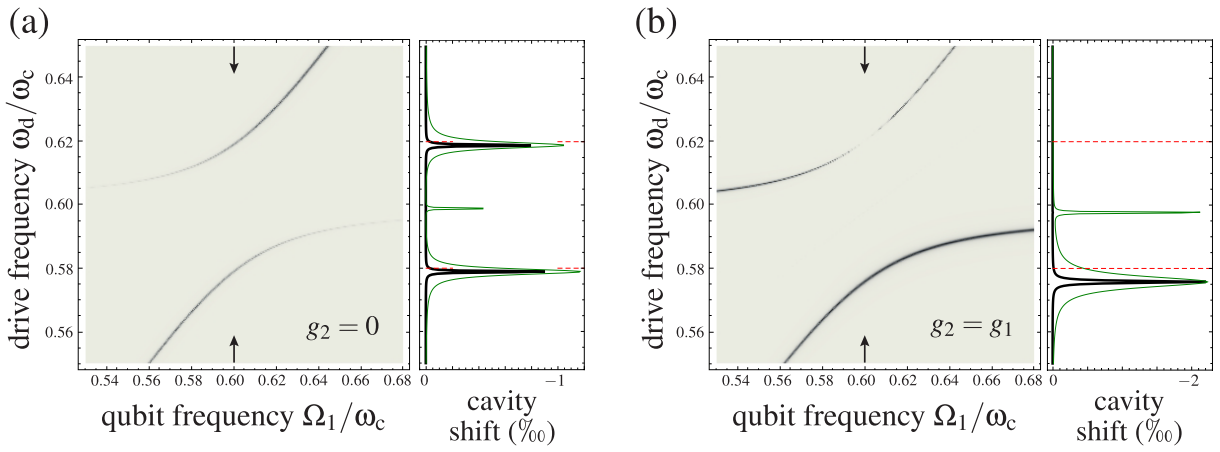

Figure 4.4: Calculated shift of the cavity frequency ω_c due to the qubit drive in a dissipative circuit QED system with two directly coupled qubits for different coupling strengths of one of the qubits and the cavity. In the density plots, the frequency of the first qubit is varied, Ω_1, and the frequency of the second qubit is constant at $\Omega_2 = 0.6$. The shift (and all other energies) are measured in units of ω_c. The color scale ranges from -2.11×10^{-3} in (a) and -2.34×10^{-3} in (b) (black) to 0 (white). In all plots, the qubit and cavity decay rates are $\gamma_j = 5 \times 10^{-5}$ for $j = 1, 2$, $\kappa = 5 \times 10^{-4}$, and the drive amplitude is $F = 2.5 \times 10^{-3}$. Moreover, $J = 0.02$, $g_1 = 0.03$, and $g_2 = 0$ in (a) and $g_2 = g_1$ in (b). The right panels in (a) and (b) show cuts through the density plots for $\Omega_1 = \Omega_2$ (black curves). The green curves result from increasing the drive amplitudes by a factor of 6. The dashed red lines indicate two of the coupled eigenfrequencies of the bare qubit system, $\Omega \pm J$.

higher. A Rabi experiment recently revealed a energy relaxation time of $T_1 = 27\,\mu$s of the cavity-coupled qubit (with sufficient detuning from the second qubit). Remarkably, this suggests that the presence of a second qubit does not significantly reduce the relaxation time of a 3D transmon. Preliminary results indicate that the same is true for the dephasing time T_2 ($\lesssim T_1$). For calculating spectra, we can therefore neglect pure dephasing without making qualitative mistakes.

The plots in Figure 4.4 are consistent with our calculations of the spectrum on the basis of Fermi's golden rule. The increasing level splitting from (a) to (b) is a consequence of the additional cavity-mediated qubit-qubit coupling which exists if $g_2 \neq 0$ (see the third line of Equation (4.10)). This effect was also present in Figure 4.3 but becomes visible only on the scale of Figure 4.4. Cuts through the density plots at the positions of the arrows show the drive-dependent cavity shift for resonant qubits $\Omega_1 = \Omega_2$ (black curves in the right panels of (a) and (b)). One can see that also in the case $g_2 = 0$, there is a slight shift of the resonances of the qubit system from $\Omega_1 \pm J = \Omega_2 \pm J$ (marked by the dashed red lines) to lower frequencies because of the dispersive coupling of the qubit system and the resonator. Both in (a) and (b), the calculated drive-induced frequency shifts of the cavity amount to a few MHz and are experimentally realistic. By numerical integration, we find that the area between zero and the black curve in (b) is approximately twice the area between zero and the black curve in (a). Thus, we can understand the formation of

the dark state for symmetric coupling $g_1 = g_2$ in (b) as an interference effect. If the drive tone can excite the qubit system via the first and the second qubit equally, these excitation pathways interfere constructively for the first excited state of the system and destructively for the second excited state of the system. To quantify this, notice that in these states the qubits are approximately in the superpositions $|\uparrow\downarrow\rangle \pm |\downarrow\uparrow\rangle$, respectively. We can estimate schematically that the transition rates from the ground state to these states (or the area between zero and the black curves) are proportional to

$$\left|\left(\langle\downarrow\uparrow| \pm \langle\uparrow\downarrow|\right)\left(g_1\sigma_+^1 + g_2\sigma_+^2\right)|\downarrow\downarrow\rangle\right|^2 = |g_1 \pm g_2|^2. \tag{4.12}$$

This estimation fits to our numerical results in the right panels of Figure 4.4 and can also be used to estimate experimentally the residual coupling g_2 by a detailed experimental analysis of the spectroscopy lines and their relative weights on resonance. Finally, we remark that both in the experiments (not shown) and in our numerics (shown for $\Omega_1 = \Omega_2$ in the right panels of (a) and (b) as green curves) another line approximately at $(\Omega_1 + \Omega_2)/2$ appears if the drive power is increased (in addition to the power broadening of the spectroscopy lines). These are caused by two-photon excitations of the qubit system to the state $|\uparrow\uparrow\rangle$ and provide further evidence for the soundness of our theoretical description of the circuit QED system.

Turning now to the goals (III) and (IV) of the spectroscopy experiments, the estimation of the homogeneity of the qubit parameters and the longer-range qubit-qubit coupling, let us first consider the experimental spectroscopy results for a six-qubit sample shown in Figure 4.5(a). For comparison, we plot the lowest excitation energies of $\mathcal{H}$ (Equation (4.3)) for $N = 6$ as a function of Ω_1 in the vicinity of the avoided crossings of the qubit system in Figure 4.5(b). As before, we encode the transition rates (4.11) from the ground state to the excited states due to the qubit drive in the color of the lines, according to the same scheme as in Figure 4.3 (where $g_2 < g_1$). We assume experimentally realistic couplings g_1 and J_j, but we make the idealizing assumptions that $g_{j>1} = 0$, $J_j = J$, and $\Omega_{j>1} = 0.6\omega_c$ (independent of j). The visibility of the spectroscopy lines in (a) roughly matches the theoretical expectation in (b). This indicates that also in this sample the undesired qubit-cavity couplings $g_{j>1}$ are small. However, the structure of the experimentally measured avoided crossings obviously deviates from the result of our calculation.

The potential sources of this non-ideal spectrum are inhomogeneities in the $\Omega_{j>1}$ and longer-range couplings in the system. In the dispersive regime, spurious qubit-cavity couplings $g_{j>1}$ have little effect. The nearest-neighbor Ising couplings J_j can inherit some disorder from the Ω_j. For transmons, they are approximately proportional to $\sqrt{\Omega_j \Omega_{j+1}}$ (see Section 4.5). The constants of proportionality, however, are determined by the geometry of the chain and thus may be expected to have no strong dependence on j (possibly except for $j = 1$). Longer-range couplings and disorder in the Ω_j can be straightforwardly implemented in the numerics to simulate their influence on the spectrum. However, for $N = 6$, the parameter space of the Ω_j and the longer-range couplings is too large to search for a parameter set yielding curves like in Figure 4.5.

To investigate the disorder and the longer-range coupling present in the experimental implementation of the quantum Ising chain, it is therefore advisable to consider the smallest system in which these detrimental effects can occur – a chain of length $N = 3$. Spectroscopic results for such a system are shown in Figure 4.6(a). The avoided crossings are found to have widths of

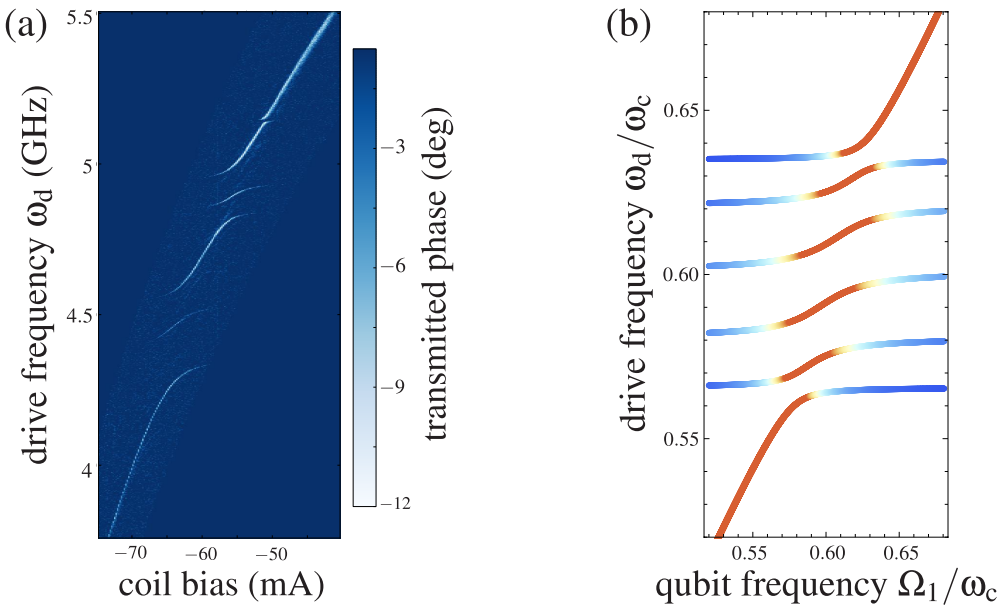

Figure 4.5: Spectrum of a circuit QED system containing six capacitively coupled qubits. The frequency of the first qubit, Ω_1, is tuned, the frequencies $\Omega_{j>1}$ of the other qubits are constant. (a) Experimental results (data by E. Henry and A. Schmidt). In the experiment, Ω_1 is tuned via a bias current through an external coil. (b) Calculated resonances of a six-qubit Ising chain coupled to a cavity as a function of Ω_1. The color code represents the calculated visibility of the resonances (blue: low, red: high; see main text for details). The parameters used in the calculation are, in units of the cavity frequency ω_c, $\Omega_{j>1} = 0.6$, $J_j = 0.02$, $g_1 = 0.03$, $g_{j>1} = 0$.

approximately 80 MHz (upper crossing) and 280 MHz (lower crossing) thus to have a ratio of about $1/3.5$. To compare this with theory, we diagonalize the Hamiltonian $\mathcal{H}$ (Equation (4.3)) for $N = 3$ and calculate the transition rates (4.11) as before. However, now we also allow for a next-nearest-neighbor coupling $-J_{1,3}\sigma_x^1\sigma_x^3$ in $\mathcal{H}$. Our calculation for the ideal case $J_{1,3} = 0$, $J_j = J$, $g_{j>1} = 0$, and $\Omega_{j>1} \equiv \Omega_>$ (independent of j), shown in Figure (4.11) (b), exhibits avoided crossings of about the same size and is not compatible with the experimental results in (a). Since residual cavity coupling $g_{j>1} > 0$ does not have a strong effect on the positions of the resonances in the dispersive regime, we may assume $g_{j>1} = 0$ for finding the source of the non-ideal positions of the resonances in (a). For completeness, we first consider the case where $J_1 \neq J_2$ and otherwise ideal parameters, which might be relevant in the measured three-qubit sample because of the different geometry of the first qubit. In this situation, the spectrum changes appreciably, see (c), but this alone cannot account for the unequal level splitting in (a). We can conclude that longer-range coupling and/or inhomogeneities of the $\Omega_{j>0}$ must play a role in the sample measured for Figure 4.6(a). These, however, are difficult to tell apart or to quantify just on the basis of the measured spectrum (a). This can be seen from the plots (d) and (e), which both agree qualitatively with (a) but have been obtained by letting $\Omega_3 > \Omega_2$ (d) and $J_{1,3} \neq 0$ (e). Of course, the spectrum (a) might also result from a combination of these uncontrolled system parameters.

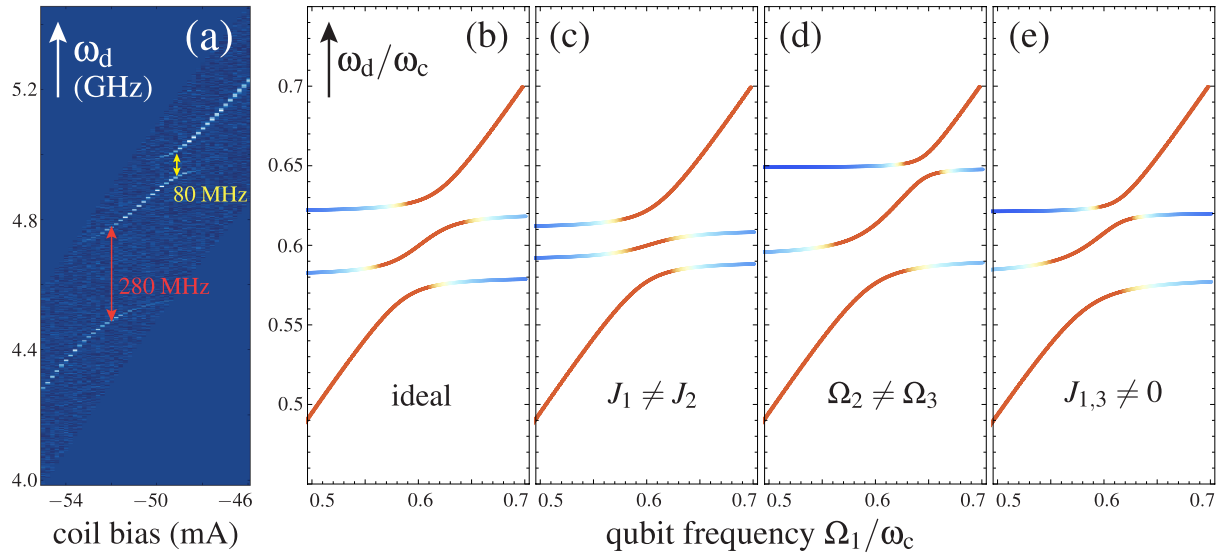

Figure 4.6: Spectrum of a circuit QED system containing $N = 3$ capacitively coupled qubits. Similar to the situation of Figure 4.5, Ω_1 is tuned and the $\Omega_{j>1}$ are constant. (a) Experimental results (data by E. Henry and A. Schmidt). (b) Calculated resonances of a three-qubit Ising chain with nearest-neighbor couplings J_1 and J_2 and next-nearest-neighbor coupling $J_{1,3}$, coupled to a cavity via the first qubit, $g_1 = 0.03$, $g_{j>1} = 0$. The calculated visibility of the resonances is color-coded as before. In the idealized situation (b), the parameters are $\Omega_{j>1} = 0.6$, $J_j = 0.02$, and $J_{1,3} = 0$. The parameters used in the plots (c-e) differ from those of (b) in that $J_2 = 0.01$ in (c), $\Omega_3 = 0.64$ (and $J_2 = J_1\sqrt{\Omega_3/\Omega_2}$) in (d), and $J_{1,3} = 0.01$ in (e).

Thus, there is still much work to be done to reach a full understanding of the Hamiltonian of the currently investigated design or to realize an improved design that comes closer to implementing the desired Hamiltonian. For instance, it might be helpful to measure several samples with identical layout. If these exhibit the same spectrum, the disorder of the $\Omega_{j>1}$ must be small (except there are systematic errors in the sample fabrication process). Such a result should allow one to assess the longer-range qubit-qubit coupling by calculations as in Figure 4.6(e). A complementary approach would be to fabricate samples with the $\Omega_{j>1}$ deliberately detuned from one another (by altering the properties of the Josephson junctions). This would allow one to determine the longer-range coupling by spectroscopy. However, its dependence on the qubit frequencies also had to be determined for being able to transfer the results of such a measurement back to the resonant case.

Time domain

An essential prerequisite for quantum simulations with our circuit QED setup is the demonstration of time-domain control over some of its degrees of freedom. Experiments with this objective are currently being prepared, based on elementary architectures as the ones discussed

in the previous section. As already mentioned, the coherence times of the qubits in such circuit QED systems are comparable to those found in usual 3D architectures, which further encourages studies in the time-domain. Two-qubit samples, for which all coupling parameters can be already well estimated by spectroscopy, allow for a straightforward comparison of theory and experiment and thus are a good starting point for benchmarking time-domain experiments. Studies of longer chains in the time domain might also be worthwhile, even at this early state of the experiments, as they might further our understanding of features such as next-nearest-neighbor coupling. In this section, we discuss possible time-domain experiments with the small versions of our quantum simulator already at hand. In particular, we analyze their feasibility given the system properties described in the last section.

A simple time-domain experiment would be to excite the first qubit of the chain, swap the excitation into the second qubit, and measure the time-dependent excitation probability of the first qubit (as proposed in Section 4.5, only with a shorter chain). The first, cavity-coupled qubit dominates the dispersive shift of the cavity (in particular if detuned from the chain), which has already been used for time-resolved measurements of the state of this qubit in Rabi and Ramsey experiments. As mentioned above, fast flux lines are not yet incorporated in the 3D architecture. These would allow one to bring the first qubit rapidly into resonance with the rest of the chain after an excitation has been created in this qubit. This can be compensated for by a fast Stark pulse on the first qubit. Experimentally realistic values for the magnitude and the time scales of the induced Stark shifts are $\Delta\Omega_1/2\pi \sim 150$ MHz and $\Delta t \sim 10$ ns, respectively.

We simulate such an experiment in a two-qubit sample to investigate whether the preparation of the system, the excitation swapping, and the revival of the first qubit could succeed under realistic conditions and in the presence of decay, dephasing, and spurious coupling of the second qubit and the cavity. We choose the parameters in our simulation such that for $\omega_c/2\pi = 7$ GHz, the Ω_j are at about $2\pi \times 4$ GHz, initially detuned by $\Delta\Omega_1/2\pi = 140$ MHz, and coupled with a strength $J/2\pi = 35$ MHz. The decay and dephasing rates we assume in our calculation are pessimistic and correspond to $T_1 \approx 0.5\ \mu$s and $T_2 \approx 0.3\ \mu$s and a cavity Q factor of $Q = 2 \times 10^3$. The result of our simulation is shown in Figure 4.7(a). We plot the cavity population $\langle a^\dagger a \rangle$ and the qubit excitation probabilities $P_\uparrow^j = (1 + \langle \sigma_z^j \rangle)/2$ as a function of the dimensionless time $\omega_c t$. Note that one time unit corresponds roughly to 1 ns. As initial condition, we set the density matrix equal to the ground state of the system. At $\omega_c t = 10$, we switch on a Rabi drive at a frequency $\omega = \Omega_1$ for a duration $\omega_c T_\pi = \pi(\omega_c - \Omega_1)/(2g_1 F) = 66$, where F is the drive amplitude. We assume here the simplest case of a (smoothed) rectangular pulse. We remark that by optimizing the pulse shape, the fidelity of the qubit excitation can be enhanced. Note that the drive also excites the second qubit, both directly via the residual coupling $g_2 = g_1/4$ and indirectly via the qubit-qubit coupling. At $\omega_c t = 90$, we tune the first qubit into resonance with the second qubit in a time $\Delta t \sim 10/\omega_c$. In an experiment, this would be done with the Stark drive (which is numerically difficult to calibrate). One can clearly see how the excitation is coherently exchanged between first and second qubit despite the various decay channels in the system. Like in the hamiltonian case, the exchange takes place in a time $T \sim \pi/J$ and should be easily resolvable in the measurement of the first qubit. Hence, the simulation suggest the feasibility of time-domain experiments on the basis of Stark pulses without further improvements

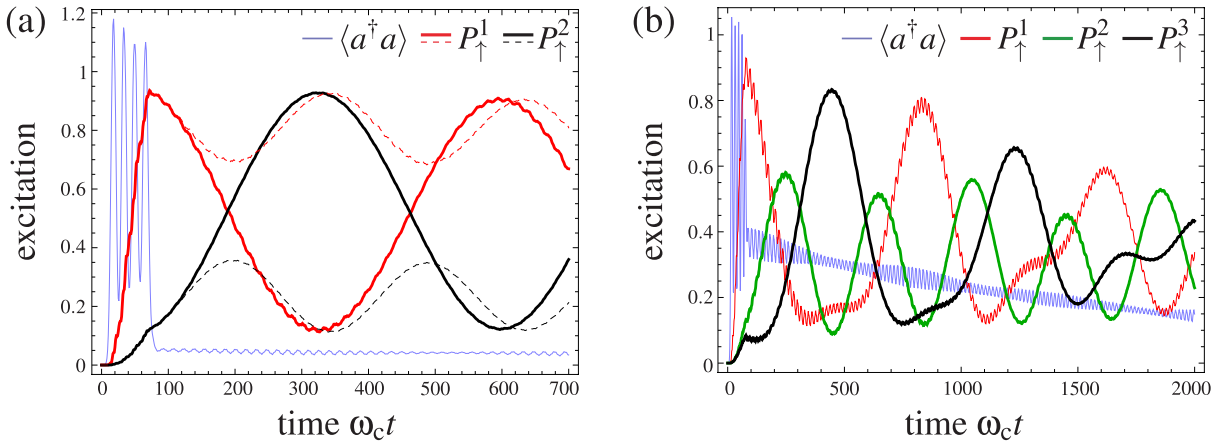

Figure 4.7: Excitation swapping on the basis of Stark pulses. Plotted are the calculated cavity population $\langle a^\dagger a\rangle$ and the qubit excitation probabilities $P_\uparrow^j = (1+\langle\sigma_z^j\rangle)/2$ as a function of time. (a) A Rabi drive with amplitude $F = 0.3$ at the frequency Ω_1 of the first qubit is applied to a two-qubit sample initially prepared in its ground state from $t = 10$ to $t = 76$. The first qubit is detuned from the second qubit by an amount of $\Delta\Omega_1 = \Omega_1 - \Omega_2 = 0.02$. The detuning is reduced to zero near $t = 90$ (solid curves). The frequency Ω_2 of the second qubit remains constant throughout whole process. For comparison, the time evolution of the qubits without this reduction of the detuning is plotted as dashed curves. The parameters used in the simulation are $\Omega_2 = 0.6$, $J = 0.005$, $g_1 = 0.03$, $g_2 = 0.0075$, $\kappa = 5\times10^{-4}$, and $\gamma_j = \gamma_{\varphi,j} = 5\times10^{-5}$ for $j = 1,2$. (b) Time evolution of the qubit and cavity excitations for the same protocol as in (a) in a sample with three qubits and otherwise identical parameters. All energies (times) are measured in units of ω_c ($1/\omega_c$).

of the circuit QED design being required. We remark that without the Stark pulse, one would still find a partial excitation exchange between the first and the second qubit owing to the small ratio of $\Delta\Omega_1/J$ (dashed lines). This implies also that if it should turn out to be necessary, in an experiment with Stark pulse, to switch off the Stark pulse for measuring the first qubit, the measurement should be fast compared to this spurious excitation exchange. This still appears to be possible.

For a three-qubit sample with identical parameters and decay rates, the same protocol generates the time evolution shown in Figure 4.7(b). Notwithstanding the stronger influence of the dissipation due to the increased evolution time and the stronger dispersion of the wave packet, decay and revivals of the first qubit should be observable also in this case. It is interesting to note the short period of relaxation of the third qubit (black curve, at $t \gtrsim 100$) after the drive has been switched off and before the excitation propagating through the chain further populates this qubit.

Finally, we mention that deviations from the time evolution predicted by Figure 4.7(b) might be helpful to quantify the next-nearest-neighbor coupling or the disorder in the qubit frequencies $\Omega_{j>1}$, which seemed to be present in the samples with $N > 2$ studied so far (see previous section). For instance, the sets of system parameters yielding the qualitatively similar spectra of

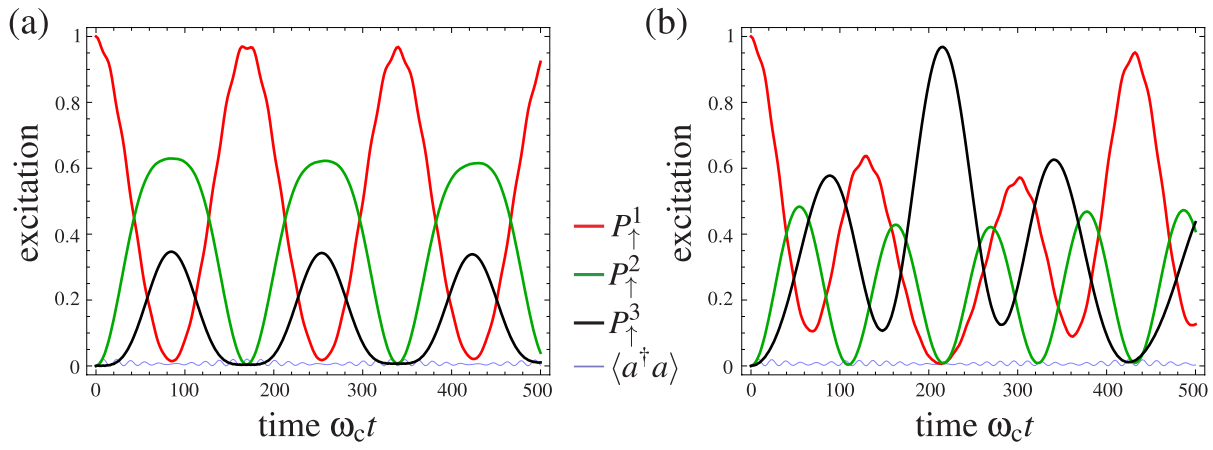

Figure 4.8: Calculated dissipative dynamics of a chain of three qubits coupled to a cavity. The system is initially prepared in the state $|\uparrow\downarrow\downarrow,0\rangle$ with $\Omega_1 = \Omega_2$ and evolves in the presence of decay and dephasing rates $\kappa = 5 \times 10^{-4}$ and $\gamma_j = \gamma_{\varphi,j} = 5 \times 10^{-5}$. (a) The non-dissipative part of the time evolution is governed by the same Hamiltonian as used for Figure 4.6(d), that is, $\Omega_3 \neq \Omega_2$. (b) The non-dissipative part of the time evolution is governed by the same Hamiltonian as used for Figure 4.6(e), that is $J_{1,3} \neq 0$.

Figures 4.6(d) and 4.6(e) would generate the time evolutions plotted in Figure 4.8(a) and 4.8(b), respectively, at $\Omega_1 = \Omega_2$ and could be easily differentiated from each other by measuring the revivals of the first qubit.[1] Of course, this would presume that one can ensure $\Omega_1 = \Omega_2$.

In summary, first results have been already obtained on the way to realize our circuit QED quantum simulator. A way to implement it in the framework of a 3D circuit QED device has been discussed. The comparison of theory and spectroscopy experiments has revealed that the cavity-coupling of the rotated qubits is indeed weak. We have been able to estimate an upper bound for this coupling and have suggested experiments to strengthen or possibly to further reduce this bound. We have identified non-ideal behavior of the samples measured so far and have found that they must incorporate longer-range coupling and/or qubit inhomogeneities. Finally, time-domain experiments with small chains on the basis of Stark pulses have been simulated under experimentally realistic conditions. The simulations indicate feasibility of such experiments without any further improvements of the sample design. Thus, we are confident that experiments on the time evolution of small versions of our quantum simulator will be successfully conducted soon. The interplay of theory and experiment will hopefully advance our understanding of the system in the near future to a point where the quantum simulator can be scaled up in a controlled way.

1. For simplicity, we do not simulate the initial π pulse and the Stark shift acting on the first qubit in these plots but start the dissipative time evolution directly from the state $|\uparrow\downarrow\downarrow,0\rangle$.

Conclusion

In this thesis, circuit QED systems with multiple Josephson qubits have been studied theoretically with respect to their ability of undergoing superradiant phase transitions and with respect to their potential as quantum simulators of interacting spin chains. We conclude by summarizing the main results of this thesis.

Superradiant phase transitions:

- Common, second-order superradiant phase transitions cannot occur in circuit QED systems with Josephson charge qubits.
- The standard theory of circuit QED is not fully reliable for multi-qubit setups.

Quantum simulations:

- A circuit QED setup that simulates the quantum Ising chain has been proposed and analyzed.
- The setup should be suited to simulate the non-equilibrium dynamics of the quantum Ising chain and might be extended to simulate non-integrable spin systems.
- Weak disorder in the qubit parameters can thereby be tolerated, strong disorder leads to interesting new physics. The tolerable amount of disorder can be estimated.
- Experimental results for small chains are already available and can be theoretically understood. They are generally very promising. Some system parameters are yet to be determined precisely.

Scaling up the system size is arguably one of the main objectives in the field of circuit QED. Rich physics promises to be accessible in such larger-scale quantum systems with many controllably interacting entities, also long before universal quantum computing comes within reach. We hope that the work presented in this thesis sheds some light on aspects of this physics.

Bibliography

Abdumalikov, A. A., O. Astafiev, A. M. Zagoskin, Yu. A. Pashkin, Y. Nakamura, and J. S. Tsai, 2010, *Electromagnetically induced transparency on a single artificial atom,* Phys. Rev. Lett. **104**, 193601.

Abdumalikov, A. A., J. M. Fink, K. Juliusson, M. Pechal, S. Berger, A. Wallraff, and S. Filipp, 2013, *Experimental realization of non-Abelian non-adiabatic geometric gates,* Nature **advance online publication**, .

Abrams, D. S., and S. Lloyd, 1997, *Simulation of many-body Fermi systems on a universal quantum computer,* Phys. Rev. Lett. **79**, 2586.

Ambegaokar, V., and A. Baratoff, 1963, *Tunneling between superconductors,* Phys. Rev. Lett. **11**, 104.

Anderson, P. W., and J. M. Rowell, 1963, *Probable observation of the Josephson superconducting tunneling effect,* Phys. Rev. Lett. **10**, 230.

Angelakis, D. G., M. F. Santos, and S. Bose, 2007, *Photon-blockade-induced Mott transitions and xy spin models in coupled cavity arrays,* Phys. Rev. A **76**, 031805.

Ansmann, Markus, H. Wang, Radoslaw C. Bialczak, Max Hofheinz, Erik Lucero, M. Neeley, A. D. O'Connell, D. Sank, M. Weides, J. Wenner, A. N. Cleland, and John M. Martinis, 2009, *Violation of Bell's inequality in Josephson phase qubits,* Nature **461**, 504.

Aspuru-Guzik, A., A. D. Dutoi, P. J. Love, and M. Head-Gordon, 2005, *Simulated quantum computation of molecular energies,* Science **309**, 1704.

Aspuru-Guzik, A., and P. Walther, 2012, *Photonic quantum simulators,* Nat. Phys. **8**, 285.

Astafiev, O., K. Inomata, A. O. Niskanen, T. Yamamoto, Yu. A. Pashkin, Y. Nakamura, and J. S. Tsai, 2007, *Single artificial-atom lasing,* Nature **449**, 588.

Astafiev, O., A. M. Zagoskin, A. A. Abdumalikov, Yu. A. Pashkin, T. Yamamoto, K. Inomata, Y. Nakamura, and J. S. Tsai, 2010, *Resonance fluorescence of a single artificial atom,* Science **327**, 840.

Baksic, A., P. Nataf, and C. Ciuti, 2013, *Superradiant phase transitions with three-level systems,* Phys. Rev. A **87**, 023813.

Bardeen, J., L. N. Cooper, and J. R. Schrieffer, 1957, *Theory of superconductivity,* Phys. Rev. **108**, 1175.

Bardyn, C.-E., and A. Imamoglu, 2012, *Majorana-like modes of light in a one-dimensional array of nonlinear cavities,* Phys. Rev. Lett. **109**, 253606.

Barenco, A., C. H. Bennett, R. Cleve, D. P. DiVincenzo, N. Margolus, P. Shor, T. Sleator, J. A. Smolin, and H. Weinfurter, 1995, *Elementary gates for quantum computation,* Phys. Rev. A **52**, 3457.

Barends, R., J. Kelly, A. Megrant, D. Sank, E. Jeffrey, Y. Chen, Y. Yin, B. Chiaro, J. Mutus, C. Neill, P. O'Malley, P. Roushan, J. Wenner, T. C. White, A. N. Cleland, and J. M. Martinis, 2013, *Coherent Josephson qubit suitable for scalable quantum integrated circuits,* arXiv:1304.2322.

Barreiro, J. T., M. Müller, P. Schindler, D. Nigg, T. Monz, M. Chwalla, M. Hennrich, C. F. Roos, P. Zoller, and R. Blatt, 2011, *An open-system quantum simulator with trapped ions,* Nature **470**, 486.

Baumann, K., C. Guerlin, F. Brennecke, and T. Esslinger, 2010, *Dicke quantum phase transition with a superfluid gas in an optical cavity,* Nature **464**, 1301.

Baur, M., S. Filipp, R. Bianchetti, J. M. Fink, M. Göppl, L. Steffen, P. J. Leek, A. Blais, and A. Wallraff, 2009, *Measurement of Autler-Townes and Mollow transitions in a strongly driven superconducting qubit,* Phys. Rev. Lett. **102**, 243602.

Bennett, C. H., and G. Brassard, 1984, *Quantum cryptography: Public key distribution and coin tossing,* in *Proceedings of the IEEE International Conference on Computers, Systems, and Signal Processing*.

Bennett, C. H., G. Brassard, C. Crépeau, R. Jozsa, A. Peres, and W. K. Wootters, 1993, *Teleporting an unknown quantum state via dual classical and Einstein-Podolsky-Rosen channels,* Phys. Rev. Lett. **70**, 1895.

Bennett, C. H., and S. J. Wiesner, 1992, *Communication via one- and two-particle operators on Einstein-Podolsky-Rosen states,* Phys. Rev. Lett. **69**, 2881.

Bergeal, N., F. Schackert, M. Metcalfe, R. Vijay, V. E. Manucharyan, L. Frunzio, D. E. Prober, R. J. Schoelkopf, S. M. Girvin, and M. H. Devoret, 2010, *Phase-preserving amplification near the quantum limit with a Josephson ring modulator,* Nature **465**, 64.

Bergquist, J. C., Randall G. Hulet, Wayne M. Itano, and D. J. Wineland, 1986, *Observation of quantum jumps in a single atom,* Phys. Rev. Lett. **57**, 1699.

Bialczak, R. C., M. Ansmann, M. Hofheinz, M. Lenander, E. Lucero, M. Neeley, A. D. O'Connell, D. Sank, H. Wang, M. Weides, J. Wenner, T. Yamamoto, A. N. Cleland, and J. M. Martinis, 2011, *Fast tunable coupler for superconducting qubits,* Phys. Rev. Lett. **106**, 060501.

Bishop, L. S., J. M. Chow, J. Koch, A. A. Houck, M. H. Devoret, E. Thuneberg, S. M. Girvin, and R. J. Schoelkopf, 2009, *Nonlinear response of the vacuum Rabi resonance,* Nat. Phys. **5**, 105.

Blais, A., J. Gambetta, A. Wallraff, D. I. Schuster, S. M. Girvin, M. H. Devoret, and R. J. Schoelkopf, 2007, *Quantum-information processing with circuit quantum electrodynamics,* Phys. Rev. A **75**, 032329.

Blais, A., R.-S. Huang, A. Wallraff, S. M. Girvin, and R. J. Schoelkopf, 2004, *Cavity quantum electrodynamics for superconducting electrical circuits: An architecture for quantum computation,* Phys. Rev. A **69**, 062320.

Blatt, R., and C. F. Roos, 2012, *Quantum simulations with trapped ions,* Nat. Phys. **8**, 277.

Bloch, I., J. Dalibard, and S. Nascimbene, 2012, *Quantum simulations with ultracold quantum gases,* Nat. Phys. **8**, 267.

Bouchiat, V., D. Vion, P. Joyez, D. Esteve, and M. H. Devoret, 1998, *Quantum coherence with a single Cooper pair,* Physica Scripta **1998**, 165.

Bouwmeester, D., J.-W. Pan, K. Mattle, M. Eibl, H. Weinfurter, and A. Zeilinger, 1997, *Experimental quantum teleportation,* Nature **390**, 575.

Bozyigit, D., C. Lang, L. Steffen, J. M. Fink, C. Eichler, M. Baur, R. Bianchetti, P. J. Leek, S. Filipp, M. P. da Silva, A. Blais, and A. Wallraff, 2011, *Antibunching of microwave-frequency photons observed in correlation measurements using linear detectors,* Nat. Phys. **7**, 154.

Braak, D., 2011, *Integrability of the Rabi model,* Phys. Rev. Lett. **107**, 100401.

Brandes, Tobias, 2005, *Coherent and collective quantum optical effects in mesoscopic systems,* Physics Reports **408**, 315.

Braun, S., J. P. Ronzheimer, M. Schreiber, S. S. Hodgman, T. Rom, I. Bloch, and U. Schneider, 2013, *Negative absolute temperature for motional degrees of freedom,* Science **339**, 52.

Britton, J. W., B. C. Sawyer, A. C. Keith, C. C. J. Wang, J. K. Freericks, H. Uys, M. J. Biercuk, and J. J. Bollinger, 2012, *Engineered two-dimensional Ising interactions in a trapped-ion quantum simulator with hundreds of spins,* Nature **484**, 489.

Broome, M. A., A. Fedrizzi, B. P. Lanyon, I. Kassal, A. Aspuru-Guzik, and A. G. White, 2010, *Discrete single-photon quantum walks with tunable decoherence,* Phys. Rev. Lett. **104**, 153602.

Brune, M., E. Hagley, J. Dreyer, X. Maître, A. Maali, C. Wunderlich, J. M. Raimond, and S. Haroche, 1996a, *Observing the progressive decoherence of the "meter" in a quantum measurement,* Phys. Rev. Lett. **77**, 4887.

Brune, M., F. Schmidt-Kaler, A. Maali, J. Dreyer, E. Hagley, J. M. Raimond, and S. Haroche, 1996b, *Quantum Rabi oscillation: A direct test of field quantization in a cavity,* Phys. Rev. Lett. **76**, 1800.

Buluta, I., and F. Nori, 2009, *Quantum simulators,* Science **326**, 108.

Büttiker, M., 1987, *Zero-current persistent potential drop across small-capacitance Josephson junctions,* Phys. Rev. B **36**, 3548.

Bylander, J., S. Gustavsson, F. Yan, F. Yoshihara, K. Harrabi, G. Fitch, D. G. Cory, Y. Nakamura, J.-S. Tsai, and W. D. Oliver, 2011, *Noise spectroscopy through dynamical decoupling with a superconducting flux qubit,* Nat. Phys. **7**, 565.

Caldeira, A. O., and A. J. Leggett, 1981, *Influence of dissipation on quantum tunneling in macroscopic systems,* Phys. Rev. Lett. **46**, 211.

Caldeira, A.O, and A.J Leggett, 1983, *Quantum tunnelling in a dissipative system,* Annals of Physics **149**, 374.

Carmichael, H. J., C. W. Gardiner, and D. F. Walls, 1973, *Higher order corrections to the Dicke superradiant phase transition,* Physics Letters A **46**, 47.

Castellanos-Beltran, M. A., K. D. Irwin, G. C. Hilton, L. R. Vale, and K. W. Lehnert, 2008, *Amplification and squeezing of quantum noise with a tunable Josephson metamaterial,* Nat. Phys. **4**, 929.

Chan, J., T. P. M. Alegre, A. H. Safavi-Naeini, J. T. Hill, A. Krause, S. Groblacher, M. Aspelmeyer, and O. Painter, 2011, *Laser cooling of a nanomechanical oscillator into its quantum ground state,* Nature **478**, 89.

Cheneau, M., P. Barmettler, D. Poletti, M. Endres, P. Schausz, T. Fukuhara, C. Gross, I. Bloch, C. Kollath, and S. Kuhr, 2012, *Light-cone-like spreading of correlations in a quantum many-body system,* Nature **481**, 484.

Chiorescu, I., P. Bertet, K. Semba, Y. Nakamura, C. J. P. M. Harmans, and J. E. Mooij, 2004, *Coherent dynamics of a flux qubit coupled to a harmonic oscillator,* Nature **431**, 159.

Cirac, J. I., and P. Zoller, 1995, *Quantum computations with cold trapped ions,* Phys. Rev. Lett. **74**, 4091.

Cirac, J. I., and P. Zoller, 2012, *Goals and opportunities in quantum simulation,* Nat. Phys. **8**, 264.

Ciuti, C., and P. Nataf, 2012, *Comment on "Superradiant phase transitions and the standard description of circuit QED",* Phys. Rev. Lett. **109**, 179301.

Clarke, J., and A.I. Braginski, 2006, *The SQUID Handbook: Fundamentals and Technology of SQUIDs and SQUID Systems*, Bd. 1 (Wiley).

Clarke, J., and F. K. Wilhelm, 2008, *Superconducting quantum bits,* Nature **453**, 1031.

Clauser, J. F., M. A. Horne, A. Shimony, and R. A. Holt, 1969, *Proposed experiment to test local hidden-variable theories,* Phys. Rev. Lett. **23**, 880.

Cottet, A., 2002, *Implementation of a quantum bit in a superconducting circuit*, Ph.D. thesis (Université Paris).

Delanty, M., S. Rebić, and J. Twamley, 2011, *Superradiance and phase multistability in circuit quantum electrodynamics,* New Journal of Physics **13**, 053032.

DeMarco, B., and D. S. Jin, 1999, *Onset of Fermi degeneracy in a trapped atomic gas,* Science **285**, 1703.

Deutsch, D., and R. Jozsa, 1992, *Rapid solution of problems by quantum computation,* Proceedings of the Royal Society of London. Series A: Mathematical and Physical Sciences **439**, 553.

Devoret, M. H., 1997, *Quantum fluctuations in electrical circuits,* in *Quantum Fluctuations (Les Houches Session LXIII)* (Elsevier, Amsterdam) pp. 351–385.

Devoret, M. H., J. M. Martinis, and J. Clarke, 1985, *Measurements of macroscopic quantum tunneling out of the zero-voltage state of a current-biased Josephson junction,* Phys. Rev. Lett. **55**, 1908.

Devoret, M. H., and R. J. Schoelkopf, 2013, *Superconducting circuits for quantum information: An outlook,* Science **339**, 1169.

Devoret, M. H., A. Wallraff, and J. M. Martinis, 2004, *Superconducting qubits: A short review,* in *Quantum entanglement and Information Processing (Les Houches Session LXXIX)*, edited by J. M. Raimond, J. Dalibard, and D. Esteve, 443rd ed. (Elsevier) pp. 443–485, cond-mat/0411174v1.

Dewes, A., F. R. Ong, V. Schmitt, R. Lauro, N. Boulant, P. Bertet, D. Vion, and D. Esteve, 2012, *Characterization of a two-transmon processor with individual single-shot qubit readout,* Phys. Rev. Lett. **108**, 057002.

DiCarlo, L., J. M. Chow, J. M. Gambetta, L. S. Bishop, D. I. Schuster, J. Majer, A. Blais, L. Frunzio, S. M. Girvin, and R. J. Schoelkopf, 2009, *Demonstration of two-qubit algorithms with a superconducting quantum processor,* Nature **460**, 240.

DiCarlo, L., M. D. Reed, L. Sun, B. R. Johnson, J. M. Chow, J. M. Gambetta, L. Frunzio, S. M. Girvin, M. H. Devoret, and R. J. Schoelkopf, 2010, *Preparation and measurement of three-qubit entanglement in a superconducting circuit,* Nature **467**, 574.

Dicke, R. H., 1954, *Coherence in spontaneous radiation processes,* Phys. Rev. **93**, 99.

Dimer, F., B. Estienne, A. S. Parkins, and H. J. Carmichael, 2007, *Proposed realization of the Dicke-model quantum phase transition in an optical cavity QED system,* Phys. Rev. A **75**, 013804.

DiVincenzo, D. P., 2000, *The physical implementation of quantum computation,* Fortschritte der Physik **48**, 771.

Dutt, M. V. G., L. Childress, L. Jiang, E. Togan, J. Maze, F. Jelezko, A. S. Zibrov, P. R. Hemmer, and M. D. Lukin, 2007, *Quantum register based on individual electronic and nuclear spin qubits in diamond,* Science **316**, 1312.

Eichler, C., D. Bozyigit, C. Lang, L. Steffen, J. Fink, and A. Wallraff, 2011, *Experimental state tomography of itinerant single microwave photons,* Phys. Rev. Lett. **106**, 220503.

Eichler, C., C. Lang, J. M. Fink, J. Govenius, S. Filipp, and A. Wallraff, 2012, *Observation of entanglement between itinerant microwave photons and a superconducting qubit,* Phys. Rev. Lett. **109**, 240501.

Emary, C., and T. Brandes, 2003a, *Chaos and the quantum phase transition in the Dicke model,* Phys. Rev. E **67**, 066203.

Emary, C., and T. Brandes, 2003b, *Quantum chaos triggered by precursors of a quantum phase transition: The Dicke model,* Phys. Rev. Lett. **90**, 044101.

Esslinger, T., 2010, *Fermi-Hubbard physics with atoms in an optical lattice, Annual Review of Condensed Matter Physics*, Annual Review of Condensed Matter Physics **1**, 129.

Esteve, Daniel, Michel H. Devoret, and John M. Martinis, 1986, *Effect of an arbitrary dissipative circuit on the quantum energy levels and tunneling of a josephson junction,* Phys. Rev. B **34**, 158.

Faraon, A., I. Fushman, D. Englund, N. Stoltz, P. Petroff, and J. Vuckovic, 2008, *Coherent generation of non-classical light on a chip via photon-induced tunnelling and blockade,* Nat. Phys. **4**, 859.

Fazio, R., and H. van der Zant, 2001, *Quantum phase transitions and vortex dynamics in superconducting networks,* Physics Reports **355**, 235.

Fedorov, A., L. Steffen, M. Baur, M. P. da Silva, and A. Wallraff, 2012, *Implementation of a Toffoli gate with superconducting circuits,* Nature **481**, 170.

Feynman, R. P., 1982, *Simulating physics with computers,* International Journal of Theoretical Physics **21**, 467.

Fink, J. M., R. Bianchetti, M. Baur, M. Göppl, L. Steffen, S. Filipp, P. J. Leek, A. Blais, and A. Wallraff, 2009, *Dressed collective qubit states and the Tavis-Cummings model in circuit QED,* Phys. Rev. Lett. **103**, 083601.

Fink, J. M., M. Goppl, M. Baur, R. Bianchetti, P. J. Leek, A. Blais, and A. Wallraff, 2008, *Climbing the Jaynes-Cummings ladder and observing its nonlinearity in a cavity QED system,* Nature **454**, 315.

Fisher, M. P. A., P. B. Weichman, G. Grinstein, and D. S. Fisher, 1989, *Boson localization and the superfluid-insulator transition,* Phys. Rev. B **40**, 546.

Fleischhauer, M., A. Imamoglu, and J. P. Marangos, 2005, *Electromagnetically induced transparency: Optics in coherent media,* Rev. Mod. Phys. **77**, 633.

Flurin, E., N. Roch, F. Mallet, M. H. Devoret, and B. Huard, 2012, *Generating entangled microwave radiation over two transmission lines,* Phys. Rev. Lett. **109**, 183901.

Forn-Díaz, P., J. Lisenfeld, D. Marcos, J. J. García-Ripoll, E. Solano, C. J. P. M. Harmans, and J. E. Mooij, 2010, *Observation of the Bloch-Siegert shift in a qubit-oscillator system in the ultrastrong coupling regime,* Phys. Rev. Lett. **105**, 237001.

Fragner, A., M. Göppl, J. M. Fink, M. Baur, R. Bianchetti, P. J. Leek, A. Blais, and A. Wallraff, 2008, *Resolving vacuum fluctuations in an electrical circuit by measuring the Lamb shift,* Science **322**, 1357.

Frey, T., P. J. Leek, M. Beck, A. Blais, T. Ihn, K. Ensslin, and A. Wallraff, 2012, *Dipole coupling of a double quantum dot to a microwave resonator,* Phys. Rev. Lett. **108**, 046807.

Friedenauer, A., H. Schmitz, J. T. Glueckert, D. Porras, and T. Schaetz, 2008, *Simulating a quantum magnet with trapped ions,* Nat. Phys. **4**, 757.

Friedman, J. R., V. Patel, W. Chen, S. K. Tolpygo, and J. E. Lukens, 2000, *Quantum superposition of distinct macroscopic states,* Nature **406**, 43.

Fukuhara, T., A. Kantian, M. Endres, M. Cheneau, P. Schausz, S. Hild, D. Bellem, U. Schollwöck, T. Giamarchi, C. Gross, I. Bloch, and S. Kuhr, 2013, *Quantum dynamics of a mobile spin impurity,* Nat. Phys. **9**, 235.

Fulton, T. A., and G. J. Dolan, 1987, *Observation of single-electron charging effects in small tunnel junctions,* Phys. Rev. Lett. **59**, 109.

Gerritsma, R., G. Kirchmair, F. Zahringer, E. Solano, R. Blatt, and C. F. Roos, 2010, *Quantum simulation of the Dirac equation,* Nature **463**, 68.

Gerritsma, R., B. P. Lanyon, G. Kirchmair, F. Zähringer, C. Hempel, J. Casanova, J. J. García-Ripoll, E. Solano, R. Blatt, and C. F. Roos, 2011, *Quantum simulation of the Klein paradox with trapped ions,* Phys. Rev. Lett. **106**, 060503.

Giaever, I., 1965, *Detection of the AC Josephson effect,* Phys. Rev. Lett. **14**, 904.

Ginzburg, V.L., and L.D. Landau, 1950, *On the theory of superconductivity,* Zh. Eksp. Teor. Fiz. **20**, 1064.

Girvin, S. M., 2013, *Basic concepts in quantum information,* arXiv:1302.5842.

Gor'kov, L.P., 1959, *Microscopic derivation of the Ginzburg-Landau equations in the theory of superconductivity,* Sov. Phys. JETP **36**, 1364.

Goy, P., J. M. Raimond, M. Gross, and S. Haroche, 1983, *Observation of cavity-enhanced single-atom spontaneous emission,* Phys. Rev. Lett. **50**, 1903.

Greentree, A. D., C. Tahan, J. H. Cole, and L. C. L. Hollenberg, 2006, *Quantum phase transitions of light,* Nat. Phys. **2**, 856.

Greif, D., T. Uehlinger, G. Jotzu, L. Tarruell, and T. Esslinger, 2013, *Short-range quantum magnetism of ultracold fermions in an optical lattice,* Science **340**, 1307.

Greiner, M., O. Mandel, T. Esslinger, T. W. Hänsch, and I. Bloch, 2002a, *Quantum phase transition from a superfluid to a Mott insulator in a gas of ultracold atoms,* Nature **415**, 39.

Greiner, M., O. Mandel, Theodor W. Hänsch, and I. Bloch, 2002b, *Collapse and revival of the matter wave field of a Bose-Einstein condensate,* Nature **419**, 51.

Greiner, M., C. A. Regal, and D. S. Jin, 2003, *Emergence of a molecular Bose-Einstein condensate from a Fermi gas,* Nature **426**, 537.

Gross, M., and S. Haroche, 1982, *Superradiance: An essay on the theory of collective spontaneous emission,* Physics Reports **93**, 301.

Grover, L. K., 1996, *A fast quantum mechanical algorithm for database search,* in *Annual ACM symposium on theory of computing* (ACM) pp. 212–219.

Hagley, E., X. Maître, G. Nogues, C. Wunderlich, M. Brune, J. M. Raimond, and S. Haroche, 1997, *Generation of Einstein-Podolsky-Rosen pairs of atoms,* Phys. Rev. Lett. **79**, 1.

Hartmann, M. J., F. G. S. L. Brandao, and M. B. Plenio, 2006, *Strongly interacting polaritons in coupled arrays of cavities,* Nat. Phys. **2**, 849.

Hatridge, M., S. Shankar, M. Mirrahimi, F. Schackert, K. Geerlings, T. Brecht, K. M. Sliwa, B. Abdo, L. Frunzio, S. M. Girvin, R. J. Schoelkopf, and M. H. Devoret, 2013, *Quantum back-action of an individual variable-strength measurement,* Science **339**, 178.

Helmer, F., M. Mariantoni, A. G. Fowler, J. von Delft, E. Solano, and F. Marquardt, 2009, *Cavity grid for scalable quantum computation with superconducting circuits,* EPL (Europhysics Letters) **85**, 50007.

Hennessy, K., A. Badolato, M. Winger, D. Gerace, M. Atature, S. Gulde, S. Falt, E. L. Hu, and A. Imamoglu, 2007, *Quantum nature of a strongly coupled single quantum dot-cavity system,* Nature **445**, 896.

Hepp, K., and E. H. Lieb, 1973, *On the superradiant phase transition for molecules in a quantized radiation field: the Dicke maser model,* Annals of Physics **76**, 360.

Hofheinz, M., H. Wang, M. Ansmann, R. C. Bialczak, E. Lucero, M. Neeley, A. D. O'Connell, D. Sank, J. Wenner, J. M. Martinis, and A. N. Cleland, 2009, *Synthesizing arbitrary quantum states in a superconducting resonator,* Nature **459**, 546.

Hofheinz, M., E. M. Weig, M. Ansmann, R. C. Bialczak, E. Lucero, M. Neeley, A. D. O'Connell, H. Wang, J. M. Martinis, and A. N. Cleland, 2008, *Generation of Fock states in a superconducting quantum circuit,* Nature **454**, 310.

Holstein, T., and H. Primakoff, 1940, *Field dependence of the intrinsic domain magnetization of a ferromagnet,* Phys. Rev. **58**, 1098.

Hopfield, J. J., 1958, *Theory of the contribution of excitons to the complex dielectric constant of crystals,* Phys. Rev. **112**, 1555.

Horodecki, R., P. Horodecki, M. Horodecki, and K. Horodecki, 2009, *Quantum entanglement,* Rev. Mod. Phys. **81**, 865.

Houck, A. A., J. A. Schreier, B. R. Johnson, J. M. Chow, Jens Koch, J. M. Gambetta, D. I. Schuster, L. Frunzio, M. H. Devoret, S. M. Girvin, and R. J. Schoelkopf, 2008, *Controlling the spontaneous emission of a superconducting transmon qubit,* Phys. Rev. Lett. **101**, 080502.

Houck, A. A., D. I. Schuster, J. M. Gambetta, J. A. Schreier, B. R. Johnson, J. M. Chow, L. Frunzio, J. Majer, M. H. Devoret, S. M. Girvin, and R. J. Schoelkopf, 2007, *Generating single microwave photons in a circuit,* Nature **449**, 328.

Houck, A. A., H. E. Tureci, and J. Koch, 2012, *On-chip quantum simulation with superconducting circuits,* Nat. Phys. **8**, 292.

Hulet, R. G., E. S. Hilfer, and D. Kleppner, 1985, *Inhibited spontaneous emission by a Rydberg atom,* Phys. Rev. Lett. **55**, 2137.

Hwang, M.-J., and M.-S. Choi, 2012, *Large-scale Schrödinger-cat states and Majorana bound states in coupled circuit-QED systems,* arXiv:1207.0088.

Islam, R., E. E. Edwards, K. Kim, S. Korenblit, C. Noh, H. Carmichael, G. D. Lin, L. M. Duan, C. C. Joseph Wang, J. K. Freericks, and C. Monroe, 2011, *Onset of a quantum phase transition with a trapped ion quantum simulator,* Nat Commun **2**, 377.

Jaksch, D., C. Bruder, J. I. Cirac, C. W. Gardiner, and P. Zoller, 1998, *Cold bosonic atoms in optical lattices,* Phys. Rev. Lett. **81**, 3108.

Jaynes, E.T., and F. W. Cummings, 1963, *Comparison of quantum and semiclassical radiation theories with application to the beam maser,* Proceedings of the IEEE **51** (1), 89.

Johansson, J., S. Saito, T. Meno, H. Nakano, M. Ueda, K. Semba, and H. Takayanagi, 2006, *Vacuum Rabi oscillations in a macroscopic superconducting qubit LC oscillator system,* Phys. Rev. Lett. **96**, 127006.

Johnson, B. R., M. D. Reed, A. A. Houck, D. I. Schuster, Lev S. Bishop, E. Ginossar, J. M. Gambetta, L. DiCarlo, L. Frunzio, S. M. Girvin, and R. J. Schoelkopf, 2010, *Quantum non-demolition detection of single microwave photons in a circuit,* Nat. Phys. **6**, 663.

Johnson, M. W., M. H. S. Amin, S. Gildert, T. Lanting, F. Hamze, N. Dickson, R. Harris, A. J. Berkley, J. Johansson, P. Bunyk, E. M. Chapple, C. Enderud, J. P. Hilton, K. Karimi, E. Ladizinsky, N. Ladizinsky, T. Oh, I. Perminov, C. Rich, M. C. Thom, E. Tolkacheva, C. J. S. Truncik, S. Uchaikin, J. Wang, B. Wilson, and G. Rose, 2011, *Quantum annealing with manufactured spins,* Nature **473**, 194.

Jordan, P., and E. Wigner, 1928, *Über das Paulische Äquivalenzverbot,* Zeitschrift für Physik **47**, 631.

Jördens, R., N. Strohmaier, K. Gunter, H. Moritz, and T. Esslinger, 2008, *A Mott insulator of fermionic atoms in an optical lattice,* Nature **455**, 204.

Josephson, B.D., 1962, *Possible new effects in superconductive tunnelling,* Physics Letters **1**, 251.

Kamerlingh Onnes, H., 1911, *On the sudden change in the rate at which the resistance of mercury disappears,* Commun. Phys. Lab. Univ. Leiden. Suppl. **124c**.

Kane, B. E., 1998, *A silicon-based nuclear spin quantum computer,* Nature **393**, 133.

Kelly, W. R., Z. Dutton, J. Schlafer, B. Mookerji, T. A. Ohki, J. S. Kline, and D. P. Pappas, 2010, *Direct observation of coherent population trapping in a superconducting artificial atom,* Phys. Rev. Lett. **104**, 163601.

Ketterson, J.B., and S.N. Song, 1999, *Superconductivity* (Cambridge University Press).

Kinoshita, T., T. Wenger, and D. S. Weiss, 2006, *A quantum Newton's cradle,* Nature **440**, 900.

Kirchmair, G., B. Vlastakis, Z. Leghtas, S. E. Nigg, H. Paik, E. Ginossar, M. Mirrahimi, L. Frunzio, S. M. Girvin, and R. J. Schoelkopf, 2013, *Observation of quantum state collapse and revival due to the single-photon Kerr effect,* Nature **495**, 205.

Kitaev, A. Y., 2001, *Unpaired Majorana fermions in quantum wires,* Physics-Uspekhi **44**, 131.

Kitaev, A. Y., 2003, *Fault-tolerant quantum computation by anyons,* Annals of Physics **303**, 2.

Knill, E., R. Laflamme, and G. J. Milburn, 2001, *A scheme for efficient quantum computation with linear optics,* Nature **409**, 46.

Koch, J., T. M. Yu, J. Gambetta, A. A. Houck, D. I. Schuster, J. Majer, A. Blais, M. H. Devoret, S. M. Girvin, and R. J. Schoelkopf, 2007, *Charge-insensitive qubit design derived from the Cooper pair box,* Phys. Rev. A **76**, 042319.

Kubo, Y., C. Grezes, A. Dewes, T. Umeda, J. Isoya, H. Sumiya, N. Morishita, H. Abe, S. Onoda, T. Ohshima, V. Jacques, A. Dréau, J.-F. Roch, I. Diniz, A. Auffeves, D. Vion, D. Esteve, and P. Bertet, 2011, *Hybrid quantum circuit with a superconducting qubit coupled to a spin ensemble,* Phys. Rev. Lett. **107**, 220501.

Kuhn, W., 1925, *Über die Gesamtstärke der von einem Zustande ausgehenden Absorptionslinien,* Zeitschrift für Physik A Hadrons and Nuclei **33**, 408.

Kumar, B., and S. Jalal, 2012, *Quantum Ising dynamics and Majorana fermions in the Rabi lattice model,* arXiv:1210.6922.

Lang, C., C. Eichler, L. Steffen, J. M. Fink, M. J. Woolley, A. Blais, and A. Wallraff, 2013, *Correlations, indistinguishability and entanglement in Hong-Ou-Mandel experiments at microwave frequencies,* Nat. Phys. **9**, 345.

Lanyon, B. P., C. Hempel, D. Nigg, M. Müller, R. Gerritsma, F. Zähringer, P. Schindler, J. T. Barreiro, M. Rambach, G. Kirchmair, M. Hennrich, P. Zoller, R. Blatt, and C. F. Roos, 2011, *Universal digital quantum simulation with trapped ions,* Science **334**, 57.

Lanyon, B. P., J. D. Whitfield, G. G. Gillett, M. E. Goggin, M. P. Almeida, I. Kassal, J. D. Biamonte, M. Mohseni, B. J. Powell, M. Barbieri, A. Aspuru-Guzik, and A. G. White, 2010, *Towards quantum chemistry on a quantum computer,* Nat Chem **2**, 106.

Law, C. K., and J. H. Eberly, 1996, *Arbitrary control of a quantum electromagnetic field,* Phys. Rev. Lett. **76**, 1055.

Leek, P. J., J. M. Fink, A. Blais, R. Bianchetti, M. Göppl, J. M. Gambetta, D. I. Schuster, L. Frunzio, R. J. Schoelkopf, and A. Wallraff, 2007, *Observation of Berry's phase in a solid-state qubit,* Science **318**, 1889.

Leggett, A. J., 1980, *Macroscopic quantum systems and the quantum theory of measurement,* Progress of Theoretical Physics Supplement **69**, 80.

Leggett, A. J., and A. Garg, 1985, *Quantum mechanics versus macroscopic realism: Is the flux there when nobody looks?*. Phys. Rev. Lett. **54**, 857.

Lieb, E., T. Schultz, and D. Mattis, 1961, *Two soluble models of an antiferromagnetic chain,* Annals of Physics **16**, 407.

Lieb, E. H., and D. W. Robinson, 1972, *The finite group velocity of quantum spin systems,* Communications in Mathematical Physics **28**, 251.

Lin, Y. J., R. L. Compton, K. Jimenez-Garcia, J. V. Porto, and I. B. Spielman, 2009, *Synthetic magnetic fields for ultracold neutral atoms,* Nature **462**, 628.

Lloyd, S., 1996, *Universal quantum simulators,* Science **273**, 1073.

London, F., 1950, *Superfluids* (John Wiley & Sons).

Loss, Daniel, and David P. DiVincenzo, 1998, *Quantum computation with quantum dots,* Phys. Rev. A **57**, 120.

Lucero, E., R. Barends, Y. Chen, J. Kelly, M. Mariantoni, A. Megrant, P. O'Malley, D. Sank, A. Vainsencher, J. Wenner, T. White, Y. Yin, A. N. Cleland, and J. M. Martinis, 2012, *Computing prime factors with a Josephson phase qubit quantum processor,* Nat. Phys. **8**, 719.

Lutchyn, Roman M., Jay D. Sau, and S. Das Sarma, 2010, *Majorana fermions and a topological phase transition in semiconductor-superconductor heterostructures,* Phys. Rev. Lett. **105**, 077001.

Ma, X.-S., B. Dakic, W. Naylor, A. Zeilinger, and P. Walther, 2011, *Quantum simulation of the wavefunction to probe frustrated Heisenberg spin systems,* Nat. Phys. **7**, 399.

Majer, J., J. M. Chow, J. M. Gambetta, J. Koch, B. R. Johnson, J. A. Schreier, L. Frunzio, D. I. Schuster, A. A. Houck, A. Wallraff, A. Blais, M. H. Devoret, S. M. Girvin, and R. J. Schoelkopf, 2007, *Coupling superconducting qubits via a cavity bus,* Nature **449**, 443.

Makhlin, Y., G. Schön, and A. Shnirman, 2001, *Quantum-state engineering with Josephson-junction devices,* Rev. Mod. Phys. **73**, 357.

Mallet, F., M. A. Castellanos-Beltran, H. S. Ku, S. Glancy, E. Knill, K. D. Irwin, G. C. Hilton, L. R. Vale, and K. W. Lehnert, 2011, *Quantum state tomography of an itinerant squeezed microwave field,* Phys. Rev. Lett. **106**, 220502.

Mallet, F., F. R. Ong, A. Palacios-Laloy, F. Nguyen, P. Bertet, D. Vion, and D. Esteve, 2009, *Single-shot qubit readout in circuit quantum electrodynamics,* Nat. Phys. **5**, 791.

Manucharyan, V. E., J. Koch, L. I. Glazman, and M. H. Devoret, 2009, *Fluxonium: Single Cooper-pair circuit free of charge offsets,* Science **326**, 113.

Mariantoni, M., H. Wang, R. C. Bialczak, M. Lenander, E. Lucero, M. Neeley, A. D. O'Connell, D. Sank, M. Weides, J. Wenner, T. Yamamoto, Y. Yin, J. Zhao, J. M. Martinis, and A. N. Cleland, 2011a, *Photon shell game in three-resonator circuit quantum electrodynamics,* Nat. Phys. **7**, 287.

Mariantoni, M., H. Wang, T. Yamamoto, M. Neeley, R. C. Bialczak, Y. Chen, M. Lenander, E. Lucero, A. D. O'Connell, D. Sank, M. Weides, J. Wenner, Y. Yin, J. Zhao, A. N. Korotkov, A. N. Cleland, and J. M. Martinis, 2011b, *Implementing the quantum von Neumann architecture with superconducting circuits,* Science **334**, 61.

Marquardt, F., and C. Bruder, 2001, *Superposition of two mesoscopically distinct quantum states: Coupling a Cooper-pair box to a large superconducting island,* Phys. Rev. B **63**, 054514.

Martinis, J. M., M. H. Devoret, and J. Clarke, 1985, *Energy-level quantization in the zero-voltage state of a current-biased Josephson junction,* Phys. Rev. Lett. **55**, 1543.

Martinis, J. M., S. Nam, J. Aumentado, and C. Urbina, 2002, *Rabi oscillations in a large Josephson-junction qubit,* Phys. Rev. Lett. **89**, 117901.

Mattis, D. C., and J. Bardeen, 1958, *Theory of the anomalous skin effect in normal and superconducting metals,* Phys. Rev. **111**, 412.

McCumber, D. E., 1968, *Effect of AC impedance on DC voltage-current characteristics of superconductor weak-link junctions,* Journal of Applied Physics **39**, 3113.

Meekhof, D. M., C. Monroe, B. E. King, W. M. Itano, and D. J. Wineland, 1996, *Generation of nonclassical motional states of a trapped atom,* Phys. Rev. Lett. **76**, 1796.

Meissner, W., and R. Ochsenfeld, 1933, *Ein neuer Effekt bei Eintritt der Supraleitfähigkeit,* Naturwissenschaften **21**, 787.

Menzel, E. P., R. Di Candia, F. Deppe, P. Eder, L. Zhong, M. Ihmig, M. Haeberlein, A. Baust, E. Hoffmann, D. Ballester, K. Inomata, T. Yamamoto, Y. Nakamura, E. Solano, A. Marx, and R. Gross, 2012, *Path entanglement of continuous-variable quantum microwaves,* Phys. Rev. Lett. **109**, 250502.

Meschede, D., H. Walther, and G. Müller, 1985, *One-atom maser,* Phys. Rev. Lett. **54**, 551.

Monroe, C., D. M. Meekhof, B. E. King, W. M. Itano, and D. J. Wineland, 1995, *Demonstration of a fundamental quantum logic gate,* Phys. Rev. Lett. **75**, 4714.

Monroe, C., D. M. Meekhof, B. E. King, and D. J. Wineland, 1996, *A "Schrödinger cat" superposition state of an atom,* Science **272**, 1131.

Mooij, J. E., T. P. Orlando, L. Levitov, L. Tian, C. H. van der Wal, and S. Lloyd, 1999, *Josephson persistent-current qubit,* Science **285**, 1036.

Murch, K. W., U. Vool, D. Zhou, S. J. Weber, S. M. Girvin, and I. Siddiqi, 2012, *Cavity-assisted quantum bath engineering,* Phys. Rev. Lett. **109**, 183602.

Nagourney, W., J. Sandberg, and H. Dehmelt, 1986, *Shelved optical electron amplifier: Observation of quantum jumps,* Phys. Rev. Lett. **56**, 2797.

Nakamura, Y., C. D. Chen, and J. S. Tsai, 1997, *Spectroscopy of energy-level splitting between two macroscopic quantum states of charge coherently superposed by Josephson coupling,* Phys. Rev. Lett. **79**, 2328.

Nakamura, Y., Yu. A. Pashkin, and J. S. Tsai, 1999, *Coherent control of macroscopic quantum states in a single Cooper-pair box,* Nature **398**, 786.

Nakamura, Y., Yu. A. Pashkin, T. Yamamoto, and J. S. Tsai, 2002, *Charge echo in a Cooper-pair box,* Phys. Rev. Lett. **88**, 047901.

Nataf, P., and C. Ciuti, 2010a, *Vacuum degeneracy of a circuit QED system in the ultrastrong coupling regime,* Phys. Rev. Lett. **104**, 023601.

Nataf, P., and C. Ciuti, 2010b, *No-go theorem for superradiant quantum phase transitions in cavity QED and counter-example in circuit QED,* Nat Commun **1**, 72.

Neeley, M., R. C. Bialczak, M. Lenander, E. Lucero, M. Mariantoni, A. D. O'Connell, D. Sank, H. Wang, M. Weides, J. Wenner, Y. Yin, T. Yamamoto, A. N. Cleland, and J. M. Martinis, 2010, *Generation of three-qubit entangled states using superconducting phase qubits,* Nature **467**, 570.

Neuhauser, W., M. Hohenstatt, P. Toschek, and H. Dehmelt, 1978, *Optical-sideband cooling of visible atom cloud confined in parabolic well,* Phys. Rev. Lett. **41**, 233.

Neuhauser, W., M. Hohenstatt, P. E. Toschek, and H. Dehmelt, 1980, *Localized visible Ba^+ mono-ion oscillator,* Phys. Rev. A **22**, 1137.

Nielsen, M.A., and I.L. Chuang, 2000, *Quantum Computation and Quantum Information* (Cambridge University Press).

Niemczyk, T., F. Deppe, H. Huebl, E. P. Menzel, F. Hocke, M. J. Schwarz, J. J. Garcia-Ripoll, D. Zueco, T. Hummer, E. Solano, A. Marx, and R. Gross, 2010, *Circuit quantum electrodynamics in the ultrastrong-coupling regime,* Nat. Phys. **6**, 772.

Nigg, S. E., H. Paik, B. Vlastakis, G. Kirchmair, S. Shankar, L. Frunzio, M. H. Devoret, R. J. Schoelkopf, and S. M. Girvin, 2012, *Black-box superconducting circuit quantization,* Phys. Rev. Lett. **108**, 240502.

Niskanen, A. O., K. Harrabi, F. Yoshihara, Y. Nakamura, S. Lloyd, and J. S. Tsai, 2007, *Quantum coherent tunable coupling of superconducting qubits,* Science **316**, 723.

O'Brien, Jeremy L., 2007, *Optical quantum computing,* Science **318**, 1567.

O'Connell, A. D., M. Hofheinz, M. Ansmann, R. C. Bialczak, M. Lenander, E. Lucero, M. Neeley, D. Sank, H. Wang, M. Weides, J. Wenner, J. M. Martinis, and A. N. Cleland, 2010, *Quantum ground state and single-phonon control of a mechanical resonator,* Nature **464**, 697.

Oreg, Y., G. Refael, and F. von Oppen, 2010, *Helical liquids and Majorana bound states in quantum wires,* Phys. Rev. Lett. **105**, 177002.

van Oudenaarden, A., and J. E. Mooij, 1996, *One-dimensional Mott insulator formed by quantum vortices in Josephson junction arrays,* Phys. Rev. Lett. **76**, 4947.

Paik, H., D. I. Schuster, L. S. Bishop, G. Kirchmair, G. Catelani, A. P. Sears, B. R. Johnson, M. J. Reagor, L. Frunzio, L. I. Glazman, S. M. Girvin, M. H. Devoret, and R. J. Schoelkopf, 2011, *Observation of high coherence in Josephson junction qubits measured in a three-dimensional circuit QED architecture,* Phys. Rev. Lett. **107**, 240501.

Palacios-Laloy, A., F. Mallet, F. Nguyen, P. Bertet, D. Vion, D. Esteve, and A. N. Korotkov, 2010, *Experimental violation of a Bell's inequality in time with weak measurement,* Nat. Phys. **6**, 442.

Paredes, B., A. Widera, V. Murg, O. Mandel, S. Folling, I. Cirac, G. V. Shlyapnikov, T. W. Hänsch, and I. Bloch, 2004, *Tonks-Girardeau gas of ultracold atoms in an optical lattice,* Nature **429**, 277.

Perets, H. B., Y. Lahini, F. Pozzi, M Sorel, R. Morandotti, and Y. Silberberg, 2008, *Realization of quantum walks with negligible decoherence in waveguide lattices,* Phys. Rev. Lett. **100**, 170506.

Peruzzo, A., M. Lobino, J. C. F. Matthews, N. Matsuda, A. Politi, K. Poulios, X.-Q. Zhou, Y. Lahini, N. Ismail, K. Wörhoff, Y. Bromberg, Y. Silberberg, M. G. Thompson, and J. L. OBrien, 2010, *Quantum walks of correlated photons,* Science **329**, 1500.

Petersson, K. D., L. W. McFaul, M. D. Schroer, M. Jung, J. M. Taylor, A. A. Houck, and J. R. Petta, 2012, *Circuit quantum electrodynamics with a spin qubit,* Nature **490**, 380.

Petta, J. R., A. C. Johnson, J. M. Taylor, E. A. Laird, A. Yacoby, M. D. Lukin, C. M. Marcus, M. P. Hanson, and A. C. Gossard, 2005, *Coherent manipulation of coupled electron spins in semiconductor quantum dots,* Science **309**, 2180.

Pfeuty, P., 1970, *The one-dimensional Ising model with a transverse field,* Annals of Physics **57**, 79.

Pirkkalainen, J. M., S. U. Cho, Jian Li, G. S. Paraoanu, P. J. Hakonen, and M. A. Sillanpaa, 2013, *Hybrid circuit cavity quantum electrodynamics with a micromechanical resonator,* Nature **494**, 211.

Pla, J. J., K. Y. Tan, J. P. Dehollain, W. H. Lim, J. J. L. Morton, F. A. Zwanenburg, D. N. Jamieson, A. S. Dzurak, and A. Morello, 2013, *High-fidelity readout and control of a nuclear spin qubit in silicon,* Nature **496**, 334.

Polkovnikov, A., K. Sengupta, A. Silva, and M. Vengalattore, 2011, *Colloquium : Nonequilibrium dynamics of closed interacting quantum systems,* Rev. Mod. Phys. **83**, 863.

Pollet, L., 2012, *Recent developments in quantum Monte Carlo simulations with applications for cold gases,* Reports on Progress in Physics **75**, 094501.

Porras, D., and J. I. Cirac, 2004, *Effective quantum spin systems with trapped ions,* Phys. Rev. Lett. **92**, 207901.

Purcell, E. M., 1946, *Spontaneous emission probabilities at radio frequencies,* Phys. Rev. **69**, 674.

Raimond, J. M., M. Brune, and S. Haroche, 2001, *Manipulating quantum entanglement with atoms and photons in a cavity,* Rev. Mod. Phys. **73**, 565.

Reed, M. D., L. DiCarlo, B. R. Johnson, L. Sun, D. I. Schuster, L. Frunzio, and R. J. Schoelkopf, 2010, *High-fidelity readout in circuit quantum electrodynamics using the Jaynes-Cummings nonlinearity,* Phys. Rev. Lett. **105**, 173601.

Reed, M. D., L. DiCarlo, S. E. Nigg, L. Sun, L. Frunzio, S. M. Girvin, and R. J. Schoelkopf, 2012, *Realization of three-qubit quantum error correction with superconducting circuits,* Nature **482**, 382.

Regal, C. A., M. Greiner, and D. S. Jin, 2004, *Observation of resonance condensation of fermionic atom pairs,* Phys. Rev. Lett. **92**, 040403.

Reiche, F., and W. Thomas, 1925, *Über die Zahl der Dispersionselektronen, die einem stationären Zustand zugeordnet sind,* Zeitschrift für Physik A Hadrons and Nuclei **34**, 510.

Rempe, G., H. Walther, and N. Klein, 1987, *Observation of quantum collapse and revival in a one-atom maser,* Phys. Rev. Lett. **58**, 353.

Rigetti, C., J. M. Gambetta, S. Poletto, B. L. T. Plourde, J. M. Chow, A. D. Córcoles, J. A. Smolin, S. T. Merkel, J. R. Rozen, G. A. Keefe, M. B. Rothwell, M. B. Ketchen, and M. Steffen, 2012, *Superconducting qubit in a waveguide cavity with a coherence time approaching 0.1 ms,* Phys. Rev. B **86**, 100506.

Rzażewski, K., K. Wódkiewicz, and W. Żakowicz, 1975, *Phase transitions, two-level atoms, and the A^2 term,* Phys. Rev. Lett. **35**, 432.

Sachdev, S., 1999, *Quantum Phase Transitions* (Cambridge University Press).

Sauter, Th., W. Neuhauser, R. Blatt, and P. E. Toschek, 1986, *Observation of quantum jumps,* Phys. Rev. Lett. **57**, 1696.

Schindler, P., M. Müller, D. Nigg, J. T. Barreiro, E. A. Martinez, M. Hennrich, T. Monz, S. Diehl, P. Zoller, and R. Blatt, 2013, *Quantum simulation of dynamical maps with trapped ions,* Nat. Phys. **9**, 361.

Schmidt, S., D. Gerace, A. A. Houck, G. Blatter, and H. E. Türeci, 2010, *Nonequilibrium delocalization-localization transition of photons in circuit quantum electrodynamics,* Phys. Rev. B **82**, 100507.

Schmidt, S., and J. Koch, 2013, *Circuit QED lattices: Towards quantum simulation with superconducting circuits,* Annalen der Physik **525**, 395.

Schmidt-Kaler, F., H. Haffner, M. Riebe, S. Gulde, G. P. T. Lancaster, T. Deuschle, C. Becher, C. F. Roos, J. Eschner, and R. Blatt, 2003, *Realization of the Cirac-Zoller controlled-NOT quantum gate,* Nature **422**, 408.

Schneider, U., L. Hackermüller, S. Will, Th. Best, I. Bloch, T. A. Costi, R. W. Helmes, D. Rasch, and A. Rosch, 2008, *Metallic and insulating phases of repulsively interacting fermions in a 3D optical lattice,* Science **322**, 1520.

Schoelkopf, R. J., and S. M. Girvin, 2008, *Wiring up quantum systems,* Nature **451**, 664.

Schollwöck, U., 2011, *The density-matrix renormalization group in the age of matrix product states,* Annals of Physics **326**, 96.

Schrieffer, J.R., 1983, *Theory of superconductivity* (Advanced Book Program, Perseus Books).

Schuster, D. I., A. A. Houck, J. A. Schreier, A. Wallraff, J. M. Gambetta, A. Blais, L. Frunzio, J. Majer, B. Johnson, M. H. Devoret, S. M. Girvin, and R. J. Schoelkopf, 2007, *Resolving photon number states in a superconducting circuit,* Nature **445**, 515.

Schuster, D. I., A. Wallraff, A. Blais, L. Frunzio, R.-S. Huang, J. Majer, S. M. Girvin, and R. J. Schoelkopf, 2005, *AC stark shift and dephasing of a superconducting qubit strongly coupled to a cavity field,* Phys. Rev. Lett. **94**, 123602.

Scully, M.M.O., and M.S. Zubairy, 1997, *Quantum Optics* (Cambridge University Press).

Sears, A. P., A. Petrenko, G. Catelani, L. Sun, H. Paik, G. Kirchmair, L. Frunzio, L. I. Glazman, S. M. Girvin, and R. J. Schoelkopf, 2012, *Photon shot noise dephasing in the strong-dispersive limit of circuit QED,* Phys. Rev. B **86**, 180504.

Shapiro, S., 1963, *Josephson currents in superconducting tunneling: The effect of microwaves and other observations,* Phys. Rev. Lett. **11**, 80.

Shor, P., 1994, *Polynomial-time algorithms for prime factorization and discrete logarithms on a quantum computer,* in *Proc. 35th Annual Symp. Foundations of Computer Science*, pp. 124–134.

Shor, P. W., 1995, *Scheme for reducing decoherence in quantum computer memory,* Phys. Rev. A **52**, R2493.

Siddiqi, I., R. Vijay, F. Pierre, C. M. Wilson, M. Metcalfe, C. Rigetti, L. Frunzio, and M. H. Devoret, 2004, *RF-driven Josephson bifurcation amplifier for quantum measurement,* Phys. Rev. Lett. **93**, 207002.

Siewert, J., T. Brandes, and G. Falci, 2009, *Advanced control with a Cooper-pair box: Stimulated Raman adiabatic passage and Fock-state generation in a nanomechanical resonator,* Phys. Rev. B **79**, 024504.

da Silva, M. P., D. Bozyigit, A. Wallraff, and A. Blais, 2010, *Schemes for the observation of photon correlation functions in circuit QED with linear detectors,* Phys. Rev. A **82**, 043804.

Simmonds, R. W., K. M. Lang, D. A. Hite, S. Nam, D. P. Pappas, and J. M. Martinis, 2004, *Decoherence in Josephson phase qubits from junction resonators,* Phys. Rev. Lett. **93**, 077003.

Simon, J., W. S. Bakr, R. Ma, M. E. Tai, P. M. Preiss, and M. Greiner, 2011, *Quantum simulation of antiferromagnetic spin chains in an optical lattice,* Nature **472**, 307.

Sjöqvist, E., D. M. Tong, L. M. Andersson, B. Hessmo, M. Johansson, and K. Singh, 2012, *Non-adiabatic holonomic quantum computation,* New Journal of Physics **14**, 103035.

Skribanowitz, N., I. P. Herman, J. C. MacGillivray, and M. S. Feld, 1973, *Observation of Dicke superradiance in optically pumped hf gas,* Phys. Rev. Lett. **30**, 309.

Somaroo, S., C. H. Tseng, T. F. Havel, R. Laflamme, and D. G. Cory, 1999, *Quantum simulations on a quantum computer,* Phys. Rev. Lett. **82**, 5381.

Sørensen, A., and K. Mølmer, 1999, *Quantum computation with ions in thermal motion,* Phys. Rev. Lett. **82**, 1971.

Srinivasan, S. J., A. J. Hoffman, J. M. Gambetta, and A. A. Houck, 2011, *Tunable coupling in circuit quantum electrodynamics using a superconducting charge qubit with a v-shaped energy level diagram,* Phys. Rev. Lett. **106**, 083601.

Steffen, L., A. Fedorov, M. Oppliger, Y. Salathe, P. Kurpiers, M. Baur, G. Puebla-Hellmann, C. Eichler, and Wallraff A., 2013, *Realization of deterministic quantum teleportation with solid state qubits,* arXiv:1302.5621.

Steffen, M., S. Kumar, D. P. DiVincenzo, J. R. Rozen, G. A. Keefe, M. B. Rothwell, and M. B. Ketchen, 2010, *High-coherence hybrid superconducting qubit,* Phys. Rev. Lett. **105**, 100502.

Stewart, W. C., 1968, *Current-voltage characteristics of Josephson junctions,* Applied Physics Letters **12**, 277.

Tavis, M., and F. W. Cummings, 1968, *Exact solution for an n-molecule—radiation-field Hamiltonian,* Phys. Rev. **170**, 379.

Teufel, J. D., D. Li, M. S. Allman, K. Cicak, A. J. Sirois, J. D. Whittaker, and R. W. Simmonds, 2011, *Circuit cavity electromechanics in the strong-coupling regime,* Nature **471**, 204.

Thomas, W., 1925, *Über die Zahl der Dispersionselektronen, die einem stationären Zustand zugeordnet sind. (Vorläufige Mitteilung),* Naturwissenschaften **13**, 627.

Thompson, R. J., G. Rempe, and H. J. Kimble, 1992, *Observation of normal-mode splitting for an atom in an optical cavity,* Phys. Rev. Lett. **68**, 1132.

Tinkham, M., 1996, *Introduction to superconductivity*, Dover Books on Physics Series (Dover Publications, Incorporated).

Trotter, H. F., 1959, *On the product of semi-groups of operators,* Proc. Amer. Math. Soc. **10**, 545.

Trotzky, S., Y-A. Chen, A. Flesch, I. P. McCulloch, U. Schollwöck, J. Eisert, and I. Bloch, 2012, *Probing the relaxation towards equilibrium in an isolated strongly correlated one-dimensional Bose gas,* Nat. Phys. **8**, 325.

Van Dyck, R. S., P. B. Schwinberg, and H. G. Dehmelt, 1987, *New high-precision comparison of electron and positron g factors,* Phys. Rev. Lett. **59**, 26.

Vandersypen, L. M. K., and I. L. Chuang, 2005, *Nmr techniques for quantum control and computation,* Rev. Mod. Phys. **76**, 1037.

Vandersypen, L. M. K., M. Steffen, G. Breyta, C. S. Yannoni, M. H. Sherwood, and I. L. Chuang, 2001, *Experimental realization of Shor's quantum factoring algorithm using nuclear magnetic resonance,* Nature **414**, 883.

Viehmann, O., J. von Delft, and F. Marquardt, 2012a, *Reply to Comment on "Superradiant phase transitions and the standard description of circuit QED,* arXiv:1202.2016.

Viehmann, O., C. Eltschka, and J. Siewert, 2011, *Polynomial invariants for discrimination and classification of four-qubit entanglement,* Phys. Rev. A **83**, 052330.

Viehmann, O., C. Eltschka, and J. Siewert, 2012b, *Rescaling multipartite entanglement measures for mixed states,* Applied Physics B: Lasers and Optics **106**, 533.

Vijay, R., C. Macklin, D. H. Slichter, S. J. Weber, K. W. Murch, R. Naik, A. N. Korotkov, and I. Siddiqi, 2012, *Stabilizing Rabi oscillations in a superconducting qubit using quantum feedback,* Nature **490**, 77.

Vijay, R., D. H. Slichter, and I. Siddiqi, 2011, *Observation of quantum jumps in a superconducting artificial atom,* Phys. Rev. Lett. **106**, 110502.

Vion, D., A. Aassime, A. Cottet, P. Joyez, H. Pothier, C. Urbina, D. Esteve, and M. H. Devoret, 2002, *Manipulating the quantum state of an electrical circuit,* Science **296**, 886.

Voss, Richard F., and Richard A. Webb, 1981, *Macroscopic quantum tunneling in 1-μm nb Josephson junctions,* Phys. Rev. Lett. **47**, 265.

van der Wal, C. H., A. C. J. ter Haar, F. K. Wilhelm, R. N. Schouten, C. J. P. M. Harmans, T. P. Orlando, S. Lloyd, and J. E. Mooij, 2000, *Quantum superposition of macroscopic persistent-current states,* Science **290**, 773.

Wallraff, A., D. I. Schuster, A. Blais, L. Frunzio, R.-S. Huang, J. Majer, S. Kumar, S. M. Girvin, and R. J. Schoelkopf, 2004, *Strong coupling of a single photon to a superconducting qubit using circuit quantum electrodynamics,* Nature **431**, 162.

Wallraff, A., D. I. Schuster, A. Blais, L. Frunzio, J. Majer, M. H. Devoret, S. M. Girvin, and R. J. Schoelkopf, 2005, *Approaching unit visibility for control of a superconducting qubit with dispersive readout,* Phys. Rev. Lett. **95**, 060501.

Walls, D.F., and G.J. Milburn, 1994, *Quantum Optics* (Springer-Verlag).

Wang, Y. K., and F. T. Hioe, 1973, *Phase transition in the Dicke model of superradiance,* Phys. Rev. A **7**, 831.

Wiesner, S. J., 1983, *Conjugate coding,* SIGACT News **15**, 78.

Wilczek, F., and A. Zee, 1984, *Appearance of gauge structure in simple dynamical systems,* Phys. Rev. Lett. **52**, 2111.

Wilson, C. M., G. Johansson, A. Pourkabirian, M. Simoen, J. R. Johansson, T. Duty, F. Nori, and P. Delsing, 2011, *Observation of the dynamical Casimir effect in a superconducting circuit,* Nature **479**, 376.

Wineland, D., P. Ekstrom, and H. Dehmelt, 1973, *Monoelectron oscillator,* Phys. Rev. Lett. **31**, 1279.

Wineland, D. J., R. E. Drullinger, and F. L. Walls, 1978, *Radiation-pressure cooling of bound resonant absorbers,* Phys. Rev. Lett. **40**, 1639.

Wootters, W. K., and W. H. Zurek, 1982, *A single quantum cannot be cloned,* Nature **299**, 802.

Yang, C.-P., S.-I Chu, and S. Han, 2003, *Possible realization of entanglement, logical gates, and quantum-information transfer with superconducting-quantum-interference-device qubits in cavity QED,* Phys. Rev. A **67**, 042311.

Yoshie, T., A. Scherer, J. Hendrickson, G. Khitrova, H. M. Gibbs, G. Rupper, C. Ell, O. B. Shchekin, and D. G. Deppe, 2004, *Vacuum Rabi splitting with a single quantum dot in a photonic crystal nanocavity,* Nature **432**, 200.

You, J. Q., and F. Nori, 2003, *Quantum information processing with superconducting qubits in a microwave field,* Phys. Rev. B **68**, 064509.

Yurke, B., and J. S. Denker, 1984, *Quantum network theory,* Phys. Rev. A **29**, 1419.

Zanardi, P., and M. Rasetti, 1999, *Holonomic quantum computation,* Physics Letters A **264**, 94.

Acknowledgments

I am greatly indebted to my PhD advisors Florian Marquardt and Jan von Delft. Florian guided me through the work on this thesis. Without his expertise and creativity, this thesis would not have been possible. Jan's advice, provided at the important stages of the work, was also invaluable. I would like to mention that I always enjoyed working with and learning from Florian and Jan, and I am very grateful for their support in various ways.

I appreciated very much to be engaged in collaborations with Christopher Eltschka, Jens Siewert, Edward Henry, Andrew Schmidt, and Irfan Siddiqi.

A part of the work on this thesis was done in the group of Irfan Siddiqi at UC Berkeley. I would like to thank him and the members of his group for their hospitality.

Many thanks to Dennis Schimmel and Boris Nowak for help with proofreading, and to all my colleagues at the LMU Munich and the FAU Erlangen for the friendly working atmosphere.

Most importantly, I am deeply grateful for help whenever needed from my dear parents and my dear brother, and for continuous support from my beloved Aleksandra.

Finally, I gratefully acknowledge funding from the German Research Foundation (DFG) through the SFB 631 and the Cluster of Excellence "Nanosystems Initiative Munich" (NIM).